UNIVERSITÀ
DEGLI STUDI
DI BRESCIA

Dottorato di ricerca in
*Ingegneria Civile, Ambientale, della Cooperazione*
*Internazionale e di Matematica*

Settore scientifico-disciplinare
*ICAR/08 Scienza delle Costruzioni*

*Metodi e Modelli Matematici per l'Ingegneria*

Ciclo XXXVI

# Modeling pathogens and cells actin-based motility

Dottoranda

***Claudia Bonanno***

Supervisore

***Prof. Alberto Salvadori***

Co-supervisore

***Prof. Vivek Shenoy***, University of Pennsylvania

# Contents

## I Pathogens ABM 23

# Abstract

In this thesis, we theoretically investigate the actin-based motility (ABM) of pathogens and cells.

ABM refers to the movement of several biological systems powered by the polymerization and depolymerization of actin filaments. Actin is a protein that can chemically transform from a monomer form (G-actin) into a network form (F-actin) and vice versa. It plays a crucial role in eukaryotic cells by providing structural support and facilitating various cellular processes. In ABM, the assembly and disassembly of actin filaments generate the force necessary for promoting movement and deformation of several biological systems. In this thesis, we study two phenomena that are particularly prominent in eukaryotic cells: pathogen ABM and cell ABM.

Pathogen ABM refers to the ability of certain microorganisms that cause diseases to move within host cells by hijacking the host cell's actin cytoskeleton. This phenomenon is particularly well studied in certain bacteria and parasites that have evolved mechanisms to exploit the host cell's machinery for their movement and survival. One of the most well-known examples of the pathogen ABM is the bacterium Listeria monocytogenes. Once inside the host cell, Listeria uses a protein called ActA to recruit host cell actin and induce the polymerization of actin filaments. These actin filaments form a tail-like structure at one end of the bacterium, propelling it through the host cell cytoplasm and allowing it to spread from cell to cell without exposure to the extracellular environment or the host immune system. Pathogens that exploit ABM often possess specific virulence factors or proteins that manipulate the host cell's actin dynamics. These mechanisms allow pathogens to move within the host, disseminate, and establish infection while avoiding detection by the host immune system.

Cell ABM, instead, refers to the ability of eukaryotic cells to move and change their shape through the dynamic assembly and disassembly of actin filaments in the cytoskeleton. This process is essential for many physiological functions, including cell migration, immune responses, and tissue development. Regulation of actin dynamics is tightly controlled by various signaling pathways and regulatory proteins. For example, the Arp2/3 complex and formins are proteins that play a role in nucleating actin filaments and promoting their growth. The dynamic nature of actin allows cells to respond to external signals, adapt to their environment, and perform essential functions for development, tissue repair, and immune responses.

Because pathogen and cell ABM share common features, their behavior can be investigated through similar continuum multi-physical frameworks. Specifically, we herein illustrate two original models, both based on a continuum multi-physics model, stemming from chemotransport-mechanics continuity equations that account for the actin chemical kinetics. The core of these two models is represented by the difference in the partial molar volumes between F-actin and G-actin, which embodies the mechanical essence of the polymerization motor. The rearrangement of monomers results in a volume variation, which is captured by a multiplicative decomposition of the deformation gradient into chemical and elastic parts, with the chemical part motivated by the actin chemical transformation from a monomer form into a polymerized network form and vice versa.

The pathogen ABM is represented by the first model. It captures the general features of pathogen motility observed in experimental studies, including the signal dependence of the polymerization of the F-actin network on the bacterium tail and the F-actin network distribution during pathogen motility. The second model, inspired by the first one, extends the pathogen ABM model to represent cell ABM, encompassing the lamellipodia protrusion mechanism at the leading edge of the cell. Additionally, some results that come from the Deshpande-McMeeking model for F-actin network contractility are obtained, and two different theories that model cell-substrate interaction are introduced. The former theory is an original contribution representing at a continuum level the receptor relocation and complex formation on an advecting cellular membrane. The latter, already present in the literature, is a probabilistic theory, that extensively studies the role of the viscoelastic behavior of the substrate on cell spreading and motility. For completeness, the extensive bibliographic research that was carried out during the Ph.D. is illustrated to have a general overview of the models already present in the literature representing cellular adhesion, cellular contractility, and receptor relocation on the advecting membrane.

We believe that elucidating the phenomena that underlie ABM may be of paramount importance for describing, interpreting, and predicting the key mechanisms that govern the behavior of several biological systems.

# Compendio

In questa tesi, approfondiamo a livello teorico la motilità basata sull' actina (ABM) di agenti patogeni e cellule.

La motilità basata sull' actina (ABM) si riferisce al movimento di diversi sistemi biologici dovuto alla polimerizzazione e/o depolimerizzazione dei filamenti di actina. L' actina è una proteina in grado di trasformarsi chimicamente in un network di filamenti (F-actina) partendo da una forma monomerica (G-actina) e viceversa. Essa svolge un ruolo cruciale nelle cellule eucariote, fornendo supporto strutturale e facilitando vari processi cellulari. Nell' ABM, l' assemblaggio e il disassemblaggio dei filamenti di actina generano la forza necessaria per promuovere il movimento e la deformazione di diversi sistemi biologici. In questa tesi studiamo due processi particolarmente importanti nelle cellule eucariotiche: l' ABM dei patogeni e l' ABM delle cellule.

La motilità basata sull' actina di agenti patogeni si riferisce alla capacità di alcuni microrganismi che causano malattie di muoversi all' interno delle cellule ospiti modificandone il citoscheletro di actina. Questo fenomeno è particolarmente studiato in alcuni batteri e parassiti che hanno sviluppato la capacità di sfruttare i meccanismi di funzionamento della cellula ospite per il proprio movimento e la propria sopravvivenza. Uno degli esempi più noti di motilità basata sull' actina riguarda il batterio Listeria monocytogenes. Una volta all' interno della cellula, il Listeria utilizza una proteina chiamata "ActA" per reclutare l' actina cellulare e indurre la polimerizzazione dei filamenti di actina. Questi filamenti formano una struttura a coda ad un' estremità del batterio, che permette al batterio di spingersi all'interno del citoplasma cellulare e di diffondersi da cellula a cellula senza esporsi all' ambiente extracellulare o al sistema immunitario ospite. Gli agenti patogeni che sfruttano la motilità basata sull' actina spesso possiedono specifici fattori di virulenza o proteine che manipolano la dinamica dell' actina. Questi meccanismi consentono agli agenti patogeni di spostarsi all' interno dell' ospite, diffondendo l' infezione e evitando di essere rilevati del

sistema immunitario ospite.

La motilità cellulare basata sull' actina, invece, si riferisce alla capacità delle cellule eucariote di muoversi e cambiare forma attraverso l' assemblaggio e il disassemblaggio dinamico dei filamenti di actina nel citoscheletro. Questo processo è essenziale per molte funzioni fisiologiche, tra cui la migrazione cellulare, le risposte immunitarie e lo sviluppo dei tessuti. La regolazione della dinamica dell' actina è strettamente controllata da varie vie di segnalazione e proteine regolatrici. Ad esempio, il complesso Arp2/3 e le formine sono proteine che svolgono un ruolo nella nucleazione dei filamenti di actina e nella promozione della loro crescita. La natura dinamica dell' actina consente alle cellule di rispondere a segnali esterni, adattarsi al loro ambiente e svolgere funzioni essenziali per lo sviluppo, la riparazione dei tessuti e le risposte immunitarie.

Poiché l' ABM del patogeno e della cellula condividono caratteristiche comuni, il loro comportamento può essere studiato attraverso modelli multifisici continui simili. Nello specifico, qui illustriamo due modelli originali, entrambi basati su un modello multi-fisico del continuo, derivanti da equazioni di continuità chemio-meccaniche-di-trasporto che tengono conto della cinetica chimica dell' actina. Il cuore di questi due modelli, che costituisce il motore della polimerizzazione, è rappresentato dalla differenza dei volumi molari parziali tra F-actina e G-actina. Il riarrangiamento dei monomeri, infatti, comporta una variazione di volume, che viene rappresentata meccanicamente dalla decomposizione moltiplicativa del gradiente di deformazione in parte chimica ed elastica, con la parte chimica motivata dalla trasformazione chimica dell' actina da una forma monomerica a una forma polimerizzata e viceversa.

Il processo di ABM per il patogeno è rappresentato dal primo modello. Questo modello riproduce le caratteristiche generali della motilità dei patogeni osservate negli studi sperimentali, inclusa la dipendenza dal segnale della polimerizzazione della rete di F-actina sulla coda del batterio e la distribuzione della rete di F-actina durante la motilità dei patogeni. Il secondo modello, ispirato al primo, estende il modello di ABM del patogeno per descrivere l' ABM cellulare, in particolare il meccanismo di protrusione dei lamellipodi sul fronte della cellula.

Inoltre, vengono mostrati alcuni risultati che provengono dal modello Deshpande - McMeeking per la contrattilità della rete di F-actina e vengono presentate due diverse teorie che rappresentano l'interazione cellula-substrato. La prima teoria è un contributo originale che descrive attraverso un modello continuo la rilocazione dei recettori e la formazione di complessi su una membrana cellulare avvettrice. La seconda teoria, già presente in letteratura, è una teoria probabilistica, che studia approfonditamente il ruolo della viscoelastà dell' ECM sulla diffusione e motilità cellulare. Per completezza, inoltre, è stata riportata l'estesa ricerca bibliografica realizzata per avere una panoramica generale dei modelli già presenti in letteratura che rappresentano l'adesione cellulare, la contrattilità cellulare e la rilocazione di recettori sulla membrana cellulare.

Riteniamo che chiarire i processi alla base dell' ABM possa essere di fondamentale importanza per descrivere, interpretare e prevedere i meccanismi chiave che regolano il comportamento di diversi sistemi biologici.

# Chapter 1

# Introduction

Actin is one of the most powerful and abundant proteins in eukaryotic cells. Like molecular motors such as myosin, actin can generate physical forces that are responsible for several biological systems' movement and deformation (see figure 1.1) [1]. For example, locomotion of certain types of cells, such as fibroblast, requires two types of forces, i.e., protrusion and traction, which are both actin-dependent. The protrusion force allows the extension of the cell's leading edge margin forward, and the traction force allows the translocation of the rear cell body. Lipid vesicles are another type of biological system that is drastically deformed by actin. When the monomer actin is enclosed in a lipid vesicle and polymerization is induced by a salt concentration increment, the vesicle transforms from a roughly spherical shape into flattened disks with filopodial-like protrusions. Actin polymerization is also often employed to generate forces during fertilization. When the sea cucumber Thyone comes into contact with the egg jelly coat, it triggers a rapid actin polymerization reaction, that leads to the extension of an acrosomal process, allowing the sperm plasma membrane to come into contact and combine with the egg's plasma membrane. A similar process occurs during Chlamydomonas mating. Cells of opposite mating types (plus and minus) perceive each other through specific adhesion receptors on their flagella, and the plus mating type extends a fertilization tubule (a membrane-bound bundle of actin filaments resembling a miniature Thyone acrosome) to encounter the minus mating type. In these cases, water influx likely contributes to force generation through a hydrostatic mechanism, assisting in the extension of the membrane [1].

All these biological systems are extremely complicated, and most of them require several types of force-generation mechanisms to perform deformations

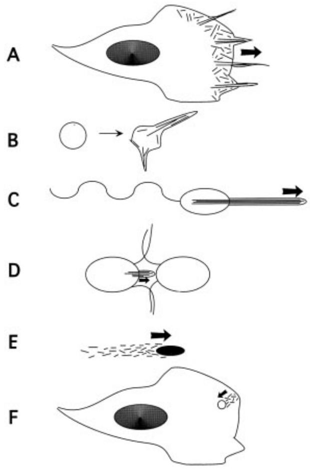

Figure 1.1: Collection of systems in which actin polymerization is linked to the generation of pushing force, with the protrusion forces indicated by the bold arrows. A) Lamellipodial and filopodial protrusion; B) Distension of an actin-containing liposome; C) Extension of the acrosomal process from Thyone sperm; D) Extension of a fertilization tubule from a Chlamydomonas cell of the plus mating type toward the minus mating type partner; E) Actin-based movement of Listeria monocytogenes; F) Inward movement of a nascent endosome [1]. Figure from [1].

and movements. Therefore, the study of the polymerization motor was initially conducted on a specific biological system that only needs actin polymerization to generate motion. This is about the ABM of intracellular bacterial and viral pathogens, the most familiar examples being Listeria monocytogenes and Shigella flexneri. These bacteria make use of particular virulence factors emitted near their surface to catalyze local polymerization of actin filaments, generating an *actin-rich comet tail*, that triggers the bacteria motion inside the cell [1].

Actin filament behavior in the *actin comet tail* is reminiscent of a simpler form of actin dynamics seen in lamellipodia, in which bacteria seem to imitate a segment of the leading edge of moving cells. The rate at which bacteria move through the cytoplasm corresponds to the rate of new actin filament formation at the front of the *actin comet tail.* It is worth noting that there is no identified myosin isoform associated with the *actin comet tail*, and the broad-spectrum myosin ATPase inhibitor butanedione monoxime, which broadly targets myosin, does not affect bacterial movement [1].

It follows that it is broadly recognized that actin polymerization, rather than myosin ATPase activity, is the same motor for bacterial movement as for cell protrusion. Recently, it was reported that *actin-rich comet tails* is also generated in normal, uninfected cells during endocytosis. *Actin comet tails* are noticed actively pushing nascent endosomes toward the cell interior, and it seems that the endosomes detach from the membrane with a rapid surge of actin polymerization. This mechanism may be a way for endosomes to transport themselves to ready microtubule tracks [1].

What ties together all these different types of actin-based movements is the common observation that force appears to emerge when a group of actin filaments undergoes polymerization in close proximity to a barrier or a load. This load could be the cell's plasma membrane, a bacterium, or an endosome. The assembly of actin filaments may take the form of a bundle (as in filopodia, Thyone sperm, and Chlamydomonas) or a cross-linked network (as seen in lamellipodia, pseudopodia, and *actin comet tails*) [2]. What is notable is that in all these phenomena, the actin filament assembly by itself seems capable of pushing the barrier forward, and there is no requirement to invoke myosin for any of these cases [1].

In this chapter, we analyze ABM from a biological and mechanical viewpoint, illustrating the biological phenomena that are present in all ABM processes. In the next chapters, we specify the processes involved in pathogens and cell ABM, introducing the chemo-transport-mechanical models representing these two phenomena.

## 1.1 Monomer and filamentous forms of actin

In cells, actin occurs in two distinct states: the monomeric form, G-actin, and the filamentous form, F-actin. The G-actin can be referred to as the globular form or subunit form of actin. When actin subunits polymerize, they can assemble head-to-tail, forming filamentous actin, which has a right-handed-double-helix-like structure consisting of two strands that spiral around the axis of the polymer (see figure 1.2). The overall diameter of the polymer is approximately 7-9 nm wide [3]. Since the asymmetrical actin subunits within a filament all orient in the same direction, these filaments exhibit polarity and possess structurally distinct ends: a slower-growing minus end and a faster-growing plus end. The minus end is often referred to as the "pointed end", while the plus end is termed the "barbed end". This nomenclature is derived from the "arrowhead" appearance created by the complex formed between actin filaments and the motor protein myosin. Inside the filament, the subunits are arranged such that their nucleotide-binding cleft faces the minus end [4]. Regulation of actin filament formation is a crucial mechanism through which cells manage their shape and movement. Although small oligomers of actin subunits can spontaneously assemble, they are inherently

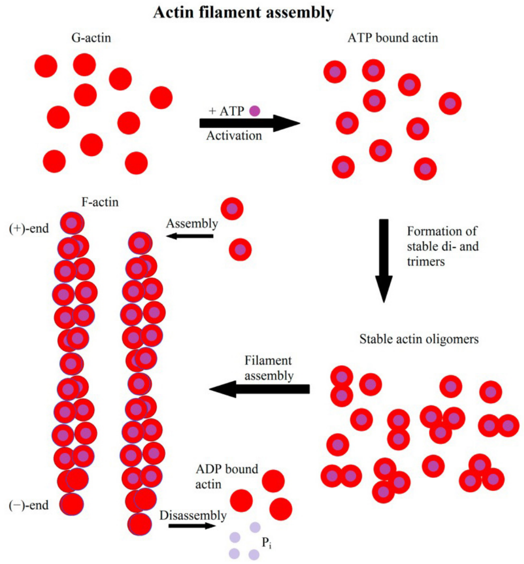

Figure 1.2: The process of actin filament formation follows a scheme. Initially, G-actin binds to ATP. Subsequently, it forms stable di- or trimers, and ultimately, filaments elongate through the addition of monomers. Hydrolysis of ATP to ADP introduces a distinction between the fast-growing (+)-end and the slower-growing or dissociating (-)-end [2]. Figure from [2]

unstable and easily disassembled because each monomer is bound to only one or two other monomers. To establish a new actin filament, the subunits must come together to form an initial aggregate or nucleus. This nucleus is stabilized by multiple subunit-subunit contacts and can then be rapidly elongated by the addition of more subunits. This process, known as filament nucleation, is primarily constrained by the production of dimers and trimers [4].

Cells regulate their shape and movement by controlling actin filament formation. Small actin subunit oligomers can spontaneously assemble, but their instability and tendency to disassemble quickly arise because each monomer is bound to only one or two other monomers. To initiate the formation of a new actin filament, subunits must come together to form an initial aggregate, or nucleus, which is stabilized by multiple subunit-subunit contacts. Subsequently, rapid elongation occurs through the addition of more subunits. This process is known as filament nucleation and is primarily restricted by the generation of dimers and trimers [4]. Once the trimer state is attained, the process of filament nucleation accelerates quickly, contingent upon the availability of the G-actin pool (refer to figure 1.2) [2].

The instability of the smaller actin aggregates creates a kinetic barrier to nucleation. When polymerization begins, a barrier introduces a lag phase during which no filaments are observed. Despite this, within this lag phase, a few of the small, unstable aggregates successfully transition to a more stable form resembling an actin filament. This sets the stage for a phase of rapid filament elongation, which is characterized by the quick addition of subunits to the ends of the nucleated filaments. Ultimately, as the concentration of actin monomers decreases, the system approaches a steady state in which the rate of adding new subunits to the filament ends precisely balances the rate of subunit dissociation [4].

Neglecting external energy input that could reverse the reaction, the polymerization process is governed by the difference in chemical potential (Gibb's free energy) between the free monomer form and the polymer form of a protein subunit, which is dictated by the effective and the critical concentration of subunits in the solution. At chemical equilibrium, the rate of addition of new subunits to the filament ends is exactly balanced by the rate of subunit dissociation

$$k_{on}[C] = k_{off} \,,$$

where $C$ is the free subunit concentration. When the free subunit concentration remaining in the solution is at equilibrium, $C$ is typically called the "critical concentration" and it is defined as

$$C = C_c = \frac{k_{off}}{k_{on}} \,,$$

which is equal to the dissociation constant, $K_d$ and the inverse of the equilibrium constant, $K$ [1].

When the subunit free energy in solution is greater than the subunit free energy in the polymer, namely when the subunit concentration in solution is higher than the critical concentration, filaments elongate spontaneously; otherwise, filaments lose subunits (when the subunit concentration in solution is less then the critical concentration and the subunit free energy in the solution is less than the subunit free energy in the polymer). In a test tube with actin, the $C_c$ for actin polymerization - that is, the free actin monomer concentration at which the fraction of actin in the polymer stops increasing - is about 0.2 *micromole* [4]. Because the cellular concentration of unpolymerized actin is generally higher, several mechanisms to avoid polymerization of monomeric actin when not necessary have been developed by cells [1].

In most biological systems, cells use external energy input to reverse the reaction and prevent polymerization from reaching its conclusion. This external energy input is typically driven by the hydrolysis of nucleoside triphosphate ATP, a process catalyzed by actin. The coupling between polymerization and nucleotide hydrolysis observed in actin and tubulin allows for continuous and steady polymerization without reaching chemical equilibrium. While the hydrolysis of free actin subunits occurs at a slow rate, its rate is accelerated when these subunits become part of filaments [1]. Following ATP hydrolysis, the free phosphate group is released from each subunit, but the ADP remains trapped within the filament structure. Consequently, two distinct types of filament structures can coexist: one with the "T form" of the nucleotide bound (ATP) and another with the "D form" bound (ADP) [4].

When the nucleotide undergoes hydrolysis, a significant portion of the free energy, released through the cleavage of the high-energy phosphate-phosphate bond, becomes stored in the polymer. In other words, the free energy of the D-containing polymer is higher than that of the T-containing polymer. As a result, the critical concentration $C_c = k_{off}/k_{on}$ (the dissociation equilibrium constant) for the D-form of the polymer is greater than that for the T-form of the same polymer. It follows that D-form polymers shrink while T-form polymers grow when the actual free subunit concentration is located between these two critical concentrations [1].

In living cells, most soluble actin subunits are in the T form, as the free concentration of ATP is approximately 10-fold higher than that of ADP [1]. Over time, there is an increasing likelihood that ATP is hydrolyzed in actin subunits. Whether the subunit at each end of a filament is in the T or D form depends on the rate of this hydrolysis compared with the rate of subunit addition. If the concentration of actin monomers is higher than the critical concentration for both T-form and D-form polymers, subunits will be added to both ends before the nucleotides in the previously added subunits undergo hydrolysis. Consequently, the tips of the actin filament will maintain the T-form. In contrast, if the subunit concentration is below the critical concentrations for both T-form and D-form polymers, hydrolysis may occur before the next subunit is added, resulting in both ends of the filament being in the D form, causing filament shrinkage [4].

In cases of intermediate concentrations of actin subunits, the rate of subunit addition can be faster than nucleotide hydrolysis at the plus end but slower than nucleotide hydrolysis at the minus end. In this scenario, the plus end of the filament remains in the T conformation, while the minus end adopts the D conformation. This leads to a net addition of subunits at the plus end while simultaneously losing subunits from the minus end, a dynamic process known as

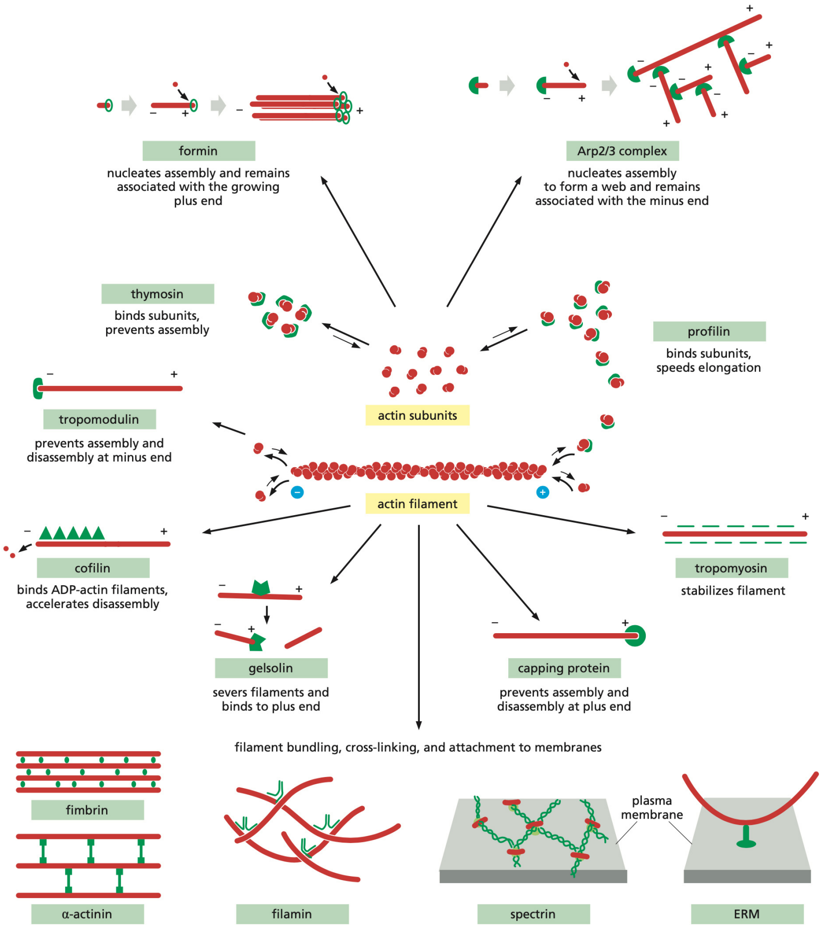

Figure 1.3: Some of the key accessory proteins of the actin cytoskeleton, with each major type represented by an example, excluding the myosin motor proteins [4]. Figure from [4].

filament "treadmilling" [4].

At a specific intermediate subunit concentration, the growth of the filament at the barbed end is precisely counteracted by filament shrinkage at the pointed end. This results in the rapid cycling of subunits between the soluble and filamentous states, maintaining a constant filament length. The cell expends chemical energy to disassemble filaments and replenish the monomer pool, ensuring that polymerization is always energetically favored and that the reaction never reaches equilibrium [1]. Under these conditions, the subunits cycle rapidly between the free and filamentous states, while the total length of the filament remains unchanged [4]. This *steady-state treadmilling* requires a constant consumption of energy in the form of ATP hydrolysis [4].

Starting with filament formation, actin can either facilitate or inhibit nucleation and elongation. Moreover, it can crosslink filaments, with the assistance of various biological factors (see figure 1.3), forming different types of structures. These factors vary depending on the specific biological system and the mechanical function of the actin filaments (refer to figure 1.3), so we delve into this topic in the upcoming chapters, focusing on each biological system. Now, we analyze the general mechanisms that allow actin to generate pushing forces and trigger motion and deformation.

## 1.2 Pushy polymerization

When a chemical reaction releases an excess of free energy ($\Delta G$), this surplus energy can potentially be harnessed and transformed into another form of energy. To illustrate how the free energy change ($\Delta G$) resulting from spontaneous polymerization can be used to generate a pushing mechanical force, a scenario involving a simple filament is considered. This filament is anchored at one end and encounters a movable load at its opposite tip, such as an actin filament coming into contact with a plasma membrane [1].

For the filament to add a single subunit, it needs to push the load forward by a distance, $\delta$, which is equivalent to the size of the protein subunit. The act of applying force over a distance to the load constitutes mechanical work. As a result, after a filament adds a subunit while pushing against a load, the final free energy state of the system is higher than that of a filament encountering no load. However, as long as the overall $\Delta G$ remains negative, this reaction will continue spontaneously, resulting in elongation and forward movement of the load [1].

Consistent with the ideas of Hill and Kirschner, the presence of the load in the case of a single filament may impact both $k_{on}$ and $k_{off}$. The addition of a subunit is hindered by the presence of an object at the filament tip, decreasing in $k_{on}$. In addition, an object pushing on the tip may weaken the bond between the terminal subunit and its neighbor, increasing $k_{off}$. The ratio between $k_{off}$ and $k_{on}$ corresponds to the critical concentration. Therefore, the presence of a load force overall increases the critical concentration, regardless of the specific underlying mechanism [1]. The precise amount by which a particular load force alters the critical concentration can be determined using thermodynamic arguments

$$C_c(\text{loaded}) = \mathrm{C_c}(\text{unloaded}) \exp\left(\frac{\delta\,\mathrm{F}}{\mathrm{k\,T}}\right),$$

where $\delta$ is the length of the subunit, $F$ is the load force, $k$ is Boltzmann's constant and $T$ is the absolute temperature [1].

By rearranging this equation, we can determine the maximum force that a polymerizing filament can generate at a specific concentration of free monomers as follows

$$F_{max} = \left(\frac{kT}{\delta}\right) \ln\left(\frac{\mathrm{k_{on}[C]}}{\mathrm{k_{off}}}\right).$$

At a concentration of 50 $\mu$M, the stall force for a single actin filament is approximately 9 pN, which is equivalent to the force exerted by several molecules of myosin [1].

In this type of force generation, the ATPase activity of actin is generally not required, because mechanical force can be induced by the chemical potential of protein polymerization. However, a limitation of this polymerization-induced force generation is that the cell can only use it once. The polymerization reaction is initiated, reaches equilibrium, and at that point, no additional chemical energy can be extracted from the polymerization, and no more force can be generated. Therefore, in most types of cell motility, an external energy input is used to effectively reverse the polymerization reaction and move it far from chemical equilibrium. The most controlled forms of this process operate in continuous cycles at the expense of nucleotide hydrolysis [1].

This mechanism allows the polymer to use the free energy released during ATP or GTP hydrolysis to convert kinetic differences between subunit addition rates at the plus and minus ends into energetic disparities. As a result, a treadmilling filament positioned between two barriers can continuously perform mechanical work. Conversely, when a treadmilling filament is anchored to a surface at one point, the entire filament appears to move forward, even though the subunits within it remain stationary. When a treadmilling filament interacts with a movable load, such as a plasma membrane or L. monocytogenes, the load can be propelled forward indefinitely while the monomer concentration remains constant, as long as ATP is abundantly available [1].

This appears to be the case in the most common forms of force generation by actin polymerization. In both the lamellipodia of moving cells and the L. monocytogenes *actin comet tail*, actin filaments remain fixed to the substrate, expanding at the front to propel the load forward. According to this thermodynamic analysis, it is predicted that the barbed end of the filament should be oriented forward for force generation through this mechanism [1].

An important point to highlight is that the production of force through protein polymerization, as emphasized in [1], does not require nucleotide hydrolysis. The sole function of ATP hydrolysis by actin in force generation is to facilitate the recycling and repeated use of the polymerization motor within a living cell. The energy needed for force generation comes from the polymerization motor, and force is exclusively generated through polymerization. Nevertheless, the speed and efficiency of this motor mechanism cannot be anticipated without a comprehensive physical model [1].

Oster et al. have proposed physical models explaining how chemomechanical energy transduction occurs at the microscopic level through protein polymerization. These models are essentially variations of the concept of the "Brownian ratchet", a perpetual motion machine proposed by Feynman [1].

It is essential to recognize that the Brownian ratchet models, as discussed in [1], do not attribute directed motion solely to thermal energy. Thermal motion, by its nature, lacks inherent directionality. The introduction of directionality arises from the presence of an asymmetric potential. In the context of force generation based on polymerization, the asymmetric potential is represented by an excess of monomers and an external source of energy [1].

Two distinct physical models proposing a Brownian ratchet mechanism for the polymerization motor have been presented (see figure 1.4). In both models, the discrete step involves the addition of a single protein subunit to a filament tip, and the energetic asymmetry is attributed to the chemical potential of protein polymerization, following the thermodynamic scheme of Hill and Kirschner. The divergence between the two models lies in the incorporation of thermal motion within the system [1].

The initial model, introduced by Peskin et al. in 1993, envisions a stationary filament encountering a movable load (see figure 1.4 A). While a valuable starting point, this model overlooks the impact of thermal motion on all components in the system, including the filament and load. In most biological scenarios, the load significantly outweighs the filament, and thermal bending of the filament is more likely to create a monomer-sized gap between the filament and the load

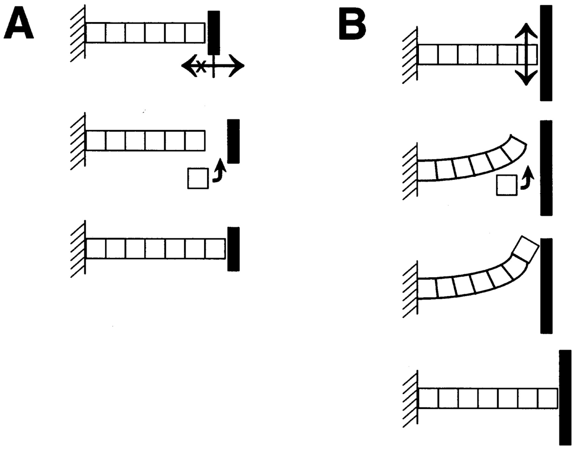

Figure 1.4: Two models proposed for the polymerization motor, both based on the Brownian ratchet concept [1]. Figure from [1].

than the diffusion of the entire load (see figure 1.4 B). Consequently, Mogilner and Oster proposed a revised "elastic" Brownian ratchet model in 1996, where the load is considered stationary, and the filament is subject to bending. In this model, the amount of force generated is predicted to depend on the stiffness (Young's modulus) of the filament and the angle between the filament and the load, but not on the diffusion coefficient of the load object. However, quantitative comparisons suggest that filament bending makes a more substantial contribution [1].

While these models offer intriguing insights, they have significant limitations, as outlined in [1]. A key assumption in both calculations is that the load force affects only $k_{on}$ and not $k_{off}$. The accuracy of the models depends on the precise nature of the interaction between the filament tip and the pushed object. These models assume that the components remain completely unattached and interact as smooth rigid bodies. Although these assumptions simplify the real situation, the current lack of sufficient quantitative experimental data in any relevant system hinders a precise assessment of how these limitations impact the accuracy of the models' predictions [1].

## 1.3 Force-velocity relation of actin-network growth

Despite several limitations, measurements of the force exerted by the actin network on generic loads have been performed by Theoriot's lab, which conducted several experiments on force and force-velocity measurements of growing actin

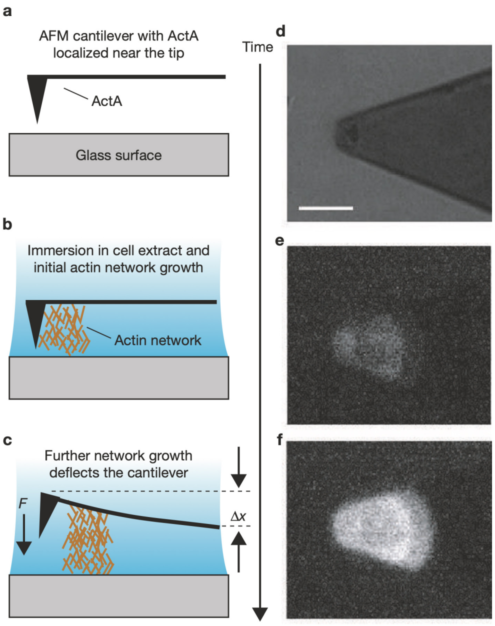

Figure 1.5: Growth of an actin network from an AFM cantilever [5]. (a-c) Illustration of the experimental geometry [5]. (d-f) Images of a cantilever before and during polymerization [5]. Figure from [5].

networks to perceive the relation between branched actin network growth velocity and the applied forces on the network [5].

Regarding the force measurement, the experiments were completed using an optical trap, a bead, and acrosomes. The bead is held onto by the optical trap and it is brought up against a micro-fabricated wall, the optical trap pulls the actin network, and the acrosomes are set into the optical trap to let the actin polymerize. In that configuration, when the bead is pushing up against the wall and the thermal fluctuations of the bead and the trap are given, the actin monomers can sneak in between the end of the acrosome and the wall and extend that bundle of actin filaments and push the bead out of the trap. The researchers successfully measured the displacement of the bead from the trap and quantified the force generated in the experiment, which is in the range of a few picoNewtons, typically around 1 or 2 pN, for these small bundles of actin filaments.

Regarding the force-velocity measurements, Theriot's lab performed measurements of actin network growth through stall against a flexible cantilever [5]. They carried out three experiments using two cantilevers: the first cantilever absorbs a nucleation promoter, ActA, initiating the formation of a localized, branched actin network between the cantilever and a nearby surface; the second cantilever compensates for the unpredictable drift between the surface and cantilevers, thus ensuring spatial stability throughout the experiment [5].

The growth of the actin network was quantified by measuring the deflection of the actin-associated cantilever using an optical lever design sensitive to nanometer-scale displacements. Actin networks exhibit elastic properties; therefore, polymerization at the cantilever's nucleating surface leads to both compression of the supporting network and deflection of the cantilevers [5]. By treating the network as a compressible spring, the fractional amount of growth transduced by the cantilever is

$$\frac{\delta}{D} = \frac{k_a}{k_a + k_c} \ ,$$

where $\delta$ is the deflection of the cantilever, $D$ is the increase in the length of the actin network due to polymerization, $k_a$ is the stiffness of the actin network, and $k_c$ is the stiffness of the cantilever. Assuming that the network is a homogeneous elastic body with an elastic modulus, E, the stiffness of the network is given by

$$k_a = \frac{EA}{L} \ ,$$

where $A$ is the area of the network and $L$ is the length of the network [5]. It results in 90%-85% of actin polymerization being transduced into cantilever deflection [5]. Therefore, since the compression of the existing network is small, only cantilever deflection is considered in the analysis. Moreover, network growth is simultaneously monitored with epifluorescence imaging of labeled actin (see figure 1.5, d-f), a force microscopy technique that is capable of exerting forces up to several hundred nN. This tool allows active adjustment of the load on the actin network and provides a flat nucleating surface that avoids ambiguities caused by surface curvature [5].

The first experiment performed by Theriot's lab aims to measure the Force-velocity relationship with the natural growth of the actin network: the actin network is allowed to grow naturally, deflecting the cantilever, so that it is subjected to increasing forces that are proportional to the cantilever deflection. The actin network grows against the cantilever until it stops at the stall force. Actin network growth exhibits three phases:

- an initial developmental phase where the network growth velocity increases against increasing forces experiments, indicating that it is a transient

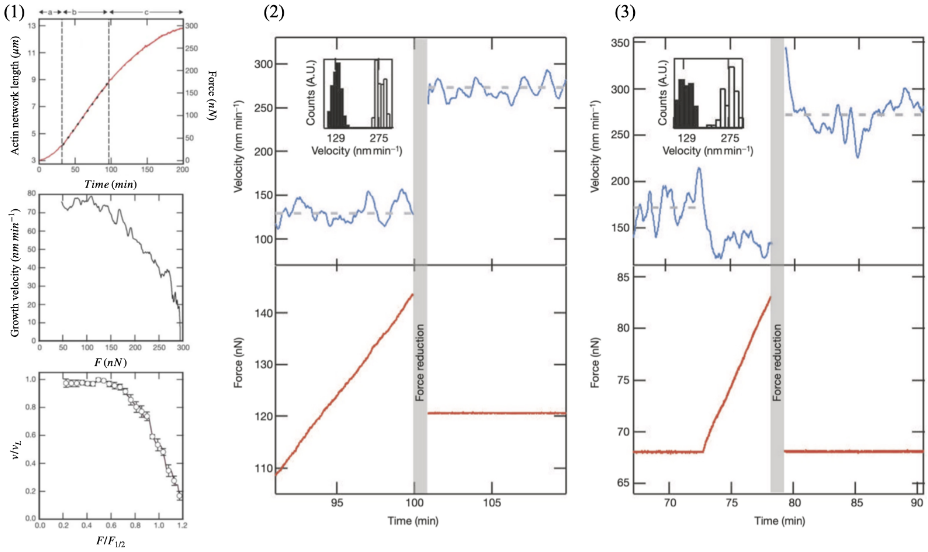

Figure 1.6: (1) First experiment: A length-force-time plot from a single experiment and normalized values [5]. (2) Second and (3) Third experiment: Force-reduction experiments showing two stable velocities at a single force [5]. Figure from [5].

phenomenon, therefore it is excluded from further analysis [5];

- a load-independent phase where the network length increases linearly with time against an increasing force. During this phase the actin network grows at a velocity $\sim 72\,\mathrm{nm\,min}^{-1}$ over a 50-160 nN range;
- a stall phase, where the rate of network elongation slows until it stalls at a force of 294 nN, corresponding to a pressure of $\sim 1\,\mathrm{nN}\,\mu\mathrm{m}^{-1}$ [5]. This observed stall is force-dependent: the network resumes its elongation with a force reduction, and there is no depletion of protein components that might cause the network stall.

The major outcome is observed in the second phase, which corresponds to a third of the force range, where the network growth velocity remains essentially load-independent (see figure 1.6). This phase is followed by a convex decline in velocity until stalling. After normalizing the velocity and force for each record, which can depend on variations in ActA density and area covered, all $Fv$ curves overlap. This result suggests that the average normalized $Fv$ trace represents a characteristic behavior for actin networks growing against increasing loads, which is independent of network area and cantilever stiffness [5].

The second experiment involves the application of a fixed force to the network. The network is allowed to grow until it reaches a force of 145 nN, exhibiting a load-independent velocity of approximately 129 nanometers per minute [5]. The applied load is then reduced to 120 nN, still within the load-independent regime by gradually retracting the surface with a piezo-electric stage [5]. Following the force reduction, the load was clamped at 120 nN, and the growth velocity was measured. Remarkably, a 17% force decrease leads to a 2.1-fold increase in velocity, reaching 275 nm/min. Surprisingly, this elevated velocity persists for more than 10 min, corresponding to almost 3 m of growth [5]. In all force-reduction experiments (n = 8), the growth velocity after a 17-98% force reduction stabilizes at a value 1.75-10.9 times higher than the original velocity, persisting during the recorded data (1-4 micrometers and up to 30 minutes) [5] (see figure 1.6).

The third experiment validates the existence of two growth velocities under identical force conditions. Force-clamp-reduction experiments were conducted by initially maintaining a constant force on the network and measuring the resulting velocity. Upon removal of the force clamp, subsequent network growth leads to increased cantilever deflection and force on the network, similar to the earlier force-reduction experiments. After a period of escalating force, the force on the network was reduced to its initial value and clamped, and the resulting velocity was measured (see figure 1.6). The velocity during the second force clamp was 1.6-fold greater than that during the first force clamp after a 19% reduction in force. In all force-clamp-reduction experiments (n = 8), the growth velocity was found to increase by a factor of 1.22-3.63 (mean = 2.3) following a 20-95% reduction in force. Additional control experiments demonstrate that this phenomenon is not dependent on network length. These results underscore the existence of different steady-state growth velocities under the same load, indicating hysteresis in the $Fv$ relationship. This suggests that the loading history of the actin network must be considered, and a single $Fv$ relationship cannot fully describe the behavior of the actin-network growth system [5].

The observed behavior in the load-independent phase, where the velocity remains constant as the force increases, can be explained by an increase in filament density with force. As the force increases, filament density may increase to sustain a constant force per filament, resulting in a consistent velocity [5].

When a lower force is applied, the filament density stabilizes, maintaining a velocity $v_2$ greater than $v_1$ instead of exponentially reducing to $v_1$. This behavior indicates structural remodeling of the actin network, which is dependent on the loading history of growing actin filaments, leading to an increase in the number of active filaments pushing the load. Velocity data suggest that network hardening with increasing force alone, resulting in an increment in network stiffness ($k_a$), cannot fully account for the observed history dependence. Beyond the load-independent regime, at forces above, the growth velocity starts to decline as the network approaches a saturating density of filaments, and growth is eventually halted. This implies a crucial role for actin filament nucleation in force production [5].

## 1.4 Motivations and research objectives

The current work aims at building multi-physical models able to describe, interpret, and predict the key mechanisms that rule ABM. It is included in a long-term plan, that aspires to realize several multiphysics models that describe the main phases of the metastasis of cancer. We identify the modeling of ABM as one of the first phases of this plan because ABM is a fundamental and ancient phenomenon that contributes to cancer metastasis in cells and it is conserved even in other organisms, such as bacteria.

To provide a consistent model that represents ABM, we first study the pathogens ABM. It represents a simpler system, that can be a paradigmatic example of the mechanical and energetical behavior of ABM. Then, a proposal for a model of cells ABM is introduced with a digression into other aspects of cell motility, e.g. receptor dynamics and substrate-cell interaction.

The description of ABM is conducted at a continuum level. The core of the model is represented by the transformation of G-actin into the F-actin network, which is described, at a macroscopic level, with a volume variation between F-actin and G-actin, which embodies the mechanical essence of the polymerization motor.

The notion of volumetric expansion is common to many types of motors. In steam engines, for example, fuel is burned and heat is used to boil water and produce steam. Heat is converted into motion when the steam expands and pushes a piston. Similarly, chemical energy is converted into motion when the polymerization of G-actin into a cross-linked network gives rise to volumetric expansion and protrusive forces.

From a conceptual point of view, physical theories and mathematical tools allow relating the mechanical principles with the behavior of living matter: thermo-mechanics of continua [24, 33] is the ideal framework to model nature's laws. Due to its intrinsic interdisciplinarity, a multi-physics approach to biological phenomena may have the potential to highlight key and limiting factors, providing innovative pathways for analysis and interpretation.

The purpose of this large-scale treatment is to describe the ABM in all its processes and to consider the global response of the actin filament network, showing that some important characteristics of the motion arise from their collective behaviors. Most of the microscopic descriptions concern the microstructural machinery of the pulling action of *single* filaments and they do not consider the global response of the F-actin network, which is relevant to the mechanical and energetical behavior of the biological system. Even if our approach lacks a clear description of the microscopic mechanism at work in the polymerization/reticulation process, it provides a novel mechanistic and energetical understanding of ABM, allowing to connect phenomena that are generally modeled separately, and it has the potential, in principle, to be extended to further phenomena where the polymerization motor is the motion trigger.

Metastasis remains the greatest challenge in the clinical management of cancer. Therefore, it is important to elucidate the mechanisms underlying ABM, with the ultimate goal of identifying combination therapies that increase the motility of beneficial cells and block the spread of harmful ones. Enhancing the ABM knowledge can lead to major improvements in the pro- and anti-angiogenic therapies, so, even if these models represent a very early step of a series of patterns characterizing the phenomenon of tumor metastasis, they can be adapted to all those processes in which ABM plays a major role.

# Chapter 2

# Notation and symbols

Scalars are indicated with lightface letters, vectors attached to points with lightface letters and arrows above them and tensors with boldface letters.

| operator | symbol |
|---|---|
| Scalars | $\alpha, b, C$ |
| Vectors | $\vec{a}, \vec{B}, \vec{c}$ |
| 2-nd order tensors | $\boldsymbol{A}, \boldsymbol{B}, \boldsymbol{c}$ |
| 4-th order tensors | $\mathbb{A}, \mathbb{B}, \mathbb{C}$ |

Table 2.1: *Operators and their symbols.*

Following the customary notation of modern Continuum Mechanics, the vectors in the *current configuration* $\Omega$ are represented with $\vec{x}$ and the vectors in the *reference configuration* $\Omega_R$ with $\vec{X}$.

The referential and spatial description of geometry-dependent scalars, vectors, and tensors are denoted with lowercase and uppercase symbols, respectively. As for mixed tensors such as the deformation gradient, we use uppercase letters and we indicate their components with one lowercase and one uppercase index.

The direct notation for gradient, curl, and divergence operators with respect to the referential and current coordinates follows the same rule. Thus, the notation for gradient, curl, and divergence operators for referential coordinates are

$$\mathrm{Grad}\,[\,] \qquad \mathrm{Curl}\,[\,] \qquad \mathrm{Div}\,[\,] \tag{2.1}$$

and for current coordinates are

$$\mathrm{grad}\,[\,] \qquad \mathrm{curl}\,[\,] \qquad \mathrm{div}\,[\,]\;, \tag{2.2}$$

respectively.

We distinguish between scalar, vector, and tensor functions, where the arguments are scalar, vector, or tensor variables respectively (see Table 2.2). The returned values can be scalars, vectors, or tensors. For the sake of simplicity, in this paragraph we do not distinguish between material and spatial coordinates, taking for granted that the above rules apply. In the first column, the function assigns a scalar $\phi$ to each scalar $t$, vector point $\vec{x}$ or tensor $\boldsymbol{b}$. In the second column, the function assigns a vector $\vec{v}$ to each scalar $t$, vector point $\vec{x}$ or tensor $\boldsymbol{b}$. In the third column, the function assigns a tensor $\boldsymbol{a}$ to each scalar, vector point $\vec{x}$ or tensor $\boldsymbol{b}$ (see Table 2.2).

| variables and values | scalar | vector | tensor |
|---|---|---|---|
| scalar | $\phi(t)$ | $\vec{v}(t)$ | $\boldsymbol{a}(t)$ |
| vector | $\phi(\vec{x})$ | $\vec{v}(\vec{x})$ | $\boldsymbol{a}(\vec{x})$ |
| tensor | $\phi(\boldsymbol{b})$ | $\vec{v}(\boldsymbol{b})$ | $\boldsymbol{a}(\boldsymbol{b})$ |

Table 2.2: *Scalar, Vector and Tensor Functions*

When the index notation is used, Einstein's summation convention is adopted, namely the "$\sum$" symbol is dropped and any index appearing twice in a product of variables is taken to be a dummy index, over which a sum is done

$$\vec{v} = \sum_{i=1}^{3} v_i\,\vec{e}_i = v_i\,e_i\;.$$

In the following, we introduce the notation used for differential operations. First ($n^{th}$) *total derivatives* with respect to a scalar argument (i.e. time $t$) are represented as

$$\begin{array}{ccc} \dot{\phi}(t) = \dfrac{\mathrm{d}\,\phi(t)}{\mathrm{d}t} & \dot{\vec{v}}(t) = \dfrac{\mathrm{d}\,\vec{v}(t)}{\mathrm{d}t} & \dot{\boldsymbol{a}}(t) = \dfrac{\mathrm{d}\,\boldsymbol{a}(t)}{\mathrm{d}t}\;, \\ \dfrac{\mathrm{d}^n\,\phi(t)}{\mathrm{d}^n t} & \dfrac{\mathrm{d}^n\,\vec{v}(t)}{\mathrm{d}^n t} & \dfrac{\mathrm{d}^n\,\boldsymbol{a}(t)}{\mathrm{d}^n t}\;. \end{array} \tag{2.3}$$

We consider *total*, *substantial* and *material derivative* as synonyms. The *partial* *derivative* is represented as

$$\frac{\partial\,\phi(t)}{\partial t}\,.$$

Vector operators, which include the gradient, divergence, and curl, are defined for scalar, vector, or tensorial fields. For vector-valued fields, the gradient is defined as

$$\underbrace{\operatorname{grad}[\,\phi\,]_{\vec{x}} = \frac{\partial\phi}{\partial x_i} = \phi_{,i}}_{\text{as for grad}\,[\,\mu\,]} \quad \operatorname{grad}[\,\vec{v}\,]_{\vec{x}} = \frac{\partial v_i}{\partial x_j} = v_{i,j} \quad \operatorname{grad}[\,\boldsymbol{a}\,]_{\vec{x}} = \frac{\partial a_{ij}}{\partial x_k} = a_{ij,k}\,, \tag{2.4}$$

and the divergence as

$$\underbrace{\operatorname{div}[\,\vec{v}\,]_{\vec{x}} = \frac{\partial v_i}{\partial x_i} = v_{i,i}}_{\text{as for div}\left[\vec{h}\right]} \qquad \operatorname{div}[\,\boldsymbol{a}\,]_{\vec{x}} = \frac{\partial a_{ij}}{\partial x_j} = a_{ij,j}\,. \tag{2.5}$$

For tensor-valued fields, the gradient is defined as

$$\underbrace{\operatorname{grad}[\,\phi\,]_{\boldsymbol{b}} = \frac{\partial\phi}{\partial b_{ij}} = \phi_{,ij}}_{\text{as for } \frac{\partial\psi(\boldsymbol{\epsilon})}{\partial\boldsymbol{\epsilon}}} \quad \operatorname{grad}[\,\vec{v}\,]_{\boldsymbol{b}} = \frac{\partial v_i}{\partial b_{jk}} = v_{i,jk} \quad \underbrace{\operatorname{grad}[\,\boldsymbol{a}\,]_{\boldsymbol{b}} = \frac{\partial a_{ij}}{\partial b_{kl}} = a_{ij,kl}}_{\text{as for } \frac{\partial\boldsymbol{S}}{\partial\boldsymbol{C}}}\,, \tag{2.6}$$

and the divergence as

$$\operatorname{div}[\,\vec{v}\,]_{\boldsymbol{b}} = \frac{\partial v_j}{\partial b_{ij}} = v_{j,ij} \qquad \operatorname{div}[\,\boldsymbol{a}\,]_{\boldsymbol{b}} = \frac{\partial a_{ij}}{\partial b_{kj}} = a_{ij,kj}\,. \tag{2.7}$$

In the following, we introduce the notation used for algebraic operations. The products between vectors are defined as

$$\vec{a}\cdot\vec{b} = a_i \cdot b_i \qquad \text{dot product}\,, \tag{2.8}$$

$$\vec{a}\times\vec{b} = e_{ijk}a_jb_k \qquad \text{vector product}\,, \tag{2.9}$$

$$\vec{a}\otimes\vec{b} = a_ib_j \qquad \text{dyadic product}\,. \tag{2.10}$$

The products between two 2nd-order tensors or a 2nd-order tensor and a vector are defined as

$$\boldsymbol{c} = \boldsymbol{a}\,\boldsymbol{b} = a_{ij}\,b_{jk} = c_{ik} \qquad \text{contraction of an index}\,, \tag{2.11}$$

$$\vec{c} = \boldsymbol{a}\,\vec{b} = a_{ij}\,b_j = c_i \qquad \text{contraction of an index}\,, \tag{2.12}$$

$$\boldsymbol{A} : \boldsymbol{B} = \mathrm{tr}\left[\,\boldsymbol{A}^T\,\boldsymbol{B}\,\right] = A_{IJ}\,B_{IJ} \qquad \text{double index contration}\,. \tag{2.13}$$

We adopt the standard superscripts $^T$ and $^{-1}$ to indicate the transpose and the inverse operations.

# Part I

# Pathogens ABM

# Chapter 3

# Pathogens biological background

This chapter is adapted from [6], "Actin based motility unveiled: How chemical energy is converted into motion, *J MECH PHYS SOLIDS*".

The polymeric network of F-actin is a critical target of several intracellular bacterial pathogens [7], e.g., *Listeria monocytogenes, Shigella, Ricketssia, Mycobacterium*, and *Burkholderia.* They exploit and manipulate the F-actin network at multiple stages of infection to support their survival and growth in the host cell environment. Because of its low virulence and its ease in experimental handling [8], mainly *Listeria monocytogenes* is chosen to investigate this form of ABM, with the result of a wider experimental literature compared to other pathogens [9, 10, 11, 12, 13].

## 3.1 Introduction

During the late 1980s, various research groups discovered that F-actin plays a significant role in the intracellular movement of two distinct bacterial pathogens, Listeria monocytogenes and Shigella flexneri, both of which reside within the host cell's cytoplasm. As L. monocytogenes is comparatively less virulent and more manageable in experimental settings than S. flexneri, most laboratories investigating this form of ABM have directed their attention toward L. monocytogenes. Hence, this chapter focuses on L. monocytogenes biological background only.

The intracellular lifestyle and motility of Listeria are thoroughly investigated through electron microscopy, giving rise to the term *actin comet tail.* This term is coined based on the observed images of F-actin accumulation at one of the bacterial poles within infected macrophages. The precise bacterial protein or factor causing actin polymerization remained mysterious until the landmark discovery of Pascale Cossart who identified the crucial role of ActA, which changed the way how actin has been studied afterward [14].

## 3.2 Listeria monocytogenes

Listeria monocytogenes is a common soil organism that was first identified in 1926 after an outbreak that affected rabbits and guinea pigs. In the 1970s it was recognized as an agent of human disease and in the 1980s it was classified as a food-borne pathogen. It has a high percentage of mortality among infected individuals (20-30%) and a low number of infections per year, with approximately 23150 cases in 2010 worldwide. Food such as salad and cheese commonly contains it in a minimum amount, but when food is heavily contaminated (up to $\sim 10^9$ bacteria) and it is ingested by humans, it can cause severe gastroenteritis. However, some categories such as children, elderly individuals, immunocompromised individuals, and pregnant women, even after ingestion of low levels of contaminated food ($\sim 10^2$ - $10^4$ bacteria) can risk bacterial sepsis, subsequent bacterial meningitis and/or infection of the fetus, resulting in abortion or complications to pregnancy [15]. Due to their adaptability, Listeria pathogens can thrive in several stressful environments. They can survive and grow at low temperatures, at high salt concentrations, and at low pH levels, making them a great concern for the food industry.

### 3.2.1 Infection process

After the ingestion of contaminated food, Listeria encounters and invades different regions of the intestinal epithelium. Upon crossing the epithelial barrier, they spread via lymph and bloodstream towards their target organs, the liver or the spleen. Listeria can also cross the blood-brain barrier in immunocompromised individuals or the fetoplacental barrier in pregnant women. At the level of infected organs, Listeria has the powerful ability to alter host physiology. Before the invasion, it secretes a toxin, that creases spores in the host membrane, promoting bacteria entry and invasion and compromising some internal cellular processes. Upon binding to the membrane receptors, bacteria trigger cytoskeletal rearrangements, leading to internalization into the cytoplasm. Once inside the

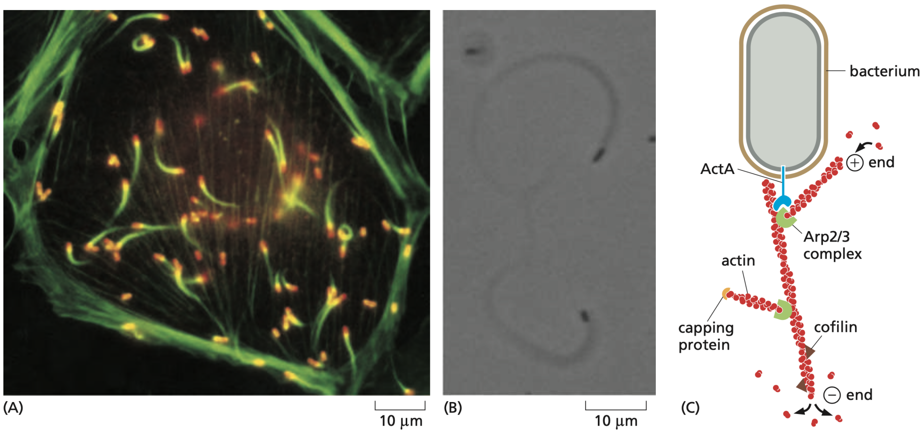

Figure 3.1: The actin-based movement of Listeria monocytogenes [4]. Figure from [4].

cell, Listeria ruptures the membrane of the internalization vacuole and it modifies its surface to become resistant to the cell's inner defenses. Then, it multiplies, populating its host, and secretes virulence factors that compromise distinct cellular functions.

Inside the cell, the bacterium expresses a particular stable protein on its surface called ActA, a bacterial factor that recruits small actin filaments from which other actin filaments rapidly grow to form an *actin comet tail*, that allows the bacterium to move inside and outside the cell (pathogens ABM) (see figure 3.1). The actin-propelled movement of the bacterium enables it to push the cell membrane into that of the neighboring cell. The double membrane vacuole is again ruptured thereby spreading the infection to the neighboring cells. In response to bacterial infection, the host immune system, composed of several cells such as neutrophils, is activated to destroy infected cells and/or bacteria and to control the spread of infection. With the help of adaptive immunity, bacteria are totally eliminated, but in immunocompromised individuals, they may lead to the most severe symptoms of listeriosis.

### 3.2.2 ABM

ABM plays a crucial role in the life cycle of Listeria monocytogenes. After the invasion, the bacterium strategically covers one of its surface poles with ActA, a bacterial protein capable of binding to various factors present in the host cell cytoplasm (see figure 3.1). These factors are essential for the nucleation of actin filaments. Two domains of ActA are particularly vital for the pathogen's ABM:

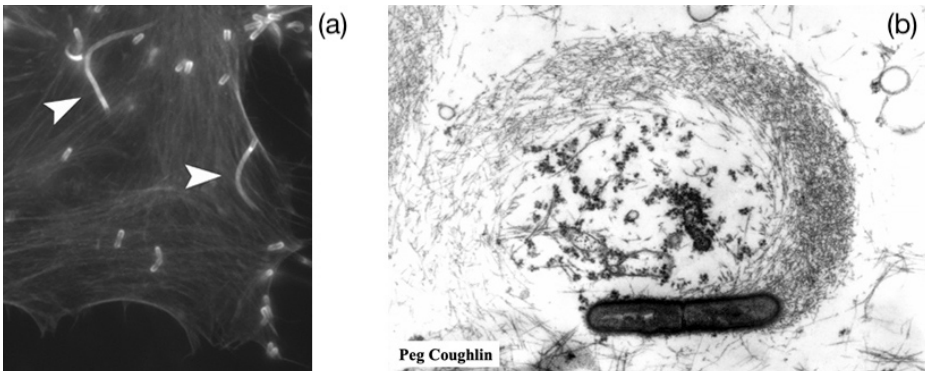

Figure 3.2: (a) Movement of Listeria monocytogenes in a cell [16]. (b) Bacterial surface proteins cause local nucleation of actin filaments [17]. Figure from [16] and [17].

the amino-terminal domain and the central proline-rich domain. The former activates actin filament nucleation through Arp2/3, while the latter enhances filament elongation by binding to VASP, which, in turn, interacts with profilin, the protein responsible for elongation. The amino-terminal domain directly binds to the nucleating complex, the Arp2/3 complex, which can then bind to the side of a preexisting actin filament in the tail. This initiation leads to the nucleation of a new filament at that location, creating a branch at a 70° angle from the original filament [8] (see figure 3.1 and 3.2).

As these filaments are nucleated, they grow by the addition of actin monomers present in the cytoplasm, landing on the ends of the filaments through diffusion. This growth is responsible for the movement, as it propels the bacterium through the cytoplasm using a force generation mechanism. Apart from factors influencing the bacterial surface, capping protein inhibits the elongation of older filaments by binding to the barbed end of actin filaments. Additionally, $\alpha$-actinin plays a role in crosslinking filaments to stabilize the tail structure, while ADF (actin depolymerizing factor) or cofilin facilitates the disassembly of old filaments [8].

Several proteins, including capping protein (CapZ) and gelsolin, possess barbed-end F-actin capping activity. ActA may indirectly suppress capping near the bacterial surface, and is strongly associated with *actin comet tails.* Gelsolin is distributed throughout the tail and is paradoxically enriched at the bacterial surface. The combined effect of suppressing barbed-end capping at the bacterial surface, exclusive localization of elongation enhancers VASP and profilin at the bacterial surface, and robust activation of Arp2/3 by ActA appears sufficient to facilitate nucleation and elongation primarily at the front of the *actin comet tail*

[8].

Immunodepletion of ADF/cofilin from cytoplasmic extracts supporting L. monocytogenes motility results in altered *actin comet tail* morphology, increasing its length fivefold compared to normal. Conversely, the addition of excess exogenous ADF/cofilin to extracts leads to the shortening of the actin tail and an acceleration of bacterial motility. ADF/cofilin is found throughout the L. monocytogenes *actin comet tail*, aligning with previous observations that depolymerization occurs uniformly across the tail [8].

Various F-actin crosslinking proteins, including fimbrin and $\alpha$-actinin, are distributed throughout the *actin comet tail*. Microinjection of a dominant-negative fragment of $\alpha$-actinin, which inhibits cross-linking by the endogenous protein, leads to the cessation of L. monocytogenes movement in infected cells. This underscores the importance of robust crosslinking for navigating through the highly viscous cytoplasm of a living cell. Actin, Arp2/3, ADF/cofilin, and capping protein are indispensable for motility, while VASP and profilin enhance the rate of movement, and $\alpha$-actinin contributes to tail stabilization [8].

One of the recent significant discoveries about actin propulsion is that the actin tail is attached to the surface of the pathogens [18]. By using an optical trap to measure the force necessary for separating the bacterial cell from the actin tail, it is revealed that a force exceeding 10 pN is required. Moreover, electron microscopy observations of the transient attachment of actin filaments from the branching network to the bead's surface demonstrate that the attachment of F-actin to either the bacteria or beads appears to facilitate stable and persistent movement. This discovery raises questions about the existence of a gap between undulating filaments and the cell surface and how it coexists with the fact that the filaments attach to the surface. The answer lies in the temporariness of the attachment: filaments transiently attach to the bacterial surface. Initially, nascent filaments associate with protein complexes on the surface, but then they disengage and grow freely until they are eventually capped and lose contact with the surface. Throughout this process, the attached fibers are under tension, resisting the forward movement of the bacterium or bead. Simultaneously, the disassociated fibers experience compression, generating the propulsive force [18].

## 3.3 Existing literature models and a new approach presentation

### 3.3.1 Existing literature models

Numerous models describing ABM of pathogens can be found in the existing literature [19, 18, 20, 21].

In [19], a mesoscopic description of Listeria motility at a length scale larger than that of individual proteins is introduced to understand the mechanisms that control the speed of the bacterium, the maximum force it can overcome, and the effect of the obstacles it encounters during the motion. The *actin comet tail* is treated as a linear elastic gel, whose shape depends on the way the gel adopts the lowest energy conformation. The addition of new actin filaments builds up a new polymerized layer at the bacterium surface, which compresses the previously formed layers and induces elastic deformations in the gel. Thus, the free energy produced by actin polymerization is not directly used for the propulsion but is rather first stored as elastic energy [19] and then triggers the motion of the bacterium after the relaxation of the strain in the tail. The shape of the gel, and therefore, the motion of the bacterium depends on the way the gel adopts the lowest energy conformation [19], so, for the sake of simplicity, the *actin comet tail* is artificially simplified in two parts: the internal gel, produced from the back part of the bacterium, and the external gel, produced on the cylindrical surface of the bacterium. Three models are considered: a one-dimensional model, in which the bacterium produces only the internal gel, a three-dimensional model, where the bacterium is pushed only by the external gel and a three-dimensional complete model in which the bacterium is pushed by both gels. Thus, the relation between the bacterium's speed and the external forces that induce the stresses on the bacterium's surface is obtained.

In [18], the "elastic ratchet model" of Mogilner and Oster is extended to incorporate the transient binding at the actin/cell interface. The "elastic ratchet model" bases its mechanism of polymerization force generation on the fluctuations of filaments against the bacterium [18] and the transient binding takes into account the attachment and detachment of actin filaments to the surface of the pathogens. A two-compartment model consisting of attached and detached filaments is formulated where the detached compressed fibers (the "working filaments") generate the protrusive force, and the attached stretched fibers resist the forward progress of the bacterium. The model consists of three ingredients: dynamic equations for the numbers of actin filaments near the surface, that describe the dynamics of the two filaments populations (attached and working filaments); a force-balance equation between the polymerization ratchet force, generated by the working filaments, that is balanced with the force of attached filaments and the load force represented by the sum of the viscous drag force on the cell and the external conservative force exerted on the cell, e.g. a laser trap; and constitutive relations describing the correlation between the velocity of propulsion and the polymerization ratchet force. The model is used to derive the force-velocity relation for Listeria, that fits the available data, and to generate testable predictions for future experiments.

In [20], a dynamical model that provides a unified mathematical description of the trajectories of the Listeria pathogen is developed. The model is defined by a set of deterministic evolution equations that incorporate not only a propulsive force included in most of the microscopic models to date but also its rotation about the body axis. A key ingredient of the model is torque, which is directed out of/into the plane in which the bacterium moves and which can arise from the rotation of the propulsive force about the body axis of the bacterium. Specifically, the torque arises if the moment of the surface force distribution about the centroid of the bacterium does not vanish, and/or it can arise from the surface moments exerted by the filaments. With different angular speeds of rotation, the analysis can obtain a rich array of 2D Listeria trajectories with a defined geometric structure, that predicts the trajectories of Listeria.

In [21], a generalized Brownian ratchet model that accounts for the interactions of actin filaments with the surface of Listeria is introduced to develop a microscopic model for the movement of Listeria propelled by actin polymerization. A key ingredient in this formulation is the coupling between the motion of Listeria and the force-dependent rate of filament growth [21]. A numerical scheme is presented to determine the force distribution among filaments and bacteria movement and, despite some limitations, the model successfully establishes a connection between the macroscopic movement of Listeria and microscopic polymerization details. Among the main findings, it is highlighted that they can represent the nonuniform distribution of propelling forces generated by spatial variation of polymerization rate, the generation of a curved bacteria trajectory due to nonuniform polymerization velocity on the sides of the *actin comet tail*, the presence of a tangential force induced by polymerizing filament, and the correlation between filaments orientations in the *actin comet tail* and movement of Listeria.

### 3.3.2 New approach presentation

To provide a unique understanding of pathogens ABM, we propose a continuum multi-physics model, stemming from chemotransport-mechanics continuity equations that account for the actin chemical kinetics. This model describes *actin comet tail*, connecting different aspects of the ABM, such as polymerization/depolymerization of actin and mechanical response/mechanical flow of the F-actin network. Moreover, it provides a novel mechanistical and energetic understanding of the phenomenon, examining the actin polymerization motor from a thermodynamical point of view. It has the potential, in principle, to provide quantitative results on F-actin and G-actin concentration variation in cells, and *actin comet tail* displacements and stresses induced by G-actin transformation. The ultimate goal of this pathogens ABM model is to provide a first simple approach to ABM that can serve as a paradigm for more complicated phenomena, such as cells ABM.

# Chapter 4

# A model for Pathogens ABM

This chapter is adapted from [6], "Actin based motility unveiled: How chemical energy is converted into motion, *J MECH PHYS SOLIDS*".

## 4.1 Kinematics

Kinematics of a continuum body is the study of motion of a continuum body *per se* without any reference to the *causes* of motion, exactly as the kinematics of particles is completely independent of forces. So, the study of the kinematics of continuum bodies (i.e., of body motion and deformation) deals with positions, velocities, and accelerations of all points of the system at study, without relating them to the causes that generate the motion [22, 23].

In this chapter, we introduce the continuum deformable body and its configurations, various measures of deformation, and rates of deformation and we define them in the realm of affine space, the mathematical model of the physical space $\mathcal{S}$. In the "theater" of physical space $\mathcal{S}$, in which Mechanics takes place, the "actors" of Continuum Mechanics are *material bodies* [22, 23].

A material body is identified with a reference configuration $\Omega_R$, namely a subset of the physical space $\mathcal{S}$ representing a particular placement of the body in space, from which it is *mathematically and geometrically convenient* to study the motion of the body. So, a *configuration* of the body $\Omega_R$ is a *point map*

$$\phi : \Omega_R \to \mathcal{S} : \vec{X} \mapsto \vec{x} = \vec{\chi}(\vec{X}) \ ,$$

i.e. a map such that both its domain and codomain are point sets. The *image* of $\Omega_R$ through the configuration $\vec{\chi}$ is a subset of $\mathcal{S}$ denoted $\Omega$, and it is called the *current configuration* of the body $\Omega_R$ [22, 23].

The definition of configuration map is static, so to describe the *motion* of the body, the *time* $t \in \mathcal{I}$ is introduced as a parameter, where $\mathcal{I} \subset \mathbb{R}$ is an interval of real numbers. So, a *motion* of $\Omega_R$ can be described by the *one-parameter family of configurations*

$$\vec{\chi} : \Omega_R \times \mathcal{I} \to \mathcal{S} : (\vec{X}, t) \mapsto \vec{x} = \vec{\chi}(\vec{X}, t) \ ,$$

where $\vec{\chi}(\vec{X}, t)$ is a map that assigns to each material point at time $t$ a location which is referred to as the spatial point occupied by $\vec{X}$ at time $t$ [22, 23, 24]. We will name *deformation* $\vec{\chi}_t$ a motion at a *fixed* time t

$$\vec{\chi}_t(\vec{X}) = \vec{\chi}(\vec{X}, t) \ .$$

To characterize the deformation of the body in a neighborhood of a point, the non-symmetric deformation gradient $\boldsymbol{F}$ is introduced. The deformation gradient is the most important measure of deformation, from which all the other measures of deformation descend. It is a two-point tensor involving points in two distinct configurations and it is closely related to the differentiability of the configuration map $\vec{\chi}$. The configuration map $\vec{\chi}$ is *differentiable* at point $\vec{X}$ if, and only if, there exists a two-point tensor $\boldsymbol{F}$, such that, for every vector $\vec{W}$

$$[\boldsymbol{F}(\vec{X})]\, \vec{W} = (\partial_{\vec{W}} \vec{\chi})(\vec{X}) \in T_x\mathcal{S} \ , \tag{4.1}$$

which states that a point map such as the configuration map $\vec{\chi}$ is differentiable at $\vec{X}$ if its directional derivative with respect to $\vec{W}$ at $\vec{X}$ is a linear function of the direction $\vec{W}$, so it is the differential of the configuration map $\vec{\chi}$ at point $\vec{X}$ [22, 23].

The mathematical restriction for the deformation gradient on its determinant is

$$J = \det [\, \boldsymbol{F} \,] > 0 \, ,$$

i.e., the deformation gradient has to be strictly positive: it has to be non-zero to guarantee the invertibility of the deformation gradient $\boldsymbol{F}$, and it has to be positive so that the transformation described by $\boldsymbol{F}$ preserves the orientation of space, namely $J$ must be positive to prevent the occurrence of a volume being turned "inside out" and of compenetration of matter [22, 23].

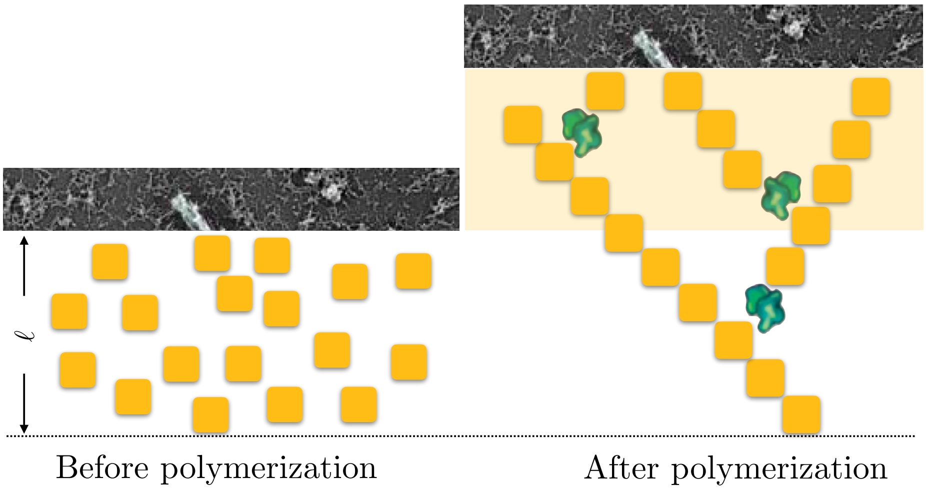

Figure 4.1: Schematic representation of volume increment upon the structural arrangement of monomers after polymerization. Figure from [25].

The transformation of G-actin into F-actin entails a structural arrangement of monomers, from a disorganized form (G), into an organized form (F). We claim that this reorganization implies a different partial molar volume between F-actin and G-actin, with the crosslinked network having a greater molar volume than monomers. We represent this as a continuum dilatation of the actin in which the dilated configuration, the F-actin network, is a mixture of cytosol and polymerized actin monomers [6]. We claim that this is the mechanical engine of the protrusion mechanism at a continuum scale. Since we consider the process at a macroscopic continuum scale, the filament bending and the discrete steps corresponding to the addition of a single protein subunit to the filament tip by insertion are not considered [22, 23].

So, we base our model on a multiplicative decomposition of the deformation gradient

$$\boldsymbol{F} = \boldsymbol{F}^e \boldsymbol{F}^c \, , \tag{4.2}$$

which splits the total deformation gradient into two contributions: a purely chemical contribution $\boldsymbol{F}^c$ and a purely mechanical contribution $\boldsymbol{F}^e$:

- $\boldsymbol{F}^c(\vec{X}, t)$ is called the *polymerization tensor* and is the local distortion of the material neighborhood of a point due to the volumetric swelling (de-swelling) of the material. This physical phenomenon is caused by the phase change of actin after polymerization, from monomeric to a network of filaments and vice versa [26].

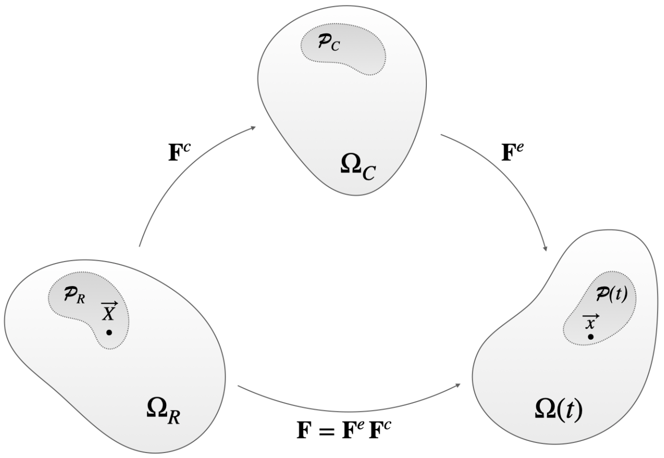

Figure 4.2: The reference $\Omega_R$, the intermediate $\Omega_{\mathcal{C}}$ and the deformed $\Omega(t)$ configuration. The arrows indicate the mapping properties of the linear transformations $\boldsymbol{F}$, $\boldsymbol{F}^e$, and $\boldsymbol{F}^c$ [6]. Figure from [6].

- $\boldsymbol{F}^e(\vec{X},t)$ is called elastic distortion and is the local distortion of the material neighborhood of a point due to the elasticity of the network [6].

$\boldsymbol{F}^c(\vec{X},t)$ is defined as

$$\boldsymbol{F}^c = \lambda^c\,\mathbb{1}\;, \tag{4.3}$$

with

$$\lambda^c\; > 0\;, \qquad \det\left[\,\boldsymbol{F}^c\,\right] = J^c = \lambda^{c3}\;, \qquad \frac{1}{J^c}\,\frac{\mathrm{d}J^c}{\mathrm{d}t} = \frac{3}{\lambda^c}\,\frac{\mathrm{d}\lambda^c}{\mathrm{d}t}\;, \tag{4.4}$$

and $\lambda^c$ is the swelling stretch.

By the definition of the deformation gradient, the right Cauchy-Green tensor $\boldsymbol{C}(\vec{X},t)$ is defined

$$\boldsymbol{C} = \boldsymbol{F}^T\boldsymbol{F}\;,$$

where right is because $\boldsymbol{F}(\vec{X},t)$ is on the right side of $\boldsymbol{C}(\vec{X},t)$.

Given the definition (4.3), the decomposition (4.2) leads to a multiplicative decomposition for the Cauchy-Green tensor, too,

$$\boldsymbol{C}(\vec{X},t) = \;\boldsymbol{C}^e\,\boldsymbol{C}^c\;, \tag{4.5}$$

with the polymerization and elastic factors

$$\boldsymbol{C}^c = \boldsymbol{F}^{c^{\mathrm{T}}}\boldsymbol{F}^c = J^{c2/3}\;\mathbb{1}\;, \qquad \boldsymbol{C}^e = \boldsymbol{F}^{e^{\mathrm{T}}}\boldsymbol{F}^e = J^{c-2/3}\;\boldsymbol{C}\;, \tag{4.6}$$

respectively [6].

The Green-Langrange strain tensor $\boldsymbol{E}$

$$\boldsymbol{E} = \frac{1}{2}\big(\boldsymbol{F}^T\boldsymbol{F} - \mathbb{1}\big) \,,$$

and its elastic counterpart, defined as

$$\boldsymbol{E}^e = \frac{1}{2}\left(\boldsymbol{C}^e - \mathbb{1}\right) \,, \tag{4.7}$$

are related by the identities

$$\boldsymbol{E} = J^{c^{2/3}}\boldsymbol{E}^e + \frac{1}{2}\big(J^{c^{2/3}} - 1\big)\mathbb{1} \,, \tag{4.8}$$

and

$$\frac{\mathrm{d}\,\boldsymbol{E}}{\mathrm{d}t} = \frac{1}{3}\left(J^{c^{-1/3}}\frac{\mathrm{d}\,J^c}{\mathrm{d}t}\boldsymbol{C}^e\right) + \left(J^{c^{2/3}}\frac{\mathrm{d}\,\boldsymbol{E}^e}{\mathrm{d}t}\right) . \tag{4.9}$$

The spatial velocity gradient, which expresses the variation of the velocity field with the point, is defined as usual as

$$\boldsymbol{l}(\vec{x},t) = \mathrm{grad}\left[\,\vec{v}(\vec{x},t)\,\right] = \frac{\mathrm{d}\,\boldsymbol{F}}{\mathrm{d}t}\,\boldsymbol{F}^{-1} \,, \tag{4.10}$$

and the following tensors

$$\boldsymbol{l}^e = \frac{\mathrm{d}\,\boldsymbol{F}^e}{\mathrm{d}t}\,\boldsymbol{F}^{e^{-1}} \,, \qquad \boldsymbol{l}^c = \frac{\mathrm{d}\,\boldsymbol{F}^c}{\mathrm{d}t}\,\boldsymbol{F}^{c^{-1}} \tag{4.11}$$

are defined in $\Omega$ and $\Omega_c$, respectively. It holds

$$\boldsymbol{l} = \boldsymbol{l}^e + \boldsymbol{F}^e\,\boldsymbol{l}^c\,\boldsymbol{F}^{e^{-1}} \,. \tag{4.12}$$

The linear field $\boldsymbol{l}(\vec{x},t)$ can be split into the rate of deformation tensor $\boldsymbol{d}(\vec{x},t)$ (symmetric) and the spin (vorticity tensor) $\boldsymbol{w}(\vec{x},t)$ (antisymmetric)

$$\boldsymbol{l}^c = \boldsymbol{d}^c + \boldsymbol{w}^c \,, \tag{4.13a}$$

$$\boldsymbol{l}^e = \boldsymbol{d}^e + \boldsymbol{w}^e \,. \tag{4.13b}$$

From eq. (4.3) and (4.4) the following transformations hold

$$\boldsymbol{w}^c = \boldsymbol{0} \,, \qquad \boldsymbol{l}^c = \boldsymbol{d}^c = \frac{1}{3\,J^c}\,\frac{\mathrm{d}\,J^c}{\mathrm{d}t}\,\mathbb{1} \,, \qquad \frac{\mathrm{d}\,J^c}{\mathrm{d}t} = J^c\,\mathrm{tr}\left[\,\boldsymbol{d}^c\,\right] \,. \tag{4.14}$$

Because of eq. (4.12) and (4.14), $\boldsymbol{l} = \boldsymbol{l}^e + \boldsymbol{l}^c$ holds [6].

In the realm of viscoelasticity [27, 28], the deformation gradient $\boldsymbol{F}^e$ is frequently defined as a multiplicative decomposition of the deformation gradient into volumetric $\boldsymbol{F}^{e^v}$ and isochoric $\boldsymbol{F}^{e^i}$ factors

$$\boldsymbol{F}^e = \boldsymbol{F}^{e^v}\,\boldsymbol{F}^{e^i}\,, \tag{4.15}$$

with volumetric factor $\boldsymbol{F}^{e^v} = J^{e\,1/3}\,\mathbb{1}$ completely identified by the determinant of $\boldsymbol{F}^e$ and for the isochoric factor det $\left[\,\boldsymbol{F}^{e^i}\,\right] = 1$ [6]. These results lead to similar relationships to those summarized above [6].

## 4.2 Transformation of geometric elements

**Vector fields**. We say that the material vector field $\vec{W}$ is the pull-back of the spatial vector field $\vec{w}$ if, for every $\vec{x} = \vec{\chi}(\vec{X})$ and corresponding $\vec{X} = \vec{\chi}^{-1}(\vec{x})$,

$$\vec{W} = \boldsymbol{F}^{-1}(\vec{x})\,\vec{w}(\vec{x}) = \boldsymbol{F}^{-1}(\vec{\chi}(\vec{X}))\,\vec{w}(\vec{\chi}(\vec{X}))\,. \tag{4.16}$$

Conversely, the spatial vector field $\vec{w}$ is the push-forward of the material vector field $\vec{W}$ if, for every $\vec{x} = \vec{\chi}(\vec{X})$ and corresponding $\vec{X} = \vec{\chi}^{-1}(\vec{x})$ [22],

$$\vec{w} = \boldsymbol{F}(\vec{X})\,\vec{W}(\vec{X}) = \boldsymbol{F}(\vec{\chi}^{-1}(\vec{x}))\,\vec{W}(\vec{\chi}^{-1}(\vec{x}))\,. \tag{4.17}$$

The prototype of a vector field is the velocity field [22].

**Covector fields**. We say that the material covector field $\Pi$ is the pull-back of the spatial covector field $\vec{\pi}$ if, for every $\vec{x} = \vec{\chi}(\vec{X})$ and corresponding $\vec{X} = \vec{\chi}(\vec{x})^{-1}$ [22],

$$\vec{\Pi} = \boldsymbol{F}^T(\vec{x})\,\vec{\pi}(\vec{x}) = \boldsymbol{F}^T(\vec{\chi}(\vec{X}))\,\vec{\pi}(\vec{\chi}(\vec{X}))\,. \tag{4.18}$$

Conversely, the spatial vector field $\vec{\pi}$ is the push-forward of the material covector field $\vec{\Pi}$ if, for every $\vec{x} = \vec{\chi}(\vec{X})$ and corresponding $\vec{X} = \vec{\chi}(\vec{x})^{-1}$ [22],

$$\vec{\pi} = \boldsymbol{F}^{-T}(\vec{X})\,\vec{\Pi}(\vec{X}) = \boldsymbol{F}^{-T}(\vec{\chi}^{-1}(\vec{x}))\,\vec{\Pi}(\vec{\chi}^{-1}(\vec{x}))\,. \tag{4.19}$$

The prototype of a covector field is the force field, linear momentum, or force density field, e.g. force per unit mass or electric field (force per unit charge) [22].

**Volume fields**. Volume forms are particular tensors, that induce the notion of volume subtended by a set of vectors, of orientation of space, and of determinant. In a $n$-dimensional space $V$, a volume form, or n-form, $\boldsymbol{\mu}$ is a completely skew-symmetric n-th-order tensor that, for every set of $n$ vectors $\vec{v}_1$, $\vec{v}_2$, ..., $\vec{v}_n \in V$

$$\boldsymbol{\mu}(\vec{v}_{i_1}\vec{v}_{i_2}...\vec{v}_{i_n}) = \epsilon_{i_1 i_2 ... i_n}\boldsymbol{\mu}(\vec{v}_1, \vec{v}_2, ..., \vec{v}_n), \tag{4.20}$$

where $\epsilon_{i_1 i_2 ... i_n}$ is the permutation symbol [22]. Therefore, the spatial and material Euclidean volume forms

$$vol(\vec{h}, \vec{l}, \vec{m}) = \det\left[\,\vec{h}, \vec{l}, \vec{m}\,\right] = \epsilon_{ijk}\, h_i l_j m_k\,, \tag{4.21}$$

$$Vol(\vec{H}, \vec{L}, \vec{M}) = \det\left[\,\vec{H}, \vec{L}, \vec{M}\,\right] = \epsilon_{IJK}\, H_I L_J M_K \tag{4.22}$$

are uniform tensor fields that are independent of $\vec{x} \in \Omega$ and $\vec{X} \in \Omega_R$, respectively [22].

The pull-back of the spatial Euclidean volume form through the configuration map $\vec{\chi}$ is defined as the material volume form [22]

$$\begin{aligned} vol(\vec{h}(\vec{x}), \vec{l}(\vec{x}), \vec{m}(\vec{x})) &= vol(\boldsymbol{F}\vec{H}, \boldsymbol{F}\vec{L}, \boldsymbol{F}\vec{M}) \\ &= (\epsilon_{ijk}\, F_{iI}\, F_{jJ}\, F_{kK} H_I L_J M_K)(\vec{X}) \\ &= J(\vec{X})\,(\epsilon_{IJK} H_I L_J M_K)(\vec{X}) \\ &= J(\vec{X})\, Vol(\vec{H}, \vec{L}, \vec{M})(\vec{X})\,, \end{aligned} \tag{4.23}$$

where

$$J = \det\left[\,\boldsymbol{F}\,\right] = \epsilon_{ijk}\, F_{i1}\, F_{j2}\, F_{k3}\,. \tag{4.24}$$

In traditional notation, the expression 4.23 reads

$$dv = J dV\,, \tag{4.25}$$

which represents the volume element transformation [22].

**Area fields**: We define the area as

$$\vec{area}(\vec{l}, \vec{m}) = \vec{l} \times \vec{m}\,. \tag{4.26}$$

Thus, the area subtended by $\vec{l}$ and $\vec{m}$ is a vector orthogonal to both $\vec{l}$ and $\vec{m}$, by definition of the cross product [22]. Indeed,

$$\vec{l} \cdot (\vec{l} \times \vec{m}) = \det\left[\,\vec{l}, \vec{l}, \vec{m}\,\right] = 0\,,$$

and similarly for $\vec{m}$. The norm of (4.26) is the measure of the area subtended by $\vec{l}$ and $\vec{m}$, and is obtained using the usual expression of the norm of the cross product [22].

The pull-back of the area is obtained through the pull-back of *vol* and the definitions of triple product and cross product

$$\vec{n}(\vec{x})\|\vec{area}(\vec{l},\vec{m})\| = J\boldsymbol{F}^{-T}\vec{N}\|\vec{Area}(\vec{L},\vec{M})\|\,, \tag{4.27}$$

which separates the area measures from the normal vectors [22].

We note how the pull-back of the area does not follow the rules of vector fields. The area element is, indeed, not a vector, but a pseudo-vector, as is obvious from its definition in terms of a cross-product [22].

In the traditional notation, the expression reads

$$\vec{n}\,da = J\boldsymbol{F}^{-T}\vec{N}\,dA\,, \tag{4.28}$$

which takes the name of Nanson's formula and transforms the areas and orientation of the face elements [22]. The expression of area elements transformation without orientation reads [22]

$$da = |J\boldsymbol{F}^{-T}\vec{N}|\,dA\,. \tag{4.29}$$

**Volume property**: The properties transformations defined over a volume, like density, read

$$a\,dv = a_R\,dV\,, \quad \text{a: volume density, mass density etc [22]}\,. \tag{4.30}$$

**Area property**: The property transformations defined over an area, like flux, read

$$\vec{a}\cdot\vec{n}\,da = \vec{A}\cdot J\boldsymbol{F}^{-T}\vec{N}\,dA\,, \tag{4.31}$$

$\vec{a}$: vector flux. It is a surface density, a flux across a surface,

$$\boldsymbol{a}\,\vec{n}\,da = \boldsymbol{A}J\boldsymbol{F}^{-T}\vec{N}\,dA\,, \tag{4.32}$$

$\boldsymbol{a}$: tensor flux. It is a surface density, like the stress tensor [22].

## 4.3 Volume and surface integral transformation theorems

The transformation of volume and area is pivotal in theorems with volume and area integral transformation. Here we enunciate the Theorem of Change of Variables for volume integrals and the analogous theorem for surface integrals, which employs the Piola transformation [28].

**Theorem of the Change of Variables in (Volume) Integrals**. We enunciate this fundamental theorem in the notation and context of Continuum Mechanics, but it is completely general. Let $\mathcal{P}_R \subseteq \Omega_R$ be subpart of the (material) domain, $\vec{\chi} : \Omega_R \to \Omega$ the configuration map, which is a diffeomorphism, and $f : \vec{\chi}(\mathcal{P}_R) \to \mathbb{R}$ a scalar field, with the current configuration of $\mathcal{P}_R$ denoted with $\mathcal{P}$. The integral of $f$ on $\mathcal{P}$ can be transformed into an integral on $\mathcal{P}_R$ via [28]

$$\int_{\mathcal{P}} f(\vec{x}, t)\, dv = \int_{\mathcal{P}_R} f(\vec{x}, t)\, J\, dV = \int_{\mathcal{P}_R} f_R(\vec{X})\, dV \tag{4.33}$$

**The Piola Transformation and Change of Variables in Surface Integrals**. Using the transformation of the area element is the most straightforward way to prove the expression of the Piola transformation, which has fundamental importance in Continuum Mechanics since it is used to transform vector fields. Let $A \subset \Omega_R$ be a (material) surface with normal $\vec{N}$, $\vec{\chi} : \Omega_R \to \Omega$ the configuration map and $a$ the current placement of the surface $A$, with normal $\vec{n}$. The vector field $\vec{w}$ is called a flux density for the physical quantity $q$ if the integral

$$\begin{aligned} Flux(q, \vec{\chi}(A)) &= \int_{\vec{\chi}(A)} \vec{w} \cdot \vec{n}\, da = \int_A \vec{W} \cdot \vec{N}\, dA \\ &= \int_A \vec{w} \cdot J\boldsymbol{F}^{-T} \vec{N}\, dA = \int_A J\boldsymbol{F}^{-1} \vec{w} \cdot \vec{N}\, dA \end{aligned} \tag{4.34}$$

measures the flux of the physical quantity $q$ across the surface a [28].

## 4.4 Divergence theorem and Reynold's theorem

**Divergence Theorem**. Let $\mathcal{P}$ be an open subset of the physical space $\Omega$ with smooth boundary $\partial\mathcal{P}$, $\vec{n}$ be the normal to $\partial\mathcal{P}$, and $\vec{w}$ be a vector field defined over $\mathcal{P}$. The Divergence Theorem enables to transform the integral of the scalar product $\vec{w} \cdot \vec{n}$ (i.e., the component of $\vec{w}$ normal to $\partial\mathcal{P}$) on the boundary

$\partial\mathcal{P}$ into a volume integral over the set $\mathcal{P}$, i.e. [28],

$$\int_{\partial\mathcal{P}} \vec{w}\cdot\vec{n}\,da = \int_{\mathcal{P}} \operatorname{div}[\,\vec{w}\,]\;dv \tag{4.35}$$

where we recall that the vector field $\vec{w}$ is said to describe a flux density and its divergence is defined as the trace of the gradient of $\vec{w}$ or, equivalently, the double contraction of the gradient with the identity tensor, i.e. [28],

$$\operatorname{div}[\,\vec{w}\,] = \operatorname{tr}[\operatorname{grad}[\,\vec{w}\,]\,] = \operatorname{grad}[\,\vec{w}\,] : \mathbb{1} = w_{i,i}. \tag{4.36}$$

**Reynolds' Transport Theorem**. The time derivative of the integral of a scalar field $f$ over a time-dependent domain is given by

$$\frac{\mathrm{d}}{\mathrm{d}t}\int_{\mathcal{P}} f\,dv = \int_{\mathcal{P}} \big(\frac{\partial f}{\partial t} + \operatorname{div}[\,f\,\vec{v}\,]\big)dv = \int_{\mathcal{P}} \frac{\partial f}{\partial t}\,dv + \int_{\partial\mathcal{P}} (f\,\vec{v}\cdot\vec{n})\,da \tag{4.37}$$

where $\int_{\partial\mathcal{P}} \big(f\,\vec{v}\cdot\vec{n}\big)\,da$ stands for the outward normal flux, or the rate of transport of $f\,\vec{v}$ across the surface (arising from moving region), with $\vec{v}$ representing the advecting velocity [28].

## 4.5 Balance laws

The reorganization of monomeric subunits into a network through polymerization induces a local volume change, which is captured in a continuum-based framework by a polymerization tensor. The process is reversible, and a volume decrement occurs upon depolymerization [6].

Such a mechanism also requires the presence of a cytosol, capable of filling all interstitials during network expansion and retreating upon shrinkage. Furthermore, the cytosol brings monomeric units into the proximity of the signal, thus stimulating the polymerization process. In the present version of our model, we do not provide the cytosol with any mechanical capability, other than a viscous drag on the F-actin network, which opposes the $F$-actin network retrograde motion $\vec{\chi}$. The cytosol is not equipped with any mechanical strength and thus it is not a *hosting lattice* in the Larché-Cahn sense. The cytosol, though, is considered a medium through which species can flow and diffuse. The mechanical strength and stiffness are provided merely by the $F$-network upon its polymerization [6].

Accordingly, at a point $\vec{X} \in \Omega_R$ we can idealize the coexistence of G actin and a polymer network in the cytosol, each of those two species being able to flow according to mass balances. Mechanical strength and stiffness at $\vec{X} \in \Omega_R$

are provided by the polymerized network; at all locations at which no network is present, the balance of momentum reduces to the trivial null identity. At all other locations, linear and angular momentum rule the transmission of loads through the interaction of the polymeric skeleton and the cytosol [6].

### 4.5.1 Mass balance

The mass balance equations rule the transformation and the flow of species that live in the cellular domain. A multitude of components coexist in the cell, but few of them are involved in pathogens ABM. For this reason, the model consists of two mass balance equations that govern the F-actin and G-actin arrangement in the cell domain, and the presence of other components (such as microtubules and microfilaments, that do not affect the pathogen's motility) is omitted. Moreover, the cytosol's role is limited to drag force on the F-actin network, even if it is the fluid in which species flow. As a consequence, a mass balance equation for cytosol arrangement is not provided and its mechanical response is neglected.

The interplay between the monomeric (G) and network (F) of actin in the cytosol is described as a chemical reaction

$$\mathrm{G} \underset{k_b}{\overset{k_f}{\rightleftarrows}} \mathrm{F} \ , \tag{4.38}$$

which models nucleation, branching, as well as cross-linking of actin and it is active in a volume surrounding the nucleation loci. It portrays how many moles of G-actin are converted into F-actin network and vice versa by the rate of the reaction (4.38), denoted with $w^{(4.38)}$ [6]. The parameters $k_b$ and $k_f$ denote the backward and forward reaction rate parameters [6]. We define a mole of the F-actin network as the result of polymerization of a mole of G-actin monomers [6].

Define

$$c_a(\vec{x}, t) \ , \qquad \text{with} \quad a = G, F \ , \tag{4.39}$$

as the molarity (moles per unit volume) reckoned per unit volume of the current configuration [6]. If necessary, the molarity of species can be rephrased in terms of density, multiplying the concentration by molecular mass ($m_G$ or $m_F$) [6].

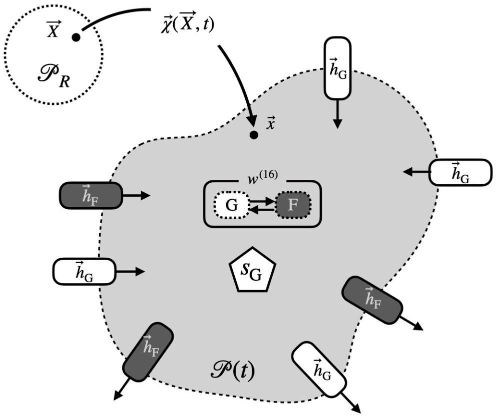

Figure 4.3: Schematic representation of the mass balance on an advecting cytosol $\mathcal{P}(t)$. A straightforward application of Reynold's theorem leads to eq. (4.44) [6]. Figure from [6].

#### 4.5.1.1 Global form of balance of mass

Consider a cell continuum body $\Omega$ with a set of particles occupying an arbitrary region $\mathcal{P}$ with boundary surface $\partial\mathcal{P}$ at time $t$. The mass balance equations of species G and F in the current configuration read

$$\frac{\mathrm{d}}{\mathrm{d}t}\int_{\mathcal{P}} c_G\, dv + \int_{\partial\mathcal{P}} \vec{h}_G \cdot \vec{n}\, da + \int_{\mathcal{P}} w^{(4.38)} - s_G\, dv = 0 \,, \tag{4.40a}$$

$$\frac{\mathrm{d}}{\mathrm{d}t}\int_{\mathcal{P}} c_F\, dv + \int_{\partial\mathcal{P}} \vec{h}_F \cdot \vec{n}\, da - \int_{\mathcal{P}} w^{(4.38)}\ dv = 0 \,. \tag{4.40b}$$

The mass flux vector $\vec{h}_a$, expressed in terms of moles per unit area per unit time, represents the flux of species $a$ out of the surface body $\partial\mathcal{P}$ [6]. The flux consists of two contributions, the transport and the advection out of the body so that $\vec{h}_a = c_a(\vec{v}_a - \vec{v}_{adv})$. $\vec{v}_{adv}$ represents the advection velocity, namely the velocity of the hosting material (cell) or the velocity of the species $a$ attached to the cell. In this case, we neglect the velocity of the cell, so the advecting velocity is null. $\vec{v}_a$ represents the velocity of the species $a$ itself, which can be due to a gradient in energy, chemical potential, or mechanics. The species needs to have a different velocity with respect to the advecting one if it leaves the material. $s_G$ is the rate in moles at which the G-actin is generated by cells. Since F-actin network production results only from the chemical reaction (4.38), the source term $s_F$ is null [6].

The mass balance equation can be defined in the reference configuration at point $\vec{X}$ and time $t$, making usage of the pushback rules (4.30) and (4.31), so every specific quantity, defined per unit volume, transforms as the density

$$c_{a_R}(\vec{X},t) = J(\vec{X},t)\; c_a(\,\vec{x}(\vec{X},t),t\,)\;, \tag{4.41a}$$

$$w_R^{(4.38)}(\vec{X},t) = \;J(\vec{X},t)\; w^{(4.38)}(\vec{x}(\vec{X},t),t)\;, \tag{4.41b}$$

$$s_{G_R}(\vec{X},t) = \;J(\vec{X},t)\; s_G(\,\vec{x}(\vec{X},t),t\,)\;, \tag{4.41c}$$

while taking advantage of Nanson's relationship, surface fluxes transform as

$$\vec{H}_a(\vec{X},t) = \;J\,\boldsymbol{F}^{-1}\;\vec{h}_a(\,\vec{x}(\vec{X},t),t\,)\;, \tag{4.42}$$

where $\vec{H}_a(\vec{X},t)$ is the reference flux vector. So, the global mass balance equation in the reference configuration reads

$$\frac{\mathrm{d}}{\mathrm{d}t}\int_{\mathcal{P}_R} c_{G_R}\,dv_R + \int_{\partial\mathcal{P}_R} \vec{H}_G\cdot\vec{N}\,da_R + \int_{\mathcal{P}_R} w_R^{(4.38)} - s_{G_R}\,dv_R = 0\;, \tag{4.43a}$$

$$\frac{\mathrm{d}}{\mathrm{d}t}\int_{\mathcal{P}_R} c_{F_R}\,dv_R + \int_{\partial\mathcal{P}_R} \vec{H}_F\cdot\vec{N}\,da_R - \int_{\mathcal{P}_R} w_R^{(4.38)}\;\;dv_R = 0\;. \tag{4.43b}$$

#### 4.5.1.2 Local form of balance of mass

Taking advantage of Reynold's theorem for the total derivative of $c_a$ with respect to time (4.37) and the Divergence Theorem for the flux (4.35), the mass balance equations of species G and F in the polymerized configuration, schematized in figure 4.3, localize as

$$\frac{\partial c_G}{\partial t} + \;\mathrm{div}\,[\,c_G\,\vec{v}_{adv}\,] + \mathrm{div}\left[\,\vec{h}_G\,\right] + \;w^{(4.38)} \;\; = s_G\;, \tag{4.44a}$$

$$\frac{\partial c_F}{\partial t} + \;\mathrm{div}\,[\,c_F\,\vec{v}_{adv}\,] + \mathrm{div}\left[\,\vec{h}_F\,\right] - \;w^{(4.38)} \;\; = 0\;. \tag{4.44b}$$

and the mass balance equations in the reference configuration localize as

$$\frac{\partial c_{G_R}}{\partial t} + \mathrm{Div}\left[\,\vec{H}_G\,\right] + w_R^{(4.38)} \;\; = s_{G_R}\;, \tag{4.45a}$$

$$\frac{\partial c_{F_R}}{\partial t} + \mathrm{Div}\left[\,\vec{H}_F\,\right] - \;w_R^{(4.38)} \;\; = 0\;. \tag{4.45b}$$

### 4.5.2 Balances of momentum

In this section, the balance of linear and angular momentum for the cell system is described. Moreover, Cauchy's first equation of motion and the symmetry of the Cauchy stress tensor are shown. These principles are valid for the whole or arbitrary parts of the continuum body $\Omega$, but, as previously mentioned, the mechanical strength in this model is provided by the polymerized network only, so mechanical balances reduce to the trivial null identity where there is no F-actin network.

Differently from several well-established theories [29], either accounting for trapping or not [30, 31], the present framework for ABM does not fall into the class of Larché-Cahn models. The notion of *hosting lattice* is meaningless, since at $t = 0\,s$ only the cytosol is assumed to exist, together with a locus at which polymerization develops at all times $t > 0$.

#### 4.5.2.1 Balance of linear and angular momentum in spatial and material description

Consider a cell continuum body $\Omega$ with a set of particles occupying an arbitrary region $\mathcal{P}$ with boundary surface $\partial\mathcal{P}$ at time $t$. It is considered a close cell system with a given motion $\vec{x} = \vec{\chi}(\vec{X}, t)$ and spatial velocity $\vec{v} = \vec{v}(\vec{x}, t)$. In addition, since the mechanical strength is supplied by the F-actin network, the spatial mass density takes into account the F-actin contribution only, $\rho_F(\vec{x}, t)$. For this reason, the total **linear momentum** $\vec{L}$ reads [28]

$$\vec{L}(t) = \int_{\mathcal{P}} \rho_F(\vec{x}, t)\, \vec{v}(\vec{x}, t)\, dv = \int_{\mathcal{P}_R} \rho_{F_R}(\vec{X})\, \vec{V}(\vec{X}, t)\, dv_R \ , \tag{4.46}$$

and the total **angular momentum** (or **momentum of momentum**) $\vec{J}$ relative to a fixed point (characterized by the position vector $\vec{x}_0$) reads [28]

$$\vec{J}(t) = \int_{\mathcal{P}} \vec{r} \times \rho_F(\vec{x}, t)\, \vec{v}(\vec{x}, t)\, dv = \int_{\mathcal{P}_R} \vec{r} \times \rho_{F_R}(\vec{X})\, \vec{V}(\vec{X}, t)\, dv_R \ , \tag{4.47}$$

where $\vec{r} = \vec{x} - \vec{x}_0 = \vec{\chi}(\vec{X}, t) - \vec{x}_0$.

In the context of continuum mechanics, the material time derivatives of linear and angular momentum result in Newton's first and second principles of motion.

The **balance of linear momentum** reads

$$\begin{aligned}\frac{\mathrm{d}\vec{L}(t)}{\mathrm{d}t} &= \frac{\mathrm{d}}{\mathrm{d}t}\int_{\mathcal{P}} \rho_F\,\vec{v}\,dv = \frac{\mathrm{d}}{\mathrm{d}t}\int_{\mathcal{P}_R} \rho_{F_R}\,\vec{V}\,dv_R \\ &= \int_{\mathcal{P}_R} \frac{\mathrm{d}\rho_{F_R}}{\mathrm{d}t}\,\vec{V} + \rho_{F_R}\frac{\mathrm{d}\vec{V}}{\mathrm{d}t}\,dv_R = \vec{F}(t)\ ,\end{aligned} \tag{4.48}$$

and the **balance of angular momentum** reads

$$\begin{aligned}\frac{\mathrm{d}\vec{J}(t)}{\mathrm{d}t} &= \frac{\mathrm{d}}{\mathrm{d}t}\int_{\mathcal{P}} \vec{r}\times\rho_F\,\vec{v}\,dv = \frac{\mathrm{d}}{\mathrm{d}t}\int_{\mathcal{P}_R} \vec{r}\times\rho_{F_R}\,\vec{V}\,dv_R \\ &= \int_{\mathcal{P}_R} \vec{r}\times\rho_{F_R}\,\frac{\mathrm{d}\vec{V}}{\mathrm{d}t} + \vec{r}\times\frac{\mathrm{d}\rho_{F_R}}{\mathrm{d}t}\,\vec{V} + \frac{\mathrm{d}\,\vec{r}}{\mathrm{d}t}\times\rho_{F_R}\,\vec{V}\,dv_R = \vec{M}(t)\ ,\end{aligned} \tag{4.49}$$

where $\vec{F}(t)$ and $\vec{M}(t)$ are vector-valued functions that represent respectively the **resultant force** and the **resultant moment** (or **resultant torque**) [28]. They represent the external forces and moments acting on the continuum body and are defined respectively as [28]

$$\vec{F}(t) = \int_{\partial\mathcal{P}} \vec{t}\,da + \int_{\mathcal{P}} \vec{b}\,dv = \int_{\partial\mathcal{P}_R} \vec{T}\,da_R + \int_{\mathcal{P}_R} \vec{B}\,dv_R\ , \tag{4.50}$$

and

$$\vec{M}(t) = \int_{\partial\mathcal{P}} \vec{r}\times\vec{t}\,da + \int_{\mathcal{P}} \vec{r}\times\vec{b}\,dv = \int_{\partial\mathcal{P}_R} \vec{r}\times\vec{T}\,da_R + \int_{\mathcal{P}_R} \vec{r}\times\vec{B}\,dv_R\ . \tag{4.51}$$

#### 4.5.2.2 Cauchy's stress theorem

Cauchy's Theorem (of Cauchy's Tetrahedron) for the Stress states that there exist unique second-order tensor fields $\boldsymbol{\sigma}$ and $\boldsymbol{P}$ such that

$$\vec{t} = \boldsymbol{\sigma}\vec{n}\ , \tag{4.52a}$$

$$\vec{T} = \boldsymbol{P}\vec{N}\ . \tag{4.52b}$$

which describe the linear relation between the surface traction $\vec{t}$ or $\vec{T}$ and the normal $\vec{n}$ or $\vec{N}$ [28].

#### 4.5.2.3 Equation of motion in spatial and material description

Applying the Cauchy's Stress Theorem (4.52) and the Divergence Theorem (4.35), the balance of linear momentum in the current and in the reference configuration, which *are written at points $\vec{x}$ and $\vec{X}$ in the comet tail*, read

$$\int_{\mathcal{P}} \operatorname{div}[\,\boldsymbol{\sigma}\,] + \vec{b} - \frac{\mathrm{d}\,\rho_F\,\vec{v}}{\mathrm{d}t}\,dv = 0\;, \tag{4.53}$$

and

$$\int_{\mathcal{P}_R} \operatorname{Div}[\,\boldsymbol{P}\,] + \vec{B} - \frac{\mathrm{d}\,\rho_{F_R}\,\vec{V}}{\mathrm{d}t}\,dv_R = 0\;, \tag{4.54}$$

respectively [28].

In the referential local form, the balance of linear momentum reads

$$\operatorname{Div}[\,\boldsymbol{P}\,] + \vec{B} = \frac{\mathrm{d}\,\rho_{F_R}\,\dot{\vec{\chi}}}{\mathrm{d}t}\;, \qquad \vec{X} \in \Omega_R \tag{4.55}$$

with $\vec{B}$ denoting external body forces per unit reference volume in the material representation, $\dot{\vec{\chi}} = \vec{V}$ denoting the referential F-actin network advection velocity and $\rho_{F_R}$ denoting the referential density of actin network. $\boldsymbol{P}$ is the nominal stress tensor (first Piola-Kirchhoff stress tensor), obeying the symmetry condition

$$\boldsymbol{P}\boldsymbol{F}^T = \boldsymbol{F}\boldsymbol{P}^T\;, \tag{4.56}$$

which is the balance of angular momentum. Among the external forces acting on the F-actin network, the cytosol viscous drag forces, that act opposite to the relative motion of the F-actin network, are included [6, 28, 32, 24, 33].

## 4.6 Chemical kinetics: mass action

The coexistence of G-actin and F-actin can be studied in terms of volume fractions, defining the volume fractions occupied by F and G, or in terms of concentrations. It is defined as an initial volume, in which no F-actin filaments are present, and a current volume, in which an amount of network is present. The molar volumes of G-actin and F-actin are considered as different and this difference constitutes the molecular motor. If this is true, there is a difference between the volume in the current and in the reference configuration, which is dictated by the amount of the F-actin network that polymerizes. The ratio between the volume in the current and in the reference configuration, in the absence of mechanical forces of elastic type, represents a swelling factor.

The concentration of G-actin within actin filaments should not be taken as an unknown field, since it is always "saturated". However, the volume occupied by the network polymer is not known, so we may use the volume fractions to characterize the evolution of the polymerization process. It reads

$$\Phi_F = \frac{v_F}{v_{tot}} \ , \qquad \Phi_G = \frac{v_G}{v_{tot}} \ , \tag{4.57}$$

where $\Phi_F$ represents the volume occupied by F-actin network and $\Phi_G$ represents the volume occupied by G-actin molecules. Combining the volume fraction and the volume occupied by the network, it follows

$$v_F = mol_F \, \omega_F \qquad \Phi_F = \frac{mol_F}{v_{tot}} \omega_F \ . \tag{4.58}$$

### 4.6.1 Swelling factor

We assume that the G-actin is partially transformed into the F-actin network by the reaction (4.38); hence, at every point $\vec{X} \in \Omega_R$ at time t, two phases G and F coexist [6]. Assume that $mol_G^0 = mol_G + mol_F$; in the initial condition the reference state is defined to be pure monomeric G-actin and in the absence of any mechanical effect, the volume of a neighborhood at $\vec{X}$ evolves as

$$\begin{aligned} \mathrm{d}v &= \mathrm{d}v_R - \mathrm{d}v_G^0 + \mathrm{d}v_G + \mathrm{d}v_F \\ &= \mathrm{d}v_R - mol_G^0 \, \omega_G + mol_G \, \omega_G + mol_F \, \omega_F \\ &= \mathrm{d}v_R - \omega_G \, (mol_G + mol_F - mol_G^0) + mol_F \, (\omega_F - \omega_G) \\ &= \mathrm{d}v_R + mol_F \, (\omega_F - \omega_G) \\ &= \mathrm{d}v_R + (mol_F) \, \Omega_F \ , \end{aligned} \tag{4.59}$$

with $\Omega_F = (\omega_F - \omega_G)$. $\omega_a$ denotes the molar volume of $a$-species (volume of the $a$-mole, presumed to be constant), which takes a different value for each species ($\omega_G$ and $\omega_F$) [6].

From eq. (4.59), the change in volume per unit reference volume can be written as

$$J^c(\vec{X}, t) = \frac{\mathrm{d}v}{\mathrm{d}v_R} = 1 + c_{F_R}(\vec{X}, t) \, \Omega_F \ , \tag{4.60}$$

with $c_{F_R}$ depicting the referential concentration of the F-actin network, namely the number of F-actin unit molecules reckoned per unit volume of the un-polymerized reference configuration, and $J^c$ representing the swelling factor, entirely due to polymerization [6]. From eq. (4.60), we can write

$$\frac{\mathrm{d}\, J^c}{\mathrm{d}t} = \Omega_F \, \frac{\mathrm{d}\, c_{F_R}}{\mathrm{d}t} \ . \tag{4.61}$$

### 4.6.2 Signal for polymerization and delay for depolymerization

The rate of the reaction (4.38) is defined via the law of mass action in the current configuration as

$$w^{(4.38)}(\vec{x},t) = k_f \, \frac{\vartheta_G}{1-\vartheta_G} - k_b \, \frac{\vartheta_F}{1-\vartheta_F} \; , \tag{4.62}$$

with $k_b$ and $k_f$ the backward and forward reaction rate parameters,

$$\vartheta_a(\vec{x},t) = \frac{c_a(\vec{x},t)}{c_a^{max}(\vec{x},t)} \qquad \text{with} \quad a = G, F \; , \tag{4.63}$$

and $c_a^{max}$ the saturation limit for every $a$-species. Taking advantage of eq. (4.41a) and (4.41b), eq. (4.62) writes in the reference configuration as

$$w_R^{(4.38)}(\vec{X},t) = k_{f_R} \, \frac{\vartheta_{G_R}}{1-\vartheta_{G_R}} - k_{b_R} \, \frac{\vartheta_{F_R}}{1-\vartheta_{F_R}} \; , \tag{4.64}$$

with $\vartheta_{a_R}$ denoting the ratio

$$\vartheta_{a_R}(\vec{X},t) = \frac{c_{a_R}(\vec{X},t)}{c_{a_R}^{max}(\vec{X},t)} \; , \qquad \text{with} \quad a = G, F \; . \tag{4.65}$$

As discussed in [34], two paradigmatic cases shall be considered for the relationship between the saturation concentration in the reference and in the current configuration [6]. Here it is assumed that the maximum number of molecules per unit volume is invariant: this case occurs when the volume occupied by each unit species is invariant, and species can relocate to occupy eventual volumetric expansions of the hosting material. Under this assumption, $c_{a_R}^{max}(\vec{X},t) = c_a^{max}(\vec{x},t)$, while $k_{f_R} = k_f$ and $k_{b_R} = k_b$ *far from saturation* [6].

Normally, the polymerization reaction begins and reaches equilibrium, where the continuous addition of new monomers to the filament is balanced by the loss of monomers, resulting in a constant filament length. In this state, no net force or energy can be derived from the process. Therefore, in most forms of ABM, an external energy input is necessary to reverse the polymerization reaction and maintain actin filaments far from chemical equilibrium. The most controlled version of this external energy input occurs in continuous cycles, primarily at the cost of ATP hydrolysis. In this process, the polymer utilizes the free energy from ATP hydrolysis to convert kinetic differences between subunit addition rates at the plus and minus ends into energetic disparities that the polymerization motor can potentially exploit [1].

In addition to hydrolysis, accessory proteins such as Arp2/3, VASP, and capping protein are recruited to support the formation of the $F$-actin network during actin polymerization [35, 8]. In the context of pathogen motility, the activator that initiates and coordinates all these processes is the ActA, a stable protein located on the surface of the bacterium.

As done in [36], we embody all these biochemical signaling pathways in a single signaling function $\mathcal{C}$ in the forward reaction rate parameter $k_f$

$$k_f = \mathcal{C}\, k_f^* \, , \tag{4.66}$$

where $k_f^*$ is a constant and $\mathcal{C}$ represents the activation signal that triggers actin polymerization and network formation [6].

The network depolymerization is also dependent on external cues; whereas biological studies are still insufficiently detailed, we include all environmental factors (such as the mechanical stress in the network, among others) into a phenomenological descriptor, a time delay $\tau$ from the onset of polymerization, which corresponds to the notion of the half-life of filaments, introduced in [8]. For this reason, the backward reaction rate parameter is defined as follows

$$\begin{aligned} k_b &= 0 && \text{if} \quad c_{F_R}(\vec{X}, t-\tau) = 0 \, , \\ k_b &= k_b^* && \text{otherwise} \, . \end{aligned} \tag{4.67}$$

Two circumstances occur

- the depolymerization does not take part at positions $\vec{X}$ of the cell in which the concentration of F-actin network at time $t-\tau > 0$ was null, namely everywhere when $t-\tau \leq 0$ or where G-actin had not been polymerized at time $t-\tau$ yet. This implies that $k_b = 0$ and it is consistent with considering that each filament has a lifetime, during which no depolymerization occurs;
- the depolymerization does take part at positions $\vec{X}$ of the cell where the F-actin network was already present at time $t-\tau$. This implies that $k_b = k_b^*$ with $k_b^* \neq 0$ and it entails that filaments start to depolymerize a period of time $\tau$ after their polymerization began [6].

The assumption that both the forward and backward reaction parameters are force-independent is a simplification of the real process since the presence of the load force can affect both $k_f$ and $k_b$ [1].

## 4.7 Construction of a thermodynamically consistent model

### 4.7.1 Energy balance

#### 4.7.1.1 Energy balance in the current configuration

Denote with $\Omega(t)$ the advecting cell and with $\partial\Omega(t)$ its membrane [6]. Consider an arbitrary region $\mathcal{P} \subset \Omega(t)$ [6]. The first law of thermodynamics (energy balance) rules the transformation from one type of energy involved in the thermodynamic process into another [6]. The energy balance for the problem at hand reads [28]

$$\frac{\mathrm{d}\,\mathcal{K}(\mathcal{P})}{\mathrm{d}t} + \frac{\mathrm{d}\,\mathcal{U}(\mathcal{P})}{\mathrm{d}t} = \mathcal{W}_u(\mathcal{P}) + \mathcal{Q}_u(\mathcal{P}) + \mathcal{T}_u(\mathcal{P}) \ , \tag{4.68}$$

where

- $\mathcal{K}(\mathcal{P})$ represents the **kinetic energy** of a continuum body occupying a region $\mathcal{P}$ at time $t$. It is a generalization of Newtonian mechanics to continuum mechanics and it is defined as

  $$\mathcal{K}(\mathcal{P}) = \int_{\mathcal{P}} \frac{1}{2} \rho_F \, \vec{v} \cdot \vec{v} \, \mathrm{d}v \ , \tag{4.69}$$

  so it is non null only when $\rho_F \neq 0$. The spatial velocity field is denoted by $\vec{v} = \dot{\vec{x}}$ [28].

- $\mathcal{U}(\mathcal{P})$ represents the **internal energy** possessed by a continuum body occupying a certain region $\mathcal{P}$. It is the sum of all the microscopic forms of energy and it is defined as

  $$\mathcal{U}(\mathcal{P}) = \int_{\mathcal{P}} u \, \mathrm{d}v \ , \tag{4.70}$$

  where $u$ is a thermodynamic extensive state variable defined per unit current volume [28].

- $\mathcal{W}_u(\mathcal{P})$ represents the **mechanical external power** or the **rate of mechanical external work**. It is the power input on a region $\mathcal{P}$ at time $t$ done by the system of forces $(\vec{t}, \vec{b})$

  $$\mathcal{W}_u(\mathcal{P}) = \int_{\partial\mathcal{P}} \vec{v} \cdot \vec{t} \, \mathrm{d}a + \int_{\mathcal{P}} \vec{v} \cdot \vec{b} \, \mathrm{d}v \ . \tag{4.71}$$

  The scalar quantities $\vec{v} \cdot \vec{t}$ and $\vec{v} \cdot \vec{b}$ give the external mechanical power per unit current surface $a$ and the current volume $v$, respectively. As mentioned before, the cytosol does not provide any mechanical capability, so the external forces act on the F-actin network only. Using the Cauchy Stress Theorem (4.52) and the Divergence Theorem (4.35), we can rewrite the eq. (4.71) as [28]

$$\begin{aligned}\mathcal{W}_u(\mathcal{P}) &= \int_{\partial\mathcal{P}} \boldsymbol{\sigma}\vec{n}\cdot\vec{v}\,\mathrm{d}a + \int_{\mathcal{P}} \vec{v}\cdot\vec{b}\,\mathrm{d}v = \int_{\partial\mathcal{P}} \boldsymbol{\sigma}\vec{v}\cdot\vec{n}\,\mathrm{d}a + \int_{\mathcal{P}} \vec{v}\cdot\vec{b}\,\mathrm{d}v \\ &= \int_{\partial\mathcal{P}} \mathrm{div}\,[\,\boldsymbol{\sigma}\vec{v}\,]\,\mathrm{d}v + \int_{\mathcal{P}} \vec{v}\cdot\vec{b}\,\mathrm{d}v \\ &= \int_{\partial\mathcal{P}} \boldsymbol{\sigma} : \mathrm{grad}\,[\,\vec{v}\,]\,\mathrm{d}v + \int_{\mathcal{P}} (\mathrm{div}\,[\,\sigma\,] + \vec{b})\cdot\vec{v}\,\mathrm{d}v \\ &= \int_{\partial\mathcal{P}} \boldsymbol{\sigma} : \boldsymbol{d}\,\mathrm{d}v + \frac{\mathrm{d}}{\mathrm{d}t}\int_{\mathcal{P}} \frac{1}{2}\rho_F\,\vec{v}\cdot\vec{v}\,\mathrm{d}v = W_u^{int}(\mathcal{P}) + \frac{\mathrm{d}\,\mathcal{K}(\mathcal{P})}{\mathrm{d}t}\ .\end{aligned} \tag{4.72}$$

- $\mathcal{Q}_u(\mathcal{P})$ represents the **thermal (non-mechanical) power** or the **rate of thermal work** [28]

$$\mathcal{Q}_u = \int_{\mathcal{P}} s_q\,\mathrm{d}v - \int_{\partial\mathcal{P}} \vec{q}\cdot\vec{n}\,\mathrm{d}a\ . \tag{4.73}$$

  where $s_q$ denotes the heat source per unit time and per unit current volume and $\vec{q}$ denotes the heat flux, which is defined per unit time and per unit current surface area. The total heat flux $\int_{\partial\mathcal{P}} \vec{q}\cdot\vec{n}\,\mathrm{d}a$ determines the rate at which heat enters (inward normal flux) the body across the current boundary surface $\partial\mathcal{P}$.

- $\mathcal{T}_u(\mathcal{P})$ represents the **power due to mass transfer**

$$\mathcal{T}_u = \int_{\mathcal{P}} {}^u\mu_G\, s_G\,\mathrm{d}v - \int_{\partial\mathcal{P}} {}^u\mu_F\,\vec{h}_F\cdot\vec{n}\ +\ {}^u\mu_G\,\vec{h}_G\cdot\vec{n}\,\mathrm{d}a_R\ , \tag{4.74}$$

  where $\vec{h}_a$ and $s_G$ are defined in paragraph 4.5.1.1 and ${}^u\mu_a$ denotes the change in specific energy (energy per mol) provided by a unit supply of moles of $a$-species [6, 28].

#### 4.7.1.2 Energy balance in the reference configuration

To express the terms of the balance of mechanical energy with respect to material coordinates at time $t$, all the contributions of the energy balance in the material coordinates must be established. So, using the rules for scalar transformation in 4.2, the contributions of eq. (4.68) can be rewritten as [28]

- $\mathcal{K}(\mathcal{P})$: considering that $\vec{v} = \vec{V}$, the **kinetic energy** in the reference configuration reads [28]

$$\begin{aligned}\mathcal{K}(\mathcal{P}) &= \int_{\mathcal{P}} \frac{1}{2}\rho_F\,\vec{v}\,\cdot\,\vec{v}\,J\,\mathrm{d}v_R = \int_{\mathcal{P}_R} \frac{1}{2}J\rho_F\,\vec{V}\,\cdot\,\vec{V}\,\mathrm{d}v_R \\ &= \int_{\mathcal{P}_R} \frac{1}{2}\rho_{F_R}\,\vec{V}\,\cdot\,\vec{V}\,\mathrm{d}v_R = \mathcal{K}(\mathcal{P}_R)\,.\end{aligned} \tag{4.75}$$

- $\mathcal{U}(\mathcal{P})$: the **internal energy** in the reference configuration reads [28]

$$\mathcal{U}(\mathcal{P}) = \int_{\mathcal{P}} u\,J\,\mathrm{d}v_R = \int_{\mathcal{P}_R} u_R\,\mathrm{d}v_R = \mathcal{U}(\mathcal{P}_R)\,. \tag{4.76}$$

- $\mathcal{W}_u(\mathcal{P})$: the **mechanical external power** in the reference configuration reads [28]

$$\begin{aligned}\mathcal{W}_u(\mathcal{P}) &= \int_{\partial\mathcal{P}_R} J\boldsymbol{\sigma} : \boldsymbol{d}\,\mathrm{d}v_R + \frac{\mathrm{d}}{\mathrm{d}t}\int_{\mathcal{P}_R} \frac{1}{2}J\rho_F\,\vec{V}\,\cdot\,\vec{V}\,\mathrm{d}v_R \\ &= \int_{\partial\mathcal{P}_R} J\boldsymbol{\sigma} : \frac{\mathrm{d}\boldsymbol{F}}{\mathrm{d}t}\boldsymbol{F}^{-1}\,\mathrm{d}v_R + \frac{\mathrm{d}}{\mathrm{d}t}\int_{\mathcal{P}_R} \frac{1}{2}\rho_{F_R}\,\vec{V}\,\cdot\,\vec{V}\,\mathrm{d}v_R \\ &= \int_{\partial\mathcal{P}_R} J\boldsymbol{\sigma}\boldsymbol{F}^{-T} : \frac{\mathrm{d}\boldsymbol{F}}{\mathrm{d}t}\,\mathrm{d}v_R + \frac{\mathrm{d}}{\mathrm{d}t}\int_{\mathcal{P}_R} \frac{1}{2}\rho_{F_R}\,\vec{V}\,\cdot\,\vec{V}\,\mathrm{d}v_R \\ &= \int_{\partial\mathcal{P}_R} \boldsymbol{P} : \frac{\mathrm{d}\boldsymbol{F}}{\mathrm{d}t}\,\mathrm{d}v_R + \frac{\mathrm{d}}{\mathrm{d}t}\int_{\mathcal{P}_R} \frac{1}{2}\rho_{F_R}\,\vec{V}\,\cdot\,\vec{V}\,\mathrm{d}v_R \\ &= W_u^{int}(\mathcal{P}_R) + \frac{\mathrm{d}\,\mathcal{K}(\mathcal{P}_R)}{\mathrm{d}t}\,.\end{aligned} \tag{4.77}$$

- $\mathcal{Q}_u(\mathcal{P})$: using the divergence theorem, the **thermal (non-mechanical) power** reads [28]

$$\begin{aligned}\mathcal{Q}_u(\mathcal{P}) &= \int_{\mathcal{P}_R} Js_q\,\mathrm{d}v_R - \int_{\partial\mathcal{P}_R} \vec{q}\cdot J\boldsymbol{F}^{-T}\vec{N}\,\mathrm{d}a_R \\ &= \int_{\mathcal{P}_R} s_{q\,R}\,\mathrm{d}v_R - \int_{\partial\mathcal{P}_R} J\boldsymbol{F}^{-1}\vec{q}\cdot\vec{N}\,\mathrm{d}a_R \\ &= \int_{\mathcal{P}_R} s_{q\,R} - \mathrm{Div}\left[\vec{Q}\right]\,\mathrm{d}v_R = \mathcal{Q}_u(\mathcal{P}_R)\,.\end{aligned} \tag{4.78}$$

- $\mathcal{T}_u(\mathcal{P})$: using the divergence theorem and the mass balance equation, the

**power due to mass transfer** reads [28]

$$
\begin{aligned}
\mathcal{T}_u(\mathcal{P}) &= \int_{\mathcal{P}_R} {}^u\mu_G \, J s_G \, \mathrm{d}v_R + \\
&- \int_{\partial\mathcal{P}_R} {}^u\mu_F \, \vec{h}_F \cdot J\boldsymbol{F}^{-T}\vec{N} \; + {}^u\mu_G \, \vec{h}_G \cdot J\boldsymbol{F}^{-T}\vec{N} \, \mathrm{d}a_R \\
&= \int_{\mathcal{P}_R} {}^u\mu_G \, s_{G_R} \, \mathrm{d}v_R - \int_{\partial\mathcal{P}} {}^u\mu_F \, \vec{H}_F \cdot \vec{N} \; + {}^u\mu_G \, \vec{H}_G \cdot \vec{N} \, \mathrm{d}a_R \\
&= \int_{\mathcal{P}_R} {}^u\mu_G \, s_{G_R} \; - \operatorname{Div}\left[ {}^u\mu_F \, \vec{H}_F \right] \; - \operatorname{Div}\left[ {}^u\mu_G \, \vec{H}_G \right] \; \mathrm{d}v_R \\
&= \int_{\mathcal{P}_R} {}^u\mu_G \, s_{G_R} \; - \operatorname{Grad}\left[ {}^u\mu_F \right] \cdot \vec{H}_F \; - {}^u\mu_F \operatorname{Div}\left[ \vec{H}_F \right] + \\
&\quad - \operatorname{Grad}\left[ {}^u\mu_G \right] \cdot \vec{H}_G \; - {}^u\mu_G \operatorname{Div}\left[ \vec{H}_G \right] \; \mathrm{d}v_R \\
&= \int_{\mathcal{P}_R} \left( {}^u\mu_G - {}^u\mu_F \right) \, w_R^{(4.38)} + {}^u\mu_G \, \frac{\partial c_{G_R}}{\partial t} \\
&\quad - \vec{H}_G \cdot \operatorname{Grad}\left[ {}^u\mu_G \right] + {}^u\mu_F \, \frac{\partial c_{F_R}}{\partial t} - \vec{H}_F \cdot \operatorname{Grad}\left[ {}^u\mu_F \right] \; \mathrm{d}v_R \\
&= \mathcal{T}_u(\mathcal{P}_R) \; .
\end{aligned}
\tag{4.79}
$$

Considering an arbitrary material region $\mathcal{P}_R$, the referential global energy balance reads [28]

$$
\frac{\mathrm{d}\,\mathcal{K}(\mathcal{P}_R)}{\mathrm{d}t} + \frac{\mathrm{d}\,\mathcal{U}(\mathcal{P}_R)}{\mathrm{d}t} = \mathcal{W}_u(\mathcal{P}_R) + \mathcal{Q}_u(\mathcal{P}_R) + \mathcal{T}_u(\mathcal{P}_R) \; . \tag{4.80}
$$

The individual contributions read

$$
\frac{\mathrm{d}\,\mathcal{K}}{\mathrm{d}t} = \frac{\mathrm{d}}{\mathrm{d}t} \int_{\mathcal{P}_R} \frac{1}{2} \rho_{F_R} \vec{V} \; \cdot \; \vec{V} \, \mathrm{d}v_R, \tag{4.81a}
$$

$$
\frac{\mathrm{d}\,\mathcal{U}}{\mathrm{d}t} = \int_{\mathcal{P}_R} \frac{\mathrm{d}\,u_R}{\mathrm{d}t} \, \mathrm{d}v_R \; , \tag{4.81b}
$$

$$
\mathcal{W}_u = \int_{\partial\mathcal{P}_R} \boldsymbol{P} : \frac{\mathrm{d}\boldsymbol{F}}{\mathrm{d}t} \, \mathrm{d}v_R + \frac{\mathrm{d}}{\mathrm{d}t} \int_{\mathcal{P}_R} \frac{1}{2} \rho_{F_R} \vec{V} \; \cdot \; \vec{V} \, \mathrm{d}v_R \; , \tag{4.81c}
$$

$$
\mathcal{Q}_u = \int_{\mathcal{P}_R} s_{q_R} - \operatorname{Div}\left[ \vec{Q} \right] \; \mathrm{d}v_R \; , \tag{4.81d}
$$

$$
\begin{aligned}
\mathcal{T}_u = \int_{\mathcal{P}_R} &\left( {}^u\mu_G - {}^u\mu_F \right) \, w_R^{(4.38)} + {}^u\mu_G \, \frac{\partial c_{G_R}}{\partial t} \\
&- \vec{H}_G \cdot \operatorname{Grad}\left[ {}^u\mu_G \right] + {}^u\mu_F \, \frac{\partial c_{F_R}}{\partial t} - \vec{H}_F \cdot \operatorname{Grad}\left[ {}^u\mu_F \right] \; \mathrm{d}v_R \; ,
\end{aligned}
\tag{4.81e}
$$

where $\dot{\vec{V}}$ represents the referential velocity, $u_R$ the internal energy density per unit volume, $s_{q_R}$ the heat source per unit reference volume and unit time generated into region $\mathcal{P}_R$ of the body, $\vec{Q}$ the heat flux vector per unit reference surface area and unit time and $\vec{N}$ the outward unit normal to the reference surface. $\vec{H}_a$ and $s_{G_R}$ are defined in paragraph 4.5.1.1 and ${}^u\mu_a$ denotes the change in specific energy provided by a unit supply of moles of $a$-species [6, 28].

The referential global energy balance eventually takes the form

$$\begin{aligned}\int_{\mathcal{P}_R} \frac{\mathrm{d}\, u_R}{\mathrm{d}t}\, \mathrm{d}v_R = \int_{\mathcal{P}_R} \boldsymbol{P} \cdot \frac{\mathrm{d}\boldsymbol{F}}{\mathrm{d}t} + s_{q_R} - \mathrm{Div}\left[\vec{Q}\right] + ({}^u\mu_G - {}^u\mu_F)\, w_R^{(4.38)} \\ + {}^u\mu_G \frac{\partial c_{G_R}}{\partial t} - \vec{H}_G \cdot \mathrm{Grad}\left[\, {}^u\mu_G \,\right] \\ + {}^u\mu_F \frac{\partial c_{F_R}}{\partial t} - \vec{H}_F \cdot \mathrm{Grad}\left[\, {}^u\mu_F \,\right]\, \mathrm{d}v_R\ . \end{aligned} \tag{4.82}$$

## 4.7.2 Entropy imbalance

The first law of thermodynamics rules the energy transformation within a thermodynamic process, but it does not consider the direction of the energy transfer. To fill this gap, the second law of thermodynamics (entropy imbalance), which governs the direction of an energy transfer process, is discussed. The entropy per unit current and reference volume

$$\eta_R = \eta_R(\vec{X}, t) \qquad \text{or} \qquad \eta = \eta(\vec{x}, t)$$

is introduced as a fundamental state variable, that can be viewed as the quantitative measure of microscopic randomness and disorder and whose physical interpretation is provided by the statistical mechanics.

### 4.7.2.1 Entropy imbalance in the current configuration

Consider an arbitrary spatial region $\mathcal{P} \subset \Omega(t)$, the difference between the change in the system's total entropy and the rate of entropy input determines the total entropy production per unit of time, which represents the current global entropy imbalance. It reads

$$\frac{\mathrm{d}\, \mathcal{S}(\mathcal{P}, t)}{\mathrm{d}t} - \mathcal{Q}_\eta(\mathcal{P}, t) - \mathcal{T}_\eta(\mathcal{P}, t) \geq 0\ , \tag{4.83}$$

where $\mathcal{S}(\mathcal{P}, t)$ represents the net internal entropy, $\mathcal{Q}_\eta(\mathcal{P}, t)$ the entropy per unit time due to heat transfer and $\mathcal{T}_\eta(\mathcal{P}, t)$ the entropy per unit time due to mass transfer. The relation defines a trend in time describing the direction of the energy transfer: it postulates the irreversibility of thermodynamic processes, which entails the increase in entropy in irreversible processes and a balance of entropy in reversible processes (the production of entropy is never negative) [28].

The individual contributions read

$$\frac{\mathrm{d}\,\mathcal{S}}{\mathrm{d}t} = \int_{\mathcal{P}} \frac{\mathrm{d}\,\eta}{\mathrm{d}t}\,\mathrm{d}v\;, \tag{4.84a}$$

$$\mathcal{Q}_\eta = \int_{\mathcal{P}} \frac{1}{T}\,s_q\,\mathrm{d}v - \int_{\partial\mathcal{P}} \frac{1}{T}\,\vec{q}\cdot\vec{n}\,\mathrm{d}a\;, \tag{4.84b}$$

$$\mathcal{T}_\eta = \int_{\mathcal{P}} {}^{\eta}\mu_G\,s_G\,\mathrm{d}v - \int_{\partial\mathcal{P}} {}^{\eta}\mu_G\,\vec{h}_G\cdot\vec{n}\;+{}^{\eta}\mu_F\,\vec{h}_F\cdot\vec{n}\,\mathrm{d}a\;, \tag{4.84c}$$

where $\eta$ is a scalar field that represents the internal entropy density per unit current volume and measures the randomness and disorder and ${}^{\eta}\mu_a$ denotes the change in specific entropy provided by a unit supply of moles of $a$-species. The rate of entropy input is provided by the amount of entropy transferred across the boundary and the entropy produced inside the region, related to the heat and mass fluxes and the heat and mass production. According to the absolute temperature definition, it is postulated that the entropy heat fluxes and entropy heat sources are related to the heat fluxes and the heat sources by the factor $\frac{1}{T}$ [28].

#### 4.7.2.2 Entropy imbalance in the reference configuration

Considering an arbitrary material region $\mathcal{P}_R$, the referential global entropy imbalance reads

$$\frac{\mathrm{d}\,\mathcal{S}(\mathcal{P}_R)}{\mathrm{d}t} - \mathcal{Q}_\eta(\mathcal{P}_R) - \mathcal{T}_\eta(\mathcal{P}_R) \geq 0\;. \tag{4.85}$$

Using the rules for scalar transformation in 4.2, each of the contributions in eq. (4.84) can be rewritten in the reference configuration as [28]

$$\frac{\mathrm{d}\,\mathcal{S}(\mathcal{P}_R)}{\mathrm{d}t} = \int_{\mathcal{P}_R} \frac{\mathrm{d}\,\eta_R}{\mathrm{d}t}\,\mathrm{d}v_R\;, \tag{4.86a}$$

$$\mathcal{Q}_\eta(\mathcal{P}_R) = \int_{\mathcal{P}_R} \frac{1}{T}\,s_{q_R}\,\mathrm{d}v_R - \int_{\partial\mathcal{P}_R} \frac{1}{T}\,\vec{Q}\cdot\vec{N}\,\mathrm{d}a_R\;, \tag{4.86b}$$

$$\mathcal{T}_\eta(\mathcal{P}_R) = \int_{\mathcal{P}_R} {}^{\eta}\mu_G\,s_{G_R}\,\mathrm{d}v_R - \int_{\partial\mathcal{P}_R} {}^{\eta}\mu_G\,\vec{H}_G\cdot\vec{N}\;+{}^{\eta}\mu_F\,\vec{H}_F\cdot\vec{N}\,\mathrm{d}a_R\;. \tag{4.86c}$$

Multiplying eq. (4.85) by $T$ and taking advantage of eq. (4.82) to re-write the term $-s_{q_R} + \mathrm{Div}\left[\vec{Q}\right]$, after some algebra eq. (4.85) in the global form reads

$$\int_{\mathcal{P}_R} T\,\frac{\mathrm{d}\,\eta_R}{\mathrm{d}t} - \frac{\mathrm{d}\,u_R}{\mathrm{d}t} + \boldsymbol{P}\cdot\frac{\mathrm{d}\,\boldsymbol{F}}{\mathrm{d}t} + \mu_G\,\frac{\partial c_{G_R}}{\partial t} + \mu_F\,\frac{\partial c_{F_R}}{\partial t} - \vec{H}_G\cdot\mathrm{Grad}\,[\,\mu_G\,] + \\ - \vec{H}_F\cdot\mathrm{Grad}\,[\,\mu_F\,] - A^{(4.38)}\,w_R^{(4.38)}\;\mathrm{d}v_R \geq 0\;, \tag{4.87}$$

having defined $\mu_a = {}^u\mu_a - T\,{}^\eta\mu_a$ for the $a$-species and $A^{(4.38)} = \mu_F - \mu_G$ [6, 28].

### 4.7.3 Helmholtz free energy

The mathematical description of a thermodynamical process requires the choice of the independent state variables that are controlled during the process. The independent state variables imply the choice of the thermodynamical potential (internal energy, Helmholtz free energy, enthalpy, or Gibbs free energy), that is obtained through the Legendre transformation.

The specific *Helmholtz free energy* per unit referential volume is the appropriate thermodynamical potential variable for processes where temperature and the kinetic variables are the independent variables, so it is a suitable thermodynamic potential in continuum mechanics [1]. It is defined in the state variables $c_{a_R}$, $\boldsymbol{E}$ and some kinematic internal variable $\boldsymbol{\xi}$ as

$$\psi_R = u_R - T\,\eta_R\;. \tag{4.88}$$

Taking advantage of eq. (4.88) and using the derivative of the *Helmholtz free energy* with respect to time at thermal equilibrium

$$\frac{\mathrm{d}\,\psi_R}{\mathrm{d}t} = \frac{\mathrm{d}\,u_R}{\mathrm{d}t} - T\,\frac{\mathrm{d}\,\eta_R}{\mathrm{d}t} - \frac{\mathrm{d}\,T}{\mathrm{d}t}\,\eta_R = \frac{\mathrm{d}\,u_R}{\mathrm{d}t} - T\,\frac{\mathrm{d}\,\eta_R}{\mathrm{d}t}\;, \tag{4.89}$$

we re-write eq. (4.87) as

$$\int_{\mathcal{P}_R} \frac{\mathrm{d}\,\psi_R}{\mathrm{d}t} - \boldsymbol{S}\cdot\frac{\partial\,\boldsymbol{E}}{\partial t} - \mu_F\,\frac{\partial c_{F_R}}{\partial t} - \mu_G\,\frac{\partial c_{G_R}}{\partial t} + A^{(4.38)}\,w_R^{(4.38)} + \\ + \vec{H}_G\cdot\mathrm{Grad}\,[\,\mu_G\,] + \vec{H}_F\cdot\mathrm{Grad}\,[\,\mu_F\,]\;\mathrm{d}v_R \leq 0\;, \tag{4.90}$$

where an alternative expression for the stress power, with the second Piola-Kirchhoff stress tensor $\boldsymbol{S}$, is employed [6]. The total time derivative of $\psi_R =$

---

[1] State variables are all referential fields. Accordingly, their total and partial derivatives with respect to time coincide. For this reason, we will use the notation of partial derivative henceforth for all state variables [6].

$\psi_R\,(c_{G_R}, c_{F_R}, \boldsymbol{E}, \boldsymbol{\xi})$ reads

$$
\begin{aligned}
\frac{\mathrm{d}\,\psi_R}{\mathrm{d}t} = {} & \left.\frac{\partial \psi_R}{\partial \boldsymbol{E}}\right|_{c_{F_R},\, c_{G_R},\, \boldsymbol{\xi}} \cdot \frac{\partial \boldsymbol{E}}{\partial t} + \left.\frac{\partial \psi_R}{\partial c_{G_R}}\right|_{c_{F_R},\, \boldsymbol{E},\, \boldsymbol{\xi}} \frac{\partial c_{G_R}}{\partial t} \\
& + \left.\frac{\partial \psi_R}{\partial c_{F_R}}\right|_{c_{G_R},\, \boldsymbol{E},\, \boldsymbol{\xi}} \frac{\partial c_{F_R}}{\partial t} + \left.\frac{\partial \psi_R}{\partial \boldsymbol{\xi}}\right|_{c_{F_R},\, c_{G_R},\, \boldsymbol{E}} \cdot \frac{\partial \boldsymbol{\xi}}{\partial t}\,.
\end{aligned}
\tag{4.91}
$$

Substituting eq. (4.91) into eq. (4.90), the Clausius-Duhem inequality arises

$$
\begin{aligned}
\int_{\mathcal{P}_R} & \left(\frac{\partial \psi_R}{\partial \boldsymbol{E}} - \boldsymbol{S}\right) \cdot \frac{\partial \boldsymbol{E}}{\partial t} + \left(\frac{\partial \psi_R}{\partial c_{F_R}} - \mu_F\right) \frac{\partial c_{F_R}}{\partial t} + \left(\frac{\partial \psi_R}{\partial c_{G_R}} - \mu_G\right) \frac{\partial c_{G_R}}{\partial t} + \\
& - \boldsymbol{\chi} \cdot \frac{\partial \boldsymbol{\xi}}{\partial t} + \vec{H}_G \cdot \mathrm{Grad}\,[\,\mu_G\,] + \vec{H}_F \cdot \mathrm{Grad}\,[\,\mu_F\,] + A^{(4.38)} w_R^{(4.38)} \mathrm{d}v_R \leq 0\,,
\end{aligned}
\tag{4.92}
$$

which can be localized at $\vec{X} \in \mathcal{P}_R$ since it holds for any arbitrary subpart $\mathcal{P}_R$ [6, 28].

### 4.7.4 Intermediate configuration

Recalling eq. (4.2), (4.11) and using the identity $\boldsymbol{P} = J \boldsymbol{\sigma} \boldsymbol{F}^{-\mathrm{T}}$, the internal power in the intermediate configuration can be written as

$$
\begin{aligned}
\int_{\mathcal{P}_R} \boldsymbol{S} \cdot \frac{\mathrm{d}\,\boldsymbol{E}}{\mathrm{d}t}\ \mathrm{d}v_R &= \int_{\mathcal{P}_R} \boldsymbol{P} \cdot \frac{\mathrm{d}\,\boldsymbol{F}}{\mathrm{d}t}\ \mathrm{d}v_R \\
&= \int_{\mathcal{P}_\mathcal{R}} \boldsymbol{P} \cdot \Big(\frac{\mathrm{d}\,\boldsymbol{F}^e}{\mathrm{d}t}\, \boldsymbol{F}^c + \boldsymbol{F}^e\, \frac{\mathrm{d}\,\boldsymbol{F}^c}{\mathrm{d}t}\Big)\, \mathrm{d}v_R \\
&= \int_{\mathcal{P}_\mathcal{R}} \boldsymbol{P} \boldsymbol{F}^{c^{\mathrm{T}}} \cdot \frac{\mathrm{d}\,\boldsymbol{F}^e}{\mathrm{d}t} + \boldsymbol{F}^{e^{\mathrm{T}}} \boldsymbol{P} \cdot \frac{\mathrm{d}\,\boldsymbol{F}^c}{\mathrm{d}t}\ \mathrm{d}v_R \\
&= \int_{\mathcal{P}_\mathcal{R}} \boldsymbol{P} \boldsymbol{F}^{c^{\mathrm{T}}} \cdot \frac{\mathrm{d}\,\boldsymbol{F}^e}{\mathrm{d}t} + \boldsymbol{F}^{e^{\mathrm{T}}} \boldsymbol{P} \boldsymbol{F}^{c^{\mathrm{T}}} \cdot \boldsymbol{l}^c\ \mathrm{d}v_R \\
&= \int_{\mathcal{P}_\mathcal{R}} J \boldsymbol{\sigma} \boldsymbol{F}^{-\mathrm{T}} \boldsymbol{F}^{c^{\mathrm{T}}} \cdot \frac{\mathrm{d}\,\boldsymbol{F}^e}{\mathrm{d}t} + \boldsymbol{F}^{e^{\mathrm{T}}} J \boldsymbol{\sigma} \boldsymbol{F}^{-\mathrm{T}} \boldsymbol{F}^{c^{\mathrm{T}}} \cdot \boldsymbol{l}^c\ \mathrm{d}v_R \\
&= \int_{\mathcal{P}_\mathcal{C}} J^e \boldsymbol{\sigma} \boldsymbol{F}^{e^{-\mathrm{T}}} \cdot \frac{\mathrm{d}\,\boldsymbol{F}^e}{\mathrm{d}t} + J^e \boldsymbol{F}^{e^{\mathrm{T}}} \boldsymbol{\sigma} \boldsymbol{F}^{e^{-\mathrm{T}}} \cdot \boldsymbol{l}^c\ \mathrm{d}v_c \\
&= \int_{\mathcal{P}_\mathcal{C}} \boldsymbol{P}^e \cdot \frac{\mathrm{d}\,\boldsymbol{F}^e}{\mathrm{d}t} + \boldsymbol{M}^e \cdot \boldsymbol{l}^c\ \mathrm{d}v_c\,,
\end{aligned}
\tag{4.93}
$$

where we have defined

$$
\boldsymbol{P}^e = J^e \boldsymbol{\sigma} \boldsymbol{F}^{e^{-\mathrm{T}}} = \boldsymbol{F}^e \boldsymbol{S}^e\,, \qquad \boldsymbol{M}^e = J^e \boldsymbol{F}^{e^{\mathrm{T}}} \boldsymbol{\sigma} \boldsymbol{F}^{e^{-\mathrm{T}}} = \boldsymbol{C}^e \boldsymbol{S}^e
\tag{4.94}
$$

as the first Piola-Kirchhoff tensors and the elastic Mandel stress tensor [6].

Taking advantage of eq. (4.4), (4.6), (4.7), and (4.94), eq. (4.93) becomes

$$\begin{aligned}
\int_{\mathcal{P}_C} \boldsymbol{P}^e \cdot \frac{\mathrm{d}\,\boldsymbol{F}^e}{\mathrm{d}t} + \boldsymbol{M}^e \cdot \boldsymbol{l}^c \,\mathrm{d}v_c &= \int_{\mathcal{P}_C} \boldsymbol{F}^e \boldsymbol{S}^e \cdot \frac{\mathrm{d}\,\boldsymbol{F}^e}{\mathrm{d}t} + \boldsymbol{C}^e \boldsymbol{S}^e \cdot \boldsymbol{l}^c \,\mathrm{d}v_c \\
&= \int_{\mathcal{P}_C} \boldsymbol{F}^e \boldsymbol{S}^e \cdot \frac{\mathrm{d}\,\boldsymbol{F}^e}{\mathrm{d}t} + \boldsymbol{C}^e \boldsymbol{S}^e \cdot \boldsymbol{l}^c \,\mathrm{d}v_c \\
&= \int_{\mathcal{P}_C} \boldsymbol{S}^e \cdot \boldsymbol{F}^{e^{\mathrm{T}}} \frac{\mathrm{d}\,\boldsymbol{F}^e}{\mathrm{d}t} + \boldsymbol{C}^e \boldsymbol{S}^e \cdot \boldsymbol{l}^c \,\mathrm{d}v_c \\
&= \int_{\mathcal{P}_C} \boldsymbol{S}^e \cdot \frac{\mathrm{d}\,\boldsymbol{E}^e}{\mathrm{d}t} + \boldsymbol{C}^e \boldsymbol{S}^e \cdot \boldsymbol{d}^c \,\mathrm{d}v_c \\
&= \int_{\mathcal{P}_C} \boldsymbol{S}^e \cdot \frac{\mathrm{d}\,\boldsymbol{E}^e}{\mathrm{d}t} + \frac{1}{3J^c} \frac{\mathrm{d}\,J^c}{\mathrm{d}t} \mathrm{tr}\left[\,\boldsymbol{C}^e \boldsymbol{S}^e\,\right] \,\mathrm{d}v_c \,.
\end{aligned} \tag{4.95}$$

where we have defined

$$\boldsymbol{S}^e = J^e \boldsymbol{F}^{e^{-1}} \boldsymbol{\sigma} \boldsymbol{F}^{e^{-\mathrm{T}}} \tag{4.96}$$

as the elastic second Piola-Kirchhoff tensors [6].

### 4.7.5 Thermodynamic restrictions

Since the Clausius-Duhem inequality (4.92) holds for every admissible process, the following thermodynamic prescriptions in the reference configuration arise through the Coleman-Noll procedure

$$\boldsymbol{S} = \left.\frac{\partial \psi_R}{\partial \boldsymbol{E}}\right|_{c_{G_R},\, c_{F_R},\, \boldsymbol{\xi}} , \tag{4.97a}$$

$$\mu_G = \left.\frac{\partial \psi_R}{\partial c_{G_R}}\right|_{c_{F_R},\, \boldsymbol{E},\, \boldsymbol{\xi}} , \tag{4.97b}$$

$$\mu_F = \left.\frac{\partial \psi_R}{\partial c_{F_R}}\right|_{c_{G_R},\, \boldsymbol{E},\, \boldsymbol{\xi}} , \tag{4.97c}$$

and the dissipation inequality in the reference configuration

$$-\underbrace{\boldsymbol{\chi} \cdot \frac{\partial \boldsymbol{\xi}}{\partial t}}_{\text{inelastic}} + \underbrace{\vec{H}_G \cdot \mathrm{Grad}\left[\,\mu_G\,\right] + \vec{H}_F \cdot \mathrm{Grad}\left[\,\mu_F\,\right]}_{\text{mass transport}} + \underbrace{w_R^{(4.38)}\, A^{(4.38)}}_{\text{chemical}} \leq 0 \tag{4.98}$$

holds, where we have denoted

$$\boldsymbol{\chi} = -\frac{\partial \psi_R}{\partial \boldsymbol{\xi}} \,. \tag{4.99}$$

The imbalance (4.98) is a sum of two factors products that represent flux and force quantities. In particular, the flux quantities $\frac{\partial \boldsymbol{\xi}}{\partial t}$, $\vec{H}_a$ and $w_R^{(4.38)}$ represent the viscous tensor flow (or the internal flux variables), the diffusion flow and the chemical reaction rate, respectively. These fluxes are associated with their force quantities, called "thermodynamic forces" or "affinities", that are related to a gradient of an intensive state variable. In the imbalance (4.98), they are $\boldsymbol{\chi}$, $\mathrm{Grad}\,[\,\mu_a\,]$ and $A^{(4.38)}$ and they represent the thermodynamic driven force associated with the internal variable $\boldsymbol{\xi}$ (its energy-conjugate force), the gradient of the chemical potential and the chemical affinity of the reaction, respectively.

#### 4.7.5.1 Curie simmetry principle

To establish the phenomenological equations between the independent fluxes and the thermodynamic forces of the expression (4.98), the Curie symmetry principle is introduced. This principle is based on the observation that the fluxes and the thermodynamic forces do not all have the same tensorial character (scalars, vectors, and tensors of second rank). This means that under rotations and reflections, the Cartesian components of these quantities transform in different ways. As a consequence, symmetry properties of the considered material system may have the effect that the components of the fluxes do not depend on all components of the thermodynamic forces [37]. Thus, it can be shown that fluxes and thermodynamic forces of different tensorial characters do not couple [37] (cap 3 sec 2).

So, adopting the Curie principle, inequality (4.98) can be written as

$$-\boldsymbol{\chi} \cdot \frac{\partial \boldsymbol{\xi}}{\partial t} \leq 0 \,, \tag{4.100a}$$

$$\vec{H}_F \cdot \mathrm{Grad}\,[\,\mu_F\,] + \vec{H}_G \cdot \mathrm{Grad}\,[\,\mu_G\,] \leq 0 \,, \tag{4.100b}$$

$$w_R^{(4.38)}\, A^{(4.38)} \leq 0 \,, \tag{4.100c}$$

The inequality (4.100c) is a priory satisfied by the mass action law (4.64) [6].

#### 4.7.5.2 Onsager reciprocal relations

To satisfy the inequality (4.100b), a phenomenological approach is normally adopted, in which a functional form is postulated and the parameters appearing in it are obtained by fitting to experimental measurements. The simplest possibility is to assume a linear relation between the arguments, so in general, it reads

$$J_i = L_{ij} Y_j \,, \tag{4.101}$$

where $J_i$ represents the fluxes and $Y_j$ the forces. The entries of the matrix $\boldsymbol{L}$ are called the *phenomenological coefficients* [33]. To respect the imbalance in eq. (4.100), the matrix $\boldsymbol{L}$ must be positive definite, which imposes constraints on its coefficients. Moreover, for systems close to equilibrium the phenomenological coefficients matrix must be symmetric, so

$$L_{ji} = L_{ij} \, .$$

This is known as the "Onsager reciprocal relation" and it is related to the property of "time reversal invariance" on phenomenological equations of individual particle motion. This property of "time reversal invariance" expresses the idea that the mechanical equations of particle motion are symmetric with respect to time, which implies that the particles retrace their former paths if all velocities are reversed [37].

In this specific case, the flows of G-actin monomers and F-actin network, $\vec{H}_G$ and $\vec{H}_F$, are linearly correlated to the gradient of their chemical potentials, $\mathrm{Grad}\,[\,\mu_G\,]$ and $\mathrm{Grad}\,[\,\mu_F\,]$, as follows

$$\vec{H}_G = -\boldsymbol{M}_{G_R}\,\mathrm{Grad}\,[\,\mu_G\,]\ , \tag{4.102a}$$

$$\vec{H}_F = -\boldsymbol{M}_{F_R}\,\mathrm{Grad}\,[\,\mu_F\,]\ , \tag{4.102b}$$

where $\boldsymbol{M}_{G_R}$ and $\boldsymbol{M}_{F_R}$ are positive definite mobility tensors of the monomeric G-actin and the network of F-actin, respectively [6]. They are taken as

$$\boldsymbol{M}_{G_R}(c_{G_R}) = \psi_{G_R}\, c_{G_R}^{max}\ \vartheta_{G_R}\ (1-\vartheta_{G_R})\ \mathbb{1}\ , \tag{4.103a}$$

$$\boldsymbol{M}_{F_R}(c_{F_R}) = \psi_{F_R}\, c_{F_R}^{max}\ \vartheta_{F_R}\ (1-\vartheta_{F_R})\ \mathbb{1}\ , \tag{4.103b}$$

with $\psi_{G_R} > 0$ and $\psi_{F_R} > 0$ the *mobilities* respectively of the monomeric G-actin and the network of F-actin [6]. The *mobilities* represents the average velocity when applying a force of $1\,\frac{\mathrm{N}}{\mathrm{mol}}$ and it is assumed not to change throughout the time [6]. It follows that the two phases representing the null concentration and the saturation limit, $c_{a_R} = 0$ and $c_{a_R} = c_{a_R}^{max}$ (saturation limit), have vanishing mobility [6]. More complex laws, of Maxwell-Stefan type [38], can be used for the G and F-actin flows in place of (4.102) [6].

Following (4.99) and the Onsager reciprocal relation for the inelastic internal entropy production, a positive definite operator $\mathbb{L}$ is chosen, in such a way that

$$\boldsymbol{\chi} = \mathbb{L}\,\frac{\partial \boldsymbol{\xi}}{\partial t}\ . \tag{4.104}$$

## 4.8 Constitutive theory

The Helmholtz free energy density $\psi_R$ can be represented by an additive decomposition

$$\psi_R(c_{G_R}, c_{F_R}, \boldsymbol{E}, \boldsymbol{\xi}) = \psi_R^{diff}(c_{G_R}, c_{F_R}) + \psi_R^{el}(c_{F_R}, \boldsymbol{E}) + \psi_R^{in}(c_{F_R}, \boldsymbol{E}, \boldsymbol{\xi}) \ , \quad (4.105)$$

which separates the diffusive contribution $\psi_R^{diff}$, the elastic contribution $\psi_R^{el}$, and the inelastic counterpart $\psi_R^{in}$ [6].

### 4.8.1 Mechanical contribution

Following [28], we define visco-elastic materials based on the multiplicative decomposition (4.15), using tensors $\boldsymbol{E}^{e^v}$ and $\boldsymbol{E}^{e^i}$. Specifically, the free energy for visco-elastic materials is defined as follows

$$\begin{aligned}\psi_R^{el}(c_{F_R}, \boldsymbol{E}) + \psi_R^{in}(c_{F_R}, \boldsymbol{E}, \boldsymbol{\xi}) = {} & \psi_R^{el,vol}(c_{F_R}, \boldsymbol{E}^{e^v}) + \psi_R^{el,iso}(c_{F_R}, \boldsymbol{E}^{e^i}) \\ & + \psi_R^{in}(c_{F_R}, \boldsymbol{E}^e - \boldsymbol{\xi}) \ ,\end{aligned} \quad (4.106)$$

where $\boldsymbol{E}^e$ depends on $\boldsymbol{E}$ via eq. (4.8) [6]. Considering the rheological model of Maxwell, for which we refer to [27] or [28], the inelastic part of the free energy is defined in such a way that

$$\frac{\partial \psi_R^{in}}{\partial \boldsymbol{E}} = -\frac{\partial \psi_R^{in}}{\partial \boldsymbol{\xi}} \ . \quad (4.107)$$

Provided that the above holds, the selection for $\psi_R^{el}$ and $\psi_R^{in}$ is arbitrary [6]. The elastic reversible behavior occurs once the viscous effects vanish (ideally at $t \to \infty$ ) and is described by $\psi_R^{el}$ [6]. The inelastic free energy accounts for the non-equilibrium response due to viscosity [6]. By thermodynamic restrictions (4.97a), (4.100a), (4.99) and identity (4.107), the following identities hold

$$\boldsymbol{\chi} = -\frac{\partial \psi_R^{in}}{\partial \boldsymbol{\xi}} = \frac{\partial \psi_R^{in}}{\partial \boldsymbol{E}} \ , \quad (4.108a)$$

$$\boldsymbol{S} = \frac{\partial \psi_R^{el}}{\partial \boldsymbol{E}} + \boldsymbol{\chi} \ . \quad (4.108b)$$

According to eq. (4.108b), tensorial internal forces $\boldsymbol{\chi}$ can be interpreted as a *non-equilibrium stress tensor* of second Piola-Kirchoff kind, that accounts for the viscous response [6].

### 4.8.2 Chemical potentials

The diffusive contribution of the Helmholtz free energy is inferred from statistical mechanical theory. In particular, the two-state system model, which is one of the simplest statistical mechanical models that describes a wide variety of physical phenomena at a basic level, is applied to identify the function density of microstates of the a-species $\Omega_a$. Taking advantage of Stirling's approximation, the combination formula for the potential conformations of actin protein concentrations inside a cell reads

$$\Omega_a = \left[\, \vartheta_a^{\vartheta_a} (1-\vartheta_a)^{(1-\vartheta_a)} \right]^{-N_A c_a^{max}} \,, \tag{4.109}$$

where $N_A$ is the Avogadro's number and a = G-actin, F-actin. By means of the Boltzmann equation, it is obtained

$$\begin{aligned} \eta_a^{diff} =& k_B \,\ln \Omega_a \\ =& k_B \,\ln \left[\, \vartheta_a^{\vartheta_a} (1-\vartheta_a)^{(1-\vartheta_a)} \right]^{-N_A c_a^{max}} \\ =& -k_B N_A \, c_a^{max} \left(\, \vartheta_a \ln[\vartheta_a] + (1-\vartheta_a) \ln\left[1-\vartheta_a\right] \right) \,, \end{aligned} \tag{4.110}$$

where $k_B N_A = R$.

Following [39], the diffusive contribution of the Helmholtz free energy for the continuum approximation of mixing is

$$\begin{aligned} \psi_R^{diff}(c_{G_R}, c_{F_R}) =& \mu_{G_R}^0 - T\eta_{G_R}^{diff} + RTc_{G_R}^{max} \theta_{G_R} (1-\theta_{G_R}) \overline{\chi} + \\ & + \mu_{F_R}^0 - T\eta_{F_R}^{diff} + RTc_{F_R}^{max} \theta_{F_R} (1-\theta_{F_R}) \overline{\chi} \,, \end{aligned} \tag{4.111}$$

where $\mu_a^0$ is the reference value of each chemical potential and $\overline{\chi}$ is a real constant that specifies the energy of interaction among species. Since the contribution of the entropy mixing is negligible, $\overline{\chi}$ is considered null.

Taking advantage of eq. (4.110), the free energy density for the continuum approximation of mixing reads

$$\begin{aligned} \psi_R^{diff}(c_{G_R}, c_{F_R}) = & \,\mu_G^0 \, c_{G_R} + \\ & + RTc_{G_R}^{max} \left[\vartheta_{G_R} \ln \vartheta_{G_R} + (1-\vartheta_{G_R}) \ln(1-\vartheta_{G_R})\right] + \\ & + \mu_F^0 \, c_{F_R} + \\ & + RTc_{F_R}^{max} \left[\vartheta_{F_R} \ln \vartheta_{F_R} + (1-\vartheta_{F_R}) \ln(1-\vartheta_{F_R})\right] \,. \end{aligned} \tag{4.112}$$

Using the thermodynamic restrictions (4.97b) and (4.97c) and following the additive decomposition of the Helmholtz free energy (5.19), the chemical potential of species $a = G, F$ can be written as

$$\mu_G = \frac{\partial \psi_R^{diff}}{\partial c_{G_R}} \, , \tag{4.113a}$$

$$\mu_F = \frac{\partial \psi_R^{diff}}{\partial c_{F_R}} + \frac{\partial \psi_R^{el,vol}}{\partial c_{F_R}} + \frac{\partial \psi_R^{el,iso}}{\partial c_{F_R}} + \frac{\partial \psi_R^{in}}{\partial c_{F_R}} \, , \tag{4.113b}$$

where mechanical contributions enter only the definition of the chemical potential of the F-actin network. The volumetric contribution $\psi_R^{el,vol}$ affects chemical potential $\mu_F$ via the swelling tensor $\boldsymbol{E}^{e^v}$, while $\boldsymbol{E}^{e^i}$ is independent on the concentration of species [6].

For the simple case of G-actin, the gradient of $\mu_G$ reads

$$\text{Grad}\,[\,\mu_G\,] = \frac{R\,T}{c_{G_R}^{max}} \, \frac{1}{\vartheta_{G_R}(1-\vartheta_{G_R})} \, \text{Grad}\,[\,c_{G_R}\,] \, , \tag{4.114}$$

and taking advantage of eq. (4.102a), (4.103a), (4.113a) and (4.114), the Fick's constitutive relation is obtained

$$\vec{H}_G = -\mathbb{D}_{G_R} \, \text{Grad}\,[\,c_{G_R}\,] \, , \tag{4.115}$$

where $\mathbb{D}_{G_R} = \mathbb{M}_R \, R\,T$ represents G-actin *diffusivity.* Following eq. (5.20), (4.113b) and (4.114), eq. (4.102b) reads

$$\begin{aligned} \vec{H}_F = & - \mathbb{K}_{F_R} \, \text{Grad}\,[\,c_{F_R}\,] \, - \, \boldsymbol{M}_{F_R} \, \text{Grad}\left[ \frac{\partial \psi_R^{el,vol}}{\partial c_{F_R}} \right] + \\ & - \, \boldsymbol{M}_{F_R} \, \text{Grad}\left[ \frac{\partial \psi_R^{el,iso}}{\partial c_{F_R}} \right] \, - \, \boldsymbol{M}_{F_R} \, \text{Grad}\left[ \frac{\partial \psi_R^{in}}{\partial c_{F_R}} \right] \, , \end{aligned} \tag{4.116}$$

where $\mathbb{K}_{F_R}$ is a term that accounts for the F-actin network transport [6].

## 4.9 Governing equations with boundary conditions

Combining the mass action law and the constitutive equations with the mass balance of species and the balance of momentum, the equations that govern all the processes are derived [6]. Taking advantage of eq. (4.64), the transport of actin is coupled with polymerization and depolymerization reactions in the mass balance equations

$$\frac{\partial c_{G_R}}{\partial t} + \mathrm{Div}\left[\,\vec{H}_G\,\right] + k_{f_R}\,\frac{\vartheta_{G_R}}{1-\vartheta_{G_R}} - k_{b_R}\,\frac{\vartheta_{F_R}}{1-\vartheta_{F_R}} = s_{G_R}\ , \tag{4.117a}$$

$$\frac{\partial c_{F_R}}{\partial t} + \mathrm{Div}\left[\,\vec{H}_F\,\right] - k_{f_R}\,\frac{\vartheta_{G_R}}{1-\vartheta_{G_R}} + k_{b_R}\,\frac{\vartheta_{F_R}}{1-\vartheta_{F_R}} = 0 \tag{4.117b}$$

with $\vec{H}_G$ and $\vec{H}_F$ from eq. (4.115) and (4.116) [6]. The balance of linear momentum (4.55) can be specified as

$$\mathrm{Div}\,[\,\boldsymbol{F}\,\boldsymbol{S}\,] + \vec{B} = \frac{\mathrm{d}\,\rho_{F_R}\,\dot{\vec{\chi}}}{\mathrm{d}t}\ , \qquad \vec{X} \in \Omega_R\ , \tag{4.118}$$

where the second Piola-Kirchhoff stress emanates from (4.97a) and

$$\boldsymbol{F} = (\,1 + c_{F_R}\,\Omega_F\,)^{\frac{1}{3}}\,\boldsymbol{F}^e\ . \tag{4.119}$$

Boundary conditions along Neumann boundaries $\partial^N\Omega_R$ read

$$\vec{H}_G \cdot \vec{N} = \overline{h}_{G_R} \qquad \vec{X} \in \partial^N\Omega_R\ , \tag{4.120a}$$

$$\vec{H}_F \cdot \vec{N} = \overline{h}_{F_R} \qquad \vec{X} \in \partial^N\Omega_R\ , \tag{4.120b}$$

$$\boldsymbol{P}\,\vec{N} = \overline{\vec{T}} \qquad \vec{X} \in \partial^N\Omega_R\ , \tag{4.120c}$$

and Dirichlet boundary conditions along $\partial^D\Omega_R$ are

$$c_{G_R} = \overline{c}_{G_R} \qquad \vec{X} \in \partial^D\Omega_R\ , \tag{4.121a}$$

$$c_{F_R} = \overline{c}_{F_R} \qquad \vec{X} \in \partial^D\Omega_R\ , \tag{4.121b}$$

$$\vec{U}(\vec{X},t) = \overline{\vec{U}} \qquad \vec{X} \in \partial^D\Omega_R\ . \tag{4.121c}$$

The associated initial conditions of eq. (4.117) for concentrations, $c_{G_R}(\vec{X}, t=0)$ and $c_{F_R}(\vec{X}, t=0)$, as well as for displacements and velocities in eq. 4.118, $\vec{U}\,(\vec{X}, t=0)$ and $\dot{\vec{\chi}}\,(\vec{X}, t=0)$, are imposed [6, 32, 40, 39, 37, 41, 24, 33].

## 4.10 Models assumptions

We verify the consistency of the chemo-mechanical engine depicted in the former sections on the motion of non-flagellated bacteria through the cytosol. Pathogens ABM has been largely investigated in the literature [42, 43, 7, 44, 45, 8], but still some of the material parameters required by our model appear not to be currently available. Hence, there is room for improvement in establishing a clearer connection between the obtained outcomes and experimental evidence. For this sake, we opened an experimental campaign to validate the model against real bacteria: outcomes will be published [6].

In this section, we summarize the model assumptions that we have taken into account, and In the next section, we limit ourselves to two proof of concepts, with experimental data summarized in the tables.

Since the internal generation of G-actin is negligible, we take the source term of G-actin as null, i.e. $s_{G_R} = 0$. Moreover, since G-actin and F-actin concentrations are far from saturation, we consider a dilute solution and the mass action law (4.64) becomes

$$w_R^{(4.38)} = k_f \, c_{G_R} \, - \, k_b \, c_{F_R} \; .$$

The governing equation of linear momentum (4.118) for pathogens motility can be rephrased as

$$\text{Div} \left[ \boldsymbol{F} \, \boldsymbol{S} \right] + \vec{B} = M_F \, \frac{\text{d} \, c_{F_R} \, \dot{\vec{\chi}}}{\text{d}t} \; , \tag{4.122}$$

with $M_F$ representing the molar mass of the F-actin network. We assume that $M_F$ is small so that the inertial effects are second-order and can be neglected [6].

Therefore, taking advantage of all previous assumptions, the set of balance equations (4.117) and (4.118) for the case of ABM of a bacterium is rewritten as

$$\frac{\partial c_{G_R}}{\partial t} + \text{Div} \left[ \vec{H}_G \right] + k_f \, c_{G_R} \, - \, k_b \, c_{F_R} \, = 0 \; , \tag{4.123a}$$

$$\frac{\partial c_{F_R}}{\partial t} + \text{Div} \left[ \vec{H}_F \right] - \, k_f \, c_{G_R} \, + \, k_b \, c_{F_R} \, = 0 \; , \tag{4.123b}$$

$$\text{Div} \left[ P_{11} \left( F_{11} \right) \right] + \vec{B} = 0 \; . \tag{4.123c}$$

Bacteria associated with *actin comet tails* move very rapidly within the host cytoplasm, at rates of up to 1 $\mu$m/s [8]. Considering the bacterium speed, we assume that viscous effects do not have sufficient time to develop in the *actin comet tail*, even if in reality some cross-link rearrangement can occur. For this reason, tensorial internal forces $\boldsymbol{\chi}$ are null and eq. (4.116) becomes

$$\vec{H}_F = - \mathbb{K}_{F_R} \, \text{Grad} \left[ c_{F_R} \right] \, - \, \boldsymbol{M}_{F_R} \, \text{Grad} \left[ \frac{\partial \psi_R^{el,vol}}{\partial c_{F_R}} \right] \, - \, \boldsymbol{M}_{F_R} \, \text{Grad} \left[ \frac{\partial \psi_R^{el,iso}}{\partial c_{F_R}} \right] \; . \tag{4.124}$$

As a simplification, we consider an elastic strain-energy function $\psi_e$ for

Saint-Venant materials in the intermediate configuration

$$\psi_e = \frac{\lambda}{2}\,\mathrm{tr}\,[\,\boldsymbol{E}^e\,]^2 + \mathrm{G}\,\boldsymbol{E}^e \cdot \boldsymbol{E}^e \ . \tag{4.125}$$

Using equations (4.9), (4.8) and (4.97a), together with volumetric transformation of the *Helmholtz free energy*

$$\psi_R^{el} = J^c\,\psi_e \ ,$$

we can derive the stress tensor $\boldsymbol{S}$ as

$$\begin{aligned} \boldsymbol{S} = \left.\frac{\partial \psi_R}{\partial \boldsymbol{E}}\right|_{c_{G_R},\,c_{F_R},\,\boldsymbol{\xi}} &= \left.\frac{\partial(\,J^c\,\psi_e\,)}{\partial \boldsymbol{E}}\right|_{c_{G_R},\,c_{F_R},\,\boldsymbol{\xi}} \\ = J^c\ \left.\frac{\partial \psi_e}{\partial \boldsymbol{E}^e}\,\frac{\partial \boldsymbol{E}^e}{\partial \boldsymbol{E}}\right|_{c_{G_R},\,c_{F_R},\,\boldsymbol{\xi}} &= J^{c^{1/3}}\,\boldsymbol{S}^e \ , \end{aligned} \tag{4.126}$$

with $\boldsymbol{S}^e$ defined as

$$\boldsymbol{S}^e = \frac{\partial \psi_e}{\partial \boldsymbol{E}^e} = \lambda\,\mathrm{tr}\,[\,\boldsymbol{E}^e\,]\ \mathbb{1} + 2\,\mathrm{G}\,\boldsymbol{E}^e \ . \tag{4.127}$$

We expect that the material properties of the $F$-actin network would depend on $c_F$ ($\mathrm{G}(c_{F_R})$, $\lambda(c_{F_R})$). According to [46, 47], "the mechanics of the actin network is defined by its mesh size, that is variously taken as the spacing between actin filaments inside the network or the distance between fixed crosslink points". There is evidence that the mesh size strongly affects the elastic modulus [48]. We leave the modeling of this behavior to further studies. In this note, we assume that all material parameters are independent of the actin network density and we take them as constant. Accordingly, eq. (4.124) becomes

$$\vec{H}_F = -\mathbb{K}_{F_R}\,\mathrm{Grad}\,[\,c_{F_R}\,] - \boldsymbol{M}_{F_R}\,\mathrm{Grad}\left[\,\frac{\partial \psi_R^{el}}{\partial c_{F_R}}\,\right] \ . \tag{4.128}$$

The cytoplasmatic fluid in which the F-actin network is immersed is accounted for through external viscous drag shear forces acting on the *actin comet tail.* In one-dimensional problems, those shear forces become bulk forces $\vec{B}$. Experimental observations [10] of the *Listeria monocytogenes* moving through the fluid show that turbulence effects can be neglected and it can be considered a purely laminar Stokes' drag. The bulk forces due to the viscous drag are thus taken as proportional to velocity

$$B = -\nu\,\dot{U}_1 \ , \tag{4.129}$$

where $\nu$ generally depends on the material properties, the geometry of the object, and the properties of the fluid. In a first approximation, we take $\nu$ as a constant [6].

# Chapter 5

# Experimental data, numerical simulations and results

In this chapter, we provide essential experimental data for the pathogens ABM models, sourced from the literature. Then, the proof of concepts that are inherited from [6], "Actin based motility unveiled: How chemical energy is converted into motion, *J MECH PHYS SOLIDS*" and from [25], "Continuum multi-physics modeling of cell and bacteria motility, submitted" are provided. The two models described in these papers differ in the definition of the signal and the Helmholtz free energy but they both descend from the model discussed in chapter 4.

## 5.1 Experimental data

In the current section, we summarize the parameters required for the multi-physics model introduced in chapter 4. Unfortunately, it is not possible to carry out a single experiment that validates the model, due to the lack of laboratories available, but a profound literature research is performed and the majority of the constitutive parameters are inferred from previous experiments. Some of these experiments do not show the same results, so it has been our concern to share all the outcomes in the literature, even if they do not correspond.

**Molar volume.** In [49], the changes in molar volume of the actin molecule during $Mg^{2+}$-induced polymerization are measured. Actin in monomeric form has a molar volume of $32.2 + 0.2\,\frac{\mathrm{l}}{\mathrm{mol}}$. As a reflection of a $Mg^{2+}$ increment and a consequent polymerization of actin, the molar volume of actin decreases sharply by $0.72\,\frac{\mathrm{l}}{\mathrm{mol}}$. This result does not agree with two other papers cited in [49], where it reported a volume increment of 391 and $63\,\frac{\mathrm{ml}}{\mathrm{mol}}$. Moreover, here it is not discussed the molar volume of the F-actin network, but of the single filament.

**Diffusivity.** The reported G-actin diffusion coefficient in the cytoplasm ranges from 3 to 30 $\mu\mathrm{m}^2/\mathrm{s}$ [50].

**Reaction rate parameters.** The parameters of the chemical reaction between G-actin and F-actin illustrated in [51], [52] and [18] are introduced.

In [51], the polymerizing actin filament is modeled as an elastic rod whose length grows by the addition of monomers at the tip at a rate $k_f M$ [$\mathrm{s}^{-1}$] and shortens by losing subunits at a rate $k_b$ [$\mathrm{s}^{-1}$], where $k_f$ [$\mathrm{s}^{-1}\mu\mathrm{M}^{-1}$] is the polymerization rate and $M$ [$\mu$M] the local molar concentration of monomers near the growing tip. The reported polymerization and depolymerization rate parameters are $k_f = 11\,\mathrm{s}^{-1}\mu\mathrm{M}^{-1}$ and $k_b = 1\,\mathrm{s}^{-1}$, respectively, and the local molar concentration of monomers near the growing tip is $M = 10 - 50\,\mu\mathrm{M}$.

In [52], fragments of fish epithelial keratocytes are used to characterize the actin turnover and the spatiotemporal lamellipodia actin organization. Four different species are taken into account: polymerizable monomers (g), non-polymerizable monomers (G), oligomers (f), and network actin (F). It is assumed that network actin disassembles into oligomers, which break up into monomers, which in turn can switch between a polymerizable and a non-polymerizable form [52]. The average concentrations for the four subpopulations (F, f, G, and g) are determined based on their results and the assumption that the assembly rate of polymerizable monomers in vivo is similar to the rates measured in vitro [52]. Because it is known the amount of filamentous actin in absolute numbers, the concentrations of the four actin subpopulations are $F \approx 800\,\mu\mathrm{M}$, $f \approx 400\,\mu\mathrm{M}$, $G \approx 1200\,\mu\mathrm{M}$, and $g \approx 20\,\mu\mathrm{M}$. The effective reaction rate parameters are not directly measured, except for the network disassembly (r), which is $r \approx 0.25\,\frac{1}{\mathrm{s}}$. The other rates, namely the effective reaction rates for oligomer disassembly (c), monomer assembly (a), and the transitions between polymerizable and non-polymerizable monomers, $b$ and $k$, are inferred from flux balance analysis and the assumption that the rate of actin-thymosin dissociation, assumed to mediate the transition of monomers from the non-polymerizable to the polymerizable pool, is the same as that measured in vitro [52]. At steady state, the number of actin subunits per unit time transitioning from the network into oligomers, $rF$, has to be equal to the number of subunits flowing from oligomers to monomers, $cf$, as well as to the number of monomers assembling back into the network, as [52]. Thus, $rF = cf = ag$, so that, $c = rF/f \approx 2r \approx 0.5\,\frac{1}{\mathrm{s}}$, and $a = \frac{rF}{g} \approx 40r \approx 10\,\frac{1}{\mathrm{s}}$ [52]. The transition rates between polymerizable and non-polymerizable monomers should similarly be related at steady state by a flux balance relation: $\beta g = kG$ [52]. To specify these transition rates separately, it is introduced a second model assumption that the rate of actin-thymosin dissociation (which is assumed to mediate the transition of an actin subunit from the non-polymerizable monomer pool to the polymerizable one) is the same as that measured in vitro, so that $k \approx 2\,\frac{1}{\mathrm{s}}$ [52]. In this case, $\beta = \frac{kG}{g} \approx 120\,\frac{1}{\mathrm{s}}$ [52].

So, the reaction rate parameters used in [52] are

- $r \approx 0.25\,\frac{1}{\mathrm{s}}$
- $c = \frac{rF}{f} \approx 0.5\,\frac{1}{\mathrm{s}}$
- $a = \frac{rF}{g} \approx 10\,\frac{1}{\mathrm{s}}$
- $\beta = \frac{kG}{g} \approx 120\,\frac{1}{\mathrm{s}}$
- $k \approx 2\,\frac{1}{\mathrm{s}}$

In [18], the "elastic ratchet model" of Mogilner and Oster is extended to incorporate the transient binding at the actin/cell interface. In order to solve the dynamic equations for the numbers of actin filaments near the surface, the nucleation rate of attached filaments is estimated as $n = 10\,(100)\,\frac{\mathrm{filaments}}{\mathrm{s}}$ and the free dissociation rate is estimated as $\delta_0 \approx 0.5\,\frac{1}{\mathrm{s}}$.

**Depolymerization.** The rate of filament depolymerization in the comet tail is independent of either position in the tail or bacterial speed, and the filaments have very short half-lives, of the order of 30 seconds [8]. According to [51], the approximate length of actin comet tail is $l \approx 10\,\mu\mathrm{m}$.

**F-actin network mechanical parameters.** Following [19], Young's modulus of the actin comet tail ranges from $Y = 10^3$ to $10^4\,\mathrm{Pa}$. Consistently with elasticity measurements on fibroblast actin cortex, which showed that the Poisson ratio is $\nu \sim 0.4$, it can be assumed that the tail is incompressible, i.e, that the volume of a material element is conserved under deformation (Poisson ratio $\nu = \frac{1}{2}$) [19].

Following the ranges of values in [53], the actin polymeric network of lamellipodia can be characterized by Young's modulus $\mathrm{E} = 0.50\,\mathrm{kPa}$ and a shear modulus $\mathrm{G} = 0.20\,\mathrm{kPa}$.

**Cytoplasm** According to [51], the viscosity of fluid component of cytoplasm is taken as $\upsilon = 0.03\,\mathrm{poise}$.

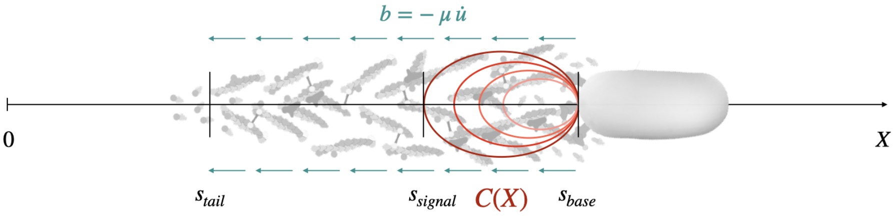

Figure 5.1: Schematic representation of ABM model [6]. Figure from [6].

## 5.2 Mechanical and entropic nature of the chemical potential: first model

This section is adapted from [6], "Actin based motility unveiled: How chemical energy is converted into motion, *J MECH PHYS SOLIDS*". The proof of concept represents the biological process of pathogens ABM.

### 5.2.1 Model assumptions

In the suspended resting state, the actin monomers are immersed in the cell cytosol. After the pathogen enters the cytosol, the polymerization of actin monomers at the surface of the bacterium tail generates the *actin comet tail*. Neglecting the curvature of the bacterium trajectory and considering that the *actin comet tail* extends mainly along one direction, we simplify the ABM of the bacterium as a one-dimensional problem.

**Signalling**. As we previously mentioned, the polymerization of G-actin is induced by a cascade of signaling pathways triggered by a stable protein on the surface of the bacterium. The precise details of the signaling processes are ignored. Rather, the activity that triggers the formation of the *actin comet tail* is considered via an activation signal, defined in the reference configuration, constantly emitted at the bacterium tail. Following eq. (4.66), we define the signal $\mathcal{C}(\vec{X}, t)$ as

$$\mathcal{C}(X) = \alpha \cdot \frac{X - s_{signal}}{\ell} \cdot \mathcal{H}(X - s_{signal}) \cdot \mathcal{H}(s_{base} - X) \,, \tag{5.1}$$

where $\alpha$ is a parameter that is related to the signal strength, $s_{base}$ is the position of the bacterium tail and $\ell = s_{base} - s_{signal}$ is the length of influence of the signal (see figure 5.1). The bacterium tail is located by definition as the first position from the right in which the F-actin network concentration is greater than 0. At initial time $t = 0\,\mathrm{s}$, it is set to $s_{base} = 10\ \mu m$.

### 5.2.2 Constitutive parameters

| parameter | symbol | value | units | ref |
|---|---|---|---|---|
| Forward reaction rate parameter | $k_f^*$ | 10.00 | $\left[\mathrm{s}^{-1}\right]$ | [52] |
| Backward reaction rate parameter | $k_b^*$ | 0.25 | $\left[\mathrm{s}^{-1}\right]$ | [52] |
| Delay time | $\tau$ | 30.00 | [s] | [8] |
| Length of influence of the signal | $\ell$ | 1.00 | [$\mu$m] | arb |
| Signal intensity parameter | $\alpha$ | 0.002 | $[-]$ | arb |
| G-actin diffusivity | $\mathbb{D}_{G_R}$ | 3.00 | $\left[\mu\mathrm{m}^2 \cdot \mathrm{s}^{-1}\right]$ | [50] |
| F-actin network diffusivity | $\mathbb{K}_{F_R}$ | 0.01 | $\left[\mu\mathrm{m}^2 \cdot \mathrm{s}^{-1}\right]$ | arb |
| Equilibrium temperature | T | 310.15 | [K] | [54] |
| Gas constant | R | 8.31 | $\left[\mathrm{J} \cdot \mathrm{K}^{-1} \cdot \mathrm{mol}^{-1}\right]$ | - |
| F-actin network Young Modulus | E | 500.00 | [Pa] | [53] |
| F-actin network Shear Modulus | G | 200.00 | [Pa] | [53] |
| Molar volume of G-actin | $\omega_G$ | 32.20 | $\left[l \cdot \mathrm{mol}^{-1}\right]$ | [49] |
| Molar volume of F-actin network | $\omega_F$ | 58.00 | $\left[l \cdot \mathrm{mol}^{-1}\right]$ | arb |
| Viscous constant | $\nu$ | $3.00 \cdot 10^{-3}$ | [Pa $\cdot$ s] | [51] |
| G-actin initial concentration | $c_{G_R}(X,0)$ | 2420.00 | [$\mu$M] | [52] |
| F-actin network initial concentration | $c_{F_R}(X,0)$ | 0.00 | [$\mu$M] | - |
| Initial displacement | $U_1(X,0)$ | 0.00 | [$\mu$m] | - |

Table 5.1: *Material parameters and other data for the numerical simulations [6].*

The parameters chosen for numerical simulations are summarized in Table 5.1, together with bibliographic references. The forward reaction constant in eq. (4.66) has been taken from [52] and amounts at $k_f^* = 10.00\,\mathrm{s}^{-1}$. The backward reaction rate parameter has been set to $k_b^* = 0.25\,\mathrm{s}^{-1}$, consistent with the *severing parameter r* in [52]. The average lifetime of actin filaments is $\tau = 30\,\mathrm{s}$ seconds in *actin comet tails* [8], while it ranges from 20 seconds to 2 minutes in lamellipodia.

The diffusivity of G-actin is assumed to be $\mathbb{D}_{G_R} = 3.00\,\mu\mathrm{m}^2\mathrm{s}^{-1}$, consistent with the values reported in [50] that range from 3 to 30 $\mu\mathrm{m}^2\mathrm{s}^{-1}$ . The transport parameter of the F-actin network $\mathbb{K}_{F_R}$ is supposed to be orders of magnitude smaller than the G-actin counterpart. The length of influence of the signal $\ell = 1.00\,\mu\mathrm{m}$, the signal strength $\alpha = 0.002$ and $\mathbb{K}_{F_R} = 0.01\,\mu\mathrm{m}^2\mathrm{s}^{-1}$ have been calibrated in order to obtain a final *actin comet tail* length of 10 $\mu$m, as described in [51].

The equilibrium temperature is assumed to be T = 310 K [54]. In accordance with [53], the actin polymeric network is characterized by a Young's modulus E = 0.50 kPa and a shear modulus G = 0.20 kPa. The molar volume of G-actin has been measured in [49] as $32.20 \pm 0.2\, l\mathrm{mol}^{-1}$. The cytosol viscosity is taken as $\nu = 3.00 \cdot 10^{-3}\,\mathrm{Pa \cdot s}$, consistent with [51]. The molar volume of the F-actin network is calibrated to obtain a bacterium velocity of about 1 $\mu\mathrm{ms}^{-1}$.

While significant effort is invested in proposing appropriate values for model parameters in numerical results, the associated uncertainties are broad. Nevertheless, since the model is at a preliminary step, no uncertainties quantifications or sensitivities analyses have been done. These detailed investigations are deferred to a more mature phase of the model.

### 5.2.3 Governing equations and boundary conditions

With $\boldsymbol{F}^c$ defined as

$$\boldsymbol{F}^c = \begin{bmatrix} {J^c}^{\frac{1}{3}} & 0 & 0 \\ 0 & 1 & 0 \\ 0 & 0 & 1 \end{bmatrix} , \tag{5.2}$$

the governing equations for the problem in hand read

$$\frac{\partial c_{G_R}}{\partial t} - \frac{\partial}{\partial X}\left[\mathbb{D}_{G_R}\,\frac{\partial c_{G_R}}{\partial X}\right] + k_f\, c_{G_R} - k_b\, c_{F_R} = 0 , \tag{5.3a}$$

$$\begin{aligned} &\frac{\partial c_{F_R}}{\partial t} - \frac{\partial}{\partial X}\left[\mathbb{K}_{F_R}\,\frac{\partial c_{F_R}}{\partial X}\right] + \\ &+ \frac{\mathbb{K}_{F_R}\Omega_F\,(\mathrm{G}+\frac{\lambda}{2})}{4\,\mathrm{R}\,\mathrm{T}}\,\frac{\partial}{\partial X}\left[c_{F_R}\,\frac{\partial}{\partial X}\left[\,3\left(\frac{J}{J^c}\right)^4 - 2\left(\frac{J}{J^c}\right)^2\,\right]\right] + \\ &- k_f\, c_{G_R} + k_b\, c_{F_R} = 0 , \end{aligned} \tag{5.3b}$$

$$\frac{\partial}{\partial X}\left[{J^c}^{-1}(1+\frac{\partial U_1}{\partial X_1})\left({J^c}^{-2}(1+\frac{\partial U_1}{\partial X_1})^2 - 1\right)\right] - \frac{\nu}{\mathrm{G}+\frac{\lambda}{2}}\,\frac{\partial\, U_1}{\partial t} = 0 , \tag{5.3c}$$

with $J^c$ from eq. (4.60).

At the initial time $t = 0\,\mathrm{s}$, we assume that: i) the displacements vanish throughout the stress-free body

$$U_1(X, 0) = 0 ; \tag{5.4}$$

ii) the G-actin concentration is uniform[1] and that no F-actin network exists

$$c_{G_R}(X,0) = 2420\ \mu\text{M}\ , \tag{5.5a}$$

$$c_{F_R}(X,0) = 0\ \mu\text{M}\ . \tag{5.5b}$$

The cellular domain boundaries are defined on $a = 0\,\mu$m and $b = 52\,\mu$m. The boundary conditions for the *actin comet tail* are prescribed on its front, $s_{base}$, and its back, $s_{tail}$, taken as the first position from the left in which the F-actin network concentration is greater than 0. The concentration of G-actin is considered to be constant on the boundaries, in accordance with the initial condition

$$c_{G_R}(a,t) = c_{G_R}(b,t) = c_{G_R}(X,0) \qquad \forall t \in [\,0, t_{end}\,]\ . \tag{5.6}$$

We consider a zero flux of F-actin network across the cell boundaries

$$h_{F_R}(a,t) \cdot n_R = h_{F_R}(b,t) \cdot n_R = 0 \qquad \forall t \in [\,0, t_{end}\,]\ . \tag{5.7}$$

The mass of the bacterium is considered to be negligible, therefore at $s_{base}$ a null Neumann condition is imposed. On the back boundary of the *actin comet tail*, bacterium displacements vanish coherently with a steady cellular cytosol, i.e.

$$U_1(s_{tail},t) = 0 \qquad \forall t \in [\,0, t_{end}\,]\ , \tag{5.8a}$$

$$P_{11}(s_{base},t) \cdot n_R = 0 \qquad \forall t \in [\,0, t_{end}\,]\ . \tag{5.8b}$$

### 5.2.4 Numerical simulations

The strong differential form equations (5.3) require the existence of the second order derivative and are defined at a continuum level, namely they must hold for every singular point in the domain $\Omega_R$ (they need pointwise condition). Generally, partial differential equations can not be solved analytically and the requirements for differentiability of the solution are too strong. So, the weak formulation of the differential problem is usually employed, which is an alternative formulation of the problem that allows for reducing the order of the derivation [55].

The weak formulation entails

---

[1] Data of [52] allow to establish the initial concentration of G-actin, taken as the sum of the four actin subpopulations concentrations ($F = 800\ \mu$M, $f = 400\ \mu$M, $G = 1200\ \mu$M, $g = 20\ \mu$M, see [52]).

- a multiplication of the equations by arbitrary test functions that are homogeneous at the Dirichlet boundaries [55];
- an integration upon the domain $\Omega_R$;
- a reduction of the order of derivation from a second-order differential problem to a first-order one, to reduce the regularity.

We start by multiplying equations (5.3) by arbitrary test functions $\hat{\mu}_G$, $\hat{\mu}_F$, $\hat{\vec{v}}$ and integrating upon the domain $\Omega_R$, we obtain

$$\begin{aligned} \int_{\Omega_R} & \hat{\mu}_G \left\{ \frac{\partial c_{G_R}}{\partial t} - \frac{\partial}{\partial X}\left[ \mathbb{D}_{G_R} \frac{\partial c_{G_R}}{\partial X} \right] + k_f c_{G_R} - k_b c_{F_R} \right\} + \\ & + \hat{\mu}_F \left\{ \frac{\partial c_{F_R}}{\partial t} - \frac{\partial}{\partial X}\left[ \mathbb{K}_{F_R} \frac{\partial c_{F_R}}{\partial X} \right] + \right. \\ & + \frac{\mathbb{K}_{F_R} \Omega_F \, (\mathrm{G} + \frac{\lambda}{2})}{4 \, \mathrm{R} \, \mathrm{T}} \frac{\partial}{\partial X} \left[ c_{F_R} \frac{\partial}{\partial X} \left[ 3 \left( \frac{J}{J^c} \right)^4 - 2 \left( \frac{J}{J^c} \right)^2 \right] \right] + \\ & \left. - \, k_f \, c_{G_R} + k_b \, c_{F_R} \right\} + \\ & + \hat{\vec{v}} \cdot \left\{ \frac{\partial}{\partial X} \left[ J^{c^{-1}} (1 + \frac{\partial U_1}{\partial X_1}) \left( J^{c^{-2}} (1 + \frac{\partial U_1}{\partial X_1})^2 - 1 \right) \right] + \right. \\ & \left. - \frac{\nu}{\mathrm{G} + \frac{\lambda}{2}} \frac{\partial \, U_1}{\partial t} \right\} \mathrm{d}v_R = 0 \, . \end{aligned} \tag{5.9}$$

We integrate by parts using the Gauss theorem, with the purpose of eliminating the second derivatives and imposing a lower regularity on the solution. We obtain

$$\begin{aligned} \int_{\Omega_R} & \left( \hat{\mu}_G \, \frac{\partial c_{G_R}}{\partial t} + \mathbb{D}_{G_R} \frac{\partial \hat{\mu}_G}{\partial X} \frac{\partial c_{G_R}}{\partial X} + k_f \, \hat{\mu}_G \, c_{G_R} - k_b \, \hat{\mu}_G \, c_{F_R} \right) + \\ & + \left( \hat{\mu}_F \, \frac{\partial c_{F_R}}{\partial t} + \mathbb{K}_{F_R} \frac{\partial \hat{\mu}_F}{\partial X} \frac{\partial c_{F_R}}{\partial X} - k_f \, \hat{\mu}_F \, c_{G_R} + k_b \, \hat{\mu}_F \, c_{F_R} + \right. \\ & \left. + \frac{\mathbb{K}_{F_R} \Omega_F \, (\mathrm{G} + \frac{\lambda}{2})}{4 \, \mathrm{R} \, \mathrm{T}} \frac{\partial \hat{\mu}_F}{\partial X} \cdot \left[ c_{F_R} \frac{\partial}{\partial X} \left[ 3 \left( \frac{J}{J^c} \right)^4 - 2 \left( \frac{J}{J^c} \right)^2 \right] \right] \right) + \\ & - \left( \hat{\vec{v}} \cdot \frac{\nu}{\mathrm{G} + \frac{\lambda}{2}} \frac{\partial \, U_1}{\partial t} + \frac{\partial \hat{\vec{v}}}{\partial X} \cdot \right. \\ & \left. \cdot \left[ J^{c^{-1}} (1 + \frac{\partial U_1}{\partial X_1}) \left( J^{c^{-2}} (1 + \frac{\partial U_1}{\partial X_1})^2 - 1 \right) \right] \right) \mathrm{d}v_R + \\ & - \int_{\partial^N \Omega_R} \hat{\mu}_G \, \overline{h}_{G_R} \, \mathrm{d}\Gamma - \int_{\partial^N \Omega_R} \hat{\mu}_F \, \overline{h}_{F_R} \, \mathrm{d}\Gamma + \int_{\partial^N \Omega_R} \hat{\vec{v}} \cdot \vec{\vec{T}} \, \mathrm{d}\Gamma = 0 \, , \end{aligned} \tag{5.10}$$

where boundary conditions (4.120) are used in the integrals on the boundaries.

Taking advantage of the boundary conditions values, the equations (5.10) read

$$\begin{aligned}\int_{\Omega_R} &\left(\hat{\mu}_G \, \frac{\partial c_{G_R}}{\partial t} + \mathbb{D}_{G_R} \frac{\partial \hat{\mu}_G}{\partial X} \frac{\partial c_{G_R}}{\partial X} + k_f \, \hat{\mu}_G \, c_{G_R} - k_b \, \hat{\mu}_G \, c_{F_R}\right) + \\ &+ \left(\hat{\mu}_F \, \frac{\partial c_{F_R}}{\partial t} + \mathbb{K}_{F_R} \frac{\partial \hat{\mu}_F}{\partial X} \frac{\partial c_{F_R}}{\partial X} - k_f \, \hat{\mu}_F \, c_{G_R} + k_b \, \hat{\mu}_F \, c_{F_R} + \right. \\ &\left. + \frac{\mathbb{K}_{F_R} \Omega_F \, (\mathrm{G} + \frac{\lambda}{2})}{4 \, \mathrm{R} \, \mathrm{T}} \, \frac{\partial \hat{\mu}_F}{\partial X} \cdot \left[ c_{F_R} \frac{\partial}{\partial X} \left[ 3 \left( \frac{J}{J^c} \right)^4 - 2 \left( \frac{J}{J^c} \right)^2 \right] \right] \right) + \\ &- \left( \hat{\vec{v}} \cdot \frac{\nu}{\mathrm{G} + \frac{\lambda}{2}} \, \frac{\partial \, U_1}{\partial t} + \frac{\partial \hat{\vec{v}}}{\partial X} \cdot \right. \\ &\left. \cdot \left[ J^{c^{-1}} (1 + \frac{\partial U_1}{\partial X_1}) \left( J^{c^{-2}} (1 + \frac{\partial U_1}{\partial X_1})^2 - 1 \right) \right] \right) \mathrm{d}v_R = 0 \, .\end{aligned} \tag{5.11}$$

Even though the first-order derivative of $H_{F_R}$ can be reduced by applying the integration by parts, its constitutive definition contains a second-order derivative. To avoid this problem, we introduce a new variable $\Sigma \, (c_{F_R}, U_1)$ defined as

$$\Sigma - \alpha(c_{F_R}, U_1) = 0 \, , \qquad \text{with} \quad \alpha = \left[ 3 \left( \frac{J}{J^c} \right)^4 - 2 \left( \frac{J}{J^c} \right)^2 \right] , \tag{5.12}$$

which is approximated as an explicit degree of freedom. Eq. (5.12) is then added to the set of governing equations (5.11) for the numerical solution of the problem, so the final weak form of the governing equations read

$$\begin{aligned}\int_{\Omega_R} &\left(\hat{\mu}_G \, \frac{\partial c_{G_R}}{\partial t} + \mathbb{D}_{G_R} \frac{\partial \hat{\mu}_G}{\partial X} \frac{\partial c_{G_R}}{\partial X} + k_f \, \hat{\mu}_G \, c_{G_R} - k_b \, \hat{\mu}_G \, c_{F_R}\right) + \\ &+ \left( \hat{w} \, \Sigma - \hat{w} \, \alpha \right) + \left(\hat{\mu}_F \, \frac{\partial c_{F_R}}{\partial t} + \mathbb{K}_{F_R} \frac{\partial \hat{\mu}_F}{\partial X} \frac{\partial c_{F_R}}{\partial X} - \mathbb{E}_{F_R} \frac{\partial \hat{\mu}_F}{\partial X} c_{F_R} \frac{\partial \alpha}{\partial X} + \right. \\ &\left. - k_f \, \hat{\mu}_F \, c_{G_R} + k_b \, \hat{\mu}_F \, c_{F_R} \right) - \left( \hat{\vec{v}} \cdot \frac{\nu}{\mathrm{G} + \frac{\lambda}{2}} \, \frac{\partial \, U_1}{\partial t} + \right. \\ &\left. + \frac{\partial \hat{\vec{v}}}{\partial X} \cdot \left[ J^{c^{-1}} (1 + \frac{\partial U_1}{\partial X_1}) \left( J^{c^{-2}} (1 + \frac{\partial U_1}{\partial X_1})^2 - 1 \right) \right] \right) \mathrm{d}v_R = 0 \, ,\end{aligned} \tag{5.13}$$

where $\mathbb{E}_{F_R}$ stands for

$$\mathbb{E}_{F_R} = \frac{\mathbb{K}_{F_R} \Omega_F \, (\mathrm{G} + \frac{\lambda}{2})}{4 \, \mathrm{R} \, \mathrm{T}} \, .$$

#### 5.2.4.1 Finite element method and finite difference scheme

To solve the problem numerically, we take advantage of two different methods to discretize the problem in space and time: the Finite Element Method for the space and Finite Difference Scheme for time.

**5.2.4.1.1 Finite element method** Speaking of space discretization, we use the finite element method by projecting the weak formulation to a finite-dimensional subspace. This means that we have finite (discrete) sets of nodes that substitute the infinite number of points of the continuum $\Omega_R$. Following the classical Bubnov-Galerkin method, the same projection is applied to both test functions ($\hat{\mu}_G$, $\hat{\mu}_F$, $\hat{\vec{v}}$) and the field variables ($c_{G_R}$, $c_{F_R}$ and $U_1$). The finite discretization implies an interpolation between nodal unknowns and it is taken as linear both for test functions and field variables. We make use of isoparametric finite elements, namely we apply the same interpolation scheme for the coordinates $X$ and the field variables.

Following the previous assumptions, the interpolation representation into the discretized weak-form field reads

$$\begin{aligned}\sum_I \sum_J \sum_K \cdots \Bigg[ & (N_{I_G}, N_{J_G} \frac{\partial c_{J_G}}{\partial t}) + \mathbb{D}_{G_R} (\frac{\partial N_{I_G}}{\partial X}, \frac{\partial N_{J_G}}{\partial X} c_{J_G}) + \\ & + k_f\, C(X,t) \big(N_{I_G}, N_{J_G} c_{J_G}\big) - k_b \big(N_{I_G}, N_{H_F} c_{H_F}\big) + \big(N_{K_F}, N_{H_F} \frac{\partial c_{H_F}}{\partial t}\big) + \\ & + \mathbb{K}_{F_R} (\frac{\partial N_{K_F}}{\partial X}, \frac{\partial N_{H_F}}{\partial X} c_{H_F}) - \mathbb{E}_{F_R} (\frac{\partial N_{K_F}}{\partial X}, N_{H_F} c_{H_F} \frac{\partial \alpha}{\partial X}) + \\ & - k_f\, C(X,t) \big(N_{K_F}, N_{J_G} c_{J_G}\big) \mathbb{E}_{F_R} (\frac{\partial N_{K_F}}{\partial X}, N_{H_F} c_{H_F} \frac{\partial \alpha}{\partial X}) + \\ & + k_b \big(N_{K_F}, N_{H_F} c_{H_F}\big) + \big(N_{E_\epsilon}, N_{N_\epsilon} \Sigma_N\big) - \big(N_{E_\epsilon}, \alpha\big) \Bigg] = 0 \,. \end{aligned} \tag{5.14}$$

where

$$(a, b) = \int_{\Omega_R} a \, \cdot \, b \, \mathrm{d}v_R \; = 0$$

and

$$\begin{bmatrix} \hat{\mu}_G \\ \hat{\mu}_F \\ \hat{\vec{v}} \\ \hat{w} \end{bmatrix} = \sum_{I,K,L,E=1}^{2} \begin{bmatrix} N_{I_G} \\ N_{K_F} \\ N_{L_u} \\ N_{E_\epsilon} \end{bmatrix} \qquad \text{and} \qquad \begin{bmatrix} c_{G_R} \\ c_{F_R} \\ U_1 \\ \Sigma \end{bmatrix} = \sum_{J,H,M,N=1}^{2} \begin{bmatrix} N_{J_G}\, c_{G_J}(t) \\ N_{H_F}\, c_{F_H}(t) \\ N_{M_u}\, U_M(t) \\ N_{N_\epsilon}\, \Sigma_N(t) \end{bmatrix} \,.$$

This is the semi discretized expression (only in space) of the weak form in the case of linear elements.

**5.2.4.1.2 Finite difference scheme** Speaking of time discretization, we make use of the finite difference method. For the mean value theorem, it exists a certain time $\bar{t} = \eta$ between $t^m$ and $t^{m+1}$ such that

$$\frac{\partial c_a}{\partial t}|_\eta = \frac{c_a^{m+1} - c_a^m}{\Delta t} \,. \tag{5.15}$$

where $\Delta t = t^{m+1} - t^m$. Consequently, the concentration can be defined as

$$c_a(\eta) = c_a^m + \frac{\partial c_a}{\partial t}|_\eta(\eta - t^m) = c_a^m\,(1-\theta) + c_a^{m+1}\theta\,, \qquad \text{with} \quad \theta = \frac{\eta - t^m}{\Delta t} \,. \tag{5.16}$$

So, the time derivatives in (5.14) are replaced by suitable difference quotients of (5.16) and an implicit scheme (Backward Euler FDM, with $\theta = 1$) has been set with a uniform time increment of 1000 time steps. Since the finite difference scheme method does not work for the equation of linear momentum balance (it results to be mesh-dependent), we make use of a Newton-Raphson scheme in which an initial guess for displacement is proposed, coming from the solution at the previous time step (or the displacement due to the swelling distortion only). Then, we obtain the velocity and we iterate until we come up with the convergency of the solution, which is dictated by the tolerance of the residual $R$. The residual comes out from the difference between the displacement solution at the current time step and the displacement solution at the previous time step. Moreover, we make use of the mass lumped matrix for mass matrices. The mass-lumping technique allows writing the mass matrix in a diagonal form (not in a tridiagonal form), called *condensed* or *lumped matrix* form, which allows not to invert the matrix and not to reduce the accuracy of the method [55].

A Newton-Raphson integration scheme has been implemented to solve the non-linear system of equations at each time step. The geometry is tessellated using 26000 isoparametric. The choice of time step and finite elements size is dictated by the convergence of the solution, so that the relative error between the solutions with different time step and finite elements size is less than $10^{-2}$. Outcomes have been obtained by coding the numerical strategies described above in MATLAB, without relying on level-set moving boundary tracking methods.

### 5.2.5 Results and discussion

**G and F-actin network concentrations distributions**. In figure 5.2 the concentration of the G-actin and F-actin network are plotted several times.

At initial time, the concentration of G-actin is uniform and the concentration of the polymerized network is null throughout the domain. The bacterium tail is located out to $s_{base} = 10\,\mu$m and so is the signal.

At time $t = 3\,$s, an incipient F-actin network develops in proximity to the

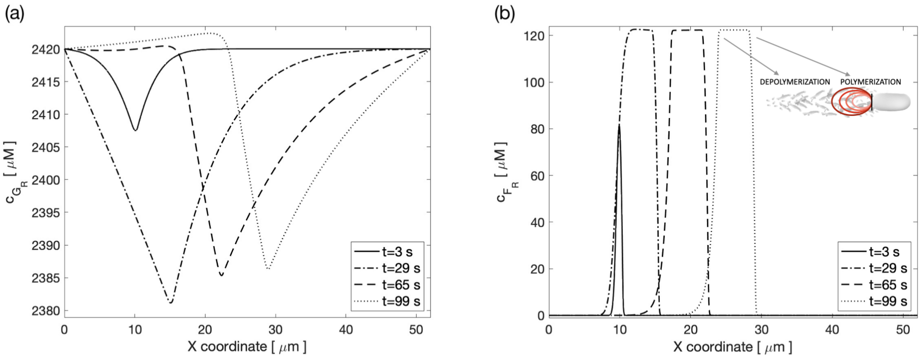

Figure 5.2: Concentrations of monomer actin and actin network at time $t = 3\,\text{s}$, $t = 29\,\text{s}$, $t = 65\,\text{s}$, $t = 99\,\text{s}$ [6] in the cell. At initial time, the bacterium tail is located out to $s_{base} = 10\,\mu\text{m}$ and so is the signal. At time $t = 3\,\text{s}$, an initial F-actin network develops in proximity to the signal, while the G-actin concentration decreases. At time $t = 29\,\text{s}$, the comet tail is almost completely formed. The polymerization of the F-actin network moves the bacterium rightward, where the G-actin reaches a minimum. The F-actin network does not depolymerize, yet, since $t < \tau$. At time $t = 65\,\text{s}$, the depolymerization is in place and the actin comet tail is divided into two parts: the *head* and the *back*. As time passes, the length of the actin comet tail and the processes described above become steady. Figure from [6].

signal (see the continuous line in figure 5.2), while the G-actin concentration decreases (see the continuous line in figure 5.2). Filaments polymerize at the bacterial surface to generate force. Far from there, the concentration profiles are unaltered.

At time $t = 29\,\text{s}$, the comet tail is almost completely formed. The dot-dashed line in figure 5.2 shows how the network concentration reaches the maximum value $122.28\,\mu\text{M}$, increasing sharply at the leading edge of the bacterium tail. The polymerization of the F-actin network moves the bacterium rightward, where the G-actin reaches a minimum (see figure 5.2). The F-actin network does not depolymerize, yet, since $t < \tau$.

At time $t = 65\,\text{s}$, the depolymerization is in place and two parts of the actin comet tail can be devised consistent with the picture in figure 5.1. The *head*, close to the signal, is characterized by a dense network of filaments, some of which have just been polymerized. The *back* consists of depolymerizing filaments whose lifetime has been exceeded. The depolymerization of the F-actin network in turn induces an increment of G-actin monomers, whose concentration exceeds the initial value at some locations.

As time passes, the length of the actin comet tail and the processes described above become steady. A snapshot at time $t = 99\,\mathrm{s}$ is depicted in figure 5.2. The bacterium moves rightward at a constant velocity.

**Displacements and Stresses**. Figure 5.3 plots the displacement field $U_1(X)$ at several times. The plots reveal that the polymerization of G-actin into the F-actin network causes a swelling distortion in the domain, which is opposed by the viscous cytosol resistance. The displacements rise as the comet tail develops in time, with a transient process (see $U_1(X)$ at $t = 3\,\mathrm{s}$) until becoming stationary (see $U_1(X)$ at $t = 99\,\mathrm{s}$).

Figure 5.3 plots also the stress $P_{11}(X)$ at several times. From $t = 0\,\mathrm{s}$ to $t = 29\,\mathrm{s}$ the F-actin network is forming and no depolymerization occurs. The body is swelling and the external drag viscous forces cause a compressive state in the F-actin network domain. After $t = \tau$ the F-actin network depolymerizes at the back of the *actin comet tail*, displacements become nearly stationary in time and so do the stresses. The body is swelling at the front of the *actin comet tail*, where a new F-actin network is forming, and it is shrinking at the back of the *actin comet tail*, where filaments depolymerize. The external forces cause a compressive state in the polymerized part of the body and a tensile state in the depolymerized part.

### 5.2.6 Concluding remarks

A bio-chemo-mechanical model for ABM of biological systems has been presented. It entails an interaction among external signaling, the elastic response of the polymerized actin network, and the kinetics of the chemical reaction between the monomeric form of G-actin and the network of F-actin. In the proof of concept, it has been shown that the model captures the general features of pathogen motility observed in experimental studies, including the signal dependence of polymerization of the F-actin network on the bacterium tail and the F-actin network distribution during pathogen motility.

The model is characterized by some features and assumptions. As highlighted in figure 3.2, filaments in the F-actin network do not seem to be aligned to a preferential direction, rather they form a matrix of arbitrarily oriented strands: fibers perpendicular to the tail direction are visible even in the depolymerized zone. For this sake, we did not account for anisotropy in the multiplicative decomposition of the deformation gradient - see eq. (4.2). The comet tail evolution is dictated by the motion of the signal, emitted at different positions in time.

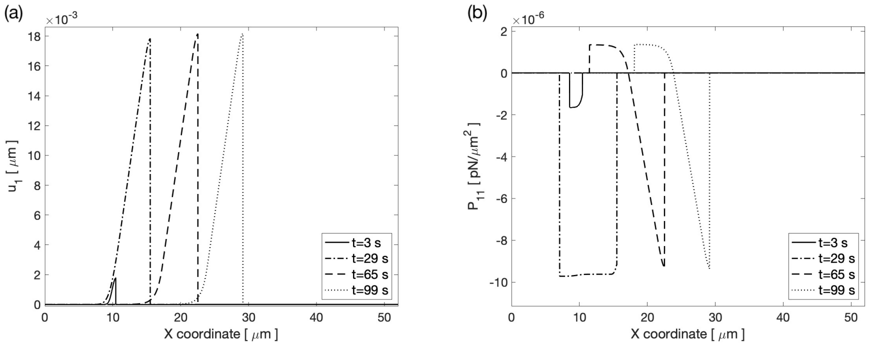

Figure 5.3: Displacements and stresses of actin network at time $t = 3\,\mathrm{s}$, $t = 29\,\mathrm{s}$, $t = 65\,\mathrm{s}$, $t = 99\,\mathrm{s}$ [6]. From time $t = 0$ s to $t = 29$ s, the F-actin network undergoes formation without any depolymerization occurring. During this period, the body expands while external viscous drag forces induce compression within the domain of the F-actin network. Upon reaching time $t = \tau$, depolymerization of the F-actin network initiates at the rear of the actin comet tail. Displacements then approach a state of near-stationarity over time, along with stress levels. Simultaneously, the body continues to expand at the front of the actin comet tail, where a new F-actin network forms, while contracting at the tail's rear, where filaments depolymerize. External forces induce a compressive state in the polymerized part of the body and a tensile state in the depolymerized part. Figure from [6].

We assumed that the maximum number of molecules per unit volume is invariant, i.e. that species in the body occupy a fixed volume and can relocate in eventual volume expansions of the hosting material. The main consequences of this assumption have been discussed in [34].

The governing equations depicted in section 4.9 hold for any specification of the Helmholtz free energy. In the model of bacterial pathogens motility developed in section 4.10 we considered an elastic strain-energy function of Saint-Venant kind, without cross-link protein rearrangement in view of the "high" speed of bacteria in the host cytoplasm. In reality, cross-link reorganization can occur in pathogens and certainly takes place in cellular motility. More sophisticated, statistically-based continuum theories can be invoked to capture the consequent rate-dependent behavior of the F-actin network upon mechanical loading [56, 57]. While the consistency of the chemo-mechanical motor has been verified for bacterial pathogen motility, we limited ourselves to the assumption of material parameters independent of F-actin concentration. To account for the role of concentration in the stiffness of the F-actin network [53], further work will be implemented.

The model shall be extended also to account for additional phenomena, such as bacteria invasion of neighboring cells. Cell-to-cell spread via protrusion- and vesicle-mediated transfer can be included by adding models that couple ABM of intracellular bacterial pathogens with the resistance of the membrane, which depends on the trafficking of tension-regulating proteins [7]. Such developments of the model permit a complete picture of the life cycles of intracellular bacteria that harness ABM.

Moreover, the same polymerization motor can be adapted to describe cellular motility, in angiogenesis or tumor metastasis. The actin polymerization motor operates both in lamellipodia and filopodia at the cellular leading edge. In this case, the model has to take into account all mechanically significant cellular structures involved in the motility, e.g., stress fibers, focal adhesions, microtubules, as well as substrate-cell interactions.

The model can be used to address one of the key challenges in cell biomechanics, namely how to measure the mechanical behavior of pathogens and cells during ABM. Because the model captures the reorganization of the actin network in response to an external stimulus, it can be used as a framework to design and interpret tailored experiments.

## 5.3 Mechanical nature of the chemical potential: second model

This section is adapted from [25], "Continuum multi-physics modeling of cell and bacteria motility, submitted". The proof of concepts is designed to represent the

- pathogens ABM;
- behavior of actin network growth discussed in 1.3, that comes from [5].

### 5.3.1 Model assumptions

**Signalling.** As stated, all biological and biochemical events that trigger actin nucleation, branching, and cross-linking have been wrapped in the activation signal function $\mathcal{C} = \mathcal{C}(\vec{x}, t)$, which localizes the signaling in (4.66) to the places in the current configuration where the protein ActA is located, such as the bacterium surface. We take $\mathcal{C}(\vec{x}, t)$ to vanish everywhere but in a domain

$$V_s = \{\vec{x} \in \text{cytosol} : \inf_{\vec{x}_b \in \partial_b} ||\vec{x} - \vec{x}_b(t)|| \leq \ell\} \tag{5.17}$$

with characteristic length $\ell$ about the nucleation surface $\partial_b$, where it holds

$$\mathcal{C}(\vec{x},t) = \inf_{\vec{x}_b \in \partial_b} \frac{||\vec{x} - \vec{x}_b(t)||}{\ell} \leq 1 \; . \tag{5.18}$$

*Differently from* [6], the signal *depends on $\vec{x}$ in order to maintain a constant length $\ell$ in the current configuration.*

**Helmholtz free energy.** The Helmholtz free energy density is defined via an additive decomposition

$$\psi_R(c_{G_R}, c_{F_R}, \mathbf{E}) = \psi_R^{en}(c_{G_R}) + \psi_R^{mech}(c_{F_R}, \mathbf{E}) \; , \tag{5.19}$$

which accounts for the entropic and the mechanical contributions.

*Differently from* [6], the entropic free energy does not involve the $F$-actin network concentration. *This choice has a fundamental consequence: the chemical potential $\mu_F$ in* (4.97c) *is not entropic in nature, it is solely due to the mechanics of protrusion via the swelling tensor defined in* (4.3)*. The same interpretation applies to the mass flux $\vec{H}_F$ in* (4.102b)*.*

The entropic free energy density

$$\psi_R^{en}(c_{G_R}) = \; \mu_G^0 \, c_{G_R} + R \, T c_{G_R} \ln \left[ \frac{c_{G_R}}{c_{G_R}^{sat}} \right] \; , \tag{5.20}$$

where $R$ is the gas constant, $T$ is temperature, $c_{G_R}^{sat}$ is the saturation limit for the actin monomers, which is inferred from statistical mechanics [39].

Experimental evidence in ABM shows a large spectrum of $F$-network velocities. The adsorption of ActA onto an Atomic Force Microscopy (AFM) cantilever beam [5] promoted a $F$-network development at about 1 nm/s. Bacteria ABM turns out to be much faster in the host cytoplasm, at rates of up to 1 $\mu$m/s [8]. The biological motivations of these 3 orders of magnitudes deserve further studies. Considering the speed of bacteria in the host cytoplasm, viscous effects do not have sufficient time to develop, even though in reality some cross-link rearrangement can occur. Accordingly, we derive the mechanical free energy density from an elastic material, i.e.

$$\psi_R^{mech}(c_{F_R}, \mathbf{E}) = J^c \; \psi_R^{el}(\mathbf{E}^e) \; , \tag{5.21}$$

with

$$\mathbf{E} = J^{c^{2/3}} \mathbf{E}^e + \frac{1}{2} (J^{c^{2/3}} - 1) \mathbb{1} \tag{5.22}$$

and $\psi_R^{el} = 0$ at vanishing $\mathbf{E}^e$. Easy algebra shows that, in view of (4.97), (5.19), and (5.21),

$$\mu_F = \frac{\partial J^c \, \psi_R^{el}}{\partial c_{F_R}} = \frac{\Omega_F}{3J^c} \, \left[ 3\psi_R^{el}(\mathbf{E}^e) - 2\mathbf{S} \cdot \mathbf{E} - \mathrm{tr}\,[\,\mathbf{S}\,] \right] \; . \tag{5.23}$$

### 5.3.2 Constitutive parameters

| parameter | symbol | value | units | ref |
|---|---|---|---|---|
| Forward reaction rate parameter | $k_f^*$ | 10.00 | $\left[\mathrm{s}^{-1}\right]$ | [52] |
| Backward reaction rate parameter | $k_b^*$ | 0.25 | $\left[\mathrm{s}^{-1}\right]$ | [52] |
| Delay time | $\tau$ | 30.00 | [s] | [8] |
| Length of influence of the signal | $\ell$ | 1.00 | [$\mu$m] | arb |
| G-actin diffusivity | $\mathbb{D}_{G_R}$ | 3.00 | $\left[\mu\mathrm{m}^2 \cdot \mathrm{s}^{-1}\right]$ | [50] |
| Equilibrium temperature | T | 310.15 | [K] | [54] |
| Gas constant | R | 8.31 | $\left[\mathrm{J} \cdot \mathrm{K}^{-1} \cdot \mathrm{mol}^{-1}\right]$ | - |
| F-actin network Young Modulus | E | 1 – 10.00 | [kPa] | [19] |
| F-actin network Poisson ratio | $v$ | 0.4 | [−] | [19] |
| Molar volume of G-actin | $\omega_G$ | 32.20 | $\left[l \cdot \mathrm{mol}^{-1}\right]$ | [49] |
| Molar volume of F-actin network | $\omega_F$ | 58.00 | $\left[l \cdot \mathrm{mol}^{-1}\right]$ | arb |
| Viscous constant | $\nu$ | $3.00 \cdot 10^{-3}$ | [Pa · s] | [51] |
| G-actin initial concentration | $c_{G_R}(X, 0)$ | 2420.00 | [$\mu$M] | [52] |
| F-actin network initial concentration | $c_{F_R}(X, 0)$ | 0.00 | [$\mu$M] | - |
| Initial displacement | $U_1(X, 0)$ | 0.00 | [$\mu$m] | - |

Table 5.2: *Material parameters and other data for the numerical simulations.*

The parameters chosen for numerical simulations are summarized in Table 5.2, together with bibliographic references. The forward reaction constant $k_f^* = 10.00\,\mathrm{s}^{-1}$ in (4.66) has been estimated for bacteria in [52]. The backward reaction rate parameter has been set to $k_b^* = 0.25\,\mathrm{s}^{-1}$, consistent with the *severing parameter r* in [52]. The rate of filament depolymerization in the *actin comet tail* is independent of the position in the tail and the bacterial speed. According to [8], filaments have a half-life in the order of $\tau = 30$ s. The G-actin diffusion coefficient in the cytoplasm $\mathbb{D}_{G_R} = 3.00\,\mu\mathrm{m}^2\mathrm{s}^{-1}$ has been reported in [50]. According to [51], the approximate length of the *actin comet tail* is $l \approx 10\,\mu$m, while the influence lengthscale of the signal is taken as a constant $\ell = 1.00\,\mu$m. Actin in monomeric form has a molar volume of $32.2\,\frac{\mathrm{l}}{\mathrm{mol}}$, according to [49]. The equilibrium temperature is assumed to be $\mathrm{T} = 310\,\mathrm{K}$ [54]. Following [19], the

Young's modulus of the *actin comet tail* ranges from $1 \div 10$ kPa. Elasticity measurements on the fibroblast actin cortex showed that the Poisson ratio is about 0.4 [19]. According to [51], the viscosity of the fluid component of cytoplasm is taken as $\nu = 0.03\,$poise.

While significant effort is invested in proposing appropriate values for model parameters in numerical results, the associated uncertainties are broad. Nevertheless, since the model is at a preliminary step, no uncertainties quantifications or sensitivities analyses have been done. These detailed investigations are deferred to a more mature phase of the model.

### 5.3.3 Governing equations and boundary conditions

With $\boldsymbol{F}^c$ defined as

$$\boldsymbol{F}^c = {J^c}^{\frac{1}{3}}\, \mathbb{1} \ , \tag{5.24}$$

the governing equations for the problem in hand read

$$\frac{\partial c_{G_R}}{\partial t} - \frac{\partial}{\partial \vec{X}} \left[ \mathbb{D}_{G_R} \frac{\partial c_{G_R}}{\partial \vec{X}} \right] + k_f \, c_{G_R} \, - \, k_b \, c_{F_R} \ = 0 \ , \tag{5.25a}$$

$$\begin{aligned} &\frac{\partial c_{F_R}}{\partial t} + \Omega_F \, \boldsymbol{M}_{F_R} \cdot \\ &\cdot \frac{\partial}{\partial \vec{X}^2} \left[ \frac{{J^c}^{-4/3}}{6} \left[ \frac{J^4}{4} (\frac{\lambda}{2} + G) + (\lambda + G) + \lambda \, J^2 \right] + {J^c}^{-2/3} (\frac{\lambda}{2} + \frac{G}{3})(\frac{J^2}{2} + 1) \right] + \\ &- \, k_f \, c_{G_R} \, + \, k_b \, c_{F_R} \ = 0 \ , \end{aligned} \tag{5.25b}$$

$$\frac{\partial}{\partial \vec{X}} \left[ J \, {J^c}^{-1} \left( (\frac{\lambda}{2} + G)(\frac{J^2}{J^{c-2/3}} - 1) + \lambda \, ({J^c}^{-2/3} - 1) \right) \right] - \frac{\nu}{\mathrm{G} + \frac{\lambda}{2}} \, \frac{\partial \vec{U}}{\partial t} = 0 \ , \tag{5.25c}$$

with $J^c$ from eq. (4.60).

To have a realistic representation of the actin comet tail, we propose a 2D model with a domain represented in figure 5.4. At the initial time $t = 0\,$s, we assume that: i) the displacements vanish throughout the stress-free body

$$\vec{U}(\vec{X}, 0) = 0 \ ; \tag{5.26}$$

ii) the G-actin concentration is uniform and no F-actin network exists

$$c_{G_R}(\vec{X}, 0) = c_{G_0} \ , \tag{5.27a}$$

$$c_{F_R}(\vec{X}, 0) = 0 \ \mu\mathrm{M} \ . \tag{5.27b}$$

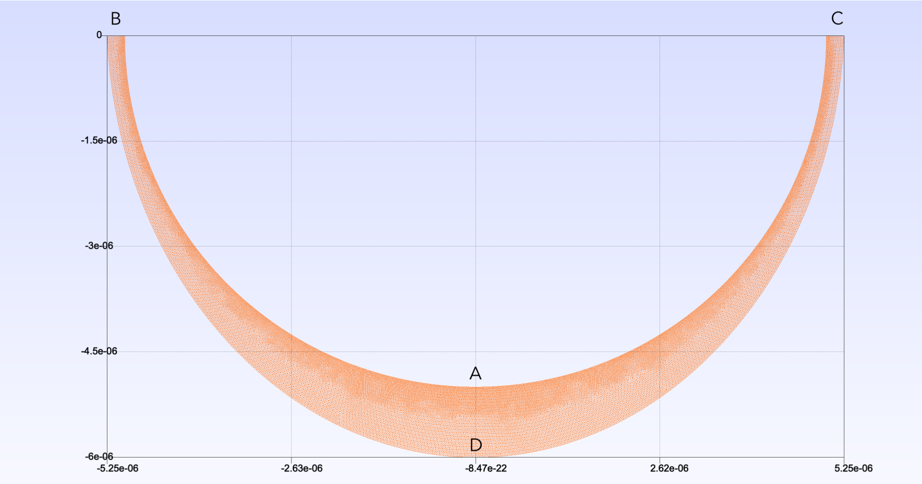

Figure 5.4: Tessellation of the 2D *actin comet tail* in the reference configuration. The tessellated area represents the area of the signal influence.

The boundary conditions for the *actin comet tail* are prescribed on its front, the curve $\widehat{BAC}$, and its back, the curve $\widehat{BDC}$. The concentration of G-actin is considered constant everywhere, in accordance with the initial condition

$$c_{G_R}(\vec{X},t) = c_{G_0} \qquad \forall t \in [\,0, t_{end}\,]\,, \tag{5.28}$$

and we consider a zero flux of the F-actin network across the curves $\widehat{BAC}$ and $\widehat{BDC}$

$$h_{F_R}(\widehat{BAC},t)\cdot n_R = 0 \qquad \forall t \in [\,0, t_{end}\,]\,, \tag{5.29a}$$

$$h_{F_R}(\widehat{BDC},t)\cdot n_R = 0 \qquad \forall t \in [\,0, t_{end}\,]\,. \tag{5.29b}$$

Since the *actin comet tail* is attached to the surface of the pathogens [18], the displacement of the *actin comet tail* on the curve $\widehat{BAC}$ is considered as null, whereas, on the curve $\widehat{BDC}$ the cytosol mechanical response is neglected, so

$$\vec{U}(\widehat{BAC},t) = \vec{0} \qquad \forall t \in [\,0, t_{end}\,]\,, \tag{5.30a}$$

$$\boldsymbol{P}(\widehat{BDC},t)\cdot \vec{n}_R = \vec{0} \qquad \forall t \in [\,0, t_{end}\,]\,. \tag{5.30b}$$

On the referential domain, a signal $C(\vec{X},t)$ is defined with a maximum value on the bacterium's vertical axis and a null value on its sides.

### 5.3.4 Numerical simulation

Numerical simulations have been obtained with an in-house code, based on the high-performance computing open library deal.ii. To this purpose, we used a semi-discrete Galerkin approximation method approximating the unknown fields with linear shape functions in space and nodal unknowns that depend solely on time [34] and tessellated the geometry using isoparametric finite elements. Proper time-advancing schemes and Newton-Raphson schemes have been set forth to solve the non-linear system of equations at each time step in a total Lagrangian framework. The time increment and the number of time steps are set to 0.05 $s$ and 7200, respectively.

### 5.3.5 Results and discussion

#### 5.3.5.1 Free expansion without disassembly

Measurements of F-actin growth in a differential AFM assay were performed in [5]. The Listeria nucleation promotion factor, ActA, was non specifically adsorbed onto one cantilever, initiating the formation of a branched actin network between the cantilever and a nearby surface. Network growth was monitored through epifluorescence imaging of labeled actin. Allowing the growing actin network to deflect the cantilever, a compressive state is induced in the F-actin network. The relationship between the F-actin growth velocity and the compressive forces was measured and reported in [5].

Before entering a stalled phase, the network length increases in a load-independent way. Although velocities ($85 \pm 68 \ \mathrm{nm\,min}^{-1}$) varied significantly among trials, it is logical to believe that their trend - as depicted in figure 1.6 - will remain unaltered at small loads, ideally at no loads whatsoever. Such a condition indeed occurs when the branched actin network is not yet in contact with the glass surface and it develops without mechanical opposition. In view of (5.23),

$$\mathrm{Grad}\,[\,\mu_F\,]|_{\mathbf{E}^e=\mathbf{0}} = 0 \,, \tag{5.31}$$

whence

- the flux $\vec{H}_F$ vanishes;
- the reference configuration is unaltered in time;
- the mass balance (4.45b) becomes an ordinary differential equation in time.

If $G$ monomers are replenished at infinite velocity in the current configuration, i.e., $c_G = c_G^0$, and disassembly is neglected, eq.(4.45b) simplifies as

$$\frac{\partial c_{F_R}}{\partial t} - \left(1 + c_{F_R}(\vec{X},t)\,\Omega_F\right)\,\mathcal{C}(\vec{x},t)\,k_f^*\,c_G^0 \;= 0\;. \tag{5.32}$$

Consider (5.32) and a *fixed* location $\vec{x}$ at which $\mathcal{C}(\vec{x},t) = 1$ at all times. It holds

$$\frac{\partial J\,c_F}{\partial t} - \,J\,k_f^*\,c_G^0 \;= 0\;. \tag{5.33}$$

Under free expansion conditions, $J = J^c$ and

$$\frac{\partial J}{\partial t} = \frac{\Omega_F\,J}{1 - \Omega_F c_F}\,\frac{\partial c_F}{\partial t}\;.$$

Eq. (5.33) thus becomes at a *fixed* location $\vec{x}$

$$\frac{\partial c_F}{\partial t} = \,k_f^*\,c_G^0\,(1 - \Omega_F c_F)\;. \tag{5.34}$$

At all places $\vec{x}$ in which $\mathcal{C}(\vec{x},t) = 1$ at all times, $c_F$ yields

$$c_F(\vec{x},t) = \frac{\exp\left[\,k_f^*\,c_G^0\,\Omega_F\,t\right] - 1}{\Omega_F}\;\exp\left[-\,k_f^*\,c_G^0\,\Omega_F\,t\right]\,. \tag{5.35}$$

The result is obtained by directly integrating the ordinary differential equation (5.34) with homogeneous initial conditions for $c_F(\vec{x},0) = 0$ at time $t = 0$ and at given location $\vec{x}$.

Figure 5.5 plots the concentration of F-actin network obtained by eq. (5.35) at different values of $\Omega_F$ and $k_f^*$. Accordingly,

- $c_F$ is limited and its asymptotic value is $c_\infty = 1/\Omega_F$. For example, for $k_f^* = 0.05$ and $\Omega_F = 0.125$, the asymptotic value $c_\infty$ is $8\,\frac{\mathrm{mol}}{\mathrm{m}^3}$;
- the higher $k_f^*\,c_G^0\,\Omega_F > 0$ the faster the convergence to such *equilibrium* condition, in the sense $\frac{\mathrm{d}c_F}{\mathrm{d}t} = 0$. For example, for $\Omega_F = 0.25$, $c_F$ converges to $c_\infty$ faster if $k_f^* = 0.5$ than $k_f^* = 0.05$ (see figure 5.5).

The limit concentration $c_\infty$ is the uniform concentration of F-actin in stress-free conditions. In view of (5.18), at all places $\vec{x}$ in which $\mathcal{C}(\vec{x},t) < 1$ the homeostatic concentration $c_\infty$ is an upper bound for $c_F$.

The referential concentration can easily be inferred from

$$c_{F_R}(\vec{X},t) = J^c\,c_F(\vec{x}(\vec{X},t),t)\,,$$

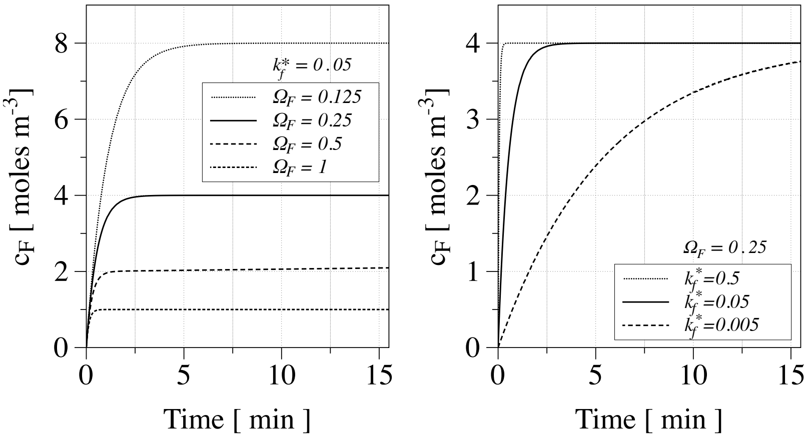

Figure 5.5: Transient evolution of $c_F$ in time, for different values of $\Omega_F$ and $k_f^*$, at $c_G^0 = 2.42$ moles m$^{-3}$. The concentration of F-actin network is limited, so for $k_f^* = 0.05$ and $\Omega_F = 0.125$, the asymptotic value is $8\,\frac{\text{mol}}{\text{m}^3}$; for $k_f^* = 0.05$ and $\Omega_F = 0.25$, the asymptotic value is $4\,\frac{\text{mol}}{\text{m}^3}$; for $k_f^* = 0.05$ and $\Omega_F = 0.5$, the asymptotic value is $2\,\frac{\text{mol}}{\text{m}^3}$; for $k_f^* = 0.05$ and $\Omega_F = 1$, the asymptotic value is $1\,\frac{\text{mol}}{\text{m}^3}$. The higher $k_f^*\, c_G^0\, \Omega_F$ is, the faster the convergence to the *equilibrium* condition is. For example, for $\Omega_F = 0.25$, $c_F$ converges faster if $k_f^*$ is higher. Figure from [25].

i.e.,

$$c_{F_R}(\vec{X}, t) = \frac{c_F}{1 - \Omega_F\, c_F} = \frac{\exp\left[\, k_f^*\, c_G^0\, \Omega_F\, t \,\right] - 1}{\Omega_F} \tag{5.36}$$

showing that $c_{F_R}$ is unbounded as $c_F \to c_\infty$. Furthermore, in view of (4.3) the hypothesis of free expansion implies

$$\mathbf{F} = \mathbb{1}\, \sqrt[3]{1 + c_{F_R}(\vec{X}, t)\, \Omega_F} \; = \exp\left[\, k_f^*\, c_G^0\, \Omega_F\, t\,/3 \,\right] \mathbb{1}\,, \tag{5.37}$$

and

$$x_i = X_i\, \exp\left[\, k_f^*\, c_G^0\, \Omega_F\, t\,/3 \,\right] \tag{5.38}$$

$$\frac{\mathrm{d}x_i}{\mathrm{d}t} = \frac{X_i}{3}\, k_f^*\, c_G^0\, \Omega_F\, \exp\left[\, k_f^*\, c_G^0\, \Omega_F\, t\,/3 \,\right] = \frac{x_i}{3}\, k_f^*\, c_G^0\, \Omega_F\,, \tag{5.39}$$

upon simple boundary conditions on displacements. Accordingly

- the $F$-network growth velocity is achieved at the length-scale $\ell > 0$, where it holds $v_F := \ell\, k_f^*\, c_G^0\, \Omega_F\,/3$;

- the pull-back of the length-scale $\ell$ in the reference configuration becomes smaller and smaller with time, for being

$$X_i|_\ell = \ell \, \exp\left[- k_f^* \, c_G^0 \, \Omega_F \, t \, / 3 \right] \tag{5.40}$$

eventually generating a boundary-layer problem, which may justify interface-based approaches as the ones in [58, 59].

#### 5.3.5.2 The influence of mechanics on the F-actin growth

Free expansion is an extremely rare event. In cellular motility, the cytoskeletal structure mechanically deforms to transmit forces to the extracellular matrix by means of focal adhesions. In bacteria motion, the viscous drag of the cytosol is a necessary constraint for the motility as well as a source of stress in the network [6], acting against external forces that resist the forward progress of the pathogen.

Mechanical stresses may foster a reorganization of actin filaments and their cross-linkers in the network, thus allowing $c_F(\vec{x}, t)$ to overcome the homeostatic limit $c_\infty$ even when the signaling function is below the unit, as per (5.18). This speculation is confirmed by numerical simulations, obtained upon the implementation of the weak form of the governing equations in a finite element code, via the high-performance computing open library deal.ii [61].

According to the findings in [62], the tail is firmly attached to the bacterium. A full restraint imposed at the bacteria surface to the $F$-network promotes the evolution of a stress field, as depicted in figure 5.6, which in turn affects the concentration $c_F$. Figure 5.6a shows that the formation of the comet tail agrees well with the images of actin polymerization in Listeria monocytogenes provided in [60, 19]. Figure 5.6b depicts actin concentration evolution in time at point A in the free expansion case and on the bacterium surface. As already explained, mechanical stresses allows $c_F(\vec{x}, t)$ to overcome the homeostatic limit $c_\infty$, which is $4 \frac{\mathrm{mol}}{\mathrm{m}^3}$ for $k_f^* = 0.05$ and $\Omega_F = 0.25$.

### 5.3.6 Concluding remarks

A chemo-transport-mechanics model for ABM has been formulated with a rigorous thermodynamic approach. The fundamental idea is to associate a volumetric increment to the organization of G-actin monomers into the F-network in the cytosol. Being aware that further improvements are necessary, we believe that our conceptual framework paves the way to *quantitative* investigations, which can help interpret biochemical experimental outcomes and address key challenges in cellular mechanobiology, such as tumor metastasis which, in view of their

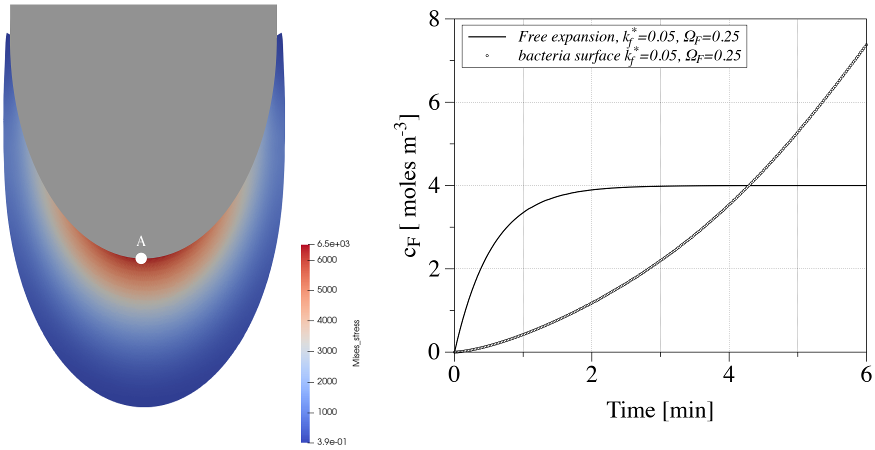

Figure 5.6: Simulation of the actin comet tail (colored) in Listeria monocytogenes (gray). a) Mises stress: the formation of the comet tail agrees well with the images of actin polymerization in Listeria monocytogenes provided in [60, 19]. b) Actin concentration evolution in time at point A in the free expansion case and on the bacterium surface. Mechanical stresses allows the F-actin network concentration to overcome the homeostatic limit $c_\infty$. Figure from [25].

timescale, can hardly be followed in vivo.

The model is characterized by several assumptions and limitations. We delay to further studies the multi-scale and multi-physics description of the energetics of the nucleation, polymerization, and branching of actin filaments into the F-network. All biological events have been condensed into a single signal, which entails the activity of the ActA protein at the nucleation loci. Since the distribution of filaments in the lamellum and in the *actin comet tail* does not show a preferential direction [63, 64], we have chosen the volume as the mechanical descriptor of swelling, with no account of anisotropy in the multiplicative decomposition of the deformation gradient.

Further developments, such as a careful investigation of the mechanobiology of the membrane resistance, are required to simulate the cellular motility [65], the cell-to-cell spread of bacteria via protrusion- and vesicle-mediated transfer, the life cycles of intracellular bacteria that exploit ABM [20].

The model welcomes any specification of the Helmholtz free energy. Since the focus of this note was the ABM engine, we arbitrarily and simplistically considered elastic strain energy of Saint-Venant kind in the numerical simulations. Viscosity was purposely neglected since it was argued that the cross-linking rearrangement in the $F$-actin network has insufficient time to develop [46]. We also neglected the dependence of material parameters on $F$-actin concentration, even if we are well aware that the mechanical behavior of the network changes during the network evolution [5]: devoted studies are required to capture the complex response of the network to external loads.

# Part II

# Cells ABM

# Chapter 6

# Cells biological background

This chapter presents the topic of cell ABM by first introducing the internal organization of cells and cell-ECM interaction. Then, an overview of cell migration is put in place and a specific case of keratocyte motility is provided. Some data on the Lamellipodia Actin Network are shown at the end of the chapter.

## 6.1 Internal organization of the cell

### 6.1.1 Membrane structure

Cell membranes are crucial for cell life [4]. The plasma membrane serves as a barrier, enclosing the cell, delineating its boundaries, and upholding crucial distinctions between the cytosol and the extracellular environment. Within eukaryotic cells, various membranes, such as those of the nucleus, endoplasmic reticulum, Golgi apparatus, mitochondria, and other membrane-bound organelles, maintain distinct differences between their contents and the cytosol. Specialized membrane proteins regulate ion gradients across membranes. These gradients, in turn, serve various functions: they aid in ATP synthesis, facilitate the transportation of specific solutes across the membrane, and in specialized cells like nerve and muscle cells, contribute to the generation and transmission of electrical signals. Moreover, the plasma membrane in all cells harbors proteins that act as receptors for external signals. These receptors function as sensors, enabling the cell to modify its behavior in response to environmental cues, including signals from neighboring cells. They facilitate the transmission of information across the membrane, rather than molecules, shaping the cell's responses.

The structure of biological membranes, despite their diverse functions, shares

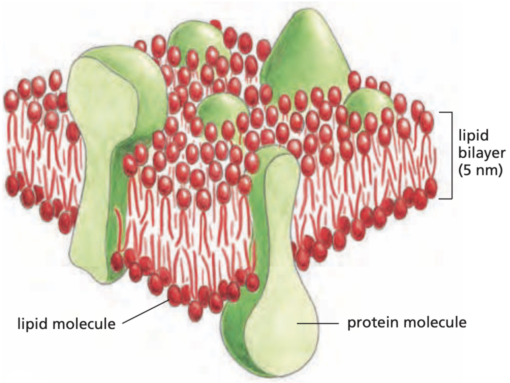

Figure 6.1: Lipid and protein constituents in a cell membrane [4]. Figure from [4].

a common overall organization: they comprise an ultra-thin layer composed of lipid and protein molecules predominantly fastened together by noncovalent interactions. These membranes are dynamic and fluid, allowing most of their molecules to move within the membrane plane. The lipid molecules are shaped as a continuous double layer with a thickness of 5 nm. This lipid bilayer provides the basic fluid structure and acts as a relatively impermeable barrier that prevents the passage of most water-soluble molecules (see figure 6.1) [4].

Many membrane proteins traverse this lipid bilayer and facilitate various functions of the membrane, including the transportation of specific molecules across it and membrane-associated reactions such as ATP synthesis. In the plasma membrane, certain transmembrane proteins act as structural connectors, linking the cytoskeleton through the lipid bilayer to either the extracellular matrix or an adjacent cell. In addition, others function as receptors to perceive and convert chemical signals from the cell's environment.

To function and interact properly with its environment, cells need all these kinds of membrane proteins. About 30% of the proteins encoded in an animal's genome are membrane proteins [4]. To better understand their function and role, in this section, we go deep into the knowledge of the structures and organizations of the two main constituents of membranes, the lipids and the proteins [4].

#### 6.1.1.1 The lipid bilayer

The lipid bilayer is the basic structure of all cell membranes [4]. Its two-layer structure is solely a result of the unique characteristics of the lipid molecules, which naturally come together to form bilayers, even under basic artificial conditions.

[4].

Around 1970, researchers first discovered that individual lipid molecules possess the capability to move freely within the lipid bilayer's plane. This revelation emerged from experiments involving synthetic (artificial) lipid bilayers, crafted as spherical vesicles known as liposomes, or in the form of planar bilayers formed across an aperture in a barrier between two aqueous compartments or on a solid surface [4].

These studies established that the lipid component of a biological membrane represents a two-dimensional liquid, enabling the constituent molecules to move laterally. Under typical circumstances, individual phospholipid molecules remain confined within their respective monolayers, posing a challenge to their synthesis. Phospholipid molecules are primarily synthesized in the cytosolic monolayer of the endoplasmic reticulum membrane. However, for the formation of new lipid bilayers, these newly synthesized molecules must promptly migrate to the noncytosolic monolayer. This migration hurdle is resolved through specialized membrane proteins known as phospholipid translocators or flippases. These proteins catalyze the swift flip-flop movement of phospholipids from one monolayer to the other [4].

Despite the fluidity of the lipid bilayer, liposomes do not spontaneously fuze when suspended in water. This lack of fusion is due to the binding of water molecules by the polar lipid head groups, which need to be displaced for the bilayers of the two different liposomes to merge. The hydration shell that maintains the separation of liposomes also serves to insulate the numerous internal membranes within eukaryotic cells, preventing uncontrolled fusion and thereby upholding the compartmental integrity of membrane-bound organelles. All instances of cell membrane fusion are orchestrated by tightly regulated fusion proteins, which bring suitable membranes into proximity, expelling the water layer that keeps the bilayers apart [4].

#### 6.1.1.2 Membrane proteins

While the lipid bilayer forms the fundamental structure of biological membranes, the membrane proteins primarily execute the specific functions of the membrane, thereby bestowing each type of cell membrane with distinctive functional properties. Accordingly, the amounts and types of proteins in the membrane are highly variable. In the myelin membrane, which primarily functions as electrical insulation for nerve cell axons, protein makes up less than 25% of the membrane mass. In contrast, membranes involved in ATP production, such as the internal membranes of mitochondria and chloroplasts, have approximately 75% protein content. A typical plasma membrane falls in between, with proteins constituting approximately half of its mass. However, due to the smaller size of lipid molecules compared to proteins, there are always many more lipid molecules than protein molecules in cell membrane, around 50 lipid molecules for each protein molecule in membranes that are 50% protein by mass. The structure and association of membrane proteins with the lipid bilayer vary widely, reflecting their diverse functions [4].

Communication among cells in multicellular organisms occurs primarily through extracellular signaling molecules. Some of these signaling molecules operate over long distances, transmitting signals to cells situated far away, whereas others specifically target nearby neighboring cells. In multicellular organisms, most cells both release and receive these signals. The reception of these signals depends on receptor proteins, typically on the cell surface, that interact with the respective signal molecules. This interaction activates the receptor, initiating one or more intracellular signaling pathways or systems within the cell. These signaling systems rely on intracellular signaling proteins, which process the received signal within the recipient cell and transmit it to the appropriate intracellular targets [4].

### 6.1.2 Cytoskeleton

For cells to operate properly, they must perform several functions. They have to manage and change their shape to grow, divide, and adapt to multiple circumstances. They must rearrange their internal components to be correctly shaped, robust, and internally structured. They must move from place to place, interacting mechanically with each other and with their environment. These spatial and mechanical functions depend on a remarkable system of filaments called the **cytoskeleton** [4].

The cytoskeleton's varied functions depend on the behavior of three families of proteins filaments, *actin filaments*, *microtubules*, and *intermediate filaments* (figure 6.2) [4]. Each type of filament has distinct mechanical properties, dynamics, and biological roles, but all three cytoskeletal filament systems share certain fundamental features [4] and must normally function collectively to give the cell its strength, its shape, and its ability to move.

The spatial organization and mechanical properties of cells are influenced by these three primary families of filaments. Actin filaments play a crucial role in shaping the cell surface, facilitating whole-cell movement, and driving cell division.

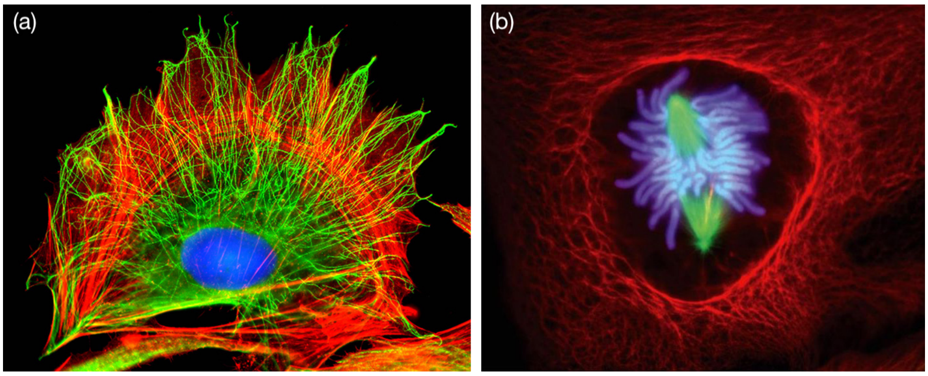

Figure 6.2: (a) A cell in culture has been fixed and labeled to show its cytoplasmic arrays of microtubules (green) and actin filaments (red) [4]. (b) This dividing cell has been labeled to show its spindle microtubules (green) and surrounding cage of intermediate filaments (red). DNA in both cells is labeled in blue [4]. Figure from [4].

Microtubules, on the other hand, determine the positions of membrane-enclosed organelles, oversee intracellular transport, and form the mitotic spindle responsible for segregating chromosomes during cell division. Intermediate filaments primarily contribute to the mechanical strength of the cell.

All of these cytoskeletal filaments interact with numerous accessory proteins that regulate and connect filaments to other cellular components and to each other. These accessory proteins play a critical role in the controlled assembly of cytoskeletal filaments in specific locations. Among these accessory proteins are the motor proteins, remarkable molecular machines capable of converting the energy derived from ATP hydrolysis into mechanical force. These motors can either move organelles along the filaments or act to move the filaments themselves (see figure 6.3).

#### 6.1.2.1 Actin filaments

The actin cytoskeleton is involved in a wide array of functions across various cell types. Actin filaments, which are described as semi-flexible, typically form dendritic or cross-linked structures. These filaments, which are semi-flexible polymers, experience bending due to thermal fluctuations, thereby offering increased resistance to forces that stretch the filament. Actin itself is known to be the most dynamically changing protein within the cytoskeleton, capable of substantial structural alterations over a period of minutes, a property that significantly impacts cell shape. In addition, actin plays multiple roles in cell

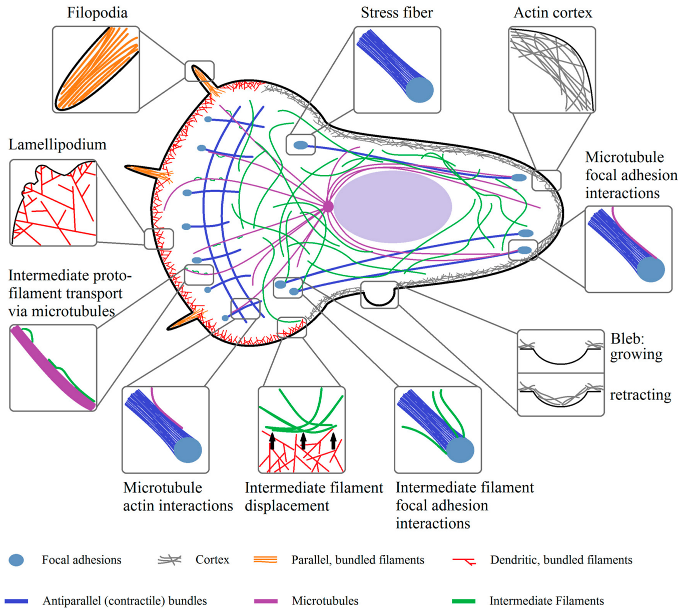

Figure 6.3: Organizational structures of actin, microtubules, and intermediate filaments inside of a cell [2]. Figure from [2].

motility: it contributes to the formation of protrusive structures in the direction of motion, such as filopodia, lamellipodia, and blebs, while also ensuring mechanical stability and contractility through stress fibers and the cell cortex [2].

**6.1.2.1.1 Lamellipodium** The lamellipodium, illustrated in figure 6.3, is a flat, sheet-like structure comprising a network of cross-linked actin filaments. Most of these filaments align within a plane parallel to the solid substrate. Lamellipodium plays a crucial role in cell movement, primarily forming through the polymerization of actin at the leading edge of the cell. Simultaneously, at the rear of the lamellipodium, ADF/cofilin aids actin depolymerization, replenishing the G-actin pool. This continuous process of (de-)polymerization across the network creates a treadmill effect and a retrograde flow of actin within the cell. This phenomenon is accentuated in certain cell types by myosin-induced depolymerization at the rear of the lamellipodium. Any flow generated by the contraction of the rear, facilitated by stress fibers, induces a flow in the opposite direction [2].

The forces produced by actin polymerization within the lamellipodium can reach values on the order of a few hundred piconewtons per micrometer. The crucial element in lamellipodium formation is the inherently inactive Arp2/3 complex, which is activated by the Scar/WAVE complex through a process initiated by the small Rho GTPase Rac1. The Arp2/3 complex nucleates a new actin filament at the site of existing filaments [2].

In a three-dimensional setting, N-WASP (in contrast to WAVE) triggers the activation of Arp2/3, and Rac1 is not prominently concentrated at the leading edge of the cell. The extension of actin is further eased by the presence of Ena/VASP family members gathering at the tip of the lamellipodium, encouraging additional actin elongation and hindering capping. Despite the active Arp2/3 complex, it is essential to have a capping protein to regulate the elongation of individual filaments. This ensures their effectiveness and prevents them from bundling with other uncapped filaments or collapsing under stress [2].

For the formation of a stable dendritic network, proteins such as cortactin cross-link the filaments. To prevent constant lamellipodium growth, a negative feedback loop is crucial. Arpin, a protein that inhibits Arp2/3 activity in the lamellipodium, possibly recruited by Rac1, could play a role in this feedback loop. Therefore, it is reasonable to suggest that the activation of Rac1 initiates the growth of lamellipodium by quickly recruiting Arp2/3 and promoting subsequent actin polymerization. Subsequently, it inhibits further growth through the recruitment of arpin. However, empirical evidence for this hypothesis is currently lacking, and a high turnover rate of arpin or a significantly higher concentration may be required to deactivate Arp2/3 [2].

Despite the influence of actin dynamics, the lamellipodium is also impacted by the cell membrane and its surface tension. Higher membrane surface tension results in more oriented actin filament polymerization, while lower tension leads to more protrusions, likely associated with the finite forces generated by the lamellipodium. Regarding the mechanical properties of the lamellipodium, it is worth noting the presence of myosin at the rear, explaining the lamellipodium's elasticity on short time scales and viscosity on long time scales [2].

Arp2/3 facilitates the connection of actin filaments in the lamellipodium, forming a dendritic structure. Intriguingly, an examination of cell speed in relation to actin orientation in the lamellipodium shows that faster cells tend to have filaments that are not precisely aligned toward movement. In contrast, slower movement is associated with parallel filament orientation [2].

**6.1.2.1.2 Lamellum** The lamellum is positioned behind the lamellipodium and is typically the widest structure in motile cells, often spanning 10-15 $\mu$m in width. Comprising primarily condensed linear actin bundles, the actin filament network within the lamella is notably more stable and less dynamic than that of the lamellipodia. In addition, the lamellum may possess resistance to compression. It is characterized by more robust and mature adhesion sites, and it also contains myosin II, a motor protein crucial for cell motility. The lamellum is a flat structure. This shape is attributed to the collaboration of the transverse arcs with the dorsal SFs. Dorsal SFs act as struts connecting the ventral adhesions with the dorsal contractile actin network. The contraction of transverse arcs generates tension on dorsal SFs, which causes them to pivot, thereby flattening the lamellum [66].

**6.1.2.1.3 Filopodium** Filopodia, a structure associated with cell motility, are present in neurons but do not seem to be essential for migration because rapidly moving corneal keratocytes lack filopodia in two dimensions. The forces generated by filopodia are considerably smaller than those produced by lamellipodium. However, in certain systems, such as three-dimensional environments, filopodia may play a role in cell migration [2].

Filopodia are characterized by parallel actin bundles with their positive ends pointing toward the cell membrane. This alignment is set in place by formins, such as FMNL2 and Ena/VASP, which can sustain extended actin polymerization. Certain forms, such as mDia2, can be triggered by the small GTPase Cdc42. Cdc42 also has the capacity to activate N-WASP and, in turn, Arp2/3, resulting in the formation of filopodia [2].

According to a widely accepted model, the initiation of filopodia involves actin polymerization in the presence of activated Arp2/3 and the absence of capping proteins. This process leads to the formation of actin bundles. However, Arp2/3 does not appear to be essential for filopodia initiation in adherent cells. An alternative model proposes that filopodia initiation occurs through clusters of activated forming in close proximity to the plasma membrane. These clusters nucleate and elongate actin filaments, contributing to the formation of filopodia. In both scenarios, the development of "mature" filopodia involves additional elongation facilitated by forming (such as mDia2) and Ena/VASP, alongside stabilization and bundling facilitated by cross-linkers like fascin [2].

In addition to their function in cell movement, filopodia play a crucial role in initiating cell-cell contacts, transmitting signals between cells, and responding to the mechanical characteristics of their environment. Interestingly, when filopodia retract toward the cell, myosins II, V, and VI do not play a role in this process. This implies that the dynamics of filopodia are solely governed by (de-)polymerization of actin and alterations in the cell cortex [2].

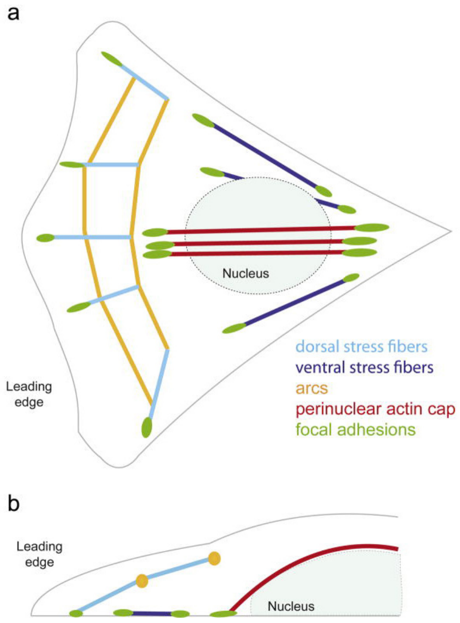

Figure 6.4: Different types of stress fiber in migrating cells. The illustration of these stress fibers in mobile cells is shown from both a top view (a) and a side view (b) [66]. Figure from [66]

**6.1.2.1.4 Stress fibers** Another category of actin-related structures is stress fibers (see figures 6.3 and 6.4), which are not found in either filopodia or the lamellipodium [2]. These actomyosin bundles are pronouncedly established in fibroblasts, endothelial cells, smooth muscle, and distinct cancer cell lines [67]. In non-motile cells, the stress fibers are rather thick and stable compared with highly motile cells, in which the stress fibers are less pronounced, deceased in numbers, thinner, and can more easily undergo dynamical remodeling [67].

Stress fibers are composed of bundles of anti-parallel actin filaments containing myosin II or parallel filaments (see figure 6.5). These fibers are made up of bundles consisting of 10-30 actin filaments interconnected by cross-linking proteins, such as $\alpha$-actinin, arranged bipolar. They form contractile actomyosin bundles that connect to focal adhesions. These adhesions serve as links through which the entire actin cytoskeleton connects to the extracellular matrix. In many animal cells, contractile stress fibers play a significant role in enhancing the cell's contractility [2].

In addition to actin and myosin, stress fibers contain actin-binding proteins and focal adhesion-associated proteins that bind and unbind rapidly. Various molecules, including cross-linkers like $\alpha$-actinin, are present within stress fibers.

This protein not only stabilizes the bundle but also interacts with kinases and signaling proteins, acting as a mediator in signaling processes. Stress fibers may also contain other cross-linkers like fascin, filamin, and paladin although their specific roles, especially beyond bundling, remain unclear. One hypothesis suggests that these proteins form a foundation for regulating cytoskeletal dynamics. For instance, paladin interacts with profilin and VASP, indicating a potential role in modulating cytoskeletal dynamics. Additional molecules, including those from the calponin, tropomyosin, caldesmon family, and others, are present in stress fibers and are suggested to participate in the regulation of the cytoskeleton and/or stress fibers [2, 67].

The formation of stress fibers is directly linked to the activation of the formin mDia1 and the small Rho GTPase RhoA, which in turn activates ROCK. Formin facilitates sustained actin polymerization of parallel filaments, which is essential for the formation of dorsal stress fibers. Conversely, ROCK activates LIM kinase (LIMK), inhibiting ADF/cofilin-induced filament severing. Furthermore, ROCK activates myosin, facilitating the formation of stress fibers. The coordinated actions of both ROCK and formin mechanisms are essential for developing contractile stress fibers. In contrast, two other Rho GTPases, Cdc42 and Rac1, play more indirect roles by inducing lamellipodial growth through Arp2/3 (Rac1) and promoting filopodia formation through the formin mDia2 (Cdc42). The collapse of both types of filaments can act as seeds for the formation of either transversal or ventral stress fibers [2, 67].

**6.1.2.1.4.1 Different stress fibers types** Stress fibers display considerable diversity in their morphology, interactions with focal adhesion proteins, and molecular characteristics. Consequently, they are classified into at least four distinct types: the perinuclear actin cap, transverse arcs/stress fibers, and dorsal and ventral stress fibers (see figure 6.4). Among these types are three classes of contractile stress fibers-ventral, transverse, and the perinuclear actin cap-identified by the presence of myosin II along the fibers [2].

Each of these contractile stress fiber types relies significantly on the presence and activity of myosin, and thus, on tension. Inhibiting myosin results in the disassembly of these stress fibers. The spacing of myosin II can undergo changes over time, underscoring that contractile stress fibers are dynamic structures with non-uniform mechanical properties. Measurements indicate that stress fibers display a stiffness of approximately 12 kPa. Disruption of myosin in stress fibers decreases the elastic modulus to 8 kPa, underscoring the vital role of myosin II in contractile stress fibers [2].

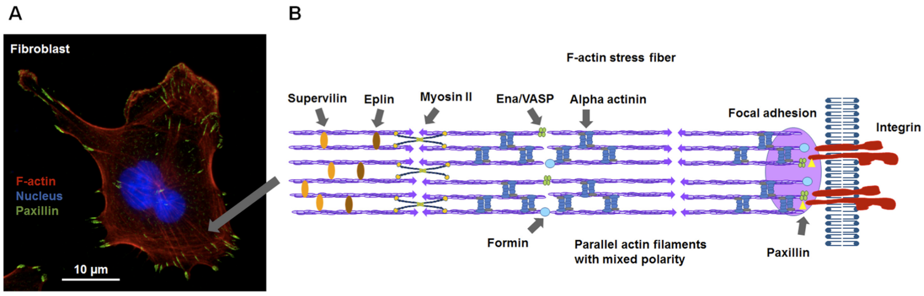

Figure 6.5: F-actin stress fibers [67]. Figure from [67].

**Dorsal stress fibers** Dorsal stress fibers, unlike other stress fiber types, typically lack myosin II and are anchored at their distal ends to focal adhesions. The absence of myosin directly results in the non-contractile nature of the dorsal stress fibers.

The precise organization of actin filaments in dorsal stress fibers is still elusive [67]. However, they display a structurally related so-called "graded polarity" of their bundles, as the distal ends consist of unipolar actin filaments with rapidly growing barbed ends facing the cell periphery, whereas the more proximal parts of the actin bundle consist of actin filaments with mixed polarity [67]: it is proposed that these fibers are composed of fast-growing (+)-ends oriented toward the cell periphery, while the more distant parts comprise actin filaments with mixed polarity. Additionally, it appears that both paladin and Rac1 play crucial roles in the formation of dorsal stress fibers. Paladin facilitates fiber assembly by recruiting VASP [2].

Functionally, dorsal stress fibers appear to serve as a platform and anchoring point for the assembly of other stress fiber types while also establishing a connection to focal adhesions. It is suggested that dorsal stress fibers are formed through actin polymerization at small adhesions developed behind the leading edge and are stabilized during the retraction phases of the lamellipodium by connecting to emerging transverse stress fibers. As the cell front extends away from the adhesion point, dorsal stress fibers elongate [2, 67].

**Trasversal stress fibers** Transverse arcs are curved bundles of actin filaments displaying a periodic alpha-actinin-myosin pattern, characteristic of contractile actomyosin bundles [67]. Positioned perpendicular to the ventral stress fibers, these structures depend on Arp2/3 for their formation and originate behind the lamellipodium. They arise from a combination of short myosin filaments and actin filaments generated at the leading edge by the Arp2/3 complex. These fibers form when the dendritic network collapses and is restructured by myosin

[67, 2].

Simulations exploring the ability of myosin to generate contractile structures suggest that the presence of both myosin and actin is sufficient to create energetically favorable anti-parallel/contractile bundles. Another source of both transverse fibers is the collapse of filopodia, which acts as a seed for stress fiber formation. Unlike arcs, which do not directly bind to focal adhesions, they transfer contractile force to the surrounding microenvironment through connections with dorsal stress fibers. A key characteristic of transverse arcs in migrating cells is their ability to flow from the cell's leading edge toward the cell's interior center, a phenomenon known as retrograde flow, which is believed to be facilitated by the continuous contraction of the arcs [67, 2].

**Trasversal stress fibers and Lamella: are there any differences between them?** In migrating cells, the lamella can be synonymous with the transverse arc network, as both structures (the lamella and the transverse arcs) contain condensed actin bundles and can undergo retrograde flow toward the cell's center [67]. Additionally, both the lamella and transverse arcs share similar protein compositions, such as tropomyosins, which are minimally present in the lamellipodium but are highly detectable in the lamella and transverse arcs. Furthermore, both the arcs and the lamella emerge through the condensation of actin filaments from the lamellipodium into arc-shaped actin bundles oriented parallel to the cell's edge.

**Ventral stress fibers** Ventral stress fibers are contractile actomyosin bundles oriented parallel to the direction of cell motion. They are connected to focal adhesions at both ends, making them a major component of the contractile machinery in many interphase cells [67]. Despite their prominence, transversal stress fibers can also contribute to overall contractility through their connection to dorsal stress fibers [2]. Typically situated at the posterior parts of the cell, ventral stress fibers, due to their location and orientation, play a role in rear contraction and are thus associated with cell motility [2]. Ventral stress fibers commonly develop from the fusion of each end of an arc with a dorsal stress fiber. The annealing of two dorsal stress fibers growing from opposite sides of a cell can also give rise to ventral stress fibers, both anchored at each end by focal adhesions [66].

**Purinuclear actin caps** The perinuclear cap represents a form of stress fibers positioned above the nucleus, which influences its shape. It is suggested to act as a mechanical link between the nucleus and the rest of the cell, potentially contributing to structural support and integrity. Identified as an actin-based assembly composed of fibers over the cell nucleus and connected to the nucleoskeleton, the perinuclear actin cap primarily regulates nuclear shape during cell migration [2].

Furthermore, perinuclear actomyosin fibers may serve as mechanotransducers that transmit forces from the cellular microenvironment to the cell nucleus. Certain stress-fiber-like structures are connected to the nuclear membrane through specific membrane proteins, stabilizing the precise position of the nucleus. Analogous to the connections between canonical stress fibers and the extracellular matrix via focal adhesions, a subset of stress fibers appears to be mechanically linked to nuclear membrane proteins, facilitating nuclear movement during overall cellular migration [67].

**6.1.2.1.5 Actin cortex and blebs** The actin cortex, a cytoplasmic structure bordering the plasma membrane, constitutes a contractile actin arrangement. This cortex is a few hundred nanometers thick and comprises a combination of filament bundles and cross-linked filaments. It features a mesh size of approximately 50-150 nm, a thickness ranging from 50 to 100 nm, and a distance to the cell membrane of less than 20 nm. While the meshwork of the cortex appears predominantly isotropic and aligned parallel to the plasma membrane, some filaments are also oriented perpendicular to the membrane [2, 67].

In addition to actin filaments, the cortex encompasses a diverse array of components, including cross-linkers (e.g., fascin, actinin, filamin), myosin, proteins that regulate actin turnover (profilin, cofilin), capping proteins, proteins from the ERM family (ezrin, radixin, moesin), nucleating factors (Arp2/3, formin mDia1), and signaling molecules such as RhoGTPases, RhoGEFs (guanine exchange factors), and RhoGAPs (GTPase activating proteins). Arp2/3 and mDia1 play crucial roles in the generation of cortical F-actin, with ERM proteins serving as connectors between the cortex and the membrane. They transmit the forces exerted on the membrane, thereby influencing cell shape [2, 67].

Depletion of cofilin-1 or capping proteins in HeLa cells leads to an augmented cortex thickness but diminished tension, indicating the involvement of actin-regulating proteins in cortical tension. The mechanical characteristics of the cortex dictate how cells undergo deformation in response to external forces. On timescales shorter than the demodulation time of the cortex, it demonstrates elastic behavior, showcasing a cell type-dependent elastic modulus ranging from a few hundred to thousands of pascals [2, 67].

Over extended timescales (>1 min), the cortex exhibits viscous behavior attributed to its adaptation to external forces through actin modulation, dissociation, and the (un-)binding of cross-linkers. If myosin is activated, the turnover times of the cortex can be further reduced, potentially involving direct disassembly or enhanced actin breakage [2].

The tension of the cortex, a critical property on both local and global scales, plays a pivotal role in regulating the cell shape of individual cells and tissues. Studies suggest that cortex tension is contingent on myosin activity and actin polymerization, where elevated myosin activity coupled with diminished actin polymerization results in heightened cortex tension levels. Conversely, lower cortex tension is associated with heightened cell protrusive activity, indirectly influencing cell motility [2, 67].

Localized decreases in cortex tension or cortex-membrane adhesion, and disruptions in the cortex, can result in blebs-distinct membrane protrusions initially lacking actin content. Blebs can form because of any form of cortex weakening or loss of cortex-membrane adhesion when a specific internal hydrostatic pressure threshold is exceeded. Although localized myosin contractions that promote cortex tearing or elevate local intracellular pressure are considered primary causes of blebbing, other mechanisms are also under discussion as potential contributors [2, 67].

The activation of myosin through ROCK or MLCK is sufficient to trigger bleb formation. The progression of a bleb can be characterized by three stages: initiation, growth, and retraction. In the initial phase, emerging blebs lack actin content, but as the bleb expands, the actin cortex reassembles at the plasma membrane. This reassembly arrests further bleb growth, ultimately leading to complete restoration, where the generated contractile forces eventually retract the bleb from the membrane [2].

It is crucial to note that bleb retraction is not always universal. In certain motile cells, blebs are stabilized and used as an alternative or supplementary method of migration. Actomyosin-induced pressure expands blebs for 5-30 seconds, causing cytosol to flow into the bleb and a simultaneous increase in surface area. This surface area increase is facilitated by the flow of lipids resulting from the tearing of the membrane from the actin cortex. The maximum size of a bleb is determined by the initial growth rate and the duration for the cortex to re-polymerize, both contingent upon cortex tension levels [2].

The notion that tension hinders bleb expansion is supported by the idea that the necessary membrane unfolding acts as a resistance to bleb growth, thereby slowing it down. Once fully matured, the cortex is reconstituted, and if the bleb lacks stabilization through adhesions, it is retracted by the re-established cortex through myosin-induced contraction [2].

#### 6.1.2.2 The microtubules

Microtubules, intricate structures composed of tubulin protein polymers, exhibit greater structural complexity than actin filaments. A microtubule is a hollow cylindrical assembly formed by 13 parallel protofilaments, each consisting of $\alpha$-tubulin and $\beta$-tubulin heterodimers stacked head to tail and folded into a tube. Despite their complexity, microtubules are dynamic and play diverse roles within the cell [4].

Microtubules act as essential tracks for cellular transport, contributing to spindle positioning during mitosis, cell migration, and the regulation of cell shape. Although most cell types may not directly engage in mechanical activities, there is a growing consensus that microtubules influence cell shape and migration by regulating the balance between RhoA and Rac1. Despite their relative stiffness compared with actin, microtubules can generate forces up to 3-4 pN during polymerization, allowing them to deform membranes and resist compressional forces. They function as load-bearing fibers in living cells, and their load-bearing capacity increases linearly with the number of microtubules per bundle. However, the load-bearing capacity of microtubules is limited, and compressional loads can induce catastrophe events, particularly at the cell edge [2].

Microtubules also contribute to force generation during the shrinkage phase. When the GTP cap is lost, microtubule protofilaments lose their lateral connection with neighboring protofilaments, forming ring-like shapes. If cargo remains attached during this process, a single microtubule can exert forces of up to 30-65 pN, surpassing the pushing force. Moreover, microtubules play a crucial role in the separation of chromosomes during cell division, where depolymerization generates the necessary forces to separate sister chromatids [2].

The relationship between microtubules and actin is intricate. While microtubules can locally regulate and be regulated by RhoGTPases and focal adhesions, certain molecules interact with both microtubules and actin. For example, APC (adenomatous polyposis coli) stabilizes microtubules and initiates actin filaments. Formin mDia1 supports actin nucleation, and mDia2, another formin, not only promotes actin nucleation but also stabilizes microtubules independently of its nucleation role. Cross-linkers like MACF1 and Arg connect actin and microtubule filaments, highlighting the intricate and coordinated interplay between the actin and microtubule cytoskeletons [2].

#### 6.1.2.3 Intermediate filaments

Intermediate filaments, the third major cytoskeletal type, are exclusive to certain metazoans like vertebrates, nematodes, and mollusks. They are notably absent in animals with rigid exoskeletons, such as arthropods and echinoderms, and are more prevalent in organisms subject to mechanical stress, contributing to the mechanical strength of tissues [4]. This suggests a role for intermediate filaments in providing structural support, particularly in animals with softer anatomy.

Intermediate filaments, organized by a diverse set of proteins encoded by at least 70 genes, form filaments with a diameter of 10 nm and are classified into five classes based on structure and sequence homology [2]. These filaments exhibit flexibility, characterized by a persistence length of less than 1 $\mu$m, and exhibit strain hardening with an increasing elastic modulus upon deformation. Their elastic properties significantly contribute to the overall viscoelastic response of cells, as observed in both measurements and simulations [2].

Despite their role as mechanical buffers and organelle anchors, intermediate filaments are dynamic components of the cytoskeleton with diverse functions in apoptosis, migration, and adhesion. They interact with other cytoskeletal elements, such as actin and microtubules, through a complex network. Post-translational modifications and the involvement of plakin proteins contribute to the regulation of intermediate filament assembly and function. Transport along actin or microtubule structures, facilitated by molecular motors like kinesin, dynein, or myosin, demonstrates the interdependence between intermediate filaments and other cytoskeletal components. The intricate interplay between intermediate filaments and the actin or microtubule cytoskeletons is evident in their mutual orientation and the influence of one on the transport dynamics of the other [2].

Intermediate filaments also interact with various cellular structures, including (hemi-)desmosomes and focal adhesions. These interactions, facilitated by proteins like plectin or integrins, contribute to the reinforcement of actin and focal adhesions. The connection between intermediate filaments and the nucleus through the LINC complex at the nuclear membrane is crucial for maintaining force transmission and nuclear positioning. Depletion or mutations in intermediate filament proteins, such as nestin, vimentin, and GFAP, impact nuclear dynamics, chromatin organization, and gene expression, highlighting their role as passive mechanotransducers in controlling cellular functions [2].

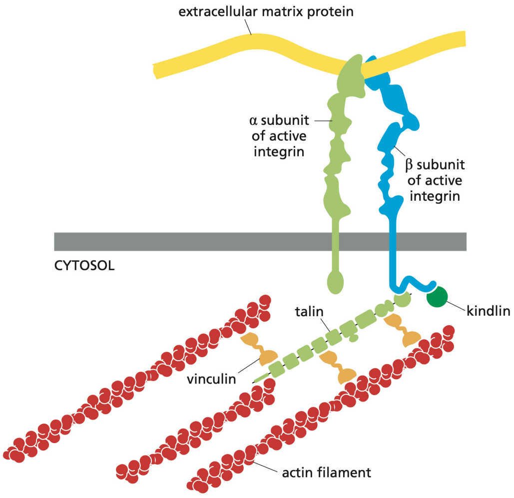

Figure 6.6: Active integrin molecule subunit structure, linking extracellular matrix to the actin cytoskeleton [4]. Figure from [4].

## 6.2 Cell and ECM interactions

The extracellular matrix (ECM) is a vital component of tissues and consists of an intricate network of macromolecules, including proteins and polysaccharides secreted and assembled around cells. Although the classes of macromolecules in the ECM are similar across various animal tissues, the different relative amounts and organization of these molecules create diverse materials with unique properties. For instance, the ECM can become rigid and calcified, as seen in bone or teeth, or form transparent structures such as the cornea. It also provides rope-like strength in tendons and comprises jelly-like substances in organisms such as jellyfish. Additionally, the ECM can create the rigid carapace found in beatles or lobsters [4].

The interplay between cells and the ECM is a crucial component of many biological processes. The ECM plays an active role in regulating the behavior of cells that come into contact with it, reside within it, or move through its structures. Its impact on cells extends across various cellular activities such as survival, development, migration, proliferation, morphology, and function. In return, cells possess the ability to produce, structure, and break down the ECM [4, 68].

The interplay between cells and the ECM is a crucial component of many biological processes. The ECM plays an active role in regulating the behavior of cells that come into contact with it, reside within it, or move through its

structures. Its impact on cells extends across various cellular activities such as survival, development, migration, proliferation, morphology, and function. In return, cells possess the ability to produce, structure, and break down the ECM [4, 68].

This bidirectional relationship is largely mediated by transmembrane cell adhesion proteins that act as receptors for the ECM. These receptors play a pivotal role in facilitating the connection between cells and the ECM, enabling a diverse array of cellular functions and behaviors [4, 68].

Receptor dynamic along cell membrane is a key factor in several biological phenomena, such as angiogenesis, tumor metastasis, endocytosis, and exocytosis. Angiogenesis is a multistep process in which cells are affected by several extracellular stimuli, including growth factors, extracellular matrix, and parenchymal and stromal cells. In this process, growth factor receptors as well as adhesion receptors convey the extracellular signaling in a coordinated intracellular pathway promoting cell proliferation, migration, and their reorganization in active vessels [69].

The ECM's effects on cells encompass not only structural support but also signaling and mechanical cues that modulate and direct cellular behavior in different physiological contexts. Similarly, cells actively contribute to the composition and organization of the ECM, resulting in a dynamic and reciprocal relationship between cells and their extracellular environment [4, 68].

The interaction between cells and the ECM is intricate and highly influential in cellular behavior. The proteins that serve as receptors for the ECM do not just mechanically link the matrix outside the cell to the cytoskeleton inside, but they also play an active role in determining a wide range of cellular functions. These matrix receptors, especially integrins, are essential in the interactions of epithelial cells with the basal lamina below them and in the interactions of connective-tissue cells with the matrix surrounding them [4, 68].

These receptors for the extracellular matrix vary in type and function. Essential among them are integrins, which are the main receptors on animal cells for binding to most ECM proteins (see figure 6.6). Integrins, similar to cadherins and other key components of the basal lamina, are crucial in the basic architecture of multicellular organisms. They belong to a substantial family of similar transmembrane adhesion molecules and possess a remarkable ability to relay signals in both directions across the plasma membrane. When a matrix component binds to an integrin, it can transmit a signal into the interior of the cell, and conditions within the cell can, in turn, influence the binding of the integrin to the matrix [4, 68].

Integrins are a family of cell adhesion receptors that support and modulate several cellular functions required for tumor metastasis. They can directly contribute to the control and progression of metastatic dissemination. During tumor development, changes in this family of receptors impact the ability of tumor cells to interact with their environment and enable metastatic cells to convert to a migratory and invasive phenotype. Integrins regulate each step of metastasis and affect tumor cell survival and interaction with changing environments during transit from the primary tumor to distant target organs [70].

Receptor-mediated endocytosis is a process by which cells absorb metabolites, hormones, proteins - and, in some cases, viruses - by the inward budding of the plasma membrane (invagination). This process forms vesicles containing the absorbed substances and is strictly mediated by receptors on the surface of the cell [71].

This bidirectional signaling enables the integrins to convey information from the external environment to the cell interior and vice versa and allows the cell to dynamically respond and adapt to changes in its surroundings. This communication facilitates the regulation of diverse cellular processes based on the cues received from the extracellular matrix [4, 68].

Integrins directly participate in binding to ECM ligands, such as RGD ligands. They establish connections with the cytoskeletal scaffold through various intermediary adaptor proteins, creating multiple points for the regulation and control of integrin adhesion. Different micrometer-scale multi-protein complexes facilitating cell-ECM adhesion are acknowledged, usually establishing links between integrins bound to the ECM and the actin cytoskeleton or intermediate filaments. These connections encompass unique configurations of various adaptor and signaling proteins [68].

Applied tension to an integrin can tighten its grip on both intracellular and extracellular structures. Conversely, the loss of tension can loosen its hold, causing molecular signaling complexes to disassemble on either side of the membrane. In this manner, integrins play a dual role: not only transmitting mechanical and molecular signals and converting one type of signal into the other. Integrins, among other transmembrane cell adhesion proteins, play a role that extends beyond simple attachment. These proteins can also activate intracellular signaling pathways, thereby regulating various aspects of a cell's behavior according to the nature of the surrounding extracellular matrix and the state of the cell's attachments to it [4].

For many types of cells, growth or proliferation does not occur in culture unless they are firmly attached to the extracellular matrix. Even with nutrients and soluble growth factors available in the culture medium, certain cells, such as epithelial, endothelial, and muscle cells, require attachment for their survival. Loss of contact with the extracellular matrix leads these cells to undergo a self-destructive process called apoptosis [4, 68].

This dependence of cell growth, proliferation, and survival on attachment to a substratum is known as "anchorage dependence". Integrins, along with the intracellular signals that they generate, play a pivotal role in this anchorage dependence. Disruptions or mutations that override this control mechanism, allowing cells to detach or escape from anchorage dependence, are observed in cancer cells and contribute significantly to their invasive behavior. This is one of the critical ways in which cancer cells deviate from the normal constraints of cellular behavior and is a significant factor in their ability to spread and invade surrounding tissues [4, 68].

### 6.2.1 Integrins

Integrins, despite their numerous variations, adhere to a common structural blueprint. Each integrin molecule consists of two glycoprotein subunits, known as $\alpha$ and $\beta$, which are non-covalently associated. These subunits traverse the cell membrane and feature short intracellular C-terminal tails and extensive N-terminal extracellular domains. Extracellular domains specifically bind to amino acid sequences in extracellular matrix proteins or, in certain cases, on the surfaces of other cells [4].

In humans, there are 24 types of integrins, resulting from the combination of products from 8 different $\beta$-chain genes and 18 different $\alpha$-chain genes. Integrin dimers, formed by these combinations, exhibit diverse properties and functions. The same integrin molecule in various cell types can display distinct ligand-binding specificities, suggesting the influence of additional cell-specific factors in modulating integrin activities [4].

The intracellular region of integrin dimers forms a connection with the cytoskeleton by binding to a complex of various proteins. In most human integrins, this linkage is established with actin filaments and involves proteins assembling at the short cytoplasmic tails of the integrin subunits. Talin, an abundant adaptor protein, is often involved in this linkage, although several other proteins also contribute. Similar to cadherin-mediated cell-cell junctions, the cell-matrix junctions formed by integrins exhibit variability in size, appearance, and duration. These junctions can range from small, transient structures to large, enduring complexes [4].

Focal adhesions, for example, represent larger and more prominent cell-matrix junctions. They form when fibroblasts establish robust attachments to a rigid surface. Myotendinous junctions are another example, linking muscle cells to tendons and facilitating the transfer of force between these tissues for efficient functioning [4].

#### 6.2.1.1 Active and an inactive integrin

The dynamic nature of cell migration and the interactions between cells and their extracellular environment, particularly the extracellular matrix, rely on the intricate and timely modulation of attachments. Cells like fibroblasts, macrophages, or epithelial cells must rapidly regulate their connections with the extracellular matrix to migrate effectively [4].

Integrin molecules, as key mediators of these attachments, cannot function as rigid, unchangeable structures. Instead, they need the capacity to switch between active and inactive states. In their active state, integrins readily engage in connections, facilitating attachment and migration. Conversely, in their inactive state, they refrain from binding. This ability to dynamically control their activity is crucial for cells to efficiently and precisely regulate their interactions with the extracellular matrix while navigating through various tissues and locations [68, 4].

Structural studies using techniques such as electron microscopy and X-ray crystallography have revealed that integrins have multiple structural conformations, reflecting different states of activity. Integrins exhibit distinct shapes depending on their activity level. In the inactive state, the external segments of the integrin dimer are tightly folded into a compact structure. In this conformation, the cytoplasmic tails of the dimer are hooked together, restricting their interaction with cytoskeletal adaptor proteins [4].

In contrast, in the active state, the integrin subunits become disengaged at the membrane, exposing the intracellular binding sites for cytoplasmic adaptor proteins. At the same time, the external domains of the integrin unfold and extend, resembling a pair of legs. This extension exposes a high-affinity binding site for matrix proteins at the subunit tips. The transition from an inactive to an active state entails a significant conformational change that reveals both the external and internal ligand-binding sites at the ends of the integrin molecule. This structural transformation effectively links external matrix binding with internal cytoskeleton linkages [68, 4].

Switching between inactive and active states is regulated by various mechanisms depending on the cell's needs. Activation can occur through an "outside-in" mechanism, in which the binding of an external matrix protein, such as the RGD sequence of fibronectin, induces certain integrins to transition from the low-affinity inactive state to the high-affinity active state. The process can also operate in reverse, working from inside to outside. This "inside-out" integrin activation typically relies on intracellular regulatory signals that enhance the ability of talin and other proteins to interact with the $\beta$ chain of the integrin. Talin competes with the integrin $\alpha$ chain for its binding site on the tail of the $\beta$ chain. Consequently, when talin binds to the $\beta$ chain, it obstructs the intracellular $\alpha$-$\beta$ linkage, enabling the two legs of the integrin molecule to separate [68, 4].

#### 6.2.1.2 Integrins cluster

Integrins, similar to other cell adhesion molecules, distinguish themselves from cell-surface receptors for hormones and other extracellular soluble signal molecules by typically binding their ligands with lower affinity. Upon activation, integrins cluster together, forming a dense plaque in which numerous integrin molecules anchor to cytoskeletal filaments. This resulting protein structure can be remarkably large and complex, as exemplified by the focal adhesion created by a fibroblast on a fibronectin-coated surface culture dish [4].

The formation of mature cell-matrix junctional complexes relies on the recruitment of numerous scaffolding and signaling proteins. While talin is a major component of many cell-matrix complexes, several other proteins make significant contributions. Integrin-linked kinase (ILK) and its binding partnerspinch and parvin, which form a trimeric complex, serve as an organizing hub at many junctions. Actin-binding proteins such as vinculin, zyxin, VASP, and $\alpha$-actinin promote the assembly and organization of actin filaments in cell-matrix junctions. Focal adhesion kinase (FAK) is another integral element in numerous cell-matrix junctions. It interacts with multiple components within these junctions and plays a pivotal role in cellular signaling processes [4].

Integrin adhesion complexes (IACs) can be categorized on the basis of various criteria such as their size, composition, organization, lifetime, localization, and function. In certain instances, differences among these categories may represent distinct steps in the maturation process, whereas in others, they may denote more specialized or cell type-specific structures. This is a list of different types of adhesions:

- *Nascent adhesions*: these are the initial adhesion structures that become noticeable during lamellipodial extension. They form at the cell edge, containing approximately 50 integrins and having a diameter of less than $0.5, \mu$m. In addition to integrin, these structures are enriched with kindlin, talin, focal adhesion kinase (FaK), paxillin, and $\alpha$-actinin. Nascent adhesions are transient, with the possibility of either disassembling or maturing into larger focal complexes;

- *Filopodia-tip adhesions*: these are small Integrin Adhesion Complexes (IACs) consisting of a distinctive subset of adhesome proteins. They are enriched in myosin X and differ from other adhesions. When stabilized, filopodia-tip adhesions have the potential to develop into nascent adhesions and further mature into focal adhesions (FAs);
- *Focal complexes*: these are small (less than $1\mu$m) dot-like adhesions that form at the transition zone between the lamellum and lamellipodium. These structures contain core Integrin Adhesion Complex (IAC) components, link to the actin cytoskeleton, and strengthen in response to forces.
- *Fas*: these are the most extensively studied and well-characterized adhesions. Focal Adhesions form as focal complexes mature in response to increased forces applied from actomyosin contractility or external forces. The recruitment of additional Integrin Adhesion Complex (IAC) proteins in response to force enhances the association between integrin and actin, leading to the assembly of ordered elongated structures with sizes of approximately $2-5\mu$m.
- *Fibrillar adhesions*: these can result from further maturation of Focal Adhesions (FAs) in certain cell types, such as fibroblasts. Fibrillar adhesions are characterized by long, thin, or beaded structures located centrally. They vary in length (approximately $1-10\mu$m) and are distinguished by the enrichment of the ECM protein fibronectin, its receptor $\alpha5\beta1$ integrin, and the cytoplasmic actin-binding protein tensin. Integrins in fibrillar adhesions play a role in mediating fibronectin fibrillogenesis, contributing to ECM remodeling [68].

The maturation of integrin adhesion complexes (IACs) is significantly influenced by various factors such as cell type, the contractility of the cell, and the composition and stiffness of the ECM substrate. The formation of adhesions is typically followed by their disassembly, which can be driven by several processes. These include local inhibition of the contractility that is usually responsible for driving adhesion IAC maturation, localized proteolysis of ECM components that integrins bind to, and local endocytosis of integrins present on the cell surface [4, 68].

Microtubule targeting of IACs can drive these processes, thereby initiating adhesion turnover. Remodeling of adhesions allows the cell to sense and respond to alterations in the local extracellular mechanical environment. For instance, cells can adjust their migration speed or direction in response to changes in ECM organization. Moreover, part of the cellular response involves feedback regulation of adhesion dynamics, enabling the cell to adapt flexibly to changes in its environment [68].

### 6.2.2 Cell-matrix adhesions mechanosensitivity

The ability of cell-matrix junctions to detect and respond to mechanical forces is crucial for various cellular functions. When cells adhere to a stiff matrix that resists pulling forces, cell-matrix junctions can sense the increased tension. In response, these junctions recruit additional integrins and associated proteins, reinforcing their structure to withstand elevated tension. Conversely, when cells attach to a less rigid matrix, reduced tension leads to a less robust cellular response. This mechanosensing mechanism allows cells to adapt to the varying stiffness of extracellular matrices in different tissues [4, 68].

Talin, a key player in cell-matrix junctions, exemplifies how mechanical force influences protein structure and function. The C-terminal tail domain of talin contains binding sites for vinculin, an actin-regulatory protein. These binding sites are initially hidden within folded protein domains but become exposed when the protein is stretched. As actin filaments are pulled by myosin motors, generating tension, the talin rod is stretched, exposing vinculin-binding sites. Vinculin molecules recruited in this process organize additional actin filaments, reinforcing the junction and increasing its strength [4, 68].

Mechanical force plays a central role in influencing the dynamics of integrin adhesion complexes (IACs). Cellular forces generated by actin polymerization and myosin II contractility are transmitted to integrins through key adaptor proteins within IACs. Traction force, transmitted through integrins to the extracellular matrix (ECM), drives various cellular processes, including cell shape changes, migration, rigidity sensing, and ECM remodeling [4, 68].

The mechanosensitivity of Integrin Adhesion Complexes (IACs) is an intricate process that involves various aspects of their structure, function, and regulation. This encompasses variations in IAC lifetime during adhesion formation, maturation, remodeling, and turnover. Alterations in the movement and interactions of individual integrin-associated complex (IAC) molecules take place in response to the recruitment of new binding partners, post-translational modifications, changes in the membrane environment, and mechanical deformations. The interplay of molecular dynamics, conformational changes, transient force-regulated protein interactions, and intracellular transport collectively contribute to the mechanosensitivity of IACs [4, 68].

#### 6.2.2.1 Single-molecule dynamics within adhesions

Single-molecule tracking studies have provided valuable insights into the dynamics of integrins within Integrin Adhesion Complexes (IACs). Contrary to expectations, these studies reveal that both immobilized integrins are present outside IACs, and diffusive integrins can be found inside IACs, highlighting the heterogeneity in the behavior of integrins [68].

Longer timescale single-molecule tracking further demonstrates that integrins exhibit repeated entry and exit from Focal Adhesions (FAs). They undergo transient arrests mediated by both the ECM and cytoskeleton, both inside and outside FAs. Notably, integrins are arrested approximately 80% of the time within adhesions, compared to around 50% of the time outside adhesions. This indicates that the dynamics of integrins within IACs significantly differ from those outside, emphasizing the unique behavior of integrins within the context of adhesion complexes [68].

The exploration of single-molecule probes for signaling molecules, such as Src, represents a promising advancement in connecting nanoscale dynamics within IACs to broader cellular functions. This innovative approach to single-molecule investigation is expected to provide crucial insights into the behavior of signaling molecules within IACs and their impact on cellular functions at a larger scale [68].

#### 6.2.2.2 Temporal responses of adhesions to applied forces.

Experiments involving the acute application of external force provide valuable insights into how the Integrin Adhesome Complex (IAC) dynamics respond to mechanical stimuli. While extended periods of mechanical factors lead to the orchestrated adjustment of IAC assembly and disassembly, resulting in cytoskeletal reorganization and changes in cell shape and migration paths, short timescales reveal rapid strengthening of cell-ECM adhesion with sub-second response times [68].

Single-cell force spectroscopy has demonstrated that at shorter timescales, cell-ECM adhesion can be rapidly strengthened. This rapid response, occurring within seconds, involves a subset of IAC components such as integrin, talin, kindlin, FAK, Src, Arp2/3, and mDia1 formin. The exact mechanisms and structures involved in this rapid response, which occurs faster than visible IAC maturation, are not fully understood. It has been suggested that pre-existing IAC structures, potentially corresponding to immobilized integrins outside IACs, play a role in these rapid responses [68].

The introduction of a substrate stretching platform compatible with super-resolution microscopy (SRM) has offered insights into the intricate responses of cells to acute force application. This includes the displacement of the actin cytoskeleton and the elastic deformation of proteins in Focal Adhesions (FAs). Notably, the extent of actin cytoskeleton displacement exceeds the deformation of the substrate, and this overcompensated actin motion is shown to be dependent on myosin II. However, the specific functional roles and underlying mechanisms are not fully understood [68].

## 6.3 Cell migration

A critical property of cells is their capacity to move, particularly notable in scenarios such as immune cells pursuing pathogens, wound closure, or the metastasis of tumor cells [2, 46].

Cell crawling, a fundamental behavior across various organisms and cell types, facilitates movement over surfaces. Predatory amoebae use this mode of locomotion to continuously search for and consume food, often preying on smaller organisms like ciliates and flagellates. In animals, most cell movement happens through crawling, except for sperm, which swims. During embryonic development, cell migration is pivotal in shaping the body's structure. For instance, neural crest cells in vertebrates migrate long distances within the embryo, playing a vital role in creating various tissues and organs [2].

Crawling is essential for constructing the nervous system. Actin-rich growth cones guide developing axons toward their eventual synaptic targets, guided by various signaling cues. In adult organisms, various cell types exhibit crawling behavior: macrophages and neutrophils crawl to sites of infection to eliminate foreign agents, osteoclasts tunnel into the bone for its continuous remodeling and renewal, fibroblasts move through connective tissues to aid in repair, and intestinal epithelial cells migrate up the sides of intestinal villi to replace lost absorptive cells [2].

Unfortunately, this cellular movement is also linked to the progression of

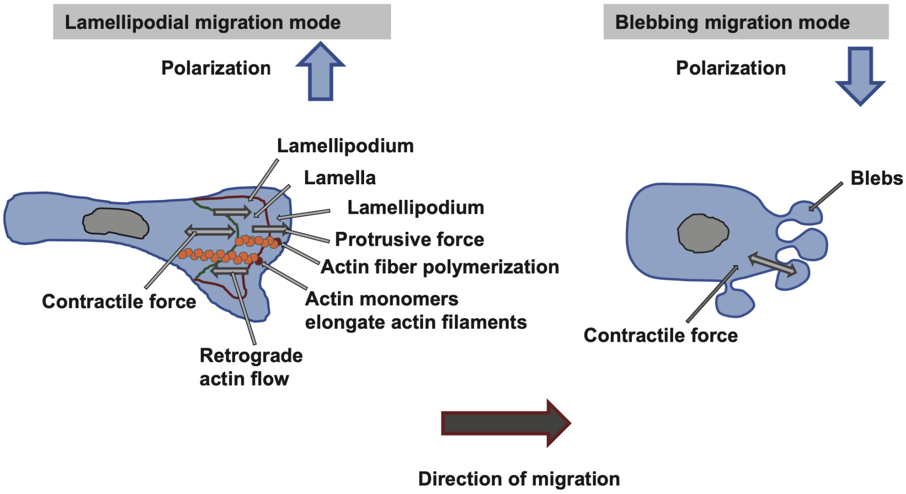

Figure 6.7: Modes of migration in 3D [67]. Figure from [67].

cancer. Cells from a primary tumor often invade neighboring tissues, travel through blood vessels or lymph vessels, and establish secondary tumors in different parts of the body in a process known as metastasis [2].

### 6.3.1 Cell migration phases

A motile cell's net movement is orchestrated by a multitude of interdependent processes, primarily actin-dependent. These processes involve

- *protrusion*: formation of protrusions in the direction of motion, in which the plasma membrane is pushed out at the front of the cell;
- *attachment*: subsequent adhesion to the substrate, in which the actin cytoskeleton connects across the plasma membrane to the substratum;
- *traction*: loss of adhesion on the rear of the cell, followed by rear-contraction, in which the bulk of the trailing cytoplasm is drawn forward [67].

Coordination of cellular events is crucial for effective cell migration. The intricate timing and synchronization of these processes determine the efficiency and directionality of cell movement. As mentioned, if the cell fails to complete the maturation of adhesions at the leading edge, an increase in contractile forces may result in the premature rupture of these nascent adhesions. This untimely detachment can hinder productive cell movement, ultimately leading to the loss of directionality or efficiency in migration. Coordination in the spatiotemporal regulation of these processes is vital to ensure successful and directed cell migration.

Cells have evolved two distinct modes of migration to achieve productive movement and appropriately time migration steps, the amoeboid and mesenchymal types (see figure 6.7) [2]

- *Amoeboid cell migration*: it is typical for rounded cells with low adhesion and high Rho-driven contractility. It involves the protrusion of structures known as blebs, which regulate cell movement independently of filopodia and lamellipodium.
- *Mesenchymal cell migration*: it is characterized by strong adhesion and Rac1-induced protrusions, reflecting the mutual negative regulation of Rac1 and RhoA [2]. It is governed by subcellular structures such as filopodia and the lamellipodium, while stress fibers and cortex ensure mechanical stability and contractility [67]. In some cells, like fish epidermal keratocytes, these activities occur simultaneously, leading to smooth forward gliding without significant changes in shape. In contrast, in other cells like fibroblasts, these activities are more independent, resulting in jerky and irregular locomotion [67].

#### 6.3.1.1 Protrusion

In mesenchymal motion, the initial step in locomotion involves the protrusion of a leading edge, often driven by forces generated through actin polymerization pushing the plasma membrane outward. Various cell types generate different types of protrusive structures, notably filopodia (also known as microspikes) and lamellipodia. The distinction between these structures lies primarily in the organization of actin facilitated by actin-cross-linking proteins (see section 6.1.2.1) [4].

The lamellipodium, found in epithelial cells, fibroblasts, and certain neurons, stands out as a primary force-generating cell structure, capable of producing pushing forces of up to 35 nN, as observed in extreme cases such as fish keratocytes. To generate these forces, actin undergoes local polymerization at the cell front facilitated by Arp2/3 and depolymerization at the back of the lamellipodium through ADF/cofilin activity (see figures 6.8 and 6.9). Interestingly, forming such as FMNL2 or FMNL3 appear to contribute to lamellipodial extension independently of Arp2/3 complex incorporation and, in certain cell types, act as primary sources of lamellipodial protrusion forces. The protein Arpin inhibits the activity of Arp2/3, introducing pause phases in lamellipodial extensions and

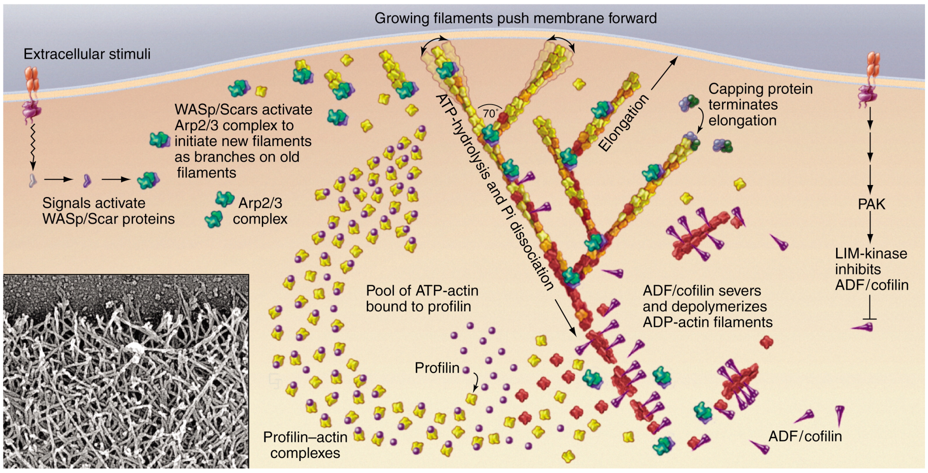

Figure 6.8: A model for actin filament assembly and disassembly at the leading edge [72]. Figure from [72].

leading to less directed motion. The continuous (de-)polymerization of actin creates a treadmilling effect, generating forces and a retrograde flow of actin [2].

Stress fiber contraction creates a flow that moves actin toward the cell front, going in the opposite direction of the retrograde flow. To secure the lamellipodium and avoid retraction caused by actin cortex tension, it is essential to establish new contacts between the cell and the extracellular matrix (ECM). Broadly, as the lamellipodium extends, new adhesions emerge, potentially developing into focal adhesions or breaking apart. Rac1 oversees the creation of these nascent adhesions, while RhoA and myosin II-induced contractility dictate their maturation. These sites serve as anchors for stress fibers, generating tension and influencing the composition of focal adhesions. The precise mechanism of actin nucleation in focal adhesions remains only partially elucidated, with formins like FHOD1 or mDia1 considered to be involved. Conversely, the genesis of nascent adhesions is believed to rely on Arp2/3 activity in the lamellipodium, attributed to its interaction with vinculin and focal adhesion kinases (FAK). Despite this, the lamellipodium is not indispensable for migration. Certain cell types, such as fibroblasts and melanoblasts, can move without the involvement of Rac and Arp2/3, although the speed of migration is notably slower [2].

Without the lamellipodium, these cells use filopodia or other pseudopods, which are likely dependent on formins, for migration. Filopodia, observed in the migrating growth cones of neurons and certain fibroblasts, are essentially one-dimensional in structure. Filopodia comprise a core of extended, bundled actin filaments, resembling those found in microvilli but characterized by being

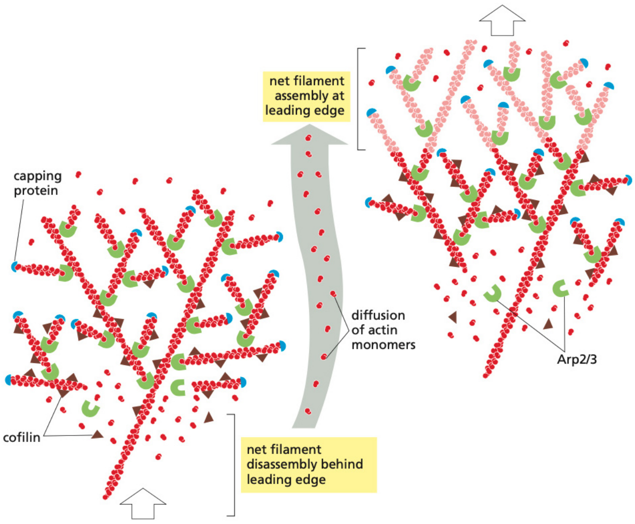

Figure 6.9: The model illustrates the protrusion of the actin meshwork at the leading edge, depicting two distinct time points during the progression of the lamellipodium [4]. Figure from [4].

longer, thinner, and more dynamic. To facilitate effective movement, it is crucial to confine actin polymerization to a specific zone. Hence, we assume that Rac1 is active only in specific local areas. The activation of Rac1 in these locales is thought to occur through Cdc42-induced pathways and microtubule capture at the leading edge, leading to localized RacGEF activation and vesicle supply. Alternatively, another mechanism might involve the Rho/ROCK pathway and actomyosin contractility, which hinders lamellipodium formation across multiple cell regions. This concept is supported by the observation of either multiple or larger lamellipodia following the inhibition of Rho or ROCK activity. This underscores the importance of maintaining a delicately balanced dynamic equilibrium between contractile and expansive forces. While RhoA/ROCK is active at the cell front, excessive activity hampers lamellipodium-based migration by inducing the retraction of the lamellipodium [2, 4].

Invadopodia and their counterparts, podosomes, constitute a distinct category of actin-rich protrusions. These structures project in three dimensions and play a pivotal role in facilitating cell penetration through tissue barriers, particularly evident when metastatic cancer cells invade the surrounding tissue. Invadopodia share numerous actin-regulatory components with filopodia and lamellipodia, and they are also implicated in extracellular matrix degradation. The degradation process involves the transport of vesicles containing proteases responsible for breaking down the matrix [4].

The second model of cell migration, termed blebbing, is evident in diverse cell types such as amoebae, tumor cells, neutrophils, and primordial germ cells. This migration mode is commonly observed in cells with minimal or weak adhesion, those navigating through a three-dimensional matrix, or in constrained environments. Additionally, it occurs when cells are cultured on a flexible extracellular matrix substratum. Blebs emerge when the plasma membrane locally separates from the underlying actin cortex, enabling cytoplasmic flow to exert pressure on the membrane, causing it to protrude outward and extend. The formation of blebs is contingent on the hydrostatic pressure within the cell, generated by the contraction of actin and myosin assemblies. After the extension of blebs, actin filaments reassemble on the bleb membrane, giving rise to a new actin cortex. Following this, myosin II is recruited, and the contraction of actin and myosin facilitates the retraction of membrane blebs. Alternatively, the generation of new blebs from existing ones can contribute to cell migration. Activation of RhoA locally, which induces myosin activation, results in heightened contractility, generating hydrostatic pressure and initiating bleb formation through hydrostatic flow. Similar to mesenchymal motion, cells employing blebbing for migration typically follow a process of "attaching" the newly formed bleb to the surroundings and "detaching" the cell rear, as proposed by most models [2, 4].

The blebbing mode of cell migration is marked by low cell adhesion and elevated cortex contractility, which promotes ameboid motion. The attachment of blebbing cells to their surroundings employs mechanisms such as "chimneying", which depends on forces perpendicular to the direction of motion and operates independently of specific adhesion molecules. An alternative model proposes that forces are transmitted through cell-substrate intercalations. In this scenario, when blebs extend and create protrusions at the side of the cell that fit into gaps in the substratum, the contractility of the reestablished cortex can generate a net force, pulling the cell body [2].

The initiation and growth of blebs are primarily regulated by myosin contractility and the link between the actin cortex and the membrane. In carcinoma cells using blebbing for migration, there is an increased level of the actin-membrane cross-linker ezrin at the cell's rear, whereas it is reduced at the front. Adjusting the levels of other ERM (ezrin-radixin-moesin) proteins similarly influences both bleb formation and bleb-induced migration [2].

The cell membrane's constrained stretchability, approximately 4%, is a crucial factor that restricts the extension of blebs and their migratory capabilities. Blebs, lacking endosomes, are believed to facilitate expansion through the localized unfolding of the membrane. Bleb expansion surpasses the speed of lamellipodial growth, can occur in diverse directions, and, owing to the absence of the cortex, can inherently adapt to three-dimensional environments. As a result, blebs may have a pivotal role in intricate three-dimensional (in vivo) settings where lamellipodial extension faces impediments [2].

#### 6.3.1.2 Attachment

The actin filament polymerization generates protrusive forces at the leading edge of a migrating cell, and these forces are then transmitted to the underlying substratum, driving the cell's motion. Coordination of protrusion at the front and contraction at the rear of the cell is essential for effective cell migration. The leading edge advances by creating membrane protrusions, followed by adhesion to the substratum. Meanwhile, at the rear, the cell body follows due to contraction coupled with de-adhesion. This interplay of actin polymerization, dynamic adhesions, and myosin contraction ensures precise regulation of migration in both space and time [4]. Myosin II operates in at least two ways to assist cell migration. The first is by helping to connect the actin cytoskeleton to the substratum through integrin-mediated adhesions. The tension at attachment sites, crucial for the maturation of these sites into focal adhesions, is generated by the combined forces of actin polymerization and myosin activity. Focal adhesions are dynamic assemblies of structural and signaling proteins that establish a connection between the migrating cell and the extracellular matrix. Another mechanism involves bipolar myosin II filaments, which connect with the actin filaments at the rear of the lamellipodium and reorient them. This sarcomere-like contraction shifts its orientation from nearly perpendicular to the leading edge to almost parallel to it. This contraction, reminiscent of a sarcomere, hinders protrusion and squeezes the sides of the advancing lamellipodium, aiding in the gathering of the cell's sides as it moves forward. The actin-mediated protrusions at the leading edge of a cell are dependent on robust interactions between the actin network and focal adhesions, which anchor the cell to the substrate (see figure 6.10). Disengagement of these interactions can cause retrograde flow, where the actin network, under the pressure of polymerization and myosin-dependent contraction, moves backward [4].

Cells exert traction forces on the substratum when they move, and this can be quantified by observing the deflection of tiny flexible posts on a surface. In

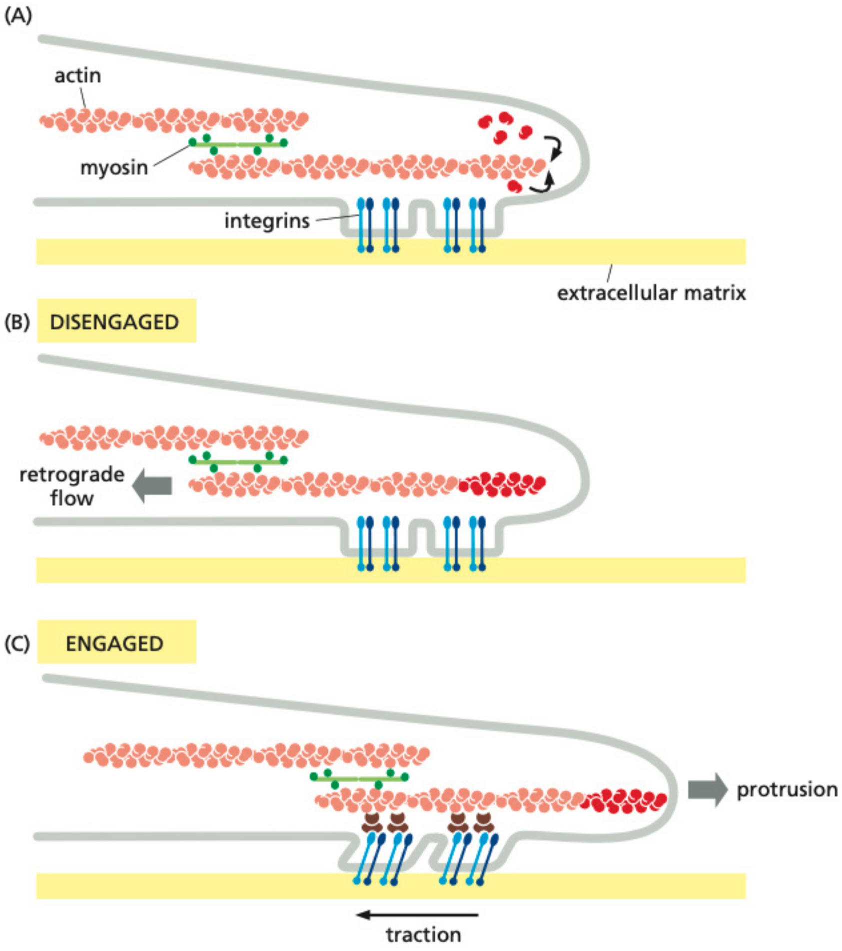

Figure 6.10: The regulation of cell-substratum adhesion at the leading edge of a migrating cell encompasses several crucial steps: (A) Actin monomers assemble at the leading edge and transmembrane integrin proteins (blue) help form focal adhesions; (B) Actin filament is driven rearward without an interaction between filaments and focal adhesions. Myosin motors (green) also contribute to filament movement. (C) Actin-binding adaptor proteins (depicted in brown) interact with integrins, establishing a connection between the actin cytoskeleton, that is polymerizing at the leading edge, and the substratum. Subsequently, myosin-mediated contractile forces are conveyed through focal adhesions, creating traction on the extracellular matrix [4]. Figure from [4].

an organism, most moving cells traverse a semi-flexible extracellular matrix substrate, which can be molded and reorganized by these cellular forces. On the other hand, external mechanical tension or stretching applied to a cell triggers the assembly of stress fibers and focal adhesions, enhancing its contractility. This reciprocal mechanical interplay between cells and their physical environment is believed to contribute to the organization of vertebrate tissues, even though its mechanisms are not fully understood [4].

#### 6.3.1.3 Traction

For efficient cell migration, the cell rear plays a critical role by contracting. Actin structures employ myosin to generate active contractions by sliding antiparallel actin filaments against each other, thereby creating contractile forces when the filaments are anchored. Stress fibers are usually directly linked to focal adhesions, effectively connecting the cell to the ECM. Notably, the formation and maturation of focal adhesions are influenced by stress, where inhibition of myosin II-generated contractility can decrease the size of focal adhesions, while external tension tends to favor their maturation. This dynamic interplay between cellular tension, focal adhesions, and actomyosin contractility is crucial for regulating cell motility and adhesion to the extracellular matrix [2].

Moreover, the forces exerted on focal adhesions can induce conformational changes in mechanosensitive proteins present within these adhesions, such as $\beta$-integrins or talin. This phenomenon enables stress fibers to translate mechanical signals into chemical cues, thereby affecting the maturation and turnover of focal adhesions. As a result, dorsal stress fibers contribute to the maturation of focal adhesions through tension at the leading edge, whereas ventral stress fibers play a role at the trailing edge. Despite their significance in cell adhesion, the role of stress fibers during cell migration remains poorly understood, particularly because they are absent in many rapidly migrating cells, such as leukocytes and Dictyostelium discoideum amoeba as well as in cells embedded in soft three-dimensional matrices [2].

Consequently, stress fibers, while being essential for certain cellular functions, may not always promote migration. Their slow turnover and contractile nature could inhibit cell motion under certain circumstances. The importance of stress fibers could be associated with their functions in deforming the ECM, stabilizing focal adhesions, and generating tension for rear contraction inside the cell. In terms of migration, the contractile forces generated by ventral stress fibers appear crucial for the disassembly of posterior adhesions and for inhibiting rear protrusions [2].

The degree of stress fiber contractility is a tightly regulated process that should be precisely balanced. Excessive activation of RhoA, a key regulator of actomyosin contractility, can inhibit cell migration by increasing contractility, whereas inhibition of contractility via Rho-associated protein kinase (ROCK) inhibition can enhance motility in specific cell types under particular conditions. Rear retraction using stress fibers aligns with the concept of an adhesion gradient, with less adhesion at the cell rear [2].

In summary, force generation for cell motility primarily arises from structures such as the lamellipodium, filopodia, and blebs, whereas contractile structures such as stress fibers or the actin cortex mainly facilitate rear contraction in migrating cells. The intricate interplay between these actin-based structures is pivotal for governing the intricate process of cell migration [2].

### 6.3.2 Cell polarization

Cell migration is a highly orchestrated process that involves cellular elements working in synchrony across the length of the cell. The cytoskeleton plays a central role in this process, not only in generating local movements such as cell protrusion and retraction but also in managing the overall cell shape, organization, and mechanical characteristics across considerable cellular distances, which can span tens of micrometers in animal cells. This enables the coordination and communication necessary for directional migration, ensuring that the front and back ends of the cell maintain their distinct functions and structures [4].

In various scenarios, including but not limited to cell migration, extensive cytoskeletal coordination manifests as the establishment of cell polarity. In this process, a cell constructs different structures with distinct molecular components at its front versus its back, or at the top versus the bottom. The initiation of cell locomotion necessitates the initial polarization of the cell to orient it in a specific direction. Precisely regulated cell polarization processes are essential not only for directed cell migration but also for oriented cell division within tissues and the formation of coherent, organized multicellular structures. Our understanding of the molecular foundations of cell polarity has largely originated from genetic studies in yeast, flies, and other model organisms. Although the mechanisms driving cell polarity in vertebrates are just beginning to be unraveled, it is evident that the cytoskeleton plays a central role, and many of the molecular components involved have been evolutionarily conserved across various species [4].

The establishment of diverse types of cell polarity depends on the localized regulation of the actin cytoskeleton by external signals. These signals commonly converge on a group of closely related monomeric GTPases within the cell, which are members of the Rho protein family-namely, Cdc42, Rac, and Rho. Similar to other monomeric GTPases, the Rho proteins act as molecular switches, undergoing transitions between an active GTP-bound state and an inactive GDP-bound state. Activation of Cdc42 on the inner surface of the plasma membrane triggers actin polymerization and bundling, leading to the formation of filopodia. Conversely, activation of Rac induces actin polymerization at the cell periphery, promoting the development of sheet-like lamellipodial extensions. Activation of Rho triggers both the bundling of actin filaments with myosin II filaments, forming stress fibers, and the clustering of integrins and associated proteins, leading to the creation of focal adhesions. These complex structural changes result from the fact that each of the three molecular switches-Cdc42, Rac, and Rho-has numerous downstream target proteins that impact actin organization and dynamics [4].

Activated Cdc42 target members of the WASp (Wiskott-Aldrich Syndrome protein) family. Individuals deficient in WASp may experience Wiskott-Aldrich Syndrome, a severe immunodeficiency condition characterized by abnormal ABM in immune system cells and impaired platelet formation. While WASp is primarily expressed in blood cells and immune system cells, other more widely expressed variants enable activated Cdc42 to promote actin polymerization in various cell types. WASp proteins can exist in both inactive folded and activated open conformations. When associated with Cdc42-GTP, the open form of WASp is stabilized, allowing it to bind to the Arp2/3 complex and significantly boost its actin-nucleating activity. Consequently, the activation of Cdc42 increases actin nucleation [4].

Rac-GTP similarly activates members of the WASp family. Moreover, it enhances the cross-linking activity of the gel-forming protein filamin and suppresses the contractile activity of the motor protein myosin II. This dual action stabilizes lamellipodia and hinders the formation of contractile stress fibers [4].

Rho-GTP targets a distinct set of proteins. Instead of activating the Arp 2/3 complex to build actin networks, Rho-GTP activates formin proteins, promoting the construction of parallel actin bundles. Simultaneously, Rho-GTP activates a protein kinase that indirectly inhibits the activity of cofilin, resulting in the stabilization of actin filaments. The protein kinase activated by Rho-GTP also inhibits a phosphatase that acts on myosin light chains. This inhibition increases the overall phosphorylation of myosin light chains, boosting the activity of contractile myosin motor proteins in the cell. This enhancement contributes to the formation of tension-dependent structures, such as stress fibers [4].

The interplay between the Rac and Rho pathways is crucial for certain cellular processes. In specific cell types, Rac-GTP activates Rho at a slower rate than its activation of the Arp2/3 complex. This temporal distinction enables cells to initiate the construction of a new actin structure through the Rac pathway and subsequently use the Rho pathway to induce contractility and generate tension within this structure. A common situation where this process occurs is in the establishment and reinforcement of cell-cell contacts [4].

The sequential activation of Rac and Rho plays a pivotal role in preserving significant differences between the leading cell front and the trailing cell rear during migration. The effective communication and coordination between these pathways contribute to the distinct functions carried out by the front and rear of a migrating cell. This coordination is essential for the orchestrated and efficient movement of the cell [4].

### 6.3.3 Cell chemotaxis

Chemotaxis, the directed movement of cells in response to chemical gradients, involves the migration of cells toward or away from a particular chemical stimulus. This process is mediated by external signals that influence the organization of the cell's motility apparatus, typically acting through proteins within the Rho family. One extensively studied instance is the chemotactic movement observed in certain white blood cells, particularly neutrophils, which are attracted to the site of bacterial infection. The cells navigate along the chemical gradient, moving in the direction of the signal to reach the source of the infection [4].

Receptor proteins on the surface of neutrophils enable them to detect extremely low concentrations of N-formylated peptides, which are derived from bacterial proteins (as prokaryotes initiate protein synthesis with N-formylmethionine). Through these receptors, neutrophils are directed to bacterial targets, relying on their capacity to discern a mere 1% difference in the concentration of these diffusible peptides on one side of the cell compared with the other. This high sensitivity enables precise guidance of neutrophils toward bacterial sources [4].

In scenarios such as the chemotaxis of neutrophils toward N-formylated peptides or the chemotaxis of Dictyostelium amebae toward cyclic AMP, the binding of the chemoattractant to its G-protein-coupled receptor triggers the activation of phosphoinositide 3-kinases (PI3Ks). These enzymes generate a signaling molecule, $PI(3,4,5)P_3$, which in turn activates Rac GTPase. Activated Rac then stimulates the Arp2/3 complex, leading to lamellipodial protrusion.

This series of events is critical for directed cell movement in response to specific signals. Through an unknown mechanism, the accumulation of the polarized actin web at the leading edge results in a local enhancement of PI3K activity, creating a positive feedback loop that strengthens the induction of protrusion. The $PI(3,4,5)P_3$ molecule, which activates Rac, cannot diffuse far from its synthesis site because it is rapidly converted back into $PI(4,5)P_2$ by a constitutively active lipid phosphatase. Concurrently, binding of the chemoattractant ligand to its receptor activates another signaling pathway that activates Rho and enhances myosin-based contractility. These coordinated processes contribute to the dynamic regulation of cell movement in response to external cues [4].

The regulation of cell migration frequently entails an antagonistic interplay between Rac and Rho activation, with Rac predominating at the front of the cell and Rho dominating at the rear. This dynamic balance enables the cell to sustain functional polarity, facilitating forward protrusion at the leading edge and rearward contraction. The coordinated activity of Rac and Rho is essential for the intricate and controlled process of cell movement [4].

Additionally, non-diffusible chemical cues anchored to the extracellular matrix or cell surfaces play a crucial role in directing cell movement. Upon activating their receptors, these cues enhance cell adhesion and promote directed actin polymerization. Long-range cell migrations in animals, such as neural crest cell migration and the navigation of neuronal growth cones, typically rely on a combination of diffusible and non-diffusible signals to guide and direct the migrating cells or growth cones to their intended destinations. This intricate interplay of signals contributes to the precision and effectiveness of cellular movements in complex biological processes [4].

## 6.4 Sufficiency of lamellipodia in motility: the keratocyte emblematic cases

Lamellipodia have been extensively studied in the epithelial cells of the epidermis of fish and frogs, specifically in cells known as keratocytes because of their abundant keratin filaments (see figure 6.11). These epithelial cells typically form a protective layer covering the animal and are specialized for rapid wound closure, exhibiting remarkable movement rates of up to 30 $\mu$m/min. In culture as individual cells, keratocytes adopt a distinctive morphology characterized by a massive lamellipodium and a small, trailing cell body that is not attached to the substratum [4].

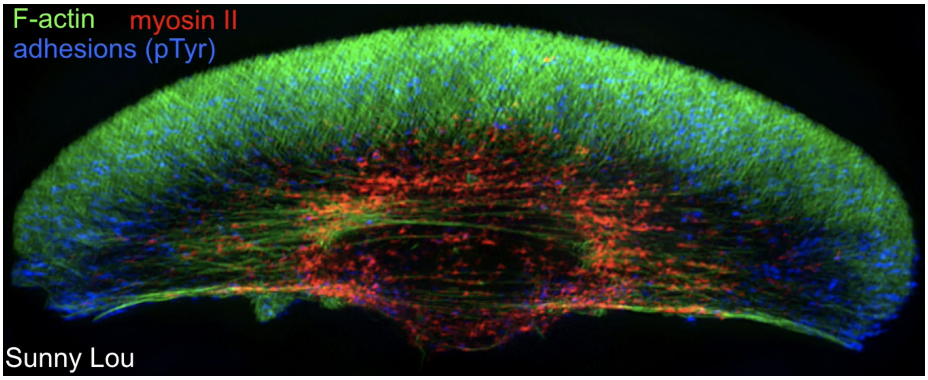

Figure 6.11: Structured illumination micrograph of a keratocytes [17]. Figure from [17].

The coordinated orchestration of these multiple cellular activities, such as actin filament assembly at the leading edge for membrane propulsion, coupled with the assembly and disassembly of adhesions at the rear, is essential for smooth cell movement. This synchrony in cellular actions allows both sides of the cell to progress uniformly, enabling a straight path of movement. Moreover, the balancing act of extending the front while retracting the rear in unison permits the cell to move forward without undergoing significant changes in size [4].

The dynamic behavior of actin filaments in the lamellipodia of keratocytes is quite fascinating (see figures 6.12 and 6.13). They move forward as a unified structure, but the actin filaments within them exhibit an intriguing pattern. While the lamellipodia are progressing, the actin filaments themselves remain largely fixed in relation to the substratum. Their orientation predominantly sees the plus ends oriented toward the leading edge, and the minus ends often connect to the sides of other actin filaments, contributing to the construction of the two-dimensional meshwork. This collective actin meshwork undergoes a phenomenon akin to treadmilling, where the assembly transpires at the front of the lamellipodia while disassembly occurs at the rear [4]. Keratocytes follow a distinct set of steps in their motility, adhering to the fundamental mechanisms of actin-based cell movement shared by various animal cells as well as numerous eukaryotic unicellular organisms such as amoeba. Initially, the cell establishes polarity, which essentially means differentiating between its front and back. It then extends the leading edge, where the force for extension is believed to be driven by actin polymerization itself. As it extends the new leading edge, it simultaneously forms new adhesions to its substrate. Simultaneously, the cell contracts its rear to propel the cell body forward and subsequently retracts and disassembles the

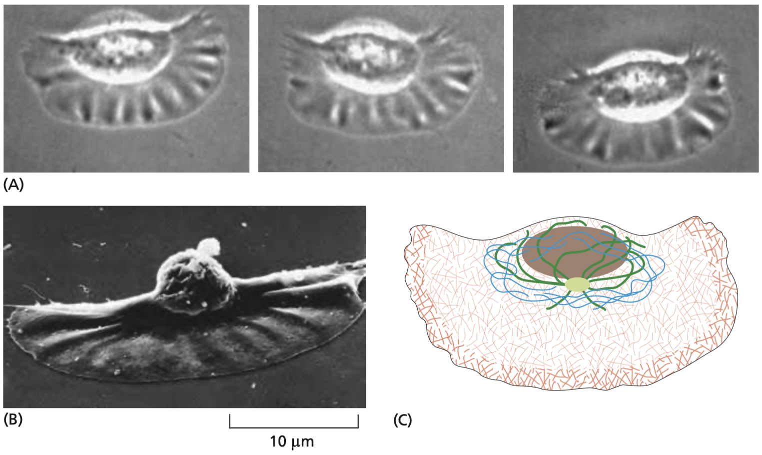

Figure 6.12: Migratory keratocytes from a fish epidermis. (A) Light micrographs of a keratocyte in culture, taken about 15 seconds apart. (B) Keratocytes observed by scanning electron microscopy. (C) Distribution of cytoskeletal filaments in this cell. Actin filaments (red) fill the large lamellipodium and are responsible for rapid cell movement. Microtubules (green) and intermediate filaments (blue) are restricted to regions close to the nucleus [4]. Figure from [4].

adhesions at the back to allow continued movement. This coordinated series of actions enables the cell's forward migration while maintaining its overall structure and integrity [4].

The sustained unidirectional motion facilitated by lamellipodia is believed to depend on the collaboration and mechanical integration of various factors. Filament nucleation is concentrated at the leading edge, where new actin filament growth predominantly takes place, propelling the plasma membrane forward. Conversely, filament depolymerization is mainly observed at sites positioned well behind the leading edge. This coordinated regulation of filament dynamics contributes to the effective and directional movement of the cell. Cofilin exhibits cooperative and preferential binding to actin filaments containing ADP-actin (the D form). Consequently, the new T-form filaments generated at the leading edge, with a high ATP content, should be resistant to depolymerization by cofilin. As these filaments age and ATP hydrolysis progress, cofilin becomes efficient at disassembling the older filaments. This delayed ATP hydrolysis by filamentous actin is considered the foundation for a mechanism that maintains an efficient, unidirectional treadmilling process in the lamellipodium. It also elucidates the intracellular movement of bacterial pathogens such as Listeria [4].

In summary, these are the most important processes for keratocyte motility:

- Chemical reaction between ligands and receptors creates complexes (see figure 6.11: adhesions in blue). Cell adhesion to the extracellular matrix enables the generation of traction so that the cell can move forward;

- External signals at the leading edge trigger the polymerization of G-actin into F-actin (see figure 6.11: F-actin in green). Actin filaments push against the membrane just a few microns back from the plasma membrane at the very leading edge;

- Complexes activate myosin (see figure 6.11: myosin in red);

- Myosin allows the clusterization of complexes;

- Myosin causes reorganization of the F-actin network and contraction of the network. The actin filament branched network is primarily oriented toward the front of the cell, and in the back of the cell the filaments are rearranged to form parallel bundles that are being re-organized by myosin;

- The tension at the back of the cell created by the myosin breaks the network, causing the F-actin network to depolymerize. This tension probably breaks also the bond between integrin and receptors.

This cell follows the same general steps of actin-based cell motility, e.g., external signaling, extension of the leading edge (driven by actin polymerization itself), new adhesion formation at the leading edge, contraction of the rear, etc., without the use of other actin structures, such as stress fibers or filopodia.

### 6.4.1 Load adaptation of the lamellipodia actin networks

As previously explained, actin polymerization is a force-dependent process. To quantitatively examine how protruding actin networks respond to varying forces, in [73] a combination of quantitative light and electron microscopy is used to describe geometric and density changes of lamellipodial actin in fish keratocytes under varying load regimes. Then, a stochastic model that elucidates how the network structure geometrically adapts to counter-forces is presented.

#### 6.4.1.1 Polymer network

Every filament originates from a nucleation event, catalyzed by various molecular machines, with the most prominent being forming and the Arp2/3 complex. Formins facilitate de novo linear nucleation, whereas the Arp2/3 complex binds to an existing filament and generates a new filament at a 70° angle.

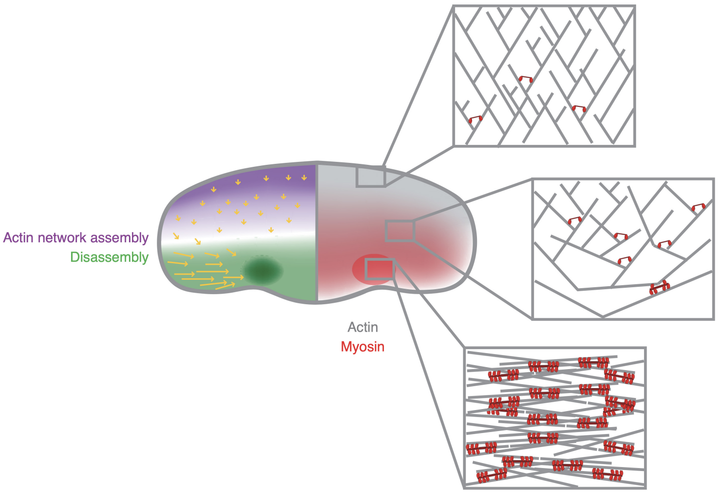

Figure 6.13: Schematic diagram for myosin II-driven actin network disassembly. Left-hand side: distribution of actin network flow (yellow arrows), net assembly (purple), and net disassembly (green). Right-hand side: distribution and organization of F-actin (gray) and myosin II (red) [17]. Figure from [17].

Elongation, which is the addition of new monomers to the growing (barbed) end of the filament, is primarily mediated by forming or proteins of the VASP family. Both nucleation and elongation are enhanced at the membrane interface, where growing filaments are protected from capping proteins. Capping proteins, under normal circumstances, terminate filament elongation by sealing the filament's barbed end [73].

Arp2/3-dependent actin polymerization is a force-sensitive process, as demonstrated in vitro. Increasing the mechanical load on a protruding reconstituted network leads to a higher network density. This indicates that the network structure can adapt to ambient mechanical conditions and support force generation and mechanical resilience under varying loads. The adaptation is partially mediated by the differential force sensitivities of nucleation, elongation, and capping, resulting in enhanced branching under higher loads. However, these kinetic effects only partially explain the changes in network density, and there is speculation that the remaining adaptation may be mediated by spatial rearrangements of the network [73].

#### 6.4.1.2 Correlation of actin density temporal fluctuations at the leading edge with projected cell area and protrusion speed

Single keratocytes expressing the actin reporter lifeact:GFP with a high spatiotemporal resolution during the migration on a planar surface are observed, and fluctuations in actin network dynamics and density together with protrusion speed and morphological parameters are monitored. It comes out that

- the projected area of a keratocyte typically fluctuates $\pm 5\%$ around a baseline. This result, confirmed by previous research, is consistent with the known discovery of a lack of major membrane reservoirs in keratocytes, which, if present, could be involved in mechanical stretching and consequently in drastic changes in the projected area;
- the lifeact:GFP intensity fluctuations within a $\sim 1\mu$m broad zone behind the leading front varies $\pm 20\%$.

The two results are strongly correlated: the normalized temporal fluctuations in the projected cell area and lifeact:GFP intensities exhibit cross-correlation peaks between 0.6 and 0.7 at a time lag of zero. The same correlation is observable in actin: GFP-expressing keratocytes but not when the plasma membrane is uniformly labeled.

Correlation analysis of consecutive 1-mm broad lamellipodial regions revealed that the time delay between correlation peaks increased with the distance between the measured regions. Dividing the respective lag times at the speed of each cell yields distances matching those between adjacent lamellipodial regions [73]. This means that

- keratocytes exhibited minimal retrograde flow of actin in relation to the substrate;
- temporal fluctuations of actin density arise at the leading edge and propagate rearward [73].

Through optical flow analysis at each pixel along the cell front, the protrusion speed is measured. This speed exhibits a negative correlation with both the projected cell area and lifeact:GFP intensity. Specifically, the protrusion speed shows a negative cross-correlation peak between -0.3 and -0.4 at time lag zero. Lifeact:GFP intensities are similarly co-fluctuating with area changes when corrected for fluctuations in protrusion speed. These analyses provide insights into the dynamic relationship between protrusion speed, cell area, and actin dynamics at the cell front [73].

These results indicate that keratocytes migrate slower and produce denser actin networks during intervals when their projected area is larger.

#### 6.4.1.3 Lamellipodial response to altered load

Following the intuition that the change in projected cell area might correspond to changes in membrane tension, the relationship between actin network density and membrane tension is investigated by forcedly changing the membrane tension.

First, the membrane tension is increased using a micropipette. Because the membrane tension equilibrates almost instantaneously over the entire cell, the lateral tension at the lamellipodial tip can be tuned. Four different vacuum levels are applied ranging from -10 to -40 mbar to increase the membrane tension, and it is found that

- Aspiration increases the lifeact:GFP signal concomitant with a moderate decrease in protrusion speed;
- Actin density and protrusion speed are dependent on the applied vacuum;
- The cell continues to protrude during aspiration, demonstrating that the increase in tension is below the stall force of the lamellipodium.

This suggests that an increase in membrane tension induces an increase in network density.

To reduce membrane tension, the researchers employed two distinct approaches. First, the formation of tethered trailing edges is used on adhesive substrates, leading to tension release upon detachment from the substrate. Lamellipodial actin responds to decreased membrane tension by reducing the network density. Second, the cells are subjected to cycles of altered osmolarity. Increasing osmolarity (resulting in water efflux and cell shrinkage) is accompanied by a decrease in the lifeact:GFP signal, and this effect is reversed when water is added (water influx and cell swelling). The data demonstrate that lamellipodial actin dynamically responds to changes in membrane tension by adjusting its density, which increases following an increase in tension and decreases following a decrease in tension [73].

#### 6.4.1.4 Network filament re-orientation

As revealed by three-dimensional electron microscopy in a steady-state migrating keratocyte, nucleation, capping, and elongation collectively generate an expanding network. This network exhibits a canonical branch geometry, which is dictated by the 70° branch structure of the Arp2/3 complex. The intricate coordination of these processes contributes to the dynamic and organized architecture of the actin network in migrating cells [73].

Following an increase in membrane tension, filament density markedly increases. This elevation in filament density is accompanied by an increase in the 0°-20° and 50°-70° fraction of filament angles, whereas filaments at intermediate angles of 20°-50° increases only moderately. These findings indicate that an increase in membrane tension induces an augmentation in network density and a change in geometry, with filaments growing at steeper angles toward the plasma membrane at higher membrane tensions [73].

In contrast, a decrease in membrane tension induced by mechanically detaching one side of a cell with a micropipette leads to a sharp drop in filament density and a configuration dominated by filaments growing perpendicularly (0°) to the membrane. This shift in network geometry results from the selective elimination of filaments: in the transition zone, the rate of filament survival strictly depends on filament orientation, with filaments at a higher angle being preferentially eliminated, while low-angle filaments have a higher rate of survival. These findings demonstrate that a decrease in membrane tension causes a reduction in network density and a change in geometry, with more filaments growing perpendicularly to the plasma membrane [73].

# Chapter 7

# A model for Cells ABM

The response of cells during ABM is dictated by several multi-physics events, which are triggered by extracellular cues and occur at different time scales. For this sake, it is not completely appropriate to provide a cell with classical notions of the mechanics of materials, as for “rheology” or “mechanical response”. Rather, a cell is an alive system with constituents that show a reproducible response, as for the *contractility* for single stress fibers or the mechanical response of a biopolymer actin network, but that reorganize in response to external cues in a non-exactly-predictable and reproducible way [26].

Whereas uncountable papers have been published on the biology of cell spreading, ABM, and the relocation of proteins on advecting lipid membranes, the mathematical modeling definitely lags behind experiments and overall received much less attention. Although nowadays a widespread literature in mechanobiology exists [74], cell ABM and protein interaction with the reorganizing cytoskeleton in the biological phenomena mentioned above is still an ongoing research topic, let alone the formulation of efficient algorithms and computational solvers for three-dimensional simulations [75, 26].

In this chapter, we attempt to define a general multi-physics scheme for modeling cells ABM and relocation of proteins on advecting lipid membranes, being inspired by [6], "Actin based motility unveiled: How chemical energy is converted into motion, *J MECH PHYS SOLIDS*", by [76], "Modeling Receptor Motility along Advecting Lipid Membranes, *MEMBRANES*", by [26], "Modeling cells spreading, motility, and receptors dynamics: a general framework, *ACTA MECH SINICA*", by [34], "Chemo-transport-mechanics in advecting membranes, *INT J ENG SCI*", by [77], "A model for the contractility of the cytoskeleton including the effects of stress-fiber formation and dissociation, *P R SOC A*" and by [78], "Matching material and cellular timescales maximizes cell spreading on viscoelastic substrates", *PNAS*.

Driven by the desire for completeness, we show several models, derived either from the existing literature or from original contributions, that describe different aspects of cells ABM, but refer to different types of cells and are not correlated in some cases, as described afterwards.

## 7.1 Existing literature models

Uncountable papers have been published on the ABM biology, whereas few mathematical models provided insights into ABM mechanisms [79, 80, 81, 82, 83, 84, 36, 85, 77, 85, 86, 87, 88, 89, 73, 89, 52, 84, 90, 91, 92, 93, 77, 94, 95, 96, 97, 98, 99, 54, 100, 101, 102, 103, 104, 105, 106, 57, 56, 107, 108, 109, 110, 111, 112, 113, 114, 115, 116, 26, 117, 118, 78, 119, 122, 124, 125, 120, 121, 123, 126, 127, 128].

In recent years there have been several notable publications that propose models for substrate-cell interactions [120, 78], for studying spatial actin densities [52], for the simulations of the dynamic behavior of actin-based cytoskeletal networks [121] and for coupling mechanisms of cell adhesion, contraction and spreading [102]. We present here a few of them.

### 7.1.1 Mechanical evolution of cell internal structures

Lamellipodia protrusion dynamics is modeled in [122] through a microscopic physicochemical computational framework, which accounts for the biochemical regulation processes and the interactions between actin filaments and the flexible lipid membrane. A profound investigation is carried out on how growing filaments generate forces to push the membrane, concluding that *polymerizing actin filaments apply the needed force on the membrane, pushing it forward.* The interactions between the cytoskeleton and the membrane are modeled by a steric repulsion between the membrane and the actin filaments. Such an approach differs drastically from the one pursued in the present thesis since it takes into account the microscopic behavior of F-actin network.

A triangulated membrane model is proposed more recently in [123], accounting for membrane-filaments interactions and membrane's elastic properties. Ni and Papoian develop an excluded volume interaction via repulsion between the filament's tip and a meshwork triangle, where essentially every point on the surface of the membrane interacts with the tip. This notion, named as responsible for cell motility, differs from the hypothesis of the present thesis, which attributes the motion to a volumetric expansion.

A mechanochemical model is recently presented by Murphy et al [128], who consider the actin filament network as a viscoelastic and contractile gel. The mechanical properties are modeled by a force balancing equation for the displacements, while the pressure and contractile forces are driven by *actin and myosin dynamics*, in turn depicted by a system of reaction-diffusion equations on a moving cell domain. Such an approach shows similarities to the one pursued in the present thesis.

In [73] a two-dimensional (2D) stochastic model of lamellipodial network growth is formulated. It considers filament elongation and Arp2/3-mediated nucleation at the leading front. Elongation is halted by capping whenever filaments detach from the membrane, leaving the zone where they are protected from capping by elongation factors such as VASP or forming. Filaments exert a force on the membrane, propelling it forward based on a force-velocity relation influenced by thermal fluctuations. In this context, the network geometry governs that increased protrusion velocity (resulting from decreased load) rapidly decreases filament density in an angle-dependent manner. Such an approach differs drastically from the one pursued in the present thesis since it takes into account the microscopic behavior of actin.

In [52], a 1D reaction-diffusion-drift model is introduced to study the spatial actin densities. The model incorporates the measured rearward drift of the actin network (V) and diffusion of oligomers ($D_f$) and monomers (D). The model equations' numerical solution gives the spatial distributions of the network actin, the diffusible oligomers, and the polymerizable and non-polymerizable monomers along the anterior-posterior direction. The main model prediction is that the steady-state density of diffusible actin is nearly uniform. Such an approach shows similarities to the one pursued in the present thesis, but it does not model the pushing network mechanisms.

Carlsson [124, 125] develops a stochastic simulation method to study the growth of branched networks against rigid obstacles. Rubinstein et al. [126] perform multiscale, two-dimensional numerical modeling of a crawling cell using a finite element approach. Atilgan et al. [127] perform theoretical and computational studies of the morphology of the lamellipodium.

In [90], a model of actin network treadmilling in an inextensible membrane bag is introduced. It provides a simple biochemical and biophysical basis for the observed morphology and behavior of motile cells. This study emphasizes the crucial regulatory function of membrane tension in determining cell shape. The assembly of actin at the leading edge and its disassembly at the rear are both influenced by the forces exerted on the actin network by the membrane. Furthermore, because membrane tension remains constant along the cell boundary, it effectively links processes such as protrusion and retraction that occur in spatially distinct regions of the cell.

In [89] a specific approach to understanding how cells sense mechanical forces and generate force during contraction is outlined. A formulation involving a mixture of fluids, solids, and solutes is presented considering four key components for cell contraction: the cytoskeleton, cytosol, SF (stress fibers), and actin monomers, along with their interactions. The model incorporates the interplay between mechanical and chemical factors in several ways: (a) a mechano-sensitive process involving the formation and dissociation of an anisotropic SF network, described by the exchange of mass between actin monomers and polymers, (b) a bio-mechanical model for SF contraction that captures established length-tension and velocity-tension relationships seen in muscle cells, and (c) a convection/diffusion description for the movement of fluid and monomers within the cell. The numerical investigations demonstrate that this multiphasic model effectively captures how cell contraction depends on the stiffness of the mechanical environment and accurately represents the development of an organized SF network observed in contracting fibroblasts.

Deshpande and co-workers propose a bio-mechanical model, widely used later on, to couple cell contractility with focal adhesions (FAs) [84, 36, 77, 85]. The mechano-sensitive properties of FAs are modeled in a continuum framework, wherein the cytoskeletal contractile forces generated by stress fibers (SFs) drive and stabilize the assembly of the FA complexes. The model accounts for the diffusion of low-affinity integrins along the cell membrane and predicts different levels of concentration of FAs. Simulations replicate high concentrations of FAs around the periphery of the cell, the increment of FAs at decreasing cell size, and the decrease in intensity of FAs if cell contractility is curtailed. Stemming from this framework, a signaling model is devised based on the generation of $IP_3$ molecules during the FA growth [91], predicting the range of $IP_3$ diffusivities at which the SF activation signal is spatially uniform. The model [84] is also employed for investigating the role of actin cytoskeleton in compression and cell adhesion [86, 87], and to account for the feedback between intracellular signaling, FA formation, and SF contractility in the osteoblasts response on a grooved substrate [92]. Simulations reveal the presence of stretched SF dominant bundles during compression for polarized and axisymmetric spread cells. Round cells are predicted to have fewer SFs and a lower resistance to compression. Highly contractile cells are revealed to provide greater resistance to compression using dominant circumferential SFs [86]. Supported by experimental observations, the substrate-dependent response of contractile cells with no predefined SF or FA arrangement is predicted. SF contractility is found to affect the substrate-dependent response of cells, including changes in nuclear stress and cell tractions. An increment in SF and FA formation is numerically predicted for stiffer substrates [87]. In [92], it is shown that the cell orientation is governed by the diffusion of signaling proteins activated at FA sites on the ridges. The responsiveness of osteoblasts to the topography of substrates is rationalized by the model. Broadening [84, 92], a non-local finite element setting is implemented in [93] to study the competition between cytoskeletal and passive elastic free energies as a driving mechanism in cell spreading. As experimentally observed, a high concentration of aligned SFs along free edges corresponds to a state with low free energy. McMeeking and Deshpande [134], while summarizing previous models [36, 77], presents a bio-chemo-mechanical model implemented in a finite element code for simulating in-vitro cell behavior. They target contractility, adhesion, signaling, cytoskeleton formation, and remodeling.

A coupled formulation of chemo-diffusive integrins with cytoskeleton, underlying cell contraction and spreading is proposed in [102]. In agreement with experimental observations, numerical simulations suggest that substrate stiffness and chemistry strongly affect cellular contraction and spreading. The relevant role of mechanics in the contraction, adhesion, and spreading of adherent cells is highlighted.

### 7.1.2 Receptors motility and cell-susbtrate interaction

Mounting evidence has demonstrated that cells can sense and react to the physical properties of the extracellular matrix (ECM), an ability that plays a key role in processes such as cell migration [142, 143, 144], spreading [145, 146], and proliferation [147, 148, 149, 78]. It is commonly believed that focal adhesions (FAs), which anchor the cell to the ECM as well as serve as hubs for the exchange of biological and mechanical stimuli [150, 151], are responsible for such mechanosensitivity of cells [78].

As already explained in chapter 6, focal adhesions are the result of a complex maturation, that is generated by the interaction between integrins on the ECM and moving receptors on the cellular membrane. In the following paragraphs, we illustrate several continuum and probabilistic models, coming from [76], "Modeling Receptor Motility along Advecting Lipid Membranes, *MEMBRANES*" that describe receptors motility along advecting lipid membranes and ECM-cell interaction. Because of the huge amount of publications in this realm, we cannot aim at being exhaustive, but we claim that sharing the partially existing literature on this topic is essential for a better understanding of the mechanisms underlying the cell ABM.

#### 7.1.2.1 Continuum models for receptor motility

Mikucki and Zhou [167], using an energetic variational principle on advecting membranes derive a curvature-driven transport equation, relating molecule concentrations to a gradient flow governed by the drift-diffusion equation. They predict the molecular localization on static membrane surfaces at locations with preferred mean curvatures, and that the generation of preferred mean curvature drives the molecular localization.

Carotenuto et al. [168] develop a multi-physics approach to investigate how ligand-receptor interactions along the cell membrane trigger raft formation. Diffusion and kinetics of binding and unbinding are studied. Understanding how transporters and active receptors trigger raft formation and clustering is of paramount relevance in membrane-mediated phenomena such as COVID-19 virus-cell interaction.

A discrete model of chemotaxis, which takes into account possible alterations in cellular motility, is presented in [99]. A derivation of the Patlak-Keller-Segel (PKS) model as a continuum limit from the discrete model is shown. Comparisons between numerical simulations of the discrete model and numerical solutions of the PKS model are performed, showing an excellent agreement between the two models.

Based on [178, 179], Gao, Shi and Freund [94] present a receptor-mediated endocytosis study, considering the role of mobile receptors in wrapping the cell membrane around a cylindrical or spherical particle coated with immobile and uniformly distributed ligands. They show the existence of a minimum value of both particle radius and receptor density below which wrapping cannot take place. An estimation of the size of the smallest and the largest particles that can be successfully wrapped is given.

A similar study is performed by Decuzzi and Ferrari [95]. They consider both elliptical and cylindrical particles, showing how the internalization is affected by size and aspect ratio.

The same model proposed in [94] allows the development of a framework for modeling uptake and release of nanoparticles in human and animal cells. In that paper, the mechanics of cell-nanomaterial interactions are investigated, showing how nanoparticles enter cells by receptor-mediated endocytosis. Coarse-grained molecular dynamics is implemented to perform simulations of nanoparticles interacting with cell membranes [96].

Further works on receptor-driven endocytosis are presented by Wiegold, Klinge, Gilbert, and Holzapfel [97, 180]. They consider viruses as a substrate with fixed receptors, whereas receptors of the host cell could relocate on its membrane. Numerical simulations performed via finite difference methods show a rapid variation of receptors density at the early stage, while approaching a steady state as time progresses.

Lee et al. [181] propose a finite-difference mathematical model to describe charged receptor transport on the cell membrane, showing the importance of cell shape in receptor diffusion and in response to an extracellular sinusoidal electric field. They illustrate how the distribution of receptors may alter transmembrane potential, and highlight the prominence of cell shape (i.e. of the mechanics that rule its evolution) in governing interactions between alternating current electric fields and receptors.

Mac Gabhann and Popel [182] model the effect of placental growth factor (PlGF) on the response of VEGF ligands in pathological angiogenesis. A set of coupled reaction-diffusion equations describes the secretion, transport, binding, and internalization of ligands. The presence of PIGF is established to determine a change in the formation of endothelial surface growth factor-VEGFR1 complexes, and a less significant increment in the number of VEGFR2 complexes. Similar equations are used in [183] to study the binding kinetics and signaling pathways of basic fibroblast growth factor (FGF-2) through a reaction-diffusion model of in vitro FGF-2 transport and receptor-ligand binding. Based on experimental results that include degradation of internalized cell surface species, formation of double triads, and dimerization of FGF-2 ligands, the role of the low-affinity heparan sulfate proteoglycans (HSPGs), the identity of the minimal signaling complex leading to FGF-2 activity, and the importance of FGF-2 dimerization is pointed out.

Rattanakul, Crooke et al. [184] model the signal transduction pathways involving G-proteins by including reaction-diffusion equations of various reactants both inside and on the extra-cellular surface membrane. They investigate the dynamic and steady-state properties of the model via weakly nonlinear stability analysis, showing the robust formation of Turing-type patterns under different system parameters, and discussing theoretical predictions against reported experimental evidence.

As an extension of [185], Earnshaw and Bresslof use reaction-diffusion equations to describe the trafficking of $\alpha$-a-3-h-5-m-4-isoxazolepropionic acid receptors (AMPA-Rs) and to evaluate how lateral diffusion contributes to the strength of a synapse [186]. They calculate the distribution of synaptic receptor numbers across the population of spines, determining the effect of lateral diffusion on the strength of a synapse.

Daniels [187] deduces a mathematical expression, in the perturbative deformation regime, to describe the diffusion-limited reaction rate. The coupling between the deformation of a curved membrane and the chemical activities along it is accounted for. The reduction of 20% of the receptor-ligand reaction rate due to the locally induced membrane curvature is theoretically derived.

#### 7.1.2.2 Statistical models for receptor motility

Kusumi et al. [188] study the relocation of E-cadherin and transferrin receptors along mouse keratinocyte cell membranes. A compartmentalization of the cell membrane in small domains, wherein receptors are confined, is suggested as a consequence of the detection of four types of receptor motion (stationary mode, simple Brownian diffusion, directed and confined diffusion). This conjecture arises from the development of a mean-square displacement (MSD) based method and the experimental comparison between single particle tracking (SPT) and fluorescence photobleaching recovery (FPR).

In investigating the non-Brownian diffusion of molecules on membranes by the STP method, Monte Carlo simulations on particles undergoing short-term confined and long-term hop diffusion within a compartment are performed. This simulation strategy detects and characterizes the anomalous diffusion by systematically varying the frame time and rate [189].

By means of a coarse-grained triangular element model, Atilgan and Sun [190] develop a Monte-Carlo methodology examining the changes in free energy during membrane shape transitions. They show how a critical value of the concentration of proteins may bring to the formation of small vesicles, therefore influencing the topology of the plasma membrane.

Bimolecular Fluorescence Complementation (BiFC)-based approach combined with Fluorescence Correlation Spectroscopy (FCS) is used to monitor the diffusion of G-protein-coupled receptors oligomers in the plasma membrane [191]. The approach is used for the first time to measure the membrane diffusional characteristics of adenosine $A_1$ and $A_{2A}$ receptor homo-and heterodimers in Chinese Hamster Ovary cells, demonstrating the differences in diffusivity between adenosine receptor homo and heterodimers.

Paszek et al. [192] develop a chemo-mechanical model in which integrin diffusion, changes in integrin activation status and integrins-ligands interactions are simulated via Kinetic Monte Carlo (KMC) algorithms. Results show the mediator role of glycocalyx in integrin-ligand interactions, which are found to be sufficient to drive integrin clustering even in the absence of cytoskeletal crosslinking or homotypic integrin-integrin interactions.

Receptor dynamics is also accounted for by Duke and Graham [193] in reviewing statistical mechanics models for receptor clustering. They account for cluster generation and discuss the equilibrium thermodynamics of receptors, ligands, and cytosolic adaptor proteins. The role of adaptor proteins in permitting cells to exert control on cluster formation, and target clustering at specific locations on the cell surface is highlighted.

A nanometer-scale mathematical model that couples membrane bending and long surface molecules (LSMs) compression is presented in [194] to reproduce the lateral mobility of LSMs by drift-diffusion equations. Size-based segregation of LSMs from a receptor-ligand complex is proposed as the mechanism of receptor triggering. Supra-diffusive segregation of LSMs from a single receptor-ligand complex is found.

The reduced mobility of receptors after aggregation processes on the membrane is modeled via both standard and density-dependent diffusion equations in [195]. Critical values of the mobility are compared with numerical simulations, showing that the formation of aggregate is quite influenced by density-dependent diffusion.

Martini et al. [196] study the kinetics of a membrane-integrated protein that locates at specific binding sites on the genome, and also acts as a transcriptional activator. Mathematical analysis and KMC simulations of lattice models are combined with fluorescence-microscopy experiments. CadC (the pH receptor of the acid stress response Cad system in E. coli) diffusion along membrane and conformational fluctuations of the genomic DNA are accounted for. They find that diffusion and captured mechanisms are potentially sufficient, for bacterial membrane proteins, to establish functional contacts with cytoplasmic targets.

#### 7.1.2.3 Continuum models for cell-substrate interaction

The interplay between cells and the substrate is a crucial component of cell ABM. Here, we collect some continuum and probabilistic cell-substrate interaction models that are fundamental for fully describing cell ABM.

Receptor-integrin-mediated cell adhesion is one of the most common and widely studied mechano-biological processes in cell-substrate interaction. In it, receptor motility plays a significant role. To the best of our knowledge, the pioneering studies of Bell [197] and co-workers [207] paved the way for the development of multi-physics models in mechanobiology. The receptor density in receptor-integrin mediated cell-cell adhesion is analyzed in a thermodynamic framework, investigating the competition between attractive receptor-integrin and repulsive electrostatic forces. The former is proved to be of greater extent [197]. An increment of receptor concentration in the adhesion zone is further proposed as a transduction mechanism for triggering different cellular responses. Similarly, the redistribution of receptors is viewed as a signal for cell polarization. Phase transitions occur in cell adhesion, and the stabilization of the cell-cell contact is achieved by means of cooperative rearrangements of the internal components [1] of the cells [207]. Goldstein et al. [208] published a theoretical study of the interaction of low density lipoprotein (LDL) receptors with coated pits (specialized cell surface structures in which receptors aggregate). They evaluate the diffusion limits for the forward rate constant of the receptor-integrin chemical interaction on a human fibroblast, as well as the average time that LDL receptors spend on the cell surface before being trapped in a coated pit. The obtained results, in agreement with the experiments, allow them to conclude that if LDL receptors are inserted at a random position in the cell membrane, they move driven by pure diffusion before being trapped in coated pits. A further study [209] finds that how coated pits return to the surface does not affect either the average time that receptors spend on the membrane, nor the forward rate constant or the fraction of receptors aggregated in coated pits at high values of the diffusion coefficient, whereas the effect is substantial for "immobile" receptors.

To mimic cell-tissue interaction, the kinetics of cell adhesion due to $\alpha_{\mathrm{II}b}\,\beta_3$ integrins and ligands binding, gravitation, Helfrich repulsion are studied in [210] for a single giant vesicle on a solid substrate. The analysis of the growth of the adhesion front reveals the prominent role of the receptor-integrin pairs: at high concentrations, the kinetics of integrin-receptor formation drives the propagation of the front of (tight) adhesion at constant velocity, whereas small ligand densities entail a diffusion-limited growth with a square root dependence on the time. The role of receptor motility on adhesive surface contact is analyzed in the transient growth of the adhesion zone by Freund and Lin [178]. They assume the flow of receptors to be proportional to the local gradient in chemical potential and formulate a continuum model of the adhesion of an initially uniformly curved

---

[1] We used literally *internal variables*. As for other terminology such as *plasticity*, this one manifests how very same words have completely different means in mechanics and biology. Such an outcome of the cultural and historical evolution of the disciplines is a further challenge in mechanobiology.

elastic plate to a flat substrate. For very large plates, they solve the problem in closed form, whereas the necessity of numerical methods emerges for limited size. Using the same model, Shenoy and Freund [179] investigate the expansion of a circular adhesion zone when binders (ligands, in this case) density is insufficient to overcome the repulsive barrier that resists cell adhesion. They explain the cross-over effect observed in [210] when the densities of ligands and receptors are equal. Indeed, the growth of the adhesion front radius with a time square root dependence observed experimentally in [210] is recovered. The radius evolves in time as

$$R(t) = 2\,a\,\sqrt{\mathbb{D}_{\mathrm{L}}\,t}\;, \tag{7.1}$$

with $t$ time, $\mathbb{D}_{\mathrm{L}}$ ligand diffusivity and $a$ coefficient depending on the ratio between the ligand and receptor concentrations, $c_{\mathrm{L}}$ and $c_{\mathrm{R}}$; particularly, $a$ assumes finite values for $c_{\mathrm{L}}/c_{\mathrm{R}} < 1$, whereas the square-root growth regime breaks off for $c_{\mathrm{L}}/c_{\mathrm{R}} \simeq 1$.

Liu et al. [201] extend the former framework [178, 179] and introduce a so-called traction-separation relation to model cell-substrate interaction. They provide an additional contribution to the flux of receptors, otherwise governed by the classic Fick's law, proportional to the traction component tangent to the membrane surface, to account for the role of non-specific force as a driving force for the recruitment of receptors towards the adhesion front. Numerical simulations via finite-element methods show that the advancing adhesion front might be stable or unstable, if exposed to small perturbations, as a function of the membrane shear modulus, the adhesive tractions, and the receptor density. Instability occurs at high adhesive tractions, soft membranes, or high ligand-receptor concentrations ratio.

The traction-separation model [201] is extended in [211], performing simulations of biotin receptor - streptavidin ligand binding mediated attachment-detachment of a red blood cell to a substrate. A surface diffusion model describes receptors' motility. The governing equations are implemented in a finite element scheme, providing results in agreement with experimental data.

Golestaneh and Nadler [82] introduce a spontaneous area dilation to account for the influence of receptors on cell deformation and adhesion. Similar to the adhesion-traction model [201, 211], a non-linear receptor-ligand binding force replicates the charge-induced dipole interactions, while Fick's law governs the diffusion of the receptors on the membrane. This study examines the nature of the coupling between electrostatic adhesive forces and the deformation of particle

[212] via a non-linear continuum model. A strong coupling is found for small and moderate membrane deformations.

## 7.2 Original models and results for cells ABM

The current section aims to illustrate two models that describe some of the cell internal structures pivotal for ABM. The first one is an original model, inspired by [6], that describes lamellipodia protrusion in keratocytes. The second one is a mechanical model coming from the existing literature, that describes the contractile response of stress fibers in fibroblasts [77], from which we obtained a numerical result. Even if the role of stress fibers in cell locomotion is still not clear, the contractility of the F-actin network in cell ABM is essential to bring forward the cell rear, so we think that a discussion of F-actin network contractility is needed.

### 7.2.1 A mechanical model for F-actin network protrusion: a general framework

The extensive mathematical description made in chapter 4 guides the modeling of F-actin protrusion, which is summarized here in a shorter shape.

Biopolymers are composed of actin, a protein termed globular or G-actin in its monomeric form, and F-actin when it forms filamentous polymers - see Fig. 7.1. In turn, actin filaments can bundle to form stress fibers, or cross-link to form polymer networks that allow the movement of the cell - see Fig. 7.1. Polymerization is usually triggered by extracellular signals. In the case of cell locomotion, for instance, the cell extends finger-like protrusions by which the cell "feels" the surrounding surface. As extensively explained in section 6.4, keratocytes can move making exclusively usage of lamellipodia structures. For this reason, we start by considering the internal organization of this specific cell, leaving to future analysis the modeling of other cell structures, such as microtubules, stress fibers, intermediate filaments, etc. So, we propose a chemo-transport-mechanical model that describes the cell internal structure pivotal for cell ABM, i.e. F-actin network protrusion. This model provides a unique continuum mechanical and energetic understanding of cells ABM, examining the actin polymerization motor from a thermodynamical point of view. It has the potential, in principle, to provide quantitative results on F-actin and G-actin concentration variation in cells, and cellular displacements and stresses induced by F-actin protrusion. Up to now, it neglects the cell-substrate interaction and

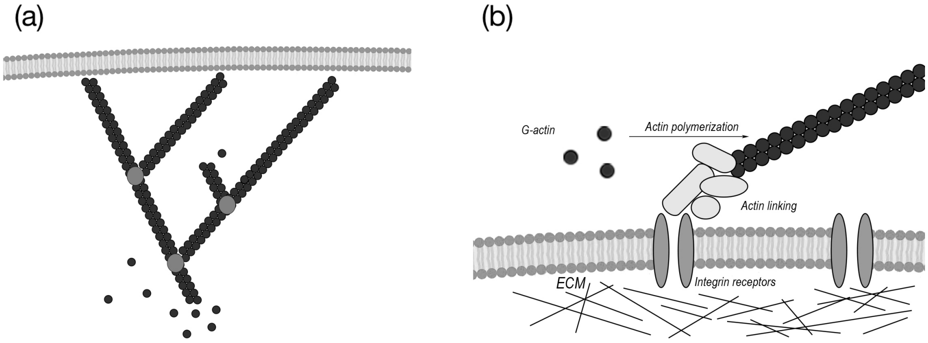

Figure 7.1: F-actin network and its interaction with ECM. (a) F-actin polymerization, triggered by integrin activity. (b) Schematic of the biopolymer network at the leading edge of a cell. Polymerization is usually triggered by extracellular signals. Figure from [26].

the mechanical behavior of other cellular internal structures, such as microtubules and stress fibers.

#### 7.2.1.1 Kinematics

Denote with $\Omega(t)$ a volume that advects, which represents the cell body, and with $\partial\Omega(t)$ its surface. A place $\vec{x} \in \Omega(t)$ is defined as the image of a point $\vec{X}$ in a reference configuration $\Omega_R$ through a smooth function $\chi(\vec{X}, t)$ termed *motion*. As we already explained, we name *deformation* the snapshot of a motion at a fixed time $t$

$$\chi_t(\vec{X}) = \chi(\vec{X}, t) \ .$$

Following chapter 4.1, the non-symmetric deformation gradient $\boldsymbol{F}$ characterizes the deformation of the cell in a neighborhood of a point. As we already explained, we claim that F-actin and G-actin have different partial molar volumes, with the cross-linked network having a molar volume larger than the monomers'. In view of this, the deformation gradient is defined as

$$\boldsymbol{F} = \boldsymbol{F}^e \boldsymbol{F}^c \ , \tag{7.2}$$

which splits the total deformation gradient into two contributions: a purely chemical contribution $\boldsymbol{F}^c$ and a purely mechanical contribution $\boldsymbol{F}^e$, where

- $\boldsymbol{F}^c(\vec{X}, t)$ is the so called *polymerization tensor*;
- $\boldsymbol{F}^e(\vec{X}, t)$ represents the elastic distortion [6].

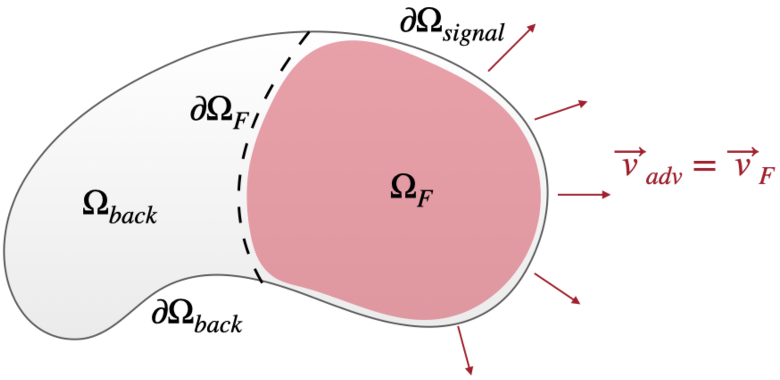

Figure 7.2: Schematic representation of cell configuration, where the cell domain is composed of two parts, as $\Omega = \Omega_F + \Omega_{back}$. $\partial\Omega_F$ represents the cell boundary part where the signal for actin polymerization and protrusion is emitted. $\partial\Omega_F$ represents the boundary between the area where F-actin protrudes and the area where F-actin contracts. $\partial\Omega_{back}$ represents the cell boundary part where the F-actin network contracts.

$\boldsymbol{F}^c(\vec{X}, t)$ is defined as

$$\boldsymbol{F}^c = \lambda^c \, \mathbb{1} \; , \tag{7.3}$$

with

$$\lambda^c > 0 \; , \qquad \det\left[\, \boldsymbol{F}^c \,\right] = J^c = \lambda^{c3} \; , \qquad \frac{1}{J^c}\,\frac{\mathrm{d}J^c}{\mathrm{d}t} = \frac{3}{\lambda^c}\,\frac{\mathrm{d}\lambda^c}{\mathrm{d}t} \; , \tag{7.4}$$

and $\lambda^c$ is the swelling stretch.

By the definition, the right Cauchy-Green tensor yields

$$\boldsymbol{C} = \boldsymbol{F}^T \boldsymbol{F} \, .$$

#### 7.2.1.2 Balance laws

Based upon the selection of the mechanisms that are supposed to govern the structural response of the cell, the balance laws of linear and angular momentum come out. Literature provides two basic approaches, whether the structural functions are demanded entirely to the cell membrane [129, 130, 131, 132, 133] or to the development of a cytoskeletal structure within the bulk of the cell [77, 36, 84, 93, 85, 91, 87, 86, 103]. The influence of curvature on the elastic stiffness of the membrane appears to be related to the size of the cell [82] and seems to be negligible for keratocyte cells. These two evidences lead us to consider the reorganization of the cytoskeleton through a network of actin and intermediate filaments and microtubules the main responsible for the mechanical response of keratocyte cells, coupled with a passive behavior dictated by the viscosity of the cytosol as in [77, 36, 103]. Accordingly, balances of linear and angular momentum will be formulated for the bulk of the cell rather than the membrane. For simplicity, we neglect mechanical contributions from the intermediate filaments, microtubules, and nucleus presence in the cell body, attributing to lamellipodia the main role in keratocyte motility.

The domain $\Omega$ is assumed to be composed of three species: cytosol, G-actin, and F-actin. For the sake of simplicity, we do not consider the cytosol passive behavior, and the mechanical response is only provided by the F-actin network.

All constituent main features are summarized as follows

- *Cytosol*: it is allowed to flow freely inside the cell domain $\Omega$ and it has a fluid behavior. It is the hosting material for G-actin only;
- *G-actin*: it is dissolved in the cytosol and it advects with it. Moreover, it can diffuse inside the cell body $\Omega$ but it does not have a mechanical role;
- *F-actin*: it forms a 3D network that is attached to an extracellular domain by integrins. This fact does not prevent the F-actin from flowing: even if F-actin does not advect with the cytosol, F-actin is permitted to self-diffuse. Moreover, F-actin is considered as an elastic body, that can deform when it is subjected to external forces. As a first approximation, we neglect the active contractility of the F-actin network at the rear of the cell and we ignore the role of ATP. There is no mechanical interaction between the F-actin network and the cytosol.

**7.2.1.2.1 Mass balance** Consider a cell $\Omega$. The mass balance equations of the G-actin and F-actin network in the current configuration read

$$\frac{\mathrm{d}}{\mathrm{d}t}\int_{\mathcal{P}} c_G \, dv + \int_{\partial\mathcal{P}} \vec{h}_G \cdot \vec{n} \, da + \int_{\mathcal{P}} w^{(4.38)} \, dv = 0 \; , \tag{7.5a}$$

$$\frac{\mathrm{d}}{\mathrm{d}t}\int_{\mathcal{P}} c_F \, dv + \int_{\partial\mathcal{P}} \vec{h}_F \cdot \vec{n} \, da - \int_{\mathcal{P}} w^{(4.38)} \, dv = 0 \; . \tag{7.5b}$$

We can rewrite equations (7.5) as

$$\int_{\mathcal{P}} \frac{\partial c_G}{\partial t} + \operatorname{div}[\, c_G \, \vec{v}_{adv} \,] \, dv + \int_{\partial\mathcal{P}} \vec{h}_G \cdot \vec{n} \, da + \int_{\mathcal{P}} w^{(4.38)} \, dv = 0 \; , \tag{7.6a}$$

$$\frac{\mathrm{d}}{\mathrm{d}t}\int_{\mathcal{P}} c_F \, dv + \int_{\partial\mathcal{P}} \vec{h}_F \cdot \vec{n} \, da - \int_{\mathcal{P}} w^{(4.38)} \, dv = 0 \; . \tag{7.6b}$$

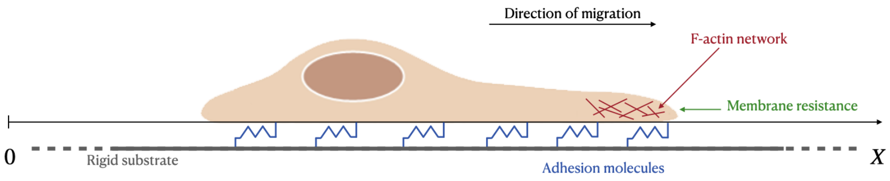

Figure 7.3: Cell migration representation.

where $\vec{h}_G$ is the flux (in moles per unit spatial area per unit time) of G-actin relative to the cytosol and $w^{(4.38)}$ is the rate at which G-actin is converted to F-actin in moles per unit spatial volume per unit time.

The mass flux vector $\vec{h}_a$, expressed in terms of moles per unit area per unit time, represents the flux of species $a$ out of the surface body $\partial\mathcal{P}$ [6]. The flux for G-actin consists of two contributions, the transport and the advection out of the body so that $\vec{h}_G = c_G(\vec{v}_G - \vec{v}_{adv})$. $\vec{v}_{adv}$ represents the advection velocity, namely the velocity of the cytosol. The species needs to have a different velocity with respect to the advecting one if it leaves the material. The flux of F-actin, instead, consists of one contribution due to F-actin self-flow. The network is attached to the substrate, so it does not advect with the cytosol.

**Local form of Balance of Mass.** The mass balance equations of species G and F in the polymerized configuration, schematized in Fig. 7.2, localize as

$$\frac{\partial c_G}{\partial t} + \operatorname{div}\left[ c_G\, \vec{v}_{adv} \right] + \operatorname{div}\left[ \vec{h}_G \right] + w^{(4.38)} = 0 \qquad \vec{x} \in \Omega\,, \tag{7.7a}$$

$$\frac{\partial c_F}{\partial t} + \operatorname{div}\left[ \vec{h}_F \right] - w^{(4.38)} = 0 \qquad \vec{x} \in \Omega\,. \tag{7.7b}$$

**7.2.1.2.2 Balances of momentum** Applying the Cauchy's Stress Theorem (4.52) and the Divergence Theorem (4.35), the balance of linear momentum in the current configuration, which *are written at points* $\vec{x}$ *in the domain* $\Omega_F$, read

$$\int_{\mathcal{P}} \operatorname{div}\left[ \boldsymbol{\sigma}_F \right] + \vec{b}\; dv = 0\,. \tag{7.8}$$

In the current local form, the balance of linear momentum reads

$$\operatorname{div}\left[ \boldsymbol{\sigma}_F \right] + \vec{b} = 0 \qquad \vec{x} \in \Omega_F\,, \tag{7.9}$$

with $\vec{b}$ denoting external body forces per unit current volume in the current configuration. The external body forces are represented by the interaction between receptors on the cell membrane and integrins on ECM, which allow the cell to adhere to the external substrate and to bring its body forward (see section 6.2).

In a one-dimensional setting, the cell interaction with integrins entails volumetric forces acting on the cell body, which can be represented with a bed of springs working in favor of the cell movement. These volumetric forces can be defined as

$$b = k_C \, u \, sgn(u) \tag{7.10}$$

where $k_C$ is proportional to the concentration of complexes ($k_C \propto c_C$) and $b$ is proportional to the sign of u ($sgn(u)$). This is because complexes generate only when they are pushed back by F-actin network retrograde flow (figure 7.9), so negative displacements of springs in a 1D problem are needed. Complexes are not pushed forward by the F-actin network and they do not work when they are compressed.

The cytosol is considered an incompressible fluid. So, the balance of linear momentum for the cytosol reads

$$\int_{\mathcal{P}} \operatorname{div} [\, \vec{v}_{adv} \,] \, dv = 0 \; , \tag{7.11a}$$

$$\int_{\mathcal{P}} \operatorname{grad} [\, p \,] + \mu \operatorname{div} [\, \operatorname{grad} [\, \vec{v}_{adv} \,] \,] \, dv = 0 \; , \tag{7.11b}$$

where the first equation represents the fact that the cytosol is an incompressible fluid and the second one is a Stokes equation. $p$ represents the pressure and $\vec{v}_{adv}$ is the cytosol velocity.

In the current local form, the balance of linear momentum reads

$$\operatorname{div} [\, \vec{v}_{adv} \,] = 0 \qquad \vec{x} \in \Omega \; , \tag{7.12a}$$

$$\operatorname{grad} [\, p \,] + \mu \operatorname{div} [\, \operatorname{grad} [\, \vec{v}_{adv} \,] \,] = 0 \qquad \vec{x} \in \Omega \; . \tag{7.12b}$$

#### 7.2.1.3 Chemical kinetics: mass action

As we already explained, we assume that G-actin is partially transformed into the F-actin network by reaction (4.38). The rate of this reaction (4.38) is defined via the law of mass action in the current configuration as

$$w^{(4.38)}(\vec{x},t) = k_f \, \frac{\vartheta_G}{1-\vartheta_G} - k_b \, \frac{\vartheta_F}{1-\vartheta_F} \; , \tag{7.13}$$

with $k_b$ and $k_f$ the backward and forward reaction rate parameters,

$$\vartheta_a(\vec{x},t) = \frac{c_a(\vec{x},t)}{c_a^{max}(\vec{x},t)} \qquad \text{with} \quad a = G, F \; , \tag{7.14}$$

and $c_a^{max}$ the saturation limit for every $a$-species.

We embody all these biochemical signaling pathways in a single signaling function $\mathcal{C}$ in the forward reaction rate parameter $k_f$

$$k_f = \mathcal{C} \, k_f^* \; , \tag{7.15}$$

where $k_f^*$ is a constant and $\mathcal{C}$ represents the activation signal that triggers actin polymerization and network formation [6].

The assumption that both the forward and backward reaction parameters are volume or surface force-independent is still a simplification of the real process since the presence of the load force can affect both $k_f$ and $k_b$ [1].

#### 7.2.1.4 Balance equations with boundary conditions

Combining the mass action law and the constitutive equations with the mass balance of species and the balance of momentum, the equations that govern all the processes are derived. Taking advantage of eq. (7.13), the transport of actin is coupled with polymerization and depolymerization reactions in the mass balance equations

$$\frac{\partial c_G}{\partial t} + \operatorname{div}\left[\, c_G \, \vec{v}_{adv} \,\right] + \operatorname{div}\left[\, \vec{h}_G \,\right] + k_f \, \frac{\vartheta_G}{1-\vartheta_G} - k_b \, \frac{\vartheta_F}{1-\vartheta_F} = 0 \qquad \vec{x} \in \Omega \, , \tag{7.16a}$$

$$\frac{\partial c_F}{\partial t} + \operatorname{div}\left[\, \vec{h}_F \,\right] - k_f \, \frac{\vartheta_G}{1-\vartheta_G} + k_b \, \frac{\vartheta_F}{1-\vartheta_F} = 0 \qquad \vec{x} \in \Omega \, . \tag{7.16b}$$

The balances of linear momentum (7.9) and (7.11) can be specified as

$$\operatorname{div}\left[\, \boldsymbol{\sigma}_F \,\right] + \vec{b} = 0 \qquad \vec{x} \in \Omega_F \; , \tag{7.17a}$$

$$\operatorname{div}\left[\, \vec{v}_{adv} \,\right] = 0 \qquad \vec{x} \in \Omega \; , \tag{7.17b}$$

$$\operatorname{grad}\left[\, p \,\right] + \mu \operatorname{div}\left[\, \operatorname{grad}\left[\, \vec{v}_{adv} \,\right] \,\right] = 0 \qquad \vec{x} \in \Omega \; . \tag{7.17c}$$

The boundary conditions are currently under development and will be presented in subsequent publications.

#### 7.2.1.5 The multiscale scenario of cell viscoelasticity

The cytoskeleton, an interconnected network of regulatory proteins and filamentous biological polymers undergoes massive reorganization during cell deformation, especially after cell rolling and adhesion [3, 105] and in mediating, sensing, and transduction of mechanical cues from the micro-environment [106]. Homogenized models for the mechanical response of a cell shall condense in effective properties

- polymerization/depolymerization of filaments;
- process of cross-linking that determines the architecture of cytoskeletal filaments;
- passive mechanical properties of the cytosol.

The thermodynamics of statistically-based continuum theories for polymers with transient networks [57, 56, 107, 89, 108] appear to be a valuable candidate for the selection of free energies $\psi_R^{el}(c_{F_R}, \boldsymbol{C})$ and $\psi_R^{in}(c_{F_R}, \boldsymbol{E}, \boldsymbol{\xi})$. At present, however, such a comprehensive model has not yet been proposed for the pseudopodia-driven cell motion. Classical models such as hyperelastic Saint-Venant [135] or Newtonian viscous fluids [110] eventually surrounded by a hyperelastic, zero-thickness membrane [111] have been used for the pseudopodia, whereas a very large amount of literature concerns pseudopod dynamics (see for instance [112] and the large literature therein) or ameboid motion [113]. Different approaches to cell motility, as for active gel theory coupled to the classical theory of thin elastic shells, are also widely used [114] but are not discussed in this thesis. The framework described herein, including myosin dynamics, and phase transformations between G-actin and F-actin, has been depicted in a set of publications by the group of H. Gomez [136, 115]. The flow of the F-actin network was treated as a Newtonian fluid and directed by its velocity. A one-dimensional yet comprehensive model has been proposed in [137].

The multiscale scenario is invoked also for cell contractility. There is evidence [138] that the interaction among filaments, motors, and cross-linkers is mechanically stimulated. As reported in [106], *myosin binding to actin fibers occurs in a force-dependent manner, as well as the contractile response of actomyosin to extracellular stiffness.* According to [139], force feedback controls motor activity and increases the density and mechanical efficiency of self-assembling branched actin networks, thus suggesting that those feedbacks could allow migratory cells to adjust their viscoelastic properties to favor migration. Mass transport and *cell contractility* have been accounted for in several publications with different degrees of complexity [89, 103, 104]: to the best of our knowledge, however, the force transmission has always been modeled stemming from the similarity between the sarcomeric structure of stress fibers and the actin-myosin interactions in muscle cells. In [77] a multi-dimensional network of stress fibers was built on the notion of a representative volume element, in which stress fibers can form in any direction with equal probability. Macroscopic stress is then recovered from the fiber tension, which in turn is generated by the cross-bridging cycles and described by a Hill-like relation [140] of viscoelastic nature. Experimental evidence, however, seems to show that such a resemblance might be questionable in the dynamics and mechanics of cell spreading [141] and hence that the predictive capability of this family of models might be poor for this family of cells.

Finally, the *passive response of the cytosol*, provided mainly by the intermediate filaments attached to the nuclear and plasma membranes, has been modeled by several authors through classical models as linear elasticity [89], the finite strain generalization of Hooke's law [77] or a Neo-Hookean potential energy

$$\psi_R^{el}(\boldsymbol{C}^e) = \frac{G_0}{2}\left(I_1(\boldsymbol{C}^e) - 3\right) , \qquad \psi_R^{in}(\boldsymbol{E}^e, \boldsymbol{\xi}) = \frac{G_0 - G_\infty}{G_0}\, \psi_R^{el}(\boldsymbol{E}^e - \boldsymbol{\xi}) \ , \tag{7.18}$$

where $G_0$ is the initial shear modulus and $G_\infty$ is the shear modulus at the end of the viscous processes. This classical choice of Helmholtz free energy is associated with efficient integration schemes, depicted in [27].

### 7.2.2 A mechanical model for F-actin network contractility: Deshpande theory

The current section provides a general model for fibroblast contractility, named after Deshpande - McMeeking [77, 36]. This model accounts for the dynamic reorganization of the cytoskeleton during cell adhesion and deformation on an engineered substrate. It prioritizes the continuum stress fibers behavior and it studies how their formation is affected by the substrate mechanical behavior. To verify the model, we propose a one-dimensional biomechanical simulation that shows the cytoskeleton contractility behavior under the effect of a support stiffness.

#### 7.2.2.1 Fundamentals

The model for the contractility of cells presented in [77] is motivated by three key biochemical processes

1. an activation signal that triggers actin polymerization and myosin phosphorylation;
2. the tension-dependent assembly of the actin and myosin into stress fibers;
3. the cross-bridge cycling between the actin and the myosin filaments that generates the tension [77].

These are the basic phenomena for stress fiber formation and functioning, as explained in chapter 6.

To devise a mechanical model, the biochemical processes occurring in the cell must link with the formation and dissociation of the stress fibers, as well as the associated generation of tension and contractility [36].

The preceding biochemistry suggests that the mechanical response of the stress fibers comprises three coupled phenomena

1. an activation signal that triggers the formation of stress fibers;
2. a fiber formation rate that depends upon the activation signal coupled with a dissociation rate tension dependent;
3. a contraction rate (contractility) for the stress fiber that depends on the tension through the cross-bridge dynamics [36].

The expressions chosen are the simplest possible without violating the biochemistry and, expressed mathematically, become the fundamental concepts underlying the model [77].

**7.2.2.1.1 Activation signal** The activation signal triggers the formation of stress fibers by activating actin polymerization and myosin phosphorylation, both involved in fiber formation. The signal can either be an internal or an external signal, insofar as it is induced either by a nervous impulse inside the cell or by an external stimulus, that comes from the cell perception of the ECM rigidity surface.

The stress fiber formation, as described in chapter 6, is triggered by protein-protein interactions and by the activation of several signaling pathways at different times. In this model, all processes are abridged in a single activation signal, that sums up all these biochemical phenomena. Therefore, the activation signal is assumed as given by

$$C = exp(-\frac{t-\xi}{\theta}), \tag{7.19}$$

where

- $\theta$ is the decay constant of the signal;
- $\xi$ is the time from last signal emission;
- $t$ is the current time.

Over the time scales of the contractile activity of the cell (of the order of hours), it is assumed there are no spatial gradients in $C$ and that the level is dominated by the most recent signal [77]. The signal varies from 0 to 1. When the signal decays, the actin depolymerizes and the fibers dissociate. On the contrary, when the signal starts, the actin polymerizes to create the stress fibers.

**7.2.2.1.2 Fiber activation level** The transduction of the signal results in the

- polymerization of the actin filaments and the bundling of these filaments by $\alpha$-actinin;
- phosphorylation of myosin II, which promotes the assembly of the myosin into bipolar filaments [77]. The interaction between the myosin II heads and the actin filaments forms contractile bundles [77].

So, the activation signal sparks the stress fibers formation, which is related to the activation level $\eta$. $\eta$ is a nondimensional parameter, $\eta$ $(0 \leq \eta \leq 1)$, which describes the level of recruitment of actin and myosin in a stress fiber bundle. The amount $\eta = 1$ is the maximum recruitment allowed by the biochemistry.

The activation level can be written as a ratio of two concentrations

$$\eta = \frac{c_f}{c_f^{max}}, \tag{7.20}$$

where

- $c_f$ is the concentration of the polymerized actin and phosphorylated myosin in the bundle;
- $c_f^{max}$ is the saturation concentration [36].

The balance of mass is expressed by the formula

$$\frac{\partial}{\partial t} c_f = \omega, \tag{7.21}$$

where $\omega$ is the mass supply due to the polymerization and phosphorylation, quantified via the law of mass action. The equation (7.21) represents the change over time in the concentration of polymerized actin and phosphorylated myosin in the bundle.

The mass action law can be written in a non-standard way as follows, according to the [36]

$$\omega = [(c_f^{max} - c_f)\frac{C\overline{k}_f}{\theta}] - [c_f(1 - \frac{T_a}{T_{a_o}})\frac{\overline{k}_b}{\theta}], \tag{7.22}$$

where

- $\overline{k}_f$ and $\overline{k}_b$ are the two parameters that govern the rate of formation and dissociation of the stress fibers, respectively;
- $T_a$ is the active tension in the fiber bundle;
- $T_{a_o} = \eta T_{a_{max}}$, where $T_{a_{max}}$ is the active tensile strength at full activation, namely the tension when the concentration of the polymerized actin and phosphorylated myosin is the maximum permitted by the biochemistry [77].

Dividing both members by $c_f^{max}$, the equation (7.22) becomes

$$\frac{\omega}{c_f^{max}} = [\frac{(c_f^{max} - c_f)}{c_f^{max}}\frac{C\overline{k}_f}{\theta}] - [\frac{c_f}{c_f^{max}}(1 - \frac{T_a}{T_{a_o}})\frac{\overline{k}_b}{\theta}]. \tag{7.23}$$

Replacing the equation (7.20) in equation (7.23), it becomes

$$\frac{\partial \eta}{\partial t} = [(1 - \eta)k_p] - [\eta k_d], \tag{7.24}$$

where

- $\eta = \frac{c_f}{c_f^{max}}$,
- $k_p = \frac{C\overline{k}_f}{\theta}$,
- $k_d = \left(1 - \frac{T_a}{T_{a_o}}\right)\frac{\overline{k}_b}{\theta}$.

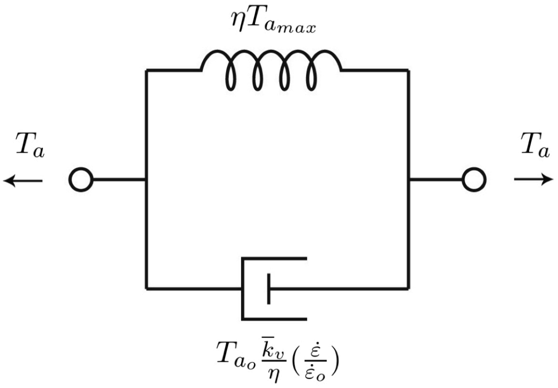

Figure 7.4: The model for the second branch of the constitutive equation that expresses $T_a$ as a function of $\varepsilon$. Figure from Claudia Bonanno's Dissertation titled "Mechanical and Biological Insights of Endothelial Cell Spreading".

Formula (7.24) is the first-order kinetic scheme, that represents the formation and the dissociation rate of the stress fibers.

The over-dot denotes differentiation to time $t$, measured from the instant of the application of the first signal [77]. The key features of equation (7.24) are the followings

1. the rate of the formation of the stress fiber (first square bracket) decreases with increasing fiber activation $\eta$ and is proportional to the strength of the decaying signal;

2. the rate of dissociation (second square bracket) is proportional to the concentration of the polymerized actin and phosphorylated myosin II [77]. Moreover, to allow the contractile bundles to be held together by the tension, it is proposed a dissociation term dependent on the tension; namely, the dissociation rate is zero when the fibers are held at the tension $T_{a_{max}}$, but increases linearly at lower tension [77].

**7.2.2.1.3 Mechanical model** The bundle contraction/extension rate $\dot{\varepsilon}$ is related to the stress by the cross-bridge dynamics [36]. The constitutive equation that connects the applied tensions $T_a$ to small strain rate $\dot{\varepsilon}$ is described in [77] by the equation

$$\frac{T_a}{T_{a_o}} = \begin{cases} 0 & \frac{\dot{\varepsilon}}{\dot{\varepsilon}_o} < -\frac{\eta}{\bar{k}_v} \\ 1 + \frac{\bar{k}_v}{\eta}(\frac{\dot{\varepsilon}}{\dot{\varepsilon}_o}) & -\frac{\eta}{\bar{k}_v} \leq \frac{\dot{\varepsilon}}{\dot{\varepsilon}_o} \leq 0 \\ 1 & \frac{\dot{\varepsilon}}{\dot{\varepsilon}_o} > 0 \end{cases}, \tag{7.25}$$

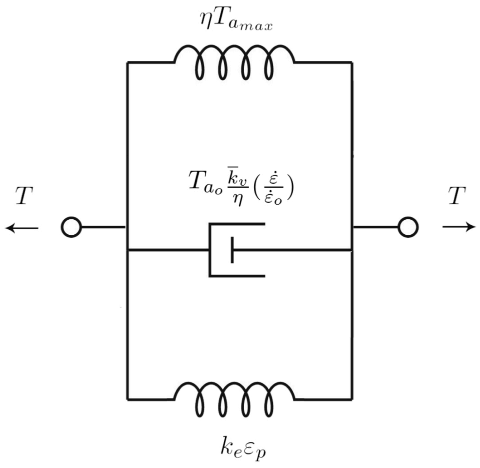

Figure 7.5: The model that expresses $T$ as a sum of active and passive tension. Figure from Claudia Bonanno's Dissertation titled "Mechanical and Biological Insights of Endothelial Cell Spreading".

where

- $\overline{k}_v$ is a nondimensional constant that represents the fractional reduction in fiber tension upon increasing the shortening rate by reference value $\dot{\varepsilon_o}$ [77];
- $\dot{\varepsilon}$ is the rate of change of the length of stress fiber (positive for lengthening and negative for shortening) [77];
- $\dot{\varepsilon_o}$ is the reference strain rate.

For $\frac{\dot{\varepsilon}}{\dot{\varepsilon}_o} > 0$ the fibers are getting longer and the fibers' behavior is neither elastic nor viscoelastic because the tension has the constant value $T = T_{a_o}$.

For $\frac{\dot{\varepsilon}}{\dot{\varepsilon}_o} < -\frac{\eta}{\overline{k}_v}$ the bundle is not subjected to tension, therefore it tends to dissociate. The tension is equal to 0.

For $\frac{\eta}{\overline{k}_v} \leq \frac{\dot{\varepsilon}}{\dot{\varepsilon}_o} \leq 0$ the fibers have a viscous elastic behavior because the tension $T_a$ is linearly dependent to the strain rate $\dot{\varepsilon}$.

The formula (7.25) is a simplified version of the Hill relation and accounts for the fiber lengthening (see figure 7.4).

The contractile response of a cell includes a contribution from the passive elasticity due to the intermediate filaments of the cytoskeleton that are attached to the nuclear and plasma membranes. This elastic passive element acts in parallel with the active element. Therefore the total tension is a sum of active

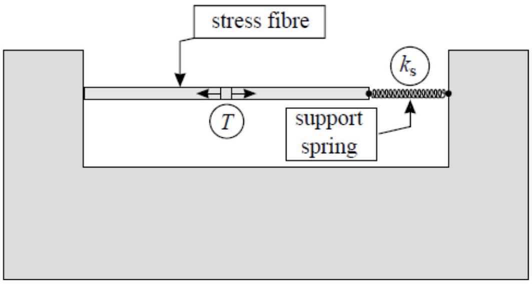

Figure 7.6: A stress fibers bundle and a spring in series between two rigid supports. Figure from [77]. Figure from Claudia Bonanno's Dissertation titled "Mechanical and Biological Insights of Endothelial Cell Spreading".

and passive tensions

$$T = T_a + T_p, \tag{7.26}$$

where

- $T_a$ is the active tension, defined by the equation (7.25);
- $T_p$ is the elastic passive tension (see figure 7.5).

The passive tension can be defined as the product of the elastic constant $k_e$ and the deformation $\varepsilon_p$, so the (7.26) becomes

$$T = T_a + k_e \varepsilon_p, \tag{7.27}$$

where the passive deformation $\varepsilon_p$ is equal to the total deformation, viz.

$$\varepsilon_{tot} = \varepsilon_a = \varepsilon_p = \varepsilon\,. \tag{7.28}$$

Such passive elastic contributions are considered only in the two-dimensional model of [77], but are neglected in the one-dimensional model to better illustrate the essential features of the stress fiber constitutive relation.

#### 7.2.2.2 Effect of support stiffness

This example describes the evolution of bundle behavior on an elastic support. For simplicity, the fiber is assumed to be completely inactive at time $t = 0\,s$ [77] and the contribution of passive tension is neglected, therefore

$$T_a = T_{tot} = T. \tag{7.29}$$

Consider a stress fiber held between two rigid foundations through a support spring in series, characterized by a spring constant $k_s$ [77] (figure 7.6). This spring constant is defined via the relation $F_m = k_s \Delta x$, where $F_m$ is the force generated by the spring for an extension $\Delta x$ [77].

After the activation of the signal, $\eta$ increases, and the fiber shortens. At the same time, the spring applies a force to the bundle to get back to the configuration at rest.

The sum of the fiber length $l_f$ and the spring length $\Delta x$ is a constant

$$l_f + \Delta x = const, \tag{7.30}$$

hence

$$\dot{l_f} + \dot{\Delta x} = 0. \tag{7.31}$$

The fiber deformation is

$$\varepsilon_f = \frac{l_f}{l}. \tag{7.32}$$

Denote with

$$\varepsilon_m = \frac{\Delta x}{l}, \tag{7.33}$$

where $l$ is the total length of the support. The parameter $l$ is a constant over time, thus, the time derivative of fiber deformation is

$$\dot{\varepsilon_f} = \frac{\dot{l_f}}{l} \tag{7.34}$$

and the time derivative of spring "deformation" is

$$\dot{\varepsilon}_m = \frac{\dot{\Delta x}}{l}. \tag{7.35}$$

Replacing the equations (7.35) and (7.34) in (7.31) the latter becomes

$$\frac{\dot{l_f}}{l} = -\frac{\dot{\Delta x}}{l}, \tag{7.36}$$

so

$$\dot{\varepsilon}_f = -\dot{\varepsilon}_m. \tag{7.37}$$

When $\Delta x$ increases, the fiber shortens by the same length. Thus the tension in the spring is

$$\dot{T}_m = k_s \dot{\varepsilon}_m. \tag{7.38}$$

The internal force in the bundle is equal to the force generated by the spring

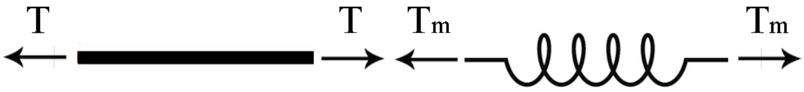

Figure 7.7: Tension in the fiber bundle and in the spring. Figure from Claudia Bonanno's Dissertation titled "Mechanical and Biological Insights of Endothelial Cell Spreading".

(see figure 7.7)

$$T_m = T. \tag{7.39}$$

The equation (7.38) can be written as

$$\dot{T} = \dot{T}_m = k_s \dot{\varepsilon}_m = -k_s \dot{\varepsilon}_f. \tag{7.40}$$

Solving for $\dot{\varepsilon}_f$, the equation becomes

$$\dot{\varepsilon}_f = -\frac{\dot{T}}{k_s}. \tag{7.41}$$

Replacing $\dot{\varepsilon}_f$ in the second-branch of (7.25), it becomes

$$\frac{T}{T_o} = 1 - \frac{\overline{k}_v}{\eta \varepsilon_o}(\frac{\dot{T}}{k_s}), \tag{7.42}$$

which can be written as an ordinary differential equation for T

$$\dot{T} = \begin{cases} \frac{k_s \varepsilon_o}{k_o}(\eta - \frac{T}{T_{max}}) & 0 < T < T_o \\ 0 & otherwise \end{cases}. \tag{7.43}$$

The resulting coupled governing equations are (7.24) and (7.43) equations, with initial conditions $\eta = T = 0$ at $t = 0\,s$.

**Dimensionless formulas** The problem is fully specified by four independent non-dimensional variables: $\overline{k}_f$, $\overline{k}_b$, the non-dimensional support stiffness,

$$\overline{k}_s \equiv \frac{k_s \varepsilon_o \theta}{T_{max} \overline{k}_v} \tag{7.44}$$

and the non-dimensional time, $\overline{t} \equiv \frac{t}{\theta}$ [77]. The resulting solution-dependent variables are the non-dimensional tension in the stress fiber (and spring)

$$\bar{T} = \frac{T}{T_{max}} \tag{7.45}$$

and the non-dimensional extension of the support spring [77]

$$\Delta\bar{x} \equiv \Delta x \frac{\overline{k}_v}{\varepsilon_o}\theta. \tag{7.46}$$

Unless otherwise specified, the reaction rate constants are taken as $\overline{k}_f = 10.0$ and $\overline{k}_b = 1.0$, referred to as the reference case. The non-dimensional spring constant is varied in the range $0.5 \leq \overline{k}_s \leq 80$ [77].

In range $0 < T < T_o$, dividing both members by $T_{max}$ and multiplying by $\theta$, the equation (7.43) becomes

$$\theta\frac{\partial\overline{T}}{\partial t} = -\overline{k}_s(\overline{T} - \eta). \tag{7.47}$$

Introducing the dimensionless time $\overline{t} = \frac{t}{\theta}$, the activation signal becomes

$$C = exp(-\overline{t}), \tag{7.48}$$

whereas the activation level obeys the evolution equation

$$\frac{\partial\eta}{\partial\overline{t}} = (1-\eta)Ck_p - \eta(1 - \frac{\overline{T}}{\eta})k_d, \tag{7.49}$$

where $\frac{\partial\eta}{\partial t} = \theta\frac{\partial\eta}{\partial\overline{t}}$ and

$$\dot{\overline{T}} = \frac{\partial\overline{T}}{\partial\overline{t}} = -\overline{k}_s(\overline{T} - \eta), \tag{7.50}$$

where $\frac{\partial\overline{T}}{\partial t} = \frac{\partial\overline{T}}{\partial\overline{t}}\frac{\partial\overline{t}}{\partial t} = \theta\frac{\partial\overline{T}}{\partial\overline{t}}$.

**Governing equations** The governing equations are

$$\begin{cases} \frac{\partial\overline{T}}{\partial\overline{t}} = -\overline{k}_s(\overline{T} - \eta) \\ \frac{\partial\eta}{\partial\overline{t}} = k_p(1-\eta)exp(-\overline{t}) - k_d\eta(1 - \frac{\overline{T}}{\eta}) \end{cases}, \tag{7.51}$$

with the initial condition $\eta = T = 0$ at $t = 0\,s$. The activation signal $C$ is expressed as

$$C = exp(-\overline{t}). \tag{7.52}$$

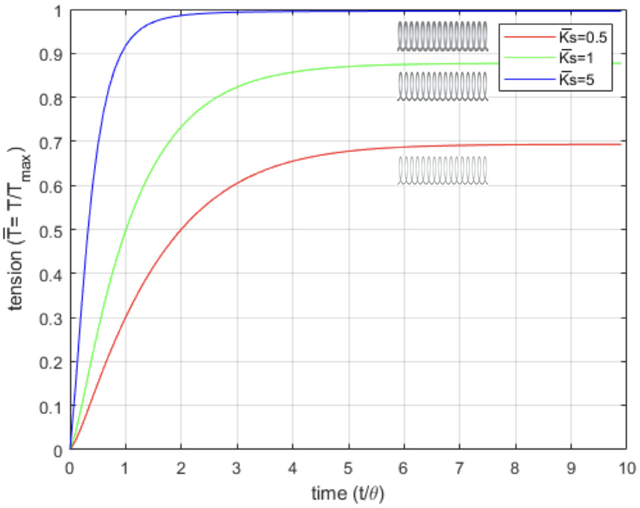

Figure 7.8: The tension as a function of time in three springs with $\overline{k}_s = 0.5$, 1.0, 5.0. For stiff springs ($\overline{k}_s > 5.0$), the steady-state tension always reaches $T_{max}$. Conversely, compliant springs ($\overline{k}_s \leq 1.0$) are unable to sustain significant tension until the stress fiber has undergone substantial contraction. Figure from Claudia Bonanno's Dissertation titled "Mechanical and Biological Insights of Endothelial Cell Spreading".

The numerical solution is given by the backward $\theta$-method, a finite difference method, which discretizes the problem over time.

With the backward $\theta$-method, the discretized governing equations become

$$\begin{cases} \frac{\overline{T}_{n+1}-\overline{T}_n}{\Delta\bar{t}} = -\overline{k}_s(\overline{T}_{n+1} - \eta_{n+1}) \\ \frac{\overline{\eta}_{n+1}-\overline{\eta}_n}{\Delta\bar{t}} = k_p(1-\eta_{n+1})exp(-\bar{t}) - k_d\eta_{n+1}(1 - \frac{\overline{T}_{n+1}}{\eta_{n+1}}) \end{cases} . \tag{7.53}$$

Easy algebra leads to

$$\overline{T}_{n+1}(1 + \overline{k}_s\Delta\bar{t}) - \overline{k}_s\Delta\bar{t}\eta_{n+1} = \overline{T}_n \tag{7.54}$$

and

$$-k_d\Delta\bar{t}\overline{T}_{n+1} + \eta_{n+1}(1 + \Delta\bar{t}k_pexp(-\bar{t}) + \Delta\bar{t}k_d) = \overline{\eta}_n + \Delta\bar{t}k_pexp(-\bar{t}), \tag{7.55}$$

therefore the linear system dicrete solution $\overline{T}_{n+1}$, $\eta_{n+1}$ solves

$$\begin{bmatrix} 1+\overline{k}_s\Delta\bar{t} & -\overline{k}_s\Delta\bar{t} \\ -k_d\Delta\bar{t} & 1+k_p\Delta\bar{t}exp(-\bar{t})+k_d\Delta\bar{t} \end{bmatrix} \begin{bmatrix} \overline{T}_{n+1} \\ \eta_{n+1} \end{bmatrix} = \begin{bmatrix} \overline{T}_n \\ \eta_n + k_p\Delta\bar{t}exp(-\bar{t}) \end{bmatrix}. \tag{7.56}$$

**Remarks** The effect of the spring stiffness $\overline{k}_s$ on the evolution of tension $\overline{T}$ with time is plotted in figure 7.8. The results are in agreement with [77]. Specifically, for stiff springs ($\overline{k}_s > 5.0$), the steady-state tension always reaches $T_{max}$. Conversely, compliant springs ($\overline{k}_s \leq 1.0$) are unable to sustain significant tension until the stress fiber has undergone substantial contraction. Whereupon, $\eta$ increases more slowly and the stress fiber does not achieve full activation before the signal $C$ has decayed [77]. Consequently, the steady-state levels of $\eta$ and $\overline{T}$ are both less than unity [77].

### 7.2.3 A continuum model for receptor dynamics: a general framework

Receptor motility along cell membranes is involved in several biological processes, such as cell, bacteria, virus adhesion, and motility, endocytosis, and exocytosis, to cite a few [152, 153, 154, 155, 156, 157]. The cell membrane plays a crucial role in cellular protection, in control and transport of nutrients [158], and regulates the interchange of different substances in the cell [159]. Its structure facilitates directional or Brownian diffusion of receptors, internalization, and segregation. Acting as a barrier between the extra-cellular and intra-cellular environments, the cell membrane controls the flux of matter across and on its surface [160]. Being constituted of two sheets of phospholipid (amphoteric) molecules, cell membranes in an aqueous environment acquire the conformation of a phospholipid bilayer, with the hydrophobic end inside the bilayer and the hydrophilic outside. Such a conformation, including the various embedded proteins (receptors, ion channels, transporters, other proteins), constitutes the so-called *fluid-mosaic* model [161]. Membrane fluidity represents one of the most critical membrane properties [158], and it is still object of several studies [158, 162, 159, 163, 164, 165, 160, 166]

Our mechanobiology group studied the relocation of transmembrane receptors along advecting cell membranes, as for Vascular Endothelial Growth Factor Receptors 2 (VEGFR2) and $\alpha_v\beta_3$ integrins, by designing chemo-transport-mechanical multi-physics formulations [54, 30, 101, 169, 170] to describe how the mechanical behavior of an endothelial cell (EC) affects receptor dynamics during the early

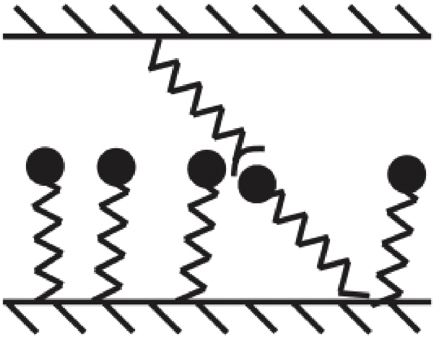

Figure 7.9: Molecular clutches

phases of tumor angiogenesis. VEGFR2 dynamics on cell membrane is studied in [54] for EC adhesion onto a rigid substrate coated with specific immobilized ligands, on the basis of the established role as an activator of the angiogenic process of the chemical interactions between soluble non-canonical ligands, as gremlin [171, 172], released by cancer cells. Although strongly simplified assumptions on cell mechanics are taken, VEGFR2 dynamics is well captured and validated against co-designed experimental investigations [173]. The emergence of three different phases of VEGFR2 relocation and complex generation is unveiled and related to distinct mechanisms, such as (*i*) the initial cell-substrate contact interaction and the VEGFR2-gremlin high chemical reaction rate, (*ii*) the mechanical deformation of the cell due to complex phenomena inside its bulk, (*iii*) the VEGFR2 relocation on EC membrane due to diffusion. The mathematical description of the model is detailed in a companion paper [100]. The model, framed in the mechanics and thermodynamics of continua, follows a general description proposed in [30], and takes advantage of successful descriptions of physically similar systems [174, 175, 176]. The model is broadened [101, 169] to account for the interplay between VEGFR2 and VEGF-A or gremlin, $\alpha_v\beta_3$ integrin and the glycoprotein fibronectin embedded in the extracellular matrix, and the experimentally revealed interaction between $\alpha_v\beta_3$ integrin and the VEGFR2-gremlin complex [177]. The induced receptor polarization is identified in cell protrusions and in the basal aspect of ECs. Relocation and reaction of $\alpha_v\beta_3$ receptors along cell membranes is also included in a general framework for cell spreading, motility, and receptor dynamics [170, 169]. The mechanics of the cell is accounted for, in the field of finite strain theory in continuum mechanics and in a consistent (continuum) thermodynamic setting, together with the modeling of relocation and reaction of actin proteins to form biopolymer structures.

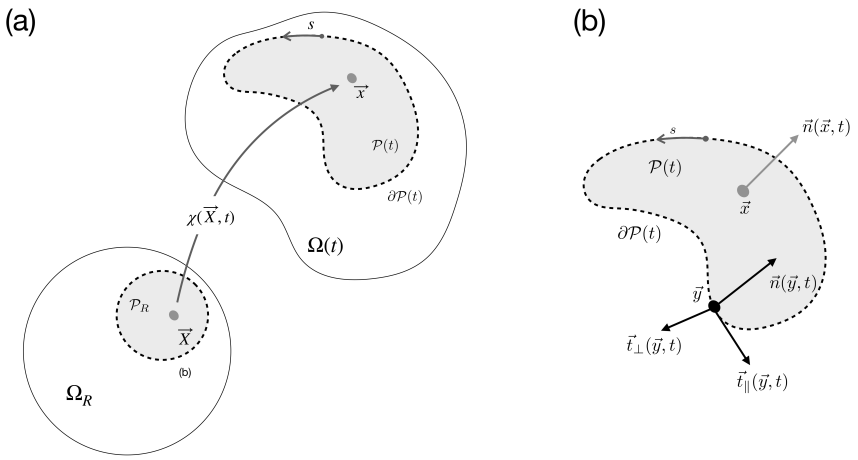

Figure 7.10: Notation. (a) The reference body $\Omega_R$ and the deformed body $\Omega(t)$. Note that $\vec{x} \in \mathcal{P}(t)$ implies $\vec{X} \in \mathcal{P}_R$. (b) Frenet frame at point $\vec{y} \in \partial\mathcal{P}(t)$ and the normal vector $\vec{n}$ at point $\vec{x} \in \mathcal{P}(t)$. Figure from [26].

We attempt here to sum up the multi-physics scheme for modeling the relocation of proteins on advecting lipid membranes presented by our group in the papers mentioned before. We focus here on the motility of receptor proteins, without distinguishing between different types of receptors in terms of structure and second-messenger systems, framing the mathematical setting within the mechanics and thermodynamics of continua [24]. The active mechanical behavior of the cell due to actin polymerization is here neglected.

#### 7.2.3.1 Definitions

Interactions between Ligands on the substrate (Ligands=L) and Receptors on the cell membrane (Receptors=R) generate nascent adhesions (Complexes=C) which act as bounds between the cell and the substrate. The association and formation of a protein complex follow a two-step mechanism; the formation of an encounter complex, in which previously free proteins show few specific interactions and assume many orientations, and the evolution of the encounter complex in the final complex. The binding-unbinding interaction

$$\mathrm{L} + \mathrm{R} \underset{k_b}{\overset{k_f}{\rightleftarrows}} \mathrm{C} \tag{7.57}$$

accounts for both mechanisms [197]. A similar approach has been taken in [54, 100] for the relocation of VEGFR-2 receptors and in [101] for integrins. Coefficients $k_f$ and $k_b$ are the kinetic constants of the forward and backward reactions, respectively. The rate of reaction (7.57), denoted with $w^{(7.57)}$ and measured in $\left[\frac{mol}{m^2\,s}\right]$, quantifies the net formation of (C) on the advecting membrane as the difference between the forward and backward reactions [26].

Receptors (either free or bound into the complex) are distributed along the membrane together with other lipid species and proteins. They are assumed to freely move laterally, effects due to steric hindrance are not accounted for. The amount of proteins per unit area that can be placed at a membrane location $\vec{x}$ is thus limited by the actual size of the protein itself. This evidence ushers the definition of a saturation limit for the species, $c_a^{max}(\vec{x}, t)$ [26].

Denote with $\Omega(t)$ a volume that advects, and with $\partial\Omega(t)$ its surface. A point $\vec{x} \in \Omega(t)$ is defined as the image of a point $\vec{X}$ in a reference configuration $\Omega_R$ through a smooth function $\chi(\vec{X}, t)$ termed *motion*. Following [24], we will name *deformation* the snapshot of a motion at a fixed time $t$

$$\chi_t(\vec{X}) = \chi(\vec{X}, t) \; .$$

The deformation is assumed to be a one-to-one map. In addition, denoting the deformation gradient with

$$\boldsymbol{F} = \text{Grad}\,[\,\vec{\chi}_t\,] \; ,$$

the requirement $J = \det[\,\boldsymbol{F}\,] > 0$ holds. Define on the surface a part $\mathcal{P}(t) \subset \partial\Omega(t)$ as in figure 7.10, and consider a scalar function $f(\vec{x}, t)$ with $\vec{x} \in \mathcal{P}(t)$. Denote with

$$\vec{v}_{adv}(\vec{x}, t) = \mathrm{d}\vec{x}/\mathrm{d}t$$

the velocity of advection at location $\vec{x}$ and time $t$; such a velocity has an arbitrary direction, i.e. it is not necessarily tangent to $\partial\Omega(t)$.

The *Frenet-Serret* reference frame at a generic point $\vec{y} \in \partial\mathcal{P}(t)$ is defined as in Fig. 7.10, in terms of the two unit vectors $\vec{t}_{\|}(\vec{y}, t)$ (tangent) and $\vec{t}_{\perp}(\vec{y}, t)$ (normal). The vector $\vec{n}(\vec{y}, t)$ (binormal) is here taken of non-unit length, being the image in $\Omega(t)$ of a unit vector $\vec{n}_R$ in the reference configuration $\Omega_R$, by means of the contravariant transformation

$$\vec{n} = \boldsymbol{F}^{-T}\,\vec{n}_R \; .$$

On the other hand, the following covariant transformations hold

$$\vec{t}_{\parallel_R} = \boldsymbol{F}^{-1}\,\vec{t}_{\parallel} \;, \qquad \vec{t}_{\perp_R} = \boldsymbol{F}^{-1}\,\vec{t}_{\perp} \;,$$

with the obvious implication that $\vec{t}_{\parallel_R}$ and $\vec{t}_{\perp_R}$ are not unit vectors. The Frenet formulae hold, namely

$$\kappa\,\vec{t}_{\perp} = -\partial\vec{t}_{\parallel}/\partial s \;, \qquad \tau\,\vec{t}_{\perp} = \partial\frac{\vec{n}}{|\vec{n}|}/\partial s \;, \qquad \kappa\,\vec{t}_{\parallel} - \tau\,\frac{\vec{n}}{|\vec{n}|} = \partial\vec{t}_{\perp}/\partial s \;,$$

where $\kappa$ denotes the curvature and $\tau$ the torsion.

The *projected gradient operator* of a scalar field $f$ on a surface $\mathcal{P}$ is defined as follows

$$\nabla_{\mathcal{P}}\left[\,f\,\right] = \operatorname{grad}\left[\,f\,\right] - \frac{\vec{n}\cdot\operatorname{grad}\left[\,f\,\right]}{|\vec{n}|^2}\,\vec{n} \;, \tag{7.58a}$$

in the current configuration, whereas in the reference configuration, it reads

$$\operatorname{Grad}_{\mathcal{P}}\left[\,f\,\right] = \operatorname{Grad}\left[\,f\,\right] - \;\vec{n}_R\cdot\operatorname{Grad}\left[\,f\,\right]\,\vec{n}_R \;. \tag{7.58b}$$

The *projected divergence operator* of a vector field $\vec{v}$, which has an arbitrary direction, on a surface $\mathcal{P}$ is defined as follows

$$\operatorname{div}_{\mathcal{P}}\left[\,\vec{v}\,\right] = \operatorname{div}\left[\,\vec{v}\,\right] - \;\frac{\vec{n}\cdot\boldsymbol{l}\vec{n}}{|\vec{n}|^2} \;, \tag{7.59a}$$

$$\operatorname{Div}_{\mathcal{P}_R}\left[\,\vec{v}_R\,\right] = \operatorname{Div}\left[\,\vec{v}\,\right] - \;\vec{n}_R\cdot\operatorname{Grad}\left[\,\vec{v}_R\,\right]\vec{n}_R \;, \tag{7.59b}$$

in the current and reference configurations, respectively. Tensor $\boldsymbol{l}$ is the gradient of $\vec{v}$, $\boldsymbol{l} = \operatorname{grad}\left[\,\vec{v}\,\right]$. Note that $\boldsymbol{l}$ in eq. (7.59a) can be replaced by its symmetric part $\boldsymbol{d} = \operatorname{sym}\left[\,\boldsymbol{l}\,\right]$, since for any skew-symmetric tensor $\boldsymbol{w}$ it holds $\vec{n}\cdot\boldsymbol{w}\vec{n} = 0$ . Alternative forms for the projected divergence operators are

$$\operatorname{div}_{\mathcal{P}}\left[\,\vec{v}\,\right] = \operatorname{curl}\left[\,\frac{\vec{n}}{|\vec{n}|}\times\vec{v}\,\right]\cdot\frac{\vec{n}}{|\vec{n}|} \;, \qquad \operatorname{Div}_{\mathcal{P}_R}\left[\,\vec{v}\,\right] = \operatorname{Curl}\left[\,\frac{\vec{n}_R}{|\vec{n}_R|}\times\vec{v}_R\,\right]\cdot\frac{\vec{n}_R}{|\vec{n}_R|} \;. \tag{7.60a}$$

Provided sufficient smoothness, the divergence theorem holds also for advecting membranes, in the form

$$\int_{\mathcal{P}(t)} \operatorname{div}_{\mathcal{P}}\left[\,\vec{g}\,\right]\;\mathrm{d}a = \int_{\partial\mathcal{P}(t)} \vec{g}\cdot\vec{t}_{\perp}\,\mathrm{d}\ell \;. \tag{7.61}$$

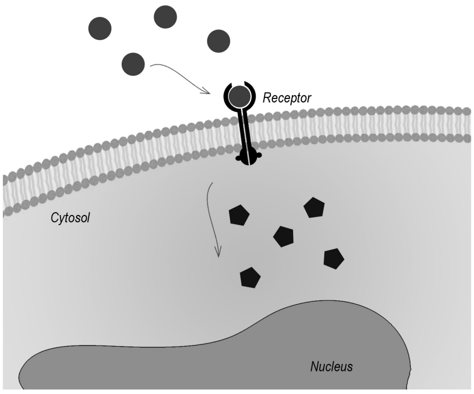

Figure 7.11: Receptors-ligands interaction on the membrane, modeled via equation (7.57). Figure from [26].

The proof of this theorem, as well as for all other theorems not explicitly stated in this thesis, can be found in [169, 26].

#### 7.2.3.2 Receptors' relocation and reaction on an advecting membrane

**7.2.3.2.1 Reynold's theorem on an advecting surface** Reynold's theorem on $\mathcal{P}(t)$ reads as follows [169]

$$\frac{\mathrm{d}}{\mathrm{d}t}\int_{\mathcal{P}(t)} f \,\mathrm{d}a = \int_{\mathcal{P}(t)} \frac{\partial f}{\partial t} + \operatorname{div}_{\mathcal{P}}\left[ f\, \vec{v}_{adv} \right] \,\mathrm{d}a \;, \tag{7.62}$$

where $\vec{v}_{adv}(\vec{x}, t)$ is the velocity of advection at location $\vec{x}$ and time $t$. By taking $f = 1$, eq. (7.62) depicts the area evolution of $\mathcal{P}(t)$ as

$$\frac{\mathrm{d}}{\mathrm{d}t}\int_{\mathcal{P}(t)} \mathrm{d}a = \int_{\mathcal{P}(t)} \operatorname{div}_{\mathcal{P}}\left[ \vec{v}_{adv} \right] \,\mathrm{d}a \;.$$

Intuitively, advection with velocity in the tangent plane has the potential to modify the surface area, however, even $\vec{v}_{adv}(\vec{x}, t) \propto \vec{n}(\vec{x}, t)$ can do so, as for the homothetic expansion of a rubber balloon. Reynold's theorem (7.62) can be also restated as

$$\frac{\mathrm{d}}{\mathrm{d}t}\int_{\mathcal{P}(t)} f(\vec{x}, t) \,\mathrm{d}a = \int_{\mathcal{P}(t)} \frac{\mathrm{d}\, f(\vec{x}, t)}{\mathrm{d}t} + f(\vec{x}, t)\, \operatorname{div}_{\mathcal{P}}\left[ \vec{v}_{adv} \right] \,\mathrm{d}a \;, \tag{7.63}$$

and is a restriction on surfaces of the classical Reynold's transport relation on volumes (see [24], section 16 among others) [26].

**7.2.3.2.2 Mass transport on an advecting surface** **Mass balance in the current configuration** Consider a generic species $a$ at a point $\vec{x}$ on the surface $\partial\Omega(t)$. Species $a$ convects with velocity $\vec{v}_a(\vec{x},t)$. The latter entails the dragging, or advection, velocity $\vec{v}_{adv}(\vec{x},t)$ and another velocity that is due to many possible physics, as for diffusion or migration. If *internalization of species from the membrane* is not allowed, the net velocity $\vec{v}_a - \vec{v}_{adv}$ lays in the tangent plane of the membrane and

$$(\vec{v}_a - \vec{v}_{adv}) \cdot \vec{n} = 0 \; . \tag{7.64}$$

Since species are modeled on a membrane, which is a two-dimensional manifold, the surface density $\rho_a$ of species $a$ measures the mass of the species per unit surface. The *density* flux vector of species $a$, denoted with $\vec{\hbar}_a$, is the product of the surface density times the net velocity of species $a$, i.e.

$$\vec{\hbar}_a = \rho_a \, (\vec{v}_a - \vec{v}_{adv}) \; . \tag{7.65}$$

Define on the surface a part $\mathcal{P}(t) \subset \partial\Omega(t)$ as in Fig. 7.10. The flux of species $a$ across the boundary $\partial\mathcal{P}(t)$ is

$$\int_{\partial\mathcal{P}(t)} \vec{\hbar}_a \cdot \vec{t}_\perp \, \mathrm{d}\ell$$

and the mass balance of species $a$ in the advecting configuration $\mathcal{P}(t)$ reads

$$\frac{\mathrm{d}}{\mathrm{d}t} \int_{\mathcal{P}(t)} \rho_a(\vec{x},t) \, \mathrm{d}a + \int_{\partial\mathcal{P}(t)} \vec{\hbar}_a \cdot \vec{t}_\perp \, \mathrm{d}\ell = \int_{\mathcal{P}(t)} \overline{s}_a(\vec{x},t) \, \mathrm{d}a \; , \tag{7.66}$$

where $\overline{s}_a(\vec{x},t)$ is the surface mass supply[2] of species $a$. By means of the divergence theorem (7.61) and of Reynold's transport theorem in the form (7.63), balance law (7.66) becomes

$$\int_{\mathcal{P}(t)} \frac{\mathrm{d}\rho_a}{\mathrm{d}t} + \rho_a \, \mathrm{div}_{\mathcal{P}} \left[ \vec{v}_{adv} \right] + \mathrm{div}_{\mathcal{P}} \left[ \vec{\hbar}_a \right] \, \mathrm{d}a = \int_{\mathcal{P}(t)} \overline{s}_a(\vec{x},t) \, \mathrm{d}a \; .$$

Since it holds for all $\mathcal{P}(t)$, it eventually localizes as

$$\frac{\mathrm{d}\rho_a}{\mathrm{d}t} + \rho_a \, \mathrm{div}_{\mathcal{P}} \left[ \vec{v}_{adv} \right] + \mathrm{div}_{\mathcal{P}} \left[ \vec{\hbar}_a \right] \; = \; \overline{s}_a(\vec{x},t) \; . \tag{7.67}$$

---

[2] As an example, in biology cells may produce proteins that move to the lipid membranes from the cytosol.

This formulation of the mass conservation law has been considered also in [167]. The mass balance can be finally written in terms of surface molarity $c_a$ (in moles or molecules per unit surface), by dividing by the molar or molecular mass ($m_a$) of species $a$. By denoting with $c_a = \rho_a / m_a$, $s_a = \overline{s}_a / m_a$, and $\vec{h}_a = \vec{\hbar}_a / m_a$ the local balance (7.67) becomes

$$\frac{\mathrm{d}c_a}{\mathrm{d}t} + c_a \, \mathrm{div}_{\mathcal{P}} \left[ \vec{v}_{adv} \right] + \mathrm{div}_{\mathcal{P}} \left[ \vec{h}_a \right] \; = \; s_a(\vec{x}, t) \; . \tag{7.68}$$

**Mass balance in the reference configuration** The mass balance (7.68) can be rephrased in the reference configuration at point $\vec{X}$ and time $t$. To this aim, define the reference molarity of species $a$ as

$$c_{a_R}(\vec{X}, t) = \; c_a( \, \vec{x}(\vec{X}, t \, ), t \, ) \; j(\vec{X}, t) \; , \tag{7.69}$$

the reference flux vector $\vec{h}_{a_R}(\vec{X}, t)$ and the reference mass supply $s_{a_R}(\vec{X}, t)$ as

$$\vec{h}_{a_R} = \; j \, \boldsymbol{F}^{-1} \, \vec{h}_a( \, \vec{x}(\vec{X}, t \, ), t \, ) \; , \qquad s_{a_R} = \; j \, s_a( \, \vec{x}(\vec{X}, t \, ), t \, ) \; , \tag{7.70}$$

respectively, where [24, 32]

$$j = J \, |\boldsymbol{F}^{-T} \vec{n}_R| = J \, \sqrt{\vec{n}_R \cdot \boldsymbol{C}^{-1} \vec{n}_R} \; . \tag{7.71}$$

The referential form of the mass balance (7.68) can be derived from the mass balance in the form (7.66), and reads

$$\frac{\partial c_{a_R}}{\partial t} + \, \mathrm{Div}_{\mathcal{P}_R} \left[ \vec{h}_{a_R} \right] = s_{a_R} \; . \tag{7.72}$$

For the sake of brevity, the proof has been here omitted, interested readers may find it in [169, 26].

**7.2.3.2.3 Relocation and reaction** During their life, cells and their membranes undergo major *macroscopic* mechanical deformations. Studies on the red blood cell [198] suggest that the membrane deformation occurs at constant area, but this evidence does not appear to be supported by experiments in endothelial cells during spreading [141]. Individual proteins and phospholipids can easily move laterally within the membrane, which results in a very low shear stiffness. The *fluid mosaic model* [199] captures this evidence, adding a questionable high resistance to areal expansion. Indeed the mechanisms that are in charge of areal expansion during cell spreading are complex and involve the micro-structural topology[3] of the membrane (as for flattening of invaginated membrane domains [200], i.e. the role of the caveolae as membrane surface repository readily made available for fast geometrical evolution as during filopodia extension). The structure of the lipid membranes, however, induces us to suppose that the saturation concentration $c_a^{max}(\vec{x},t)$, i.e. the maximum number of moles or molecules per unit area for any species $a$, remains unchanged in time in the current configuration. This choice in turn entails that the number of moles or molecules per unit area in the reference configuration is not constant and evolves in time following eq. (7.69), i.e.

$$c_{a_R}^{max}(\vec{X},t) = c_a^{max}(\vec{x}(\vec{X},t),t)\, j(\vec{X},t) \ . \tag{7.73}$$

Accordingly, the value of the non-dimensional ratio between the concentration of species $a$ and its amount $c_a^{max}$ at saturation,

$$\vartheta_a = c_a / c_a^{max} \tag{7.74}$$

in the current configuration remains unchanged in the reference configuration

$$\vartheta_{a_R}(\vec{X},t) = \vartheta_a(\vec{x},t) \ . \tag{7.75}$$

The kinetics of reaction (7.57) is modeled for ideal systems via the law of mass action [37]

$$w^{(7.57)} = k_f \, \frac{\vartheta_L}{(1-\vartheta_L)} \, \frac{\vartheta_R}{(1-\vartheta_R)} - k_b \, \frac{\vartheta_C}{(1-\vartheta_C)} \ . \tag{7.76}$$

At chemical equilibrium, as $w^{(7.57)} = 0$, the concentrations obey the relation

$$\frac{k_f}{k_b} = \frac{\vartheta_C^{\rm eq}}{(1-\vartheta_C^{\rm eq})} \, \frac{(1-\vartheta_R^{\rm eq})}{\vartheta_R^{\rm eq}} \, \frac{(1-\vartheta_L^{\rm eq})}{\vartheta_L^{\rm eq}} = K_{\rm eq}^{(7.57)} \tag{7.77}$$

which defines the constant of equilibrium $K_{\rm eq}^{(7.57)}$ of reaction (7.57).

Far from the saturation limit, $(1-\vartheta_a) \sim 1$ for all $a$. Accordingly, the mass action law (7.76) simplifies as

$$w^{(7.57)} = \tilde{k}_f \, c_L \, c_R - \tilde{k}_b \, c_C \tag{7.78}$$

---

[3] Multiscale investigations, however, fall out of the scope of the present thesis.

once the new constants

$$\tilde{k}_f = k_f (c_L^{max} c_R^{max})^{-1} \,, \qquad \tilde{k}_b = k_b (c_C^{max})^{-1}$$

are defined.

The diffusion of receptors and the viscous evolution of the cell during adhesion and migration appear to be much slower than the interaction kinetics, i.e. the time required to reach chemical equilibrium is orders of magnitude smaller than the time scale of other processes. For this reason, thermodynamic equilibrium may be invoked in place of a transient evolution, thus inferring the constraint $w^{(7.57)} = 0$ to the concentrations of species at all times. Far from saturation, equating (7.78) to zero implies that

$$c_C = \frac{c_R \, c_L}{\alpha} \,, \tag{7.79}$$

having denoted with $\alpha$ the following constant

$$\alpha = \frac{\tilde{k}_b}{\tilde{k}_f} = \frac{c_R^{max} \, c_L^{max}}{c_C^{max}} \, \frac{1}{K_{\rm eq}^{(7.57)}} \,. \tag{7.80}$$

In view of identity (7.79), the two concentrations $c_R$ and $c_L$ describe the problem in full, and the concentration of the complex can be deduced a posteriori.

In vivo experiments show that the complex molecules usually have a much smaller mobility than receptors, perhaps induced by their size. For in vitro experiments [54, 100, 101], ligands are prevented from flowing onto the substrate: given that complex molecules result from the interaction with immobile ligands, they are macroscopically steady as well. Since receptors move along the membrane, reaction (7.57) traps mobile receptors and vice versa [30]. In this work, analogously to [201], ligands and complex are assumed to be motionless, i.e.

$$\vec{h}_L = \vec{h}_C = \vec{0} \,. \tag{7.81}$$

The reaction rate $w^{(7.57)}(\vec{x}, t)$, being a mass supply, shall transform as $s_a(\vec{x}, t)$ according to eq. (7.70). The invariance of $\vartheta_a$ with the configuration and the analysis of the mass action law (7.76) imply that the forward and backward "constants", which encompass the dimensionality of $w^{(7.57)}(\vec{x}, t)$, are not actually constants in the reference configuration. They rather change with time and with point $\vec{X}$ according to

$$k_{f_R}(\vec{X},t) = j(\vec{X},t)\,k_f \;, \qquad k_{b_R}(\vec{X},t) = j(\vec{X},t)\,k_b \tag{7.82}$$

with $j(\vec{X},t)$ as in (7.71). The equilibrium constant in the reference configuration, being the ratio of $k_{f_R}$ and $k_{b_R}$ remains independent upon the configuration. Eventually, the mass action law (7.76) in the reference configuration writes

$$w_R^{(7.57)} = k_{f_R}\,\frac{\vartheta_L}{(1-\vartheta_L)}\,\frac{\vartheta_R}{(1-\vartheta_R)} - k_{b_R}\,\frac{\vartheta_C}{(1-\vartheta_C)}\;. \tag{7.83}$$

In view of all the considerations made so far, the local form (7.72) of the mass balance specify as follows (omitting the dependency upon $\vec{X}$ and $t$):

$$\frac{\partial c_{R_R}}{\partial t} + \mathrm{Div}_{\mathcal{P}_R}\left[\vec{h}_{R_R}\right] + w_R^{(7.57)} = s_{R_R}\;, \tag{7.84a}$$

$$\frac{\partial c_{L_R}}{\partial t} + w_R^{(7.57)} = 0\;, \tag{7.84b}$$

$$\frac{\partial c_{C_R}}{\partial t} - w_R^{(7.57)} = 0\;. \tag{7.84c}$$

Equation (7.84a) is defined on the membrane surface $\partial\Omega_R$, where the receptors flow. The supply $s_{R_R}$ accounts for the internalization or generation of proteins: it is the number of receptors that are generated within the cell and reach the membrane or that internalize. It can be related to the change in the membrane area through a parameter $\kappa_{R_R}$ as

$$\begin{aligned} s_{R_R}(\vec{X},t) &= \kappa_{R_R}\,\frac{\partial j}{\partial t} \\ &= \kappa_{R_R}\left[\,|\boldsymbol{F}^{-T}\,\vec{n}_R|\,J\,\mathrm{tr}\,[\,\boldsymbol{l}\,] - \frac{J}{2}\,\frac{1}{|\boldsymbol{F}^{-T}\,\vec{n}_R|}\,\vec{n}_R\cdot\boldsymbol{C}^{-1}\,\frac{\partial \boldsymbol{C}}{\partial t}\,\boldsymbol{C}^{-1}\,\vec{n}_R\right]\;. \end{aligned} \tag{7.85}$$

At all points at which ligands and receptors do not interact, the reaction rate $w_R^{(7.57)}$ vanishes. Equation (7.84b) is rather defined in the location where ligands stand. In vitro, a given amount of ligands which can be thought of as the initial condition of eq. (7.84b) are spread upon a microscope slide. Finally, eq. (7.84c) is defined in the contact zone between the cell and the slide where reaction (7.57) takes place.

It is convenient to rephrase eq. (7.84b) in terms of the "ligands made available for the reaction” in place of the "ligands spread on the slide". The former ligands are the ones “felt” at a point on the membrane as the distance from such a point and the substrate, where ligands are spread out, becomes sufficiently small.

Such a distance can be understood as a cutoff, within which the formation of an encounter complex, C$^*$, becomes possible as a consequence of diffusion, as made clear in [202, 203, 197, 204]. Despite the size of the cutoff distance remaining inaccurately estimated, it is established to be on the order of tens nanometers [197, 178]. It arises from the interplay of attractive and repulsive forces between either two cells or a cell and a substrate. Indeed, the negative electrical charge carried by cells generates repulsive electrostatic forces - *repulsive barrier* - which is further enriched by an additional resistance provided by the compression of the glycocalyx proteins. Rather, electrodynamic van der Waals forces are expected to be attractive [197]. Both van der Waals and compressive forces are characterized as non-specific long-ranged forces, whereas cell adhesion is generally mediated by the specific short-ranged receptor-ligand interactions, which can cause cell adhesion much more tightly than the non-specific electrical forces [197, 201]. Cells separated by a distance less than, or equal to, the cutoff distance should form a zone of adhesion with the substrate by means of local fluctuations in receptors density [178].

This point of view, which corresponds to the picture of the tight receptor-ligand bond as a set of weak noncovalent physical interactions [205], is made explicit by a supply function $s_{L_R}$, that vanishes at long ranges and rapidly reaches the initial concentration of ligands available for the reaction at short distances

$$\frac{\partial c_{L_R}}{\partial t} + w_R^{(7.57)} = s_{L_R} \ . \tag{7.86}$$

The ligand supply $s_{L_R}(\vec{X}, t)$ becomes available for the reaction during the spreading of the cell on the substrate riched of ligands. It seems to be logically related to i) a gap function between the substrate rich in ligands and the cell membrane *in the current configuration*; ii) a lag in time, namely a point-wise function of an internal variable that activates when the gap function is below some threshold and is related to the chemical kinetics of the binding-unbinding reaction (7.57). In this form, all three equations (7.84a), (7.84c), (7.86) can be written on the membrane $\vec{X} \in \partial\Omega_R$.

Assuming that the time scale of the chemical reaction is much faster than other processes, the concentrations of species may be governed by thermodynamic equilibrium at all times. The concentration of complex $c_{C_R}$ relates then to the others by the equation $w^{(7.57)} = 0$, which leads to eq. (7.79) in the current configuration. Making use of mapping (7.69), eq. (7.79) relates the concentration of complex in the reference configuration $c_{C_R}$ to the concentration of ligands and receptors in the same configuration $c_{L_R}$, $c_{R_R}$ as follows

$$c_{C_R} = \frac{c_{R_R}\, c_{L_R}}{\alpha_R(\vec{X},t)} \; , \qquad \alpha_R(\vec{X},t) = \alpha\, j(\vec{X},t) \; , \tag{7.87a}$$

with constant $\alpha$ defined in eq. (7.80). Transformation (7.87a) is consistent with the assumption (7.73) made on how saturations transform.

In conclusion, exploiting identity (7.87a), the two concentrations $c_{R_R}$ and $c_{L_R}$ fully describe the problem in the assumption of infinitely fast kinetics, whereas the concentration of the complex can be deduced a posteriori. The two governing equations descended from equations (7.84) read

$$\frac{\partial c_{R_R}}{\partial t} + \frac{\partial c_{C_R}}{\partial t} + \mathrm{Div}_{\mathcal{P}_R}\left[\vec{h}_{R_R}\right] = s_{R_R} \; , \qquad \vec{X} \in \partial\Omega_R \; , \tag{7.87b}$$

$$\frac{\partial c_{L_R}}{\partial t} + \frac{\partial c_{C_R}}{\partial t} = s_{L_R} \; , \qquad \vec{X} \in \partial\Omega_R \; . \tag{7.87c}$$

Equations (7.87), with associated initial conditions

$$c_{R_R}(\vec{X},0) = c^0_{R_R}(\vec{X}) \; , \qquad c_{L_R}(\vec{X},0) = 0 \; , \qquad c_{C_R}(\vec{X},0) = 0$$

and Dirichlet-Neumann boundary conditions define the relocation of receptors that undergo binding-unbinding reactions on the reference configuration of a membrane that advects. These are balance equations and as such hold for any constitutive behavior for the mass flux. These equations are *coupled to the mechanical evolution of the cell* (i.e. adhesion, spreading, migration) through the function $s_{L_R}(\vec{X},t)$, which “transfers” ligands on the membrane according to the geometry of the cell.

Equations (7.87) can be rephrased in a computationally more favorable form by means of the change of variable $c_{\mathrm{S}_R} = c_{\mathrm{C}_R} + c_{\mathrm{L}_R}$. After direct time integration of (7.87c), it comes out

$$c_{\mathrm{S}_R} = \int_0^t \frac{\partial c_{\mathrm{S}_R}}{\partial t} d\tau = \int_0^t s_{\mathrm{L}_R}(\vec{X},\tau)\, \mathrm{d}\tau = S_{\mathrm{L}_R}(\vec{X},t) \qquad \vec{X} \in \partial\Omega_R \; , \tag{7.88}$$

with $c_{\mathrm{S}_R}(\vec{X},0) = c_{\mathrm{L}_R}(\vec{X},0) = c_{\mathrm{C}_R}(\vec{X},0) = 0$ on $\partial\Omega_R$. The right hand side of identity (7.88) has a neat physical meaning, because $S_{\mathrm{L}_R}(\vec{X},t)$ corresponds to the total amount of *conformationally available ligands for the reaction* (7.57), pulled back onto the reference configuration.

It is reasonable to relate $S_{\mathrm{L}_R}(\vec{X},t)$ to the gap function $g_l(\vec{X},t)$. We select the following expression

$$S_{\mathrm{L}_R}(\vec{X},t) = c^{av}_{\mathrm{L}_R} \exp\left[-\frac{g_l(\vec{X},t)}{\ell_{chem}}\right] , \tag{7.89}$$

where:

- $g_l$ identifies a gap function between the cell and the substrate. The normal vector on the substrate is unaltered in time and holds $\vec{n}_l = \vec{e}_2$. Via the minimum distance method, a point $\vec{x}$ on the manifold $\partial\Omega(t)$ projects itself onto a single point $\vec{x^*}$ on the substrate and identifies the gap function $(\vec{x}-\vec{x^*})\cdot\vec{n}$, i.e. $g_l = (\vec{x}-\vec{x_l^*})\cdot\vec{e}_2$. The interpenetration inequality constraint between the body and the substrate reads $g_l \geqslant 0$ . Frictionless contact is adopted on the substrate. A sliding motion between the surface and the obstacle allows receptors to break the bond with a ligand in favor of a chemical binding with another ligand located alongside [87]. Denoting with $p_l = \vec{\tau}_l \cdot \vec{n}_l$ the normal component of the traction vector on the substrate $\vec{\tau}_l$, the so called Hertz-Signorini-Moreau linear complementarity conditions for frictionless contact $g_l \geqslant 0$, $p_l \leqslant 0$, $p_l\, g_l = 0$ arise. We assume that the membrane sticks to the substrate and no slip occurs;
- $\ell_{chem} > 0$ is a *chemical length-scale* that tunes the amount of available ligands to the gap $g_l$ and, numerically, acquires the meaning of a regularization parameter;
- $c^{av}_{\mathrm{L}_R}$ is the maximum amount of available ligands on $\partial\Omega(t)$.

#### 7.2.3.3 Thermodynamics of receptors motion on the membrane

Following [30], receptors' motion on the lipid membrane is thermodynamically described by energy and entropy balances, imposing as usual that the internal production of entropy cannot be negative. After the definition of the referential specific Helmholtz free energy per unit volume $\psi_R$, taken as a function of temperature and concentrations, $\psi_R\left(T, c_{R_R}, c_{L_R}, c_{C_R}\right)$ the entropy imbalance in the Clausius-Duhem form is derived. Standard arguments - the so-called Coleman Noll procedure - finally allow identifying the following thermodynamic restrictions

$$\mu_{R_R} = \frac{\partial \psi_R}{\partial c_{R_R}}, \qquad \mu_{L_R} = \frac{\partial \psi_R}{\partial c_{L_R}}, \qquad \mu_{C_R} = \frac{\partial \psi_R}{\partial c_{C_R}}, \qquad \eta_R = -\frac{\partial \psi_R}{\partial T} \tag{7.90}$$

for *chemical potentials* $\mu$ and entropy $\eta_R$. Assuming further that relocation of receptors takes place in thermal equilibrium conditions, the so-called Clausius-Plank inequalities apply

$$\vec{h}_{R_R} \cdot \mathrm{Grad}_{\mathcal{P}_R} [\, \mu_{R_R} \,] \leq 0 \; , \tag{7.91a}$$

$$A_R^{(7.57)} \, w_R^{(7.57)} \leq 0 \; . \tag{7.91b}$$

with $A_R^{(7.57)}$ the *chemical affinity* of reaction (7.57). A strategy to meet the thermodynamic restriction (7.91a) is to model the flux of receptors by Fickian-diffusion, that linearly correlates $\vec{h}_{R_R}$ to the gradient of its chemical potential $\mu_{R_R}$

$$\vec{h}_{R_R} = -\boldsymbol{M}_R(c_R) \; \mathrm{Grad}_{\mathcal{P}_R} [\, \mu_{R_R} \,] \tag{7.92}$$

by means of a positive definite mobility tensor $\boldsymbol{M}_R$. The following isotropic non linear specialization for the mobility tensor $\boldsymbol{M}_R$ is chosen [29]

$$\boldsymbol{M}_R(c_{R_R}) = \mathbb{u}_R \, c_{R_R}^{max} \; \vartheta_{R_R} \; (1 - \vartheta_{R_R}) \; \mathbb{1} \; , \tag{7.93}$$

where $c_{R_R}^{max}$ is the saturation limit for receptors, and $\mathbb{u}_R > 0$ is the *mobility* of receptors. Definition (7.93) represents the physical requirement that both the pure ($c_{R_R} = 0$) and the saturated ($c_{R_R} = c_{R_R}^{max}$) phases have vanishing mobilities. Neither the mobility $\mathbb{u}_R$ nor the saturation concentration $c_{R_R}^{max}$ are assumed to change in time. Where experimental data indicate an influence of temperature, stresses, or concentrations, such a limitation can be removed without altering the conceptual picture. Noting that

$$\mathrm{Grad}_{\mathcal{P}_R} [\, \mu_{R_R} \,] = \frac{R\,T}{c_{R_R}^{max}} \, \frac{1}{\vartheta_{R_R}(1 - \vartheta_{R_R})} \; \mathrm{Grad}_{\mathcal{P}_R} [\, c_{R_R} \,] \; ,$$

Fick's Law (7.92) specializes as

$$\vec{h}_{R_R} = -\mathbb{D}_R \, \mathrm{Grad}_{\mathcal{P}_R} [\, c_{R_R} \,] \; , \tag{7.94}$$

where $\mathbb{D}_R = \mathbb{u}_R \, R\,T$ is the receptor *diffusivity.*

The chemical kinetics of reaction (7.57) is modeled via the law of mass action (7.83). Experimental evidence [54] shows that: (i) the equilibrium constant (7.77) is high, thus favoring the formation of ligand-receptor complex and the depletions of receptors and ligands; (ii) the diffusion of receptors on the cell membrane is much slower than interaction kinetics. Accordingly, it can be assumed that

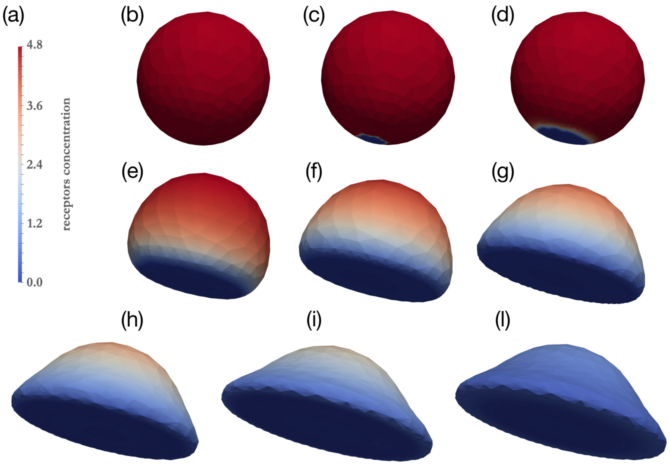

Figure 7.12: Relocation of receptors on the lipid membrane of an EC during cell floating, adhesion, and spreading. (a) Color map molecules molecules $\mu\mathrm{m}^{-2}$; (b) t = 0, the cell in suspension; (c) the cell at the beginning of the attachment; (d) the cell at the end of the attachment; (e) t = 120 s, the cell starts spreading; (f) t = 240 s; (g) t = 360 s; (h) t = 480 s; (i) t = 600 s, the cell at the end of spreading; (l) t = 7200 s, the cell at the end of the experiment. In (b-d) the (virtual) $\mu$slide is depicted for clarity. Figure from [26].

the reaction kinetics is infinitely fast, in the sense that the time required to reach chemical equilibrium is orders of magnitude smaller than the time scale of other processes. For these reasons, we assume that the concentrations of species are ruled by thermodynamic equilibrium at all times, and the concentration of complex $c_{C_R}$ is related to the others by the equation (7.87a). This very same equation could be derived by imposing

$$A^{(7.57)} = 0 \; .$$

Simple algebra allows deriving eq. (7.87a), provided that to the equilibrium constant $K_{\mathrm{eq}}^{(7.57)}$ the alternative definition

$$K_{\mathrm{eq}}^{(7.57)} = \exp\left(-\frac{\Delta G^0}{RT}\right) \tag{7.95}$$

is given, where $\Delta G^0 = \mu_C^0 - \mu_L^0 - \mu_R^0$ is the standard Gibbs free energy.

#### 7.2.3.4 An application

Although the focus of the present note stands in the establishment of a framework, rather than providing a model for any specific phenomenon, it seems to use introducing simple but concrete examples of specific problems, in which the novelties introduced in the previous sections can be used. We refer to [169] Chapter 7 and [34] for the extended dissertation of the data on model predictions and interpretation. Here, we briefly introduce the relocation of vascular endothelial growth factor receptors-2 (VEGFR2) observed in an in vitro experimental setup and replicated numerically. Such a problem was discussed in [54, 100] in the framework of *small displacements and strains* and will be extensively presented in a companion paper [206] using the finite strain multiphysics framework developed herein.

VEGFR2 is a pro-angiogenic receptor expressed on endothelial cells (ECs) and is the main mediator of the angiogenic response. The interaction between VEGFR2 and extracellular ligands, produced by tumor cells, is essential to cancer growth. Specifically, ligand stimulation causes the relocation of VEGFR2 in the basal aspect in cells plated on ligand-enriched extracellular matrix both in vitro and in vivo and ultimately receptors-ligands interactions activate the ECs division and proliferation towards tumor cells. Upon release, growth factors associate with the extracellular matrix and act as ECs guidance during neo-vessel formation.

The binding-unbinding interaction (7.57) was tailored to describe the interaction between VEGFR2 (R) and VEGF (L), which produces a receptor-ligand complex (C). Mass balance equations along the advecting membrane lead to the chemo-transport problem (7.84), which comprises the governing equations for the relocation on the membrane. At present, research on the identification of suitable free energies $\psi_R^{el,iso}(c_{F_R}, \boldsymbol{C}^{e^i}) + \psi_R^{in}(c_{F_R}, \boldsymbol{E}^e - \boldsymbol{\xi})$ for the active stress $\boldsymbol{S}_{active}$ is ongoing, based on statistical mechanics of cytoskeletal reorganization in stress fibers and pseudopodia. We thus accounted only for the passive stress $\boldsymbol{S}_{passive}$ by means of rubber visco-elasticity (7.18). Such a multi-physics initial boundary value problem in the bulk and on the membrane of the cell, rephrased in a weak form and further discretized via finite elements, has been implemented in a high-performance computing code with a staggered Newton-Raphson solver, in the deal.ii framework ( http://www.dealii.org ).

The resulting code has been used to simulate the relocation of VEGFR2 expressed on the cell membrane during the mechanical adhesion and spreading of cells onto a ligand-enriched substrate. A co-designed experimental and computational campaign unveiled the multiphysics progression of the process. The geometrical evolution of the cell was recorded for 2 hours in time-lapse microscopy. During this time span, three mechanically relevant events could be identified: the floating and adhesion of the EC on the ligand-rich $\mu$slide, and eventually the spreading onto the latter. These three events can be recognized in figure 7.12 , which depicts with different colors the relocation of VEGFR2 during the 2 hours time span of the simulation.

Three limiting processes characterize the depletion of VEGFR2. In the first phase, figure 7.12(b)-(d), the VEGFR2 depletion is dominated by the chemical interaction between receptor and ligands during the adhesion between the cell membrane and the ligand-reach substrate. The second phase, up to 600 s, illustrated in figure 7.12(d)-(i), is driven by the mechanical spreading of the cell: the cell-substrate contact dynamics stimulate the formations of complexes since the mechanical spreading makes new free receptors available for the binding with the ligands. Eventually, the last phase is dominated by a lower complex formation rate (from 600 s to 7200 s) and takes place after the EC spreading is completed, thus resulting in transport-dominated, see figure 7.12(i)-(h). Free VEGFR2, guided by concentration gradients, moves from the apical part of the cell towards the basal one, where the binding-unbinding interaction (7.57) occurs. Ultimately receptor depletion is complete on the cell membrane - see figure 7.12(l): such an event is actually unrealistic, since an immobile fraction of VEGFR2 shall be accounted for, as it is illustrated in [206].

### 7.2.4 A probabilistic model for cell-substrate interaction: Shenoy theory

In the current paragraph, an existent probabilist model that was studied during the visiting period at UPENN, University of Pennsylvania, under the supervision of Professor Vivek Shenoy, is presented and discussed. It concerns the dynamics of focal adhesions formed between the cell and the ECM and it examines how cell spreading is affected by ECM mechanical behavior with a constant polymerization speed. No reorganization of cell internal structures is discussed. Such collaboration started in April 2023 and it ended in October 2023.

#### 7.2.4.1 Theoretical insights

Mechanosensitivity of cells, the ability to sense and react to the physical properties of the ECM, is strictly related to FAs. Focal Adhesions are channels that exchange physical and chemical signals, determining the mechanosensitivity

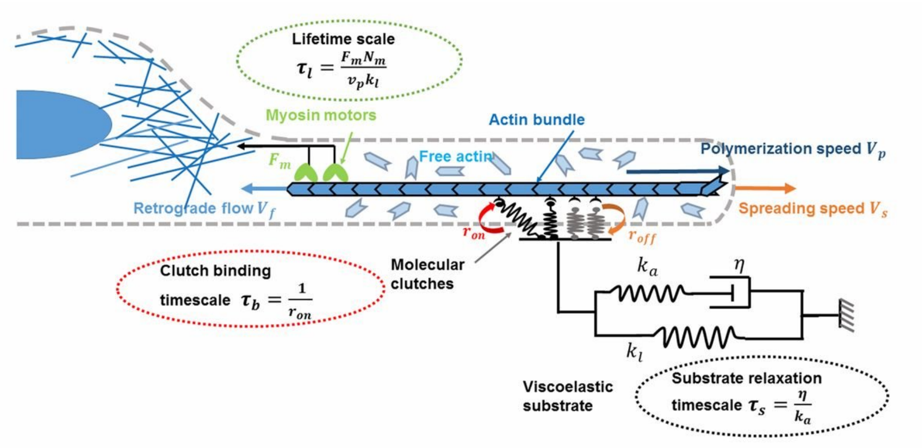

Figure 7.13: Model investigating FA and cell spreading behavior on viscoelastic substrates. Figure from [78].

of cells. Cells can test the stiffness of ECM, measuring the resistance of FAs to actin retrograde flow generated by active myosin contraction, membrane tension, and actin polymerization. Moreover, cells can actively reinforce their adhesion recruiting integrins or activating adhesion proteins, with high surrounding stiffness levels.

In [78], Shenoy's research group systematically studies the dynamics of focal adhesions (i.e. motor clutches) formed between the cell and the ECM. They use both an analytical mean-field analysis and direct Monte Carlo simulations to examine how cell spreading is affected by ECM mechanical behavior. Generally, ECMs have a viscoelastic behavior and exhibit a strong frequency-dependent mechanical response.

They observe two behaviors related to different mechanical properties of ECM. In substrates with low stiffness, viscoelastic behavior can promote cell spreading when the relaxation time ($\tau_s = \frac{\eta}{k_a}$) falls between the timescale for clutch binding ($\tau_b = \frac{1}{r_{on}}$) and its characteristic binding lifetime ($\tau_l = \frac{F_s}{v_0 k_l}$). That is, viscosity serves to stiffen soft substrates on a timescale faster than the clutch off-rate, so enhancing cell-ECM adhesion and cell spreading. In substrates with high stiffness, viscosity will not influence cell spreading, since the bound clutches are saturated by the elevated stiffness [78].

#### 7.2.4.2 Model description

Following the canonical motor-clutch model [213], schematically illustrated in Fig. 7.13, the evolution of state of each clutch is written as

$$\frac{dP_{b,i}}{dt} = (1 - P_{b,i})\, r_{on} - P_{b,i}\, r_{off,i} \;, \tag{7.96}$$

where $P_{b,i}$ represents the probability of the i-clutch to be engaged. When the i-clutch is bound with F-actin filaments, it resists the retrograde flow of actin and undergoes stretching, generating an elastic spring force $F_{c,i}$

$$F_{c,i} = k_c\,(x_{c,i} - x_s) \;, \tag{7.97}$$

where $k_c$ represents the spring stiffness, $x_{c,i}$ the displacement of the i-clutch filament end and $x_s$ the displacement of the substrate.

The reaction rate parameters are written as

$$r_{off,i} = r^0_{off,i} \cdot exp\,(\frac{F_{c,i}}{F_b}) \;, \tag{7.98a}$$

$$r_{on} = r^0_{on}\,(1 + \alpha(F_a - F_{cr})) \quad \text{with } (1 + \alpha(F_a - F_{cr})) = 1 \quad \text{if } F_a < F_{cr} \;, \tag{7.98b}$$

where $F_b$ is a characteristic force, $r^0_{off}$ represents the breaking rate of clutches in the absence of any force, $F_{cr}$ represents a force threshold and the term $(1 + \alpha(F_a - F_{cr}))$ reflects the reinforcement of FAs (through the recruitment of integrins to the adhesion complex via talin unfolding) on stiff substrates, namely once the average clutch force $F_a$ surpasses a force threshold $F_{cr}$ [78].

The ECM is represented as a standard linear viscoelastic material as

$$(k_a + k_l)\eta\frac{dx_s}{dt} + k_a k_l x_s = k_a F_s + \eta\frac{dF_s}{dt} \;, \tag{7.99}$$

where $\eta$ represents the viscosity of the dashpot, $k_a$ and $k_l$ the additional and long-term stiffness.

The total load transmitted to the substrate due to the stretching of the engaged clutches is

$$F_s = \sum_{i=1}^{n_c} F_{c,i} = \sum_{i=1}^{n_c} k_c\,(x_{c,i} - x_s) \;, \tag{7.100}$$

which represents the sum of the forces exerted by the bounded clutches. The retrograde flow speed, $V_f$, is influenced by the total load transmitted to the substrate via

$$V_f = v_u \cdot \big[1 - \frac{F_s}{n_m F_m}\big] \ . \tag{7.101}$$

The velocity of the filament end of the i-clutch depends on the retrograde flow $V_f$ and the displacement of the ECM. In particular, when the clutch is engaged, it moves at the same velocity as the retrograde flow, but when it is not engaged, it carries zero loads, so it moves with the substrate, $x_{c,i} = x_s$. Thus, the velocity of the filament end of the i-clutch is

$$\frac{dx_{c,i}}{dt} = (1 - P_{b,i})\,\frac{dx_s}{dt} + P_{b,i}\,V_f \ . \tag{7.102}$$

It has been found that the sum of retrograde flow velocity and the actin protrusion velocity remains constant. It means that the velocity of polymerization is a constant, so the spreading velocity is

$$V_s = V_p - V_f \ , \tag{7.103}$$

where $V_f$ represents the retrograde flow speed and $V_p$ represents the constant velocity of polymerization. Here, it should be noted that the spreading velocity $V_s$ is the initial spreading speed when the cells are seeded on the substrates. After this initial phase of polymerization, the outward motion of the actin filaments is countered not only by rearward forces from the myosin motors but also by the resistance of the plasma membrane, eventually leading to a steady-state configuration where the cell spreading area becomes constant. So, after the initial phase, the force of FAs is countered by the myosin pulling force and the resistance force generated by the deformed cytoskeleton and membrane. Under such circumstances, the force equilibrium becomes

$$f_{FA} = f_c + f_m \ , \tag{7.104}$$

where the resistance force $f_c$ is calculated as

$$f_c = h\,\sigma_r = h\big(k_m\,\epsilon_r + \eta_m \frac{d\epsilon_r}{dt}\big) \ . \tag{7.105}$$

The steady-state spreading area is a function of the initial spreading velocity, initial spreading radius, and the properties of the cytoskeleton and cell membrane: the spreading radius increases linearly with respect to the initial spreading speed.

Using a mean-field approach, we can average the behavior of all clutches into a single "ensemble" with effective stiffness $k_c n_c P_b$, where $P_b$ is the fraction of clutches remain engaged [78].

#### 7.2.4.3 Timescales of the model

Three timescales govern the model behavior: clutch binding timescale ($\tau_b = 1/r_{on}$), FA lifetime scale ($\tau_l = F_m N_m / v_u k_l$), and substrate relaxation timescale $\tau_s = \eta/k_a$. These are the definitions

- $\tau_l = F_m N_m / v_u k_l$: the FA lifetime scale is the characteristic time it takes the clutches to develop sufficient force to stall the motor forces. As the clutches attach to the actin filament and stretch, the force they exert on the substrate increases at a rate $v_u k_l$. The motor forces that pull the filaments are represented by $F_m N_m$. The lifetime of FA, named $t_{life}$, is proportional to $\tau_l$;
- $\tau_b = 1/r_{on}$: the clutches binding timescale defines the timescale for the clutches to bind, which is also correlated to the formation time ($t_{bind}$) of the FAs;
- $\tau_s = \eta/k_a$: the substrate relaxation timescale defines the relaxation timescale of the viscoelastic ECM. Essentially, upon loading, the effective substrate stiffness decays exponentially (with the timescale $\tau_s$) from its initial value of $k_a + k_l$ to the long-term stiffness, $k_l$.

Depending on the value of the two timescales, the FA cluster exhibits different behaviors that eventually lead to different cell spreading. Basically, depending on the values of the two timescales $\tau_b$ and $\tau_l$, which approximately describe the binding time ($t_{bind} \propto \tau_b$) and lifetime ($t_{life} \propto \tau_l$) of the FA, the clutches and cell spreading behave totally differently [78].

#### 7.2.4.4 Model flowchart

Here is the list that depicts the simulation algorithm for getting the steady-state spreading configuration:

1. **Initialization:** at $t = 0$, we have the ratio $R(0)$, the actin retrograde flow $V_f(0) = v_u$, the total load transmitted to the substrate $F_s(0) = 0$, the probability of the i-clutch to remain engaged $P_{b,i}(0) = 0$, all the forces of the i-clutch $F_{c,i}(0) = 0$, displacement of the filament end of the i-clutch $x_{c,i}(0) = 0$ and the displacement of the substrate $x_s(0) = 0$;

2. **Clutches probability:** since $r_{off,i} = r^0_{off,i}$ and $r_{on} = r^0_{on}$ at $t = 0$, we can find the probability of the i-clutch to remain engaged $P_{b,i}$ with equation

$$\frac{P_{b,i}(t+\Delta t) - P_{b,i}(t)}{\Delta t} = (1 - P_{b,i})\, r_{on} - P_{b,i}\, r_{off,i} \ ; \tag{7.106}$$

3. **Substrate/clutches displacements:** since we have $P_{b,i}$, $V_f(0) = v_u$, we can find $x_{c,i}$, $F_s$ and $x_s$ via equations

$$\frac{x_{c,i}(t+\Delta t) - x_{c,i}(t)}{\Delta t} = (1 - P_{b,i})\, \frac{x_s(t+\Delta t) - x_s(t)}{\Delta t} + P_{b,i}\, V_f \ , \tag{7.107}$$

$$F_s = \sum_{i=1}^{n_c} F_{c,i} = \sum_{i=1}^{n_c} k_c \left(x_{c,i} - x_s\right) \ , \tag{7.108}$$

$$(k_a + k_l)\eta \frac{x_s(t+\Delta t) - x_s(t)}{\Delta t} = k_a \frac{F_s(t+\Delta t) - F_s(t)}{\Delta t} + \eta \frac{dF_s}{dt} - k_a k_l x_s \ ; \tag{7.109}$$

4. **Cytoskeleton resistance force:** since we have $R(t)$, we find the cytoskeleton strain and so the resistance force via equation $f_c = h\sigma = h(k_m \epsilon_r + \eta_m \frac{d\epsilon_r}{dt})$, where $\epsilon_r = \frac{R(t) - R_0}{R_0}$;

5. **Myosin force:** based on force equilibrium and since the adhesion force is $f_{FA}$, we calculate myosin forces $f_m = f_{FA} - f_c$;

6. **Spreading velocity:** we can find actin retrograde flow as $V_f = v_u \cdot \left[1 - \frac{F_s}{n_m F_m}\right]$ and so the spreading velocity as $V_s = V_p - V_f$;

7. **Radius:** we can update the spreading radius $R(t)$, integrating the spreading speed;

8. **Time:** we can advance in time $t = t + \Delta t$ and restart from point 2.

In order to solve the problem, Kinetic Monte Carlo simulations and a mean-field approach are used. For the Mean-Field Analysis, all clutches' behaviour is averaged into one ensemble clutch with effective stiffness $k_c n_c P_b$, where $P_b$ represents the average binding probability, $x_c$ the average displacement and $F_c$ the average force transmitted of any clutch. So, the governing equations are written as

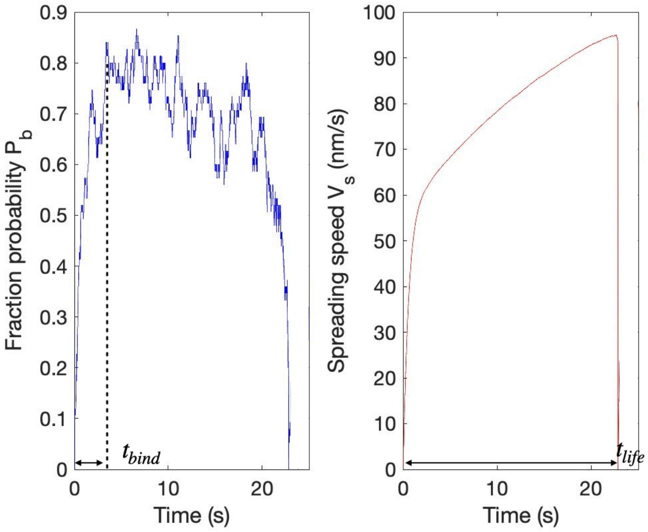

Figure 7.14: Results of the fraction of engaged clutches and spreading speed for a set of parameters ($k_a = 1pN/nm$, $k_l = 0.1pN/nm$, $\eta = 1pN \cdot s/nm$). When $t > t_{bind}$ clutches start to break. At $t = t_{life}$, all clutches break with the classical "load and fail" response [78].

$$\frac{P_b(t+\Delta t) - P_b(t)}{\Delta t} = (1 - P_b)\, r_{on} - P_b \; < r_{off} > \,, \tag{7.110a}$$

$$(k_a + k_l)\eta \frac{x_s(t+\Delta t) - x_s(t)}{\Delta t} + k_a k_l x_s = k_a F_s + \eta \frac{F_s(t+\Delta t) - F_s(t)}{\Delta t}\,, \tag{7.110b}$$

$$F_s = k_c n_c P_b (x_c - x_s)\,, \tag{7.110c}$$

$$\frac{x_c(t+\Delta t) - x_c(t)}{\Delta t} = v_u \left(1 - \frac{F_s}{n_m F_m}\right)\,, \tag{7.110d}$$

where

$$\frac{x_c(t+\Delta t) - x_c(t)}{\Delta t} = V_f \;. \tag{7.111}$$

Since the ensemble clutch is assumed to remain bounded during its lifetime, its filament end moves with the retrograde flow velocity $V_f$ [78].

The reaction rate parameters read

$$< r_{off} > = r^0_{off} \cdot exp(F_c/F_b) \ , \tag{7.112a}$$

$$r_{on} = r^0_{on} \left(1 + \alpha(F_a - F_{cr})\right) \quad \text{with } (1 + \alpha(F_a - F_{cr})) = 1 \quad \text{if } \ F_a < F_{cr} \ , \tag{7.112b}$$

with $F_a$ the average FA force (during each lifetime cycle) and $F_{cr}$ a threshold level [78].

The spreading velocity is written as

$$V_s = V_p - V_f \ , \tag{7.113}$$

with $V_p$ the polymerization speed of the actin bundle. The mean spreading velocity is evaluated over one formation-breakage cycle. A simple average of $V_f$ in every time step is recorded in KMC simulation to obtain the mean retrograde velocity. In the mean-field approach, the total clutch displacement $x_c$ is calculated in the time $t_{total}$ by solving the ODEs described above, from which the average retrograde flow speed can be estimated as

$$V_f = \frac{x_c}{t_{total}} \ . \tag{7.114}$$

#### 7.2.4.5 Outcomes

To characterize the cellular spreading behavior, they use the mean spreading speed, $V_s$, calculated by averaging the speed over the FA lifetime ($t_{life}$). The main results are the following

- Intermediate viscosity $\eta$ promote cell spreading for soft substrates;
- Spreading is optimal when substrate relaxation timescale is comparable to clutch binding timescale [78].

Using Kinetic Monte Carlo simulation, we obtain the fraction of bounded clutches and the cell spreading speed in a 1D case with a standard linear viscoelastic substrate over the FA life cycle (the time elapsed between two $P_b = 0$) (see figure 7.14).

The clutches engage at the beginning, since $F_c = 0$ (no stretching of clutches), so the spreading speed and substrate displacement increase. When $t > t_{bind}$ clutches start to break, even if the load level inside keeps increasing. At $t = t_{life}$, namely the binding lifetime for a FA, all clutches break: this is the classical "load

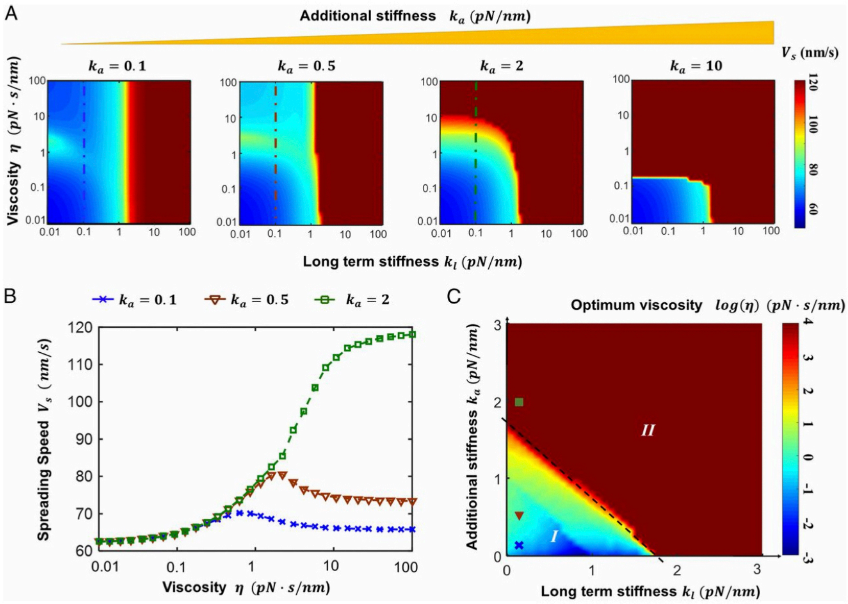

Figure 7.15: Cell spreading speed is significantly different based on the elastic and viscous parameters $(k_a, k_l, \eta)$ of the substrate [78]. Figure from [78].

and fail" response produced also by other motor-clutch models. The lifetime $t_{life}$ gradually increases with substrate stiffness (when the clutch reinforcement takes place), since it increases the binding rate $r_{on}$ and a high percentage of clutches remain engaged. Hence, the clutches would form bonds very quickly, with a characteristic binding timescale $\tau_b = 1/r_{on}$. For a stable FA formed in the load and fail regime, the binding time can be estimated (by assuming most clutches become engaged) as $t_{bind} \approx ln(N_c)/r_{on}$. As motors keep pulling the actin bundle toward the cell center, the clutches sustain higher loads and start to break. This is reflected by a gradual drop in the fractional probability $P_b$ after the initial binding stage [78]. Finally, all clutches become broken at $t = t_{life}$ (often referred to as the lifetime of FA cluster) and this effectively completes the formation-breakage cycle. Note that $t_{life}$ can be approximately estimated as $t_{life} \approx F_{s,max}/v_u k_s$, i.e. the time needed for the substrate force $F_s$ to reach its maximum at substrate deformation force rate, $v_u k_s$. Here, $k_s$ represents the effective stiffness of the substrate. Considering the limiting scenario where FAs exist for a long time, the maximum substrate force $(F_{s,max})$ in this case is simply the total myosin pulling force $F_m N_m$, while $k_s$ should be interpreted as the long-term stiffness of the substrate, leading to a characteristic lifetime scale $\tau_l = F_m N_m / v_u k_l$ [78].

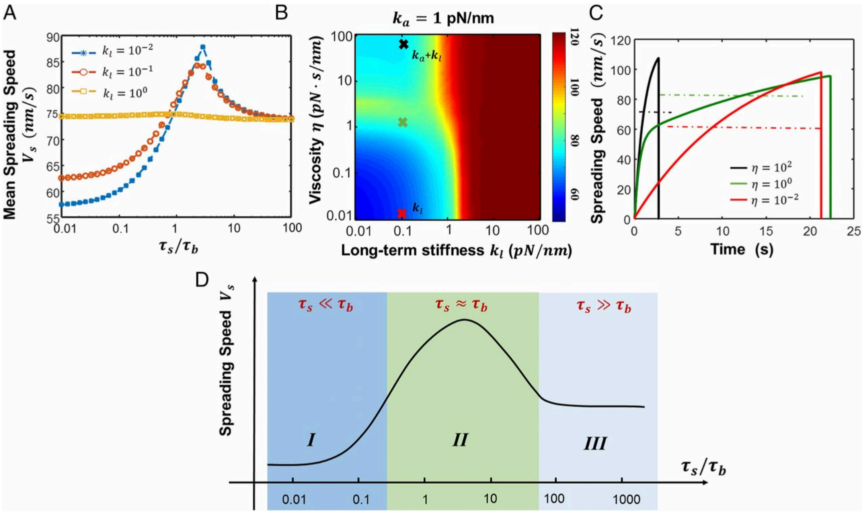

Figure 7.16: Optimal substrate viscosity is determined by the ratio between the substrate relaxation ($\eta_s$) and clutch binding ($\eta_b$) timescales [78]. Figure from [78].

In figure 7.15A-B, the response of the standard linear model is shown. It is dictated by three parameters: the long-term stiffness $k_l$, the additional stiffness $k_a$, and the viscosity $\eta$. For a constant applied substrate displacement, $k_a + k_l$ represents the initial stiffness of the substrate, $k_a$ represents the drop in stiffness as the substrate relaxes, and $k_l$ represents the equilibrium substrate stiffness. Depending on the elastic parameters, viscosity can influence cell spreading in very different ways. When the viscosity is very small, the response of cells is largely determined by the long-term ECM stiffness, which is similar to the case of purely elastic substrates [78]

$$k_l x_s = F_s \ . \tag{7.115}$$

However, as viscosity increases, the spreading behavior is highly affected by both the long-term and additional stiffness of the substrate. Specifically, viscosity was found to promote cell spreading for soft substrates (namely with relatively low long-term stiffness) as it increases the effective stiffness that cells can sense, leading to maximized cell spreading at intermediate viscosity values (see figure 7.15B). In comparison, for substrates with a large long-term stiffness ($kl > 5pN = nm$), viscosity has a negligible effect on cell spreading, as the number of clutches that can be formed has reached a plateau due to the elevated ECM rigidity in this case (see figure 7.15A) [78].

The optimum viscosity (for inducing maximized cell spreading) as a function of both the long-term and additional substrate stiffness is given in figure 7.15C. In regime I, optimal cell spreading is achieved at intermediate levels of viscosity for compliant ECMs, while, in regime II, the largest spreading occurs when viscosity is large [78].

To investigate the optimum in cell spreading that is observed at intermediate viscosities for soft substrates, the relevant timescales controlling cell spreading in the model are analyzed [78].

In figure 7.16A, the mean spreading speed is investigated with different values of $\tau_s/\tau_b$ and $k_l$. Maximal cell spreading occurs at intermediate viscosity values when the substrate relaxation timescale $\tau_s$ is within an order of magnitude of $\tau_b$. This behavior can be explained by examining the cell spreading that occurs during a single FA lifetime in relation to the three pertinent timescales ( $\tau_b$, $\tau_l$, $\tau_s$) [78].

In figure 7.16B-C, the heat map of spreading speed $V_s$ as a function of the long-term stiffness, $k_l$, and viscosity, $\eta$, and the spreading speed vs. time for three typical values of $\eta$ are plotted [78].

These are the main results:

- when $\tau_s < \tau_b$, the ECM stiffness relaxes rapidly to its long-term value faster than the clutches can fully bind to the substrate. Consequently, the FAs only sense the long-term stiffness, $k_l$, and the effect of viscosity becomes negligible. In this case, a typical clutch behavior in a one-lifetime cycle is shown by the red curve in figure 7.16C [78];

- when $\tau_b < \tau_s < \tau_l$, FAs sense a gradual change of stiffness during their formation-disruption cycle. Cells gradually sense the relaxed stiffness that helps FAs extend their lifetime corresponding to the long-term stiffness. The net outcome is that actin retrograde flow is suppressed at the beginning while a long FA lifetime is maintained, thereby maximizing cell spreading. Specifically, if $\tau_l$ is larger than $\tau_b$, a large number of clutches will remain engaged before total rupture occurs, a scenario referred to as the "load and fail" behavior. However, when the substrate becomes stiffer (corresponding to $\tau_l < 1/r_{on}^0$), the clutch reinforcement begins to take effect, while the timescale analysis does not apply. The gradually increasing integrin density due to the reinforcement mechanism elevates the binding rate, which further extends FA lifetime. These long stable FAs could offer large resistance forces to counter the retrograde flow, thus promoting cell spreading. As a comparison, they also discuss the case without clutch reinforcement. Similarly, when $\tau_b < \tau_l$ the reinforcement will not have an effect, since the average clutch force has reached a threshold value. The clutches would perform the same "load and fail" behaviors [78];

- when $\tau_s > \tau_l$, the substrate does not relax during the lifetime of the FA. As such, the ECM behaves elastically, with the effective stiffness $k_a + k_l$. A representative response of an FA in this regime is shown by the black curve in Fig. 7.16C, with a sharp increase in the spreading speed at the beginning, yet a very short lifetime [78];
- when $\tau_l < \tau_b$, clutch reinforcement takes effect and leads to saturation of the cell spreading area; in this case, viscosity has no effect on cell spreading. No stable clutches or adhesion can be formed. Instead, the FA cluster goes through rapid binding and breakage, with its lifetime typically less than 1 $s$. Under such circumstances, labeled as the "frictional slippage" regime, the substrate displacement is almost negligible, while the retrograde flow velocity is essentially the polymerization speed, resulting in stalling of cell spreading. In this case, an optimum ECM stiffness leading to maximized spreading speed can be obtained in this transitional regime when the cluster binding time equals its lifetime. Hence, a medium substrate stiffness will promote cell spreading, a conclusion that is also obtained from their results under low ECM viscosity conditions [78].

In figure 7.16D, three regimes show distinct regulation effects as the relaxation timescales are varied. Note that this only applies to soft substrates; as the long-term stiffness increases, the clutch reinforcement mechanism increases the binding rate, saturates bounded clutches, and weakens the viscosity effects. The end effect is that the substrate properties and clutch binding kinetics produce phenomenological timescales that must be precisely tuned so that substrate viscoelasticity has a significant impact on cell spreading. Specifically, for viscosity-based regulation to be significant, the material relaxation timescale $\tau_s$ should be larger than (or at least comparable to) the characteristic binding time $\tau_b$ of the clutches [78].

## 7.3 Concluding remarks

In this chapter, several continuum and probabilistic models, that illustrate different processes involved in cell ABM, have been put forward.

We summarize theoretical approaches and computational methodologies developed since the late 1970s, in modeling protein motion along advecting membranes, ECM-cell interactions by molecular clutches, and cell F-actin structure reorganization for different biological systems. It has been our aim to collect some of the most emblematic mathematical and computational methodologies, providing a broad introduction to a scientific topic that is in great development nowadays. We also aim to recollect recent publications from several schools on cell mechanics, encasing them in a unified framework, being aware that a comprehensive account of publications is significantly hard in view of the broadness of the literature in the field. We clarify that for some processes, as for contractility and protrusion, either a thermodynamically consistent formulation has not been devised yet or it stems from simplistic models that do not account for the microstructural evolution of the biopolymers. Even in this fascinating field, the last word is far from being spoken.

Moreover, we propose two novel models and some results related to two existing models that describe several phenomena pivotal for cell ABM. The two novel models describe the mechanical evolution of F-actin network protrusion in the cellular bulk and receptors motility along the advecting membrane. The results related to the existing models come from the Deshpande-McMeeeking constitutive theory and Shenoy's model.

The first new model describes cell F-actin protrusion at a continuum level, extending the model presented in [6]. The second new model is characterized by a multi-physics framework that illustrates protein relocation on the advecting lipid membrane during cell spreading and motion. It sets the (continuum) thermodynamic background for the simulations of receptor recruitment during migration, extending previous simulations proposed by our lab: simulations carried out in [54] stem from a simplified form of the framework and describe the limiting factors in vascular cell growth factor receptors relocation; similarly, in [101] the relocation of integrins on the membrane and their interactions with growth factor receptors is discussed; a companion paper [206] deals with the relocation of vascular endothelial growth factor receptors on advecting lipid membrane during endothelial cell adhesion and spreading. Those simulations may have a significant impact on biology and in the pharmacological treatment of cancer, either in view of their predictive nature in virtual experiments or by clearly identifying the sequence of processes that limit the relocation of targeted proteins during in vitro experiments.

The present works on cell ABM still have significant limitations. First of all, the profound bibliographic research carried out during the Ph.D. and the novel models presented in this chapter do not account for the behavior of a specific cell, but they represent the processes involved in the ABM of different types of cells. This course of action simplified our work because it allowed us to split the phenomena involved in ABM in different models, but it represents a big limitation for a complete and correct description of the ABM of a specific type of cell. Each cell has a peculiar biological behavior that must be taken into account in order to propose a unique and correct multi-physics model.

Moreover, many phenomena of cell ABM were not considered and many cellular behaviors have been simplified both in the existing literature and in our new models. For example, the constitutive law that represents the mechanical behavior of the F-actin network has been greatly simplified and it is far from being correctly defined. The internalization of complexes, the role of membrane resistance, and the reorganization of F-actin in cell bulk during cell motility are all occurrences not included in this work. The role of ECM mechanical behavior in cell ABM both in a 1D, 2D, and 3D setting has been insufficiently discussed here. Furthermore, in view of having a general and broad representation of cell ABM, the protein transport on the membrane and the cytoskeleton reorganization have been discussed separately, even if they are crucially coupled: the cytoskeleton reorganization is related to the motion of integrins on the membrane and the formation of focal adhesion sites is preliminary to F-actin protrusion, stress fibers generation, and contractility. So, the discussion of these two phenomena turns out to be incomplete in this thesis.

A remarkable effort must be made to couple the different models that we have presented here, so further publications will be devoted to extending these frameworks to these and other challenging tasks. Nevertheless, by illustrating a complex and rigorous scenario, these models might be a cornerstone to account for several cellular processes.

# Chapter 8

# Conclusions and future developments

In this thesis, we present several multi-physics models for the ABM of pathogens and cells. These models are suitable for investigating, describing, and predicting the key mechanisms that govern ABM processes, and they are embedded in the newly emerging scientific discipline called "mechanobiology". Mechanobiology provides the tools for describing the evolution of biological phenomena, while multi-physics models give a rationale for biological phenomena behaviors, becoming predictive methodologies for the evolution in time of several quantities of interest.

The use of physical-mathematical modeling and subsequent computational analysis uncovers the concealed key mechanisms within living matter. Consequently, interdisciplinarity is the focal point of our endeavors. The objective is to facilitate the mutual exchange of scientific knowledge and methodologies, leading to the establishment of a mechanobiology group. This group, in turn, has given rise to an *Interdepartmental Center for International Research in Mechanobiology*, capable of describing and quantifying the mechanical contributions to cellular activities.

The shared intent between biologists and engineers bestows interpretative and predictive capabilities on the models developed. The combination of current theoretical knowledge with the increasing ability to calculate and process experimental data, coupled with the greater availability of high-precision tools for biologists, necessitates the construction of an exact science. This science harmoniously integrates principles from physics, biology, and engineering to address the evolving demands of the scientific landscape. Co-designing theoretical multi-physics frameworks, numerical simulations, and experimental outcomes, allows the identification of the laws that regulate several biological events, thus opening new perspectives to support biological and medical research.

**Motivations**. The present research aims to develop multi-physics models capable of describing, interpreting, and predicting the fundamental mechanisms governing ABM. This endeavor is part of a long-term plan aimed at creating several multiphysics models delineating the primary stages of cancer metastasis. ABM modeling is prioritized due to its fundamental nature and its prevalence across various organisms, including simpler ones like bacteria.

Metastasis remains the foremost challenge in cancer clinical management. Hence, it is crucial to elucidate the mechanisms underlying ABM with the ultimate aim of identifying combination therapies that enhance the motility of beneficial cells while impeding the spread of harmful ones. A deeper understanding of ABM could lead to significant advancements in both pro- and anti-angiogenic therapies. Consequently, the development of in-silico simulations could yield substantial contributions to biology and pharmacological interventions for pathological angiogenic occurrences. These simulations hold potential significance due to their predictive capabilities in virtual experiments, as well as their ability to elucidate the sequence of ABM processes.

## 8.1 Multi-physical models and Results

Two different biological phenomena are illustrated throughout the dissertation, i.e., pathogen and cell ABM, each of which two chapters of the thesis are dedicated. The pathogen ABM is extensively examined from a biological and a mathematical point of view, and a unique multi-physics model, that expresses the mathematical coding of the mechanical behavior of the system, is proposed. Cell ABM, instead, is extensively studied from a biological point of view, illustrating a review of the different mechanical behavior of cells, and lingering on the peculiar case of keratocytes. Then, aiming at overviewing the ABM modeling, several models that come from the existing literature and original contributions are presented.

### 8.1.1 Pathogens ABM

The pathogen ABM model entails an interaction among external signaling, the elastic response of the polymerized actin network, and the kinetics of the chemical reaction between the monomeric form of G-actin and the network of F-actin. It is shown that the model captures the general features of pathogen motility observed in experimental studies, including the signal dependence of polymerization of the F-actin network on the bacterium tail and the F-actin network distribution during pathogen motility. The model is characterized by some features and assumptions. We do not account for anisotropy in the multiplicative decomposition of the deformation gradient, since generally the network is not aligned to a preferential direction. We assume an isotropic behavior of the network, with uniform swelling behavior in the area of the cell where the signal is emitted. Moreover, we neglect the dependence of the reaction rate parameters on the load, even if the production of the F-actin network can be drastically affected by the forces the network is subjected to. In the model of bacterial pathogen motility, we consider an elastic strain-energy function of the Saint-Venant type, without cross-link protein rearrangement, because of the “high” speed of bacteria in the host cytoplasm. In reality, cross-link reorganization can occur in pathogens and certainly takes place in cellular motility. More sophisticated, statistically based continuum theories can be invoked to capture the consequent rate-dependent behavior of the F-actin network upon mechanical loading. While the consistency of the chemomechanical motor is verified for bacterial pathogen motility, we limit ourselves to the assumption of material parameters independent of F-actin concentration. To account for the role of concentration in the stiffness of the F-actin network, further work is required.

### 8.1.2 Cells ABM

Cells ABM is described taking into account several models that come from the existing literature and original contributions. First, we give an overview of the state of the art, presenting several models that describe the mechanical evolution of cells' internal structures, receptor motility on the membrane, and cell-substrate interaction. Then, we introduce two new models and some results that come from the existing literature that concern several aspects of ABM.

The first one is an original model, inspired by [6], that describes the mechanical behavior of the F-actin network lamellipodia protrusion in keratocytes. The model is composed of a multi-physics framework that describes F-actin network protrusion at a continuum level and it is an extension of the pathogen ABM model described in chapter 3. We consider three different species: F-actin, G-actin, and the cytosol inside the cell. The kinematic development of the F-actin network is described by the multiplicative decomposition of the deformation gradient into a chemical and a mechanical part, whereas the mechanical behavior of G-actin is neglected and the cytosol is considered as an incompressible fluid. Then, we illustrate the Deshpande-McMeeking constitutive theory for stress fibers contractility, and we obtain a numerical result from this model [77, 36]. This model accounts for the dynamic reorganization of the cytoskeleton during cell adhesion and deformation on an engineered substrate. The result of the one-dimensional biomechanical simulation shows how the cytoskeleton contractility behaves under a defined displacement field and the effect of a support stiffness. They show that the stiffness of the substrate affects the formation of stress fibers.

Subsequently, we define a continuum multi-physics scheme for modeling the relocation of proteins on advecting lipid membranes, framing the mathematical setting within the mechanics and thermodynamics of continua [24]. The model can represent the receptor distribution along the cellular membrane and the complex formation when the receptors are in contact with the integrins on the ECM. Moreover, a concrete example of a specific problem, in which the novelties introduced in the sections can be used, is shown. In particular, we briefly describe the relocation of vascular endothelial growth factor receptors-2 (VEGFR2) observed in an in-vitro experimental setup and numerically replicate it. Such a problem is discussed in [54, 100] in the framework of small displacements and strains, and it is presented here using a finite strain multi-physics framework. In addition, a probabilistic theory that extensively studies the role of the viscoelastic behavior of ECM on cell spreading and motility is illustrated [78].

## 8.2 Future developments

The positive outcomes derived from the multi-physics models illustrated in this thesis motivate us to further enhance them through the incorporation of more detailed formulations. Future results, both from a theoretical and numerical standpoint, will be published in further works.

**Model assumptions** The model representing the F-actin network is characterized by some features and assumptions. First, we chose the volume as the mechanical descriptor of F-actin network swelling. Following [58, 59], the volumetric approach can be transformed into a boundary layer problem, where the interface is represented by the tip of the F-actin network. In this case, the tip of the F-actin network is the only part that acts against the external load, and the mechanical role of the F-actin network in the volume is neglected.

We did not account for the anisotropy in the multiplicative decomposition of the deformation gradient. As highlighted in [63, 64], filaments in the F-actin network generally do not seem to be aligned in a preferential direction, rather, they form a matrix of arbitrarily oriented strands: fibers perpendicular to the direction of motion are visible even in the depolymerized zone. F-actin network evolution is dictated by the motion of the signal, which is emitted at different positions in time. In reality, the orientation of filaments inside the F-actin network can change and assume a preferential direction depending on several factors, such as altered loads and actin density (see section 6.4.1.2).

Moreover, the assumption that both the forward and backward reaction parameters, capable of inducing the formation and decomposition of the F-actin network, are force-independent is a simplification of the real process since the presence of the load force can drastically affect both $k_f$ and $k_b$, as explained in [5].

We delayed further studies on the multi-scale and multi-physics description of the energetics of the nucleation, polymerization, and branching of actin filaments into the F-network: all biological events have been condensed into a single signal.

In addition, we neglected the presence of other networks and cell internal structures that can affect the mechanical behavior of the cell and can interact with the F-actin network, such as intermediate filaments, microtubules, and nucleus.

For this reason, further studies must be conducted to account for these structures and to propose a thermodynamically consistent formulation that can describe completely the F-actin network mechanical behavior.

**F-actin network constitutive law** As we already explained, the governing equations that define the multi-physics continuum models hold for any specification of the Helmholtz free energy. Since the focus of this thesis was the ABM engine, we arbitrarily and simplistically considered an elastic strain-energy of Saint-Venant type in all the numerical simulations, without considering cross-link protein rearrangement and F-actin network reorganization during motility. In reality, cross-link reorganization can occur in actin polymerization, and the mechanical behavior of the F-actin network is severely affected by this, as illustrated in [5, 73].

It is broadly recognized that the mechanical resistance of the F-actin network depends on the concentration of F-actin filaments in the network and the mechanical parameters that represent the F-actin network's mechanical behavior should be affected by this. While the consistency of the chemomechanical motor has been verified for bacterial pathogen motility, we limited ourselves to the assumption of material parameters independence of F-actin concentration. To account for the role of F-actin concentration in the stiffness of the network [53, 5], further work is required.

Viscosity was purposely neglected because it was argued that the cross-linking rearrangement in the F-actin network has insufficient time to develop [46] in view of the "high" speed of bacteria in the host cytoplasm. In reality, cross-link reorganization can occur in pathogens, certainly taking place in cellular motility, and the force-velocity relation of actin-network growth requires a thorough study, which started from the experiments done by Theriot's group in [5]. More sophisticated, statistically-based continuum theories can be invoked to capture the consequent rate-dependent behavior of the F-actin network upon mechanical loading [56, 57]. One of the possible models is represented by F.J. Vernerey and co-workers' [57]. The fundamental concept involves idealizing actin monomers (G-actin) as monodisperse (or polydisperse, considering other polymer networks like microtubules) polymers within the cytoplasm. Concurrently, through polymerization, these monomers become generators of F-actin chains that support the actin network in cell protrusions. The configuration of these chains can be statistically described using a distribution function. To capture the dynamics of the polymerization and depolymerization of G-actin into F-actin, and vice versa, we consider the polymerization-depolymerization process. Specifically, referring to the deformation gradient decomposition ($\boldsymbol{F} = \boldsymbol{F}^e \boldsymbol{F}^c$), we assume that the viscoelastic behavior of the F-actin network is connected to the tensor $\boldsymbol{F}^e$ and is fully described by a dynamic characterization of the evolution of the F-actin network.

In this framework, the viscoelastic machinery is outlined by the attachment and detachment of actin filaments, while the polymerization-depolymerization phenomena govern the density of the total chain available to form the actin network. This contribution, combined with the effects of the swelling distortion tensor, comprehensively describes the dense network of actin filaments within pseudopodia.

**Cells two-way coupled models** The models on cell ABM presented in this thesis have significant limitations. First of all, the profound bibliographic research carried out during the Ph.D. and the novel models presented in this chapter do not account for the behavior of a specific cell, but they represent the processes involved in the ABM of different types of cells. This course of action simplified our work since it allowed us to split several phenomena into different models, but it represents a significant limitation for a complete and correct description of ABM for a specific type of cell. Each cell has a peculiar biological behavior that must be correctly represented to propose a unique multi-physics model.

Moreover, many phenomena of cell ABM were not considered, and many cellular behaviors have been simplified both in the existing literature and in our new models. For example, the constitutive law representing the mechanical behavior of the F-actin network has been greatly simplified and it is far from being correctly defined. Additionally, to have a general and broad representation of cell ABM, the protein transport on the membrane and the cytoskeleton reorganization have been discussed separately, even if they are crucially coupled: the cytoskeleton reorganization is related to the motion of integrins on the membrane and the formation of focal adhesion sites is preliminary to F-actin protrusion, stress fiber generation, and contractility. Therefore, the discussion of these two phenomena turns out to be incomplete in this thesis.

By combining the description of the chemo-diffusive aspects of the integrin receptor on the cell membrane, including the modeling of clustering procedures observed in adhesion sites and the phenomena of internalization/externalization, with an active portrayal of the mechanical behavior of cells, it will be possible to upgrade the one-way coupled models hereto discussed in a two-way coupled formulations. In this new scheme, the activities of receptors (integrins) on the lipid bilayer collaborate to organize the mechanical response of the cell, facilitating the formation of adhesion sites and influencing the arrangement of F-actin networks.

Consequently, we aim to incorporate a thermodynamically motivated model that describes the remodeling of the F-actin network and the interaction between actin and myosin II during F-actin reorganization. If the contractile machinery of SFs within the chosen cell is similar to that observed in muscle sarcomeres, as demonstrated in fibroblasts, the model formulation proposed by [103] will be considered; otherwise, alternative and innovative models may be required. Additionally, a coarse-grained model based on principles of statistical mechanics is essential to establish connections between the microscopic properties of the actin network and the macroscopic properties determinable at the continuum scale.

Therefore, further extension of this pattern could emerge through a statistical continuum theory, enabling the study of the transient actin network in both globular (G-actin) and filamentous (F-actin) forms. This extension aims to provide an innovative characterization of the mechanical description of cell motility guided by actin polymerization, directly building upon the formulations derived in Chapter 7. Being inspired by [73], it could also be of interest to apply a multi-scale approach where the microscopic behavior of actin and receptors is correlated to the mechanical behavior of cells at a continuum level.

A remarkable effort must be made to couple the different models that we have presented here, so further publications will be devoted to extend these frameworks to these and other challenging tasks. Nevertheless, by illustrating a complex and rigorous scenario, these models might be a cornerstone to account for several processes.

**Model extension** The model could be also extended to account for additional phenomena. In the case of pathogen ABM, cell-to-cell spread via protrusion- and vesicle-mediated transfer can be included by adding models that couple ABM of intracellular bacterial pathogens with the resistance of the membrane, which depends on the trafficking of tension-regulating proteins [7]. Such developments in the model permit a complete picture of the life cycles of intracellular bacteria that harness ABM [20].

In the case of cells ABM, a careful investigation of the mechanobiology of the membrane is required to accurately depict the cellular motility [65]. Moreover, the internalization of complexes, the role of membrane resistance, and the reorganization of F-actin in cell bulk during cell motility are all occurrences that must be included for correctly representing cell ABM. Since the role of ECM in cell ABM both in a 1D, 2D, and 3D setting was insufficiently discussed here, it must be considered in further studies.

The model can be used to address one of the key challenges in cell biomechanics, namely how to measure the mechanical characteristics of pathogens and cells during ABM. Because the model captures the reorganization of the actin network in response to an external stimulus, it can be used as a framework to design and interpret tailored experiments in different fields.

Being aware that further improvements are necessary, we believe that this thesis paves the way to *quantitative* investigations, which can help interpret biological experimental outcomes and address key challenges in mechanobiology.

# Bibliography

[1] Julie A. Theriot. The polymerization motor. *TRAFFIC*, 1(1):19–28, 2022/06/06 2000.

[2] T. Hohmann and F. Dehghani. The Cytoskeleton—A Complex Interacting Meshwork. *CELLS*, 8(4):362, 2019.

[3] C.R. Jacobs, H. Huang, and R.Y. Kwon. *Introduction to Cell Mechanics and Mechanobiology.* Garland Science, Taylor and Francis Group, 2013.

[4] Bruce Alberts, John Howard Wilson, and Tim Hunt. *Molecular biology of the cell.* GS Garland Science, New York, 6. ed edition, c2015.

[5] Sapun H. Parekh, Ovijit Chaudhuri, Julie A. Theriot, and Daniel A. Fletcher. Loading history determines the velocity of actin-network growth. *NAT CELL BIOL*, 7(12):1219–1223, 2005.

[6] C. Bonanno, M. Serpelloni, M. Arricca, R.M. McMeeking, and A. Salvadori. Actin based motility unveiled: How chemical energy is converted into motion. *J MECH PHYS SOLIDS*, 175:105273, 2023.

[7] Rebecca L Lamason and Matthew D Welch. Actin-based motility and cell-to-cell spread of bacterial pathogens. *CURR OPIN CELL BIOL*, 35:48–57, 02 2017.

[8] Lisa A. Cameron, Paula A. Giardini, Frederick S. Soo, and Julie A. Theriot. Secrets of actin-based motility revealed by a bacterial pathogen. *NAT REV MOL CELL BIO*, 1(2):110–119, 2000.

[9] Jennifer R. Robbins, Angela I. Barth, Hélène Marquis, Eugenio L. de Hostos, W. James Nelson, and Julie A. Theriot. Listeria monocytogenes exploits normal host cell processes to spread from cell to cell. *J CELL BIOL*, 146(6):1333–1350, 6/7/2022 1999.

[10] James L McGrath, Narat J Eungdamrong, Charles I Fisher, Fay Peng, Lakshminarayanan Mahadevan, Timothy J Mitchison, and Scot C Kuo. The force-velocity relationship for the actin-based motility of listeria monocytogenes. *CURR BIOL*, 13(4):329–332, 2003.

[11] Catherine I. Lacayo and Julie A. Theriot. Listeria monocytogenes actin-based motility varies depending on subcellular location: A kinematic probe for cytoarchitecture. *MOL BIOL CELL*, 15(5):2164–2175, 2022/06/06 2004.

[12] Arthur M. Talman, Ryan Chong, Jonathan Chia, Tatyana Svitkina, and Hervé Agaisse. Actin network disassembly powers dissemination of listeria monocytogenes. *J CELL SCI*, 127(1):240–249, 6/6/2022 2014.

[13] Ana Catarina Costa, Filipe Carvalho, Didier Cabanes, and Sandra Sousa. Stathmin recruits tubulin to listeria monocytogenes-induced actin comets and promotes bacterial dissemination. *CELL MOL LIFE SCI*, 76(5):961–975, 2019.

[14] Sonja Kühn and Jost Enninga. The actin comet guides the way: How listeria actin subversion has impacted cell biology, infection biology and structural biology. *CELL MICROBIOL*, 22(4):e13190, 2022/05/30 2020.

[15] Lilliana Radoshevich and Pascale Cossart. Listeria monocytogenes: towards a complete picture of its physiology and pathogenesis. *NAT REV MICROBIOL*, 16(1):32–46, 2018.

[16] Sascha Pust, Helen Morrison, Jürgen Wehland, Antonio S Sechi, and Peter Herrlich. Listeria monocytogenes exploits erm protein functions to efficiently spread from cell to cell. *EMBO J*, 24(6):1287–1300, 2022/06/06 2005.

[17] Protein polymers, crawling cells and comet tails, https://www.ibiology.org/cell-biology/cell-motility, August 2015.

[18] Alex Mogilner and George Oster. Force generation by actin polymerization ii: The elastic ratchet and tethered filaments. *BIOPHYS J*, 84(3):1591–1605, 2003.

[19] F Gerbal, P Chaikin, Y Rabin, and J Prost. An elastic analysis of listeria monocytogenes propulsion. *BIOPHYS J*, 79(5):2259–2275, Nov 2000.

[20] Vivek B. Shenoy, D. T. Tambe, A. Prasad, and Julie A. Theriot. A kinematic description of the trajectories of listeria monocytogenes propelled by actin comet tails. *PNAS*, 104(20):8229–8234, 2022/06/09 2007.

[21] Yuan Lin, V. B. Shenoy, Bin Hu, and Limiao Bai. A microscopic formulation for the actin-driven motion of listeria in curved paths. *BIOPHYS J*, 99(4):1043–1052, 2022/06/09 2010.

[22] Jerrold Marsden and Thomas J. R. Hughes. *Mathematical foundations of elasticity.* Dover Publications, Inc., 1983.

[23] C. Truesdell and W. Noll. *The Non-Linear Field Theories of Mechanics*, pages 1–541. Springer Berlin Heidelberg, Berlin, Heidelberg, 1965.

[24] M.E. Gurtin, E. Fried, and L. Anand. *The Mechanics and Thermodynamics of Continua.* Cambridge University Press, 2010.

[25] A. Salvadori, C. Bonanno, M. Serpelloni, M. Arricca, and R.M. McMeeking. Continuum multi-physics modeling of cell and continuum molti-physics modeling of cell and bacteria motility. *submitted.*

[26] M. Serpelloni, M. Arricca, C. Bonanno, and A. Salvadori. Modeling cells spreading, motility, and receptors dynamics: a general framework. *ACTA MECH SINICA*, 37(6):1013–1030, 2021.

[27] J.C. Simo and T.J.R. Hughes. *Computational inelasticity.* Springer-Verlag, New York, 1998.

[28] G. Holzapfel. *Nonlinear Solid Mechanics: A Continuum Approach for Engineering.* John Wiley & Sons, Ltd., 2001.

[29] L. Anand. A Cahn-Hilliard-type theory for species diffusion coupled with large elastic-plastic deformations. *J MECH PHYS SOLIDS*, 60(12):1983–2002, 2012.

[30] A. Salvadori, R.M. McMeeking, D. Grazioli, and M. Magri. A coupled model of transport-reaction-mechanics with trapping. Part I - small strain analysis. *J MECH PHYS SOLIDS*, 114:1–30, 2018.

[31] Matteo Arricca, Luigi Cabras, Mattia Serpelloni, Claudia Bonanno, Robert M. McMeeking, and Alberto Salvadori. A coupled model of transport-reaction-mechanics with trapping, part ii: Large strain analysis. *J MECH PHYS SOLIDS*, 181:105425, 2023.

[32] S. Paolucci. *Continuum Mechanics and Thermodynamics of Matter*. Cambridge University Press, 2016.

[33] E.B. Tadmor, R.E. Miller, and R.S. Elliott. *Continuum Mechanics and Thermodynamics: From Fundamental Concepts to Governing Equations*. Cambridge University Press, 2011.

[34] M. Serpelloni, M. Arricca, C. Bonanno, and A. Salvadori. Chemo-transport-mechanics in advecting membranes. *INT J ENG SCI*, 181:103746, 2022.

[35] Javier Pizarro-Cerdá, Andreas Kühbacher, and Pascale Cossart. Entry of listeria monocytogenes in mammalian epithelial cells: an updated view. *CSH PERSPECT BIOL*, 2(11):a010009, 11 2012.

[36] Vikram S. Deshpande, Robert M. McMeeking, and A G Evans. A bio-chemo-mechanical model for cell contractility. *PNAS*, 103(45):17064–17065, 2006.

[37] S.R. De Groot and P. Mazur. *Non-Equilibrium Thermodynamics*. Dover, 1984.

[38] M. Ganser, F.E. Hildebrand, M. Kamlah, and R.M. McMeeking. A finite strain electro-chemo-mechanical theory for ion transport with application to binary solid electrolytes. *J MECH PHYS SOLIDS*, 125:681–713, 2019.

[39] S. Shell. *Thermodynamics and statistical mechanics: an integrated approach*. Cambridge University Press, 2015.

[40] R. DeHoff. *Thermodynamic in material science*. CRC Press - Taylor and Francis, 2006.

[41] G.P. Beretta. *Termodinamica*. Edizioni Cartoleria Snoopy, Brescia, 2002.

[42] M B Goldberg. Actin-based motility of intracellular microbial pathogens. *MICROBIOL MOL BIOL R*, 65(4):595–626, 12 2001.

[43] Fabian E Ortega, Elena F Koslover, Julie A Theriot, Wendy S Garrett, Kim Orth, James Slauch, and Babak Momeni. Listeria monocytogenes cell-to-cell spread in epithelia is heterogeneous and dominated by rare pioneer bacteria. *ELIFE*, 8:e40032, 2019.

[44] Julie E Choe and Matthew D Welch. Actin-based motility of bacterial pathogens: mechanistic diversity and its impact on virulence. *PATHOG DIS*, 74(8):ftw099, 5/30/2022 2016.

[45] Dominique Pantaloni, Christophe Le Clainche, and Marie-France Carlier. Mechanism of actin-based motility. *SCIENCE*, 292(5521):1502–1506, 2022/06/19 2001.

[46] Laurent Blanchoin, Rajaa Boujemaa-Paterski, Cécile Sykes, and Julie Plastino. Actin dynamics, architecture, and mechanics in cell motility. *PHYSIOL REV*, 94(1):235–263, 2022/06/06 2014.

[47] A. Kawska, K. Carvalho, J. Manzi, R. Boujemaa-Paterski, L. Blanchoin, J.L. Martiel, and Sykes C. How actin network dynamics control the onset of actin-based motility. *PNAS*, 109:14440–14445, 2012.

[48] V. Noireaux, R.M. Golsteyn, E. Friederich, J. Prost, C. Antony, D. Louvard, and C. Sykes. Growing an actin gel on spherical surfaces. *BIOPHYS J*, 278:1643–1654, 2000.

[49] F Quirion and C Gicquaud. Changes in molar volume and heat capacity of actin upon polymerization. *BIOCHEM J*, 295(3):671–672, 11 1993.

[50] Tai Kiuchi, Tomoaki Nagai, Kazumasa Ohashi, and Kensaku Mizuno. Measurements of spatiotemporal changes in G-actin concentration reveal its effect on stimulus-induced actin assembly and lamellipodium extension. *J CELL BIOL*, 193(2):365–380, 04 2011.

[51] Oster G. Mogilner A. Cell motility driven by actin polymerization. *BIOPHYS J*, 71(6):3030–3045, 1996.

[52] Dikla Raz-Ben Aroush, Noa Ofer, Enas Abu-Shah, Jun Allard, Oleg Krichevsky, Alex Mogilner, and Kinneret Keren. Actin turnover in lamellipodial fragments. *CURR BIOL*, 27(19):2963–2973.e14, 2017.

[53] Xindong Chen, Hanxing Zhu, XiQiao Feng, Xiaona Li, Yongtao Lu, Zuobin Wang, and Yacine Rezgui. Predictive assembling model reveals the self-adaptive elastic properties of lamellipodial actin networks for cell migration. *COMM BIOL*, 3(1):616, 2020.

[54] V. Damioli, A. Salvadori, G.P. Beretta, C. Ravelli, and S. Mitola. Multiphysics interactions drive VEGFR2 relocation on endothelial cells. *SCI REP-UK*, 7(1):16700, 2017.

[55] A. Quarteroni and A. Valli. *Numerical approximation of partial differential equations.* Springer Verlag, Berlin, 1997.

[56] F.J. Vernerey, R. Long, and R. Brighenti. A statistically-based continuum theory for polymers with transient networks. *J MECH PHYS SOLIDS*, 107:1 – 20, 2017.

[57] R Brighenti and F.J. Vernerey. A simple statistical approach to model the time-dependent response of polymers with reversible cross-links. *COMPOS PART B-ENG*, 115:257 – 265, 2017.

[58] S. Kiana Naghibzadeh, Noel Walkington, and Kaushik Dayal. Surface growth in deformable solids using an eulerian formulation. *J MECH PHYS SOLIDS*, 154:104499, 2021.

[59] Rohan Abeyaratne, Eric Puntel, and Giuseppe Tomassetti. Treadmilling stability of a one-dimensional actin growth model. *INT J SOLIDS STRUCT*, 198:87–98, 2020.

[60] Christine Kocks, Raymond Hellio, Pierre Gounon, Helene Ohayon, and Pascale Cossart. Polarized distribution of Listeria monocytogenes surface protein ActA at the site of directional actin assembly. *J CELL SCI*, 105(3):699–710, 07 1993.

[61] Daniel Arndt, Wolfgang Bangerth, Maximilian Bergbauer, Marco Feder, Marc Fehling, Johannes Heinz, Timo Heister, Luca Heltai, Martin Kronbichler, Matthias Maier, Peter Munch, Jean-Paul Pelteret, Bruno Turcksin, David Wells, and Stefano Zampini. The `deal.II` library, version 9.5. *J NUMER MATH*, 31(3):231–246, 2023.

[62] Fabien Gerbal, Valérie Laurent, Albrecht Ott, Marie-France Carlier, Paul Chaikin, and Jacques Prost. Measurement of the elasticity of the actin tail of listeria monocytogenes. *EUR BIOPHYS J*, 29(2):134–140, 2000.

[63] T M Svitkina and G G Borisy. Arp2/3 complex and actin depolymerizing factor/cofilin in dendritic organization and treadmilling of actin filament array in lamellipodia. *J CELL BIOL*, 145(5):1009–1026, 1999.

[64] Tatyana Svitkina. The actin cytoskeleton and actin-based motility. *CSH PERSPECT BIOL*, 10(1):a018267, 01 2018.

[65] A.D. Doyle, D.J. Sykora, G.G. Pacheco, M.L. Kutys, and K.M. Yamada. 3D mesenchymal cell migration is driven by anterior cellular contraction that generates an extracellular matrix prestrain. *DEV CELL*, 56(6):826–841, Mar 2021.

[66] Keith Burridge and Christophe Guilluy. Focal adhesions, stress fibers and mechanical tension. *EXP CELL RES*, 343(1):14–20, 2016.

[67] Claudia Tanja Mierke. *Physics of Cancer, Volume 1 (Second Edition)*. 2053-2563. IOP Publishing, 2018.

[68] Pakorn Kanchanawong and David A Calderwood. Organization, dynamics and mechanoregulation of integrin-mediated cell-ecm adhesions. *NAT REV MOL CELL BIO*, 24(2):142–161, Feb 2023.

[69] Katie Bentley and Shilpa Chakravartula. The temporal basis of angiogenesis. *PHIL TRANS R SOC B*, 372(1720):20150522, 2017.

[70] Brunhilde Felding-Habermann. Integrin adhesion receptors in tumor metastasis. *CLIN EXP METASTAS*, 20(3):203–213, 2003.

[71] W. Stillwell. *An Introduction to Biological Membranes: Composition, Structure and Function*, chapter 17 - Moving Components Through the Cell: Membrane Trafficking, pages 369–379. Elsevier B.V., 2016.

[72] Thomas Pollard, Laurent Blanchoin, and R. Mullins. Molecular mechanisms controlling actin filament dynamics in nonmuscle cells. *ANNU REV BIOPH BIOM*, 29:545–76, 02 2000.

[73] Jan Mueller, Gregory Szep, Maria Nemethova, Ingrid de Vries, Arnon D. Lieber, Christoph Winkler, Karsten Kruse, J. Victor Small, Christian Schmeiser, Kinneret Keren, Robert Hauschild, and Michael Sixt. Load adaptation of lamellipodial actin networks. *CELL*, 171(1):188–200.e16, 2017.

[74] G. Huang, F. Xu, G.M. Genin, and T.J Lu. Mechanical microenvironments of living cells: a critical frontier in mechanobiology. *ACTA MECH SINICA*, 35(2):265–269, 2019.

[75] Z. You, L. Zhou, W. Li, C. Huang, and Y. Du. Mechanical microenvironment as a key cellular regulator in the liver. *ACTA MECH SINICA*, 35(2):289–298, 2019.

[76] Matteo Arricca, Alberto Salvadori, Claudia Bonanno, and Mattia Serpelloni. Modeling receptor motility along advecting lipid membranes. *MEMBRANES*, 12(7), 2022.

[77] V. Deshpande, R.M. McMeeking, and A.G. Evans. A model for the contractility of the cytoskeleton including the effects of stress-fiber formation and dissociation. *P R SOC A*, 463:787–815, 2007.

[78] Ze Gong, Spencer E. Szczesny, Steven R. Caliari, Elisabeth E. Charrier, Ovijit Chaudhuri, Xuan Cao, Yuan Lin, Robert L. Mauck, Paul A. Janmey, Jason A. Burdick, and Vivek B. Shenoy. Matching material and cellular timescales maximizes cell spreading on viscoelastic substrates. *PNAS*, 115(12):E2686–E2695, 2022/05/30 2018.

[79] S.S. Shishvan, A. Vigliotti, and V.S. Deshpande. The homeostatic ensemble for cells. *BIOMECH MODEL MECHAN*, 17:1631–1662, 2018.

[80] V. Damioli. *A mechano-biological model of the coupling between cellular contractility and VEGFR2/VEGF interactions*. PhD thesis, University of Brescia, 2018.

[81] A. Agrawal and D. J. Steigmann. A model for surface diffusion of transmembrane proteins on lipid bilayers. *Z ANGEW MATH MECH*, 62(3):549, 2011.

[82] A.F. Golestaneh and B. Nadler. Modeling of cell adhesion and deformation mediated by receptor-ligand interactions. *BIOMECH MODEL MECHANOBIOL*, 15:371–387, 2016.

[83] R. Deshpande, Y.T Cheng, M.W. Verbrugge, and A. Timmons. Diffusion induced stresses and strain energy in a phase-transforming spherical electrode particle. *J ELECTROCHEM SOC*, 158(6):A718–A724, 2011.

[84] V Deshpande, M Mrksich, R M McMeeking, and A G Evans. A biomechanical model for coupling cell contractility with focal adhesion formation. *J MECH PHYS SOLIDS*, 56:1484–1510, 2008.

[85] R.M. McMeeking and V.S. Deshpande. A bio-chemo-mechanical model for cell contractility, adhesion, signaling, and stress-fiber remodeling. In G.A. Holzapfel and R.W. Ogden, editors, *Biomechanics: Trends in Modeling and Simulation.*, volume 20 of *Studies in Mechanobiology, Tissue Engineering and Biomaterials*, pages 53–81. Springer, 2017.

[86] W. Ronan, V.S. Deshpande, R.M. McMeeking, and J.P. McGarry. Numerical investigation of the active role of the actin cytoskeleton in the compression resistance of cells. *J MECH BEHAV BIOMED*, 14:143–157, 2012.

[87] W. Ronan, V.S. Deshpande, R.M. McMeeking, and J.P. McGarry. Cellular contractility and substrate elasticity: a numerical investigation of the actin cytoskeleton and cell adhesion. *BIOMECH MODEL MECHANOBIOL*, 13:417–435, 2014.

[88] C. Obbink-Huizer, C.W.J. Oomens, S. Loerakker, J. Foolen, C.V.C. Bouten, and Baaijens F.P.T. Computational model predicts cell orientation in response to a range of mechanical stimuli. *Biomech Model Mechanobiol*, 13(1):227–236, 2014.

[89] F.J. Vernerey and M. Farsad. A constrained mixture approach to mechano-sensing and force generation in contractile cells. *J MECH BEHAV BIOMED*, 4(8):1683–1699, 2011.

[90] Kinneret Keren, Zachary Pincus, Greg M Allen, Erin L Barnhart, Gerard Marriott, Alex Mogilner, and Julie A Theriot. Mechanism of shape determination in motile cells. *NATURE*, 453(7194):475–480, 05 2008.

[91] A. Pathak, R.M. McMeeking, A.G. Evans, and V.S. Deshpande. An analysis of the cooperative mechano-sensitive feedback between intracellular signaling, focal adhesion development, and stress fiber contractility. *J APPL MECH*, 78, 2011.

[92] A. Vigliotti, R.M. McMeeking, and V.S. Deshpande. Simulation of the cytoskeletal response of cells on grooved or patterned substrates. *J R SOC INTERFACE*, 12(20141320), 2015.

[93] E. McEvoy, V.S. Deshpande, and P. McGarry. Free energy analysis of cell spreading. *J MECH BEHAV BIOMED*, 74:283–295, 2017.

[94] H. Gao, W. Shi, and L. Freund. Mechanics of receptor-mediated endocytosis. *PNAS*, 102(27):9469–9474, 2005.

[95] P. Decuzzi and M. Ferrari. The receptor-mediated endocytosis of nonspherical particles. *BIOPHYS J*, 94(10):3790–3797, 2008.

[96] H. Gao. Probing mechanical principles of cell–nanomaterial interactions. *J MECH PHYS SOLIDS*, 62:312–339, 2014.

[97] T. Wiegold, S. Klinge, R.P. Gilbert, and G.A. Holzapfel. Computational modeling of adhesive contact between a virus and a cell during receptor driven endocytosis. *PROC APPL MATH MECH*, 19(e201900161), 2019.

[98] A. Liberman, M. Mussel, G. Kario, D. Sprinzak, and U. Nevo. Modelling cell surface dynamics and cell–cell interactions using cell studio: a three-dimensional visualization tool based on gaming technology. *J R SOC INTERFACE*, 16(20190264), 2019.

[99] F. Bubba, T. Lorenzi, and F.R. Macfarlane. From a discrete model of chemotaxis with volume-filling to a generalized patlak–keller–segel model. *PROC R SOC A*, 476(20190871), 2020.

[100] A. Salvadori, V. Damioli, C. Ravelli, and S. Mitola. Modeling and simulation of VEGF receptors recruitment in angiogenesis. *MATH PROBL ENG*, page 4705472, 2018.

[101] M Serpelloni, M Arricca, V Damioli, C Ravelli, E Grillo, S Mitola, and A Salvadori. A Model of Integrin and VEGF Receptors Recruitment on Endothelial Cells. In BE Abali and I Giorgio, editors, *Developments and Novel Approaches in Biomechanics and Metamaterials*, pages 163–198. Springer International Publishing, 2020.

[102] F.J. Vernerey and M. Farsad. A mathematical model of the coupled mechanisms of cell adhesion, contraction and spreading. *J MATH BIOL*, 68:989–1022, 2014.

[103] A. Vigliotti, W. Ronan, F.P.T. Baaijens, and V.S. Deshpande. A thermodynamically motivated model for stress-fiber reorganization. *BIOMECH MODEL MECHAN*, 15:761–789, 2016.

[104] S. Hervas-Raluy, J. M. Garcia-Aznar, and M. J. Gomez-Benito. Modelling actin polymerization: the effect on confined cell migration. *BIOMECH MODEL MECHANOBIOL*, 18(4):1177–1187, 2019.

[105] Qi Wen and Paul A. Janmey. Polymer physics of the cytoskeleton. *CURR OPIN SOLID ST M*, 15(5):177 – 182, 2011.

[106] Elias H. Barriga and Roberto Mayor. Adjustable viscoelasticity allows for efficient collective cell migration. *SEMIN CELL DEV BIOL*, 93:55 – 68, 2019.

[107] F.J. Vernerey. Transient response of nonlinear polymer networks: A kinetic theory. *J MECH PHYS SOLIDS*, 115:230 – 247, 2018.

[108] O. Lieleg, K.M. Schmoller, M.M.A.E. Claessens, and A.R. Bausch. Cytoskeletal polymer networks: Viscoelastic properties are determined by the

microscopic interaction potential of cross-links. *BIOPHYS J*, 96(11):4725 – 4732, 2009.

[109] Michael Murrell, Patrick W. Oakes, Martin Lenz, and Margaret L. Gardel. Forcing cells into shape: the mechanics of actomyosin contractility. *NAT REV MOL CELL BIO*, 16(8):486–498, 2015.

[110] EJ. Campbell and P. Bagchi. A computational model of amoeboid cell swimming. *PHYSICS OF FLUIDS*, 29(10):101902, 2017.

[111] EJ. Campbell and P Bagchi. A computational study of amoeboid motility in 3D: the role of extracellular matrix geometry, cell deformability, and cell–matrix adhesion. *BIOTECH MODEL MECHANOBIOL*, 20(1):167–191, 2021.

[112] RM Cooper, NS Wingreen, and EC Cox. An excitable cortex and memory model successfully predicts new pseudopod dynamics. *PLoS ONE*, 7(3):e33528, 2012.

[113] Zahra Eidi. Discrete modeling of amoeboid locomotion and chemotaxis in dictyostelium discoideum by tracking pseudopodium growth direction. *SCI REP-UK*, 7(1):12675, Oct 2017.

[114] C Bächer and S Gekle. Computational modeling of active deformable membranes embedded in three-dimensional flows. *PHYS REV E*, 99:062418, Jun 2019.

[115] Adrian Moure and Hector Gomez. Phase-field modeling of individual and collective cell migration. *ARCH COMPUT METHOD E*, 28(2):311–344, 2021.

[116] J.G. McGarry and P. J. Prendergast. A three-dimensional finite element model of an adherent eukaryotic cell. *EUR CELL MATER*, 7:27–33, 2004.

[117] A. Buskermolen, H. Suresh, S. Shishvan, A. Vigliotti, A. DeSimone, N. Kurniawan, C. Bouten, and V.S. Deshpande. Entropic forces drive cellular contact guidance. *BIOPHYS J*, 116(10):1994 – 2008, 2019.

[118] Jonathan Stricker, Tobias Falzone and Margaret Gardel. Mechanics of the F-actin Cytoskeleton. *J Biomech.*, 43(1):1–12, 2010.

[119] Ovijit Chaudhuri, Justin Cooper-White, Paul A. Janmey, David J. Mooney, and Vivek B. Shenoy. Effects of extracellular matrix viscoelasticity on cellular behaviour. *NATURE*, 584(7822):535–546, 2020.

[120] Ying Li, Prabhakar Bhimalapuram, and Aaron R Dinner. Model for how retrograde actin flow regulates adhesion traction stresses. *J PHYS-CONDENS MAT*, 22(19):194113, 2010.

[121] Bo Gong, Xi Wei, Jin Qian, and Yuan Lin. Modeling and simulations of the dynamic behaviors of actin-based cytoskeletal networks. *ACS BIOMATER SCI ENG*, 5(8):3720–3734, 08 2019.

[122] Longhua Hu and Garegin A Papoian. Mechano-chemical feedbacks regulate actin mesh growth in lamellipodial protrusions. *BIOPHYS J*, 98(8):1375–1384, 04 2010.

[123] Haoran Ni and Garegin A. Papoian. Membrane-medyan: Simulating deformable vesicles containing complex cytoskeletal networks. *J PHYS CHEM B*, 125(38):10710–10719, 09 2021.

[124] Anders E. Carlsson. Growth of branched actin networks against obstacles. *BIOPHYS J*, 81(4):1907 – 1923, 2001.

[125] A.E. Carlsson. Growth velocities of branched actin networks. *BIOPHYS J*, 84(5):2907 – 2918, 2003.

[126] Boris Rubinstein, K. Jacobson, and A. Mogilner. Multiscale two-dimensional modeling of a motile simple-shaped cell. *MULTISCALE MODEL SIMUL*, 3(2):413 – 439, 2005.

[127] Erdinç Atilgan, Denis Wirtz, and Sean X. Sun. Morphology of the lamellipodium and organization of actin filaments at the leading edge of crawling cells. *BIOPHYS J*, 89(5):3589 – 3602, 2005.

[128] Laura Murphy and Anotida Madzvamuse. A moving grid finite element method applied to a mechanobiochemical model for 3d cell migration. *APPL NUMER MATH*, 158:336 – 359, 2020.

[129] J. F. Joanny, K. Kruse, J. Prost, and S. Ramaswamy. The actin cortex as an active wetting layer. *EUR PHYS J E*, 36(5), 2013.

[130] K. Kruse, J. F. Joanny, F. Jülicher, J. Prost, and K. Sekimoto. Generic theory of active polar gels: A paradigm for cytoskeletal dynamics. *EUR PHYS J E*, 16(1):5–16, 2005.

[131] J. Prost, F. Jülicher, and J. F. Joanny. Active gel physics. *NAT PHYS*, 11(2):111–117, 2015.

[132] Ernest Latorre, Sohan Kale, Laura Casares, Manuel Gómez-González, Marina Uroz, Léo Valon, Roshna V. Nair, Elena Garreta, Nuria Montserrat, Aránzazu del Campo, Benoit Ladoux, Marino Arroyo, and Xavier Trepat. Active superelasticity in three-dimensional epithelia of controlled shape. *NATURE*, 563(7730):203–208, 2018.

[133] M. Rahimi and M. Arroyo. Shape dynamics, lipid hydrodynamics, and the complex viscoelasticity of bilayer membranes. *PHYS REV E*, 86:011932, Jul 2012.

[134] McMeeking R.M. and Deshpande V.S. *Biomechanics: Trends in Modeling and Simulation*, volume 20 of *Studies in Mechanobiology, Tissue Engineering and Biomaterials*. Springer International Pu, 2017.

[135] R Allena. Cell migration with multiple pseudopodia: Temporal and spatial sensing models. *B MATH BIOL*, 75(2):288–316, 2013.

[136] A Moure and H. Gomez. Three-dimensional simulation of obstacle-mediated chemotaxis. *BIOMECH MODEL MECHANOBIOL*, 17(5):1243–1268, 2018.

[137] C Giverso and L Preziosi. Mechanical perspective on chemotaxis. *PHYS REV E*, 98:062402, 2018.

[138] Jonathan Fouchard, Démosthène Mitrossilis, and Atef Asnacios. Acto-myosin based response to stiffness and rigidity sensing. *CELL ADHES MIGR*, 5(1):16–19, 2011.

[139] Alba Diz-Muñoz, Daniel A. Fletcher, and Orion D. Weiner. Use the force: membrane tension as an organizer of cell shape and motility. *TRENDS CELL BIOL*, 23(2):47 – 53, 2013.

[140] A.V. Hill. The heat of shortening and the dynamic constants of muscle. *PROC R SOC B*, 126(136-195), 1938.

[141] Cynthia A. Reinhart-King, Micah Dembo, and Daniel A. Hammer. The dynamics and mechanics of endothelial cell spreading. *BIOPHYS J*, 89(1):676–689, jul 2005.

[142] Léa Trichet, Jimmy Le Digabel, Rhoda J. Hawkins, Sri Ram Krishna Vedula, Mukund Gupta, Claire Ribrault, Pascal Hersen, Raphaël Voituriez, and Benoît Ladoux. Evidence of a large-scale mechanosensing mechanism for cellular adaptation to substrate stiffness. *PNAS*, 109(18):6933–6938, 2012.

[143] Vivek B Shenoy, Hailong Wang, and Xiao Wang. A chemo-mechanical free-energy-based approach to model durotaxis and extracellular stiffness-dependent contraction and polarization of cells. *INTERFACE FOCUS*, 6(1):20150067, Feb 2016.

[144] Raimon Sunyer, Vito Conte, Jorge Escribano, Alberto Elosegui-Artola, Anna Labernadie, Léo Valon, Daniel Navajas, JoséManuel García-Aznar, JoséJ Muñoz, Pere Roca-Cusachs, and Xavier Trepat. Collective cell durotaxis emerges from long-range intercellular force transmission. *SCIENCE*, 353(6304):1157–1161, Sep 2016.

[145] Ovijit Chaudhuri, Luo Gu, Max Darnell, Darinka Klumpers, Sidi A Bencherif, James C Weaver, Nathaniel Huebsch, and David J Mooney. Substrate stress relaxation regulates cell spreading. *NAT COMMUN*, 6:6364, Feb 2015.

[146] Noam Nisenholz, Kavitha Rajendran, Quynh Dang, Hao Chen, Ralf Kemkemer, Ramaswamy Krishnan, and Assaf Zemel. Active mechanics and dynamics of cell spreading on elastic substrates. *SOFT MATTER*, 10:7234–7246, 2014.

[147] Eric A Klein, Liqun Yin, Devashish Kothapalli, Paola Castagnino, Fitzroy J Byfield, Tina Xu, Ilya Levental, Elizabeth Hawthorne, Paul A Janmey, and Richard K Assoian. Cell-cycle control by physiological matrix elasticity and in vivo tissue stiffening. *CURR BIOL*, 19(18):1511–1518, Sep 2009.

[148] Britta Trappmann, Julien E. Gautrot, John T. Connelly, Daniel G. T. Strange, Yuan Li, Michelle L. Oyen, Martien A. Cohen Stuart, Heike Boehm, Bojun Li, Viola Vogel, Joachim P. Spatz, Fiona M. Watt, and Wilhelm T. S. Huck. Extracellular-matrix tethering regulates stem-cell fate. *NAT MATER*, 11(7):642–649, 2012.

[149] Joe Swift, Irena L Ivanovska, Amnon Buxboim, Takamasa Harada, P C Dave P Dingal, Joel Pinter, J David Pajerowski, Kyle R Spinler, Jae-Won Shin, Manorama Tewari, Florian Rehfeldt, David W Speicher, and Dennis E Discher. Nuclear lamin-a scales with tissue stiffness and enhances matrix-directed differentiation. *SCIENCE*, 341(6149):1240104, Aug 2013.

[150] Xuan Cao, Yuan Lin, Tristian P Driscoll, Janusz Franco-Barraza, Edna Cukierman, Robert L Mauck, and Vivek B Shenoy. A chemomechanical model of matrix and nuclear rigidity regulation of focal adhesion size. *BIOPHYS J*, 109(9):1807–1817, Nov 2015.

[151] J T Parsons, K H Martin, J K Slack, J M Taylor, and S A Weed. Focal adhesion kinase: a regulator of focal adhesion dynamics and cell movement. *ONCOGENE*, 19(49):5606–5613, Nov 2000.

[152] S. De, S. Kuwahara, and A. Saito. The endocytic receptor megalin and its associated proteins in proximal tubule epithelial cells. *MEMBRANES*, 4:333–355, 2014.

[153] S. C. Haering, D. Tapken, S. Pahl, and M. Hollmann. Auxiliary subunits: Shepherding ampa receptors to the plasma membrane. *MEMBRANES*, 4:469–490, 2014.

[154] C. Bucci, P. Alifano, and L. Cogli. The role of rab proteins in neuronal cells and in the trafficking of neurotrophin receptors. *MEMBRANES*, 4:642–677, 2014.

[155] S. C. Klinger, P. Siupka, and M. S. Nielsen. Retromer-mediated trafficking of transmembrane receptors and transporters. *MEMBRANES*, 5:288–306, 2015.

[156] R. Kawaguchi, M. Zhong, M. Kassai, M. Ter-Stepanian, and H. Sun. Vitamin a transport mechanism of the multitransmembrane cell-surface receptor stra6. *MEMBRANES*, (425–453), 2015.

[157] T Azad, R. Singaravelu, M. J. F. Crupi, T. Jamieson, J. Dave, E. E. F. Brown, R. Rezaei, Z. Taha, S. Boulton, N. T. Martin, A. Surendran, J. Poutou, M. Ghahremani, K. Nouri, J. T. Whelan, J. Doung, S. Tucker, J-S Diallo, J. C. Bell, and C. S. Ilkow. Implications for sars-cov-2 vaccine design: Fusion of spike glycoprotein transmembrane domain to receptor-binding domain induces trimerization. *MEMBRANES*, 10(215), 2020.

[158] M. C. Klaiss-Luna and M. Manrique-Moreno. Infrared spectroscopic study of multi-component lipid systems: A closer approximation to biological membrane fluidity. *MEMBRANES*, 12(534), 2022.

[159] A. Aragón-Muriel, Y. Lisciano, D. Morales-Morales, D. Polo-Cerón, and J. Oñate-Garzón. A study of the interaction of a new benzimidazole schiff base with synthetic and simulated membrane models of bacterial and mammalian membranes. *MEMBRANES*, 11(449), 2021.

[160] E. Brémaud, C. Favard, and D. Mariaux. Deciphering the assembly of enveloped viruses using model lipid membranes. *MEMBRANES*, 12(441), 2022.

[161] A. Fletcher. The cell membrane and receptors. *ANAESTH INTENS CARE MED*, 18(6):316–320, 2017.

[162] J. Martí and C. Calero. Modeling and simulation of lipid membranes. *MEMBRANES*, 12(549), 2022.

[163] N. Zec, G. Mangiapia, A. C. Hendry, R. Barker, A. Koutsioubas, H. Frielinghaus, M. Campana, J. L. Ortega-Roldan, and S. Bush. Mutually beneficial combination of molecular dynamics computer simulations and scattering experiments. *MEMBRANES*, 11(507), 2021.

[164] N. Radhakrishnan, S. C. Kaul, R. Wadhwa, D. Sundar, and A. Hernández-Machado. Phosphatidylserine exposed lipid bilayer models for understanding cancer cell selectivity of natural compounds: A molecular dynamics simulation study. *MEMBRANES*, 12(64), 2022.

[165] C. Trejo-Soto, Làzaro G. R., I. Pagonabarraga, and A. Hernández-Machado. Microfluidics approach to the mechanical properties of red blood cell membrane and their effect on blood rheology. *MEMBRANES*, 12(217), 2022.

[166] L. Sessa, S. Concilio, P. Walde, T. Robinson, P. S. Dittrich, A. Porta, B. Panunzi, U. Caruso, and S. Piotto. Study of the interaction of a novel semi-synthetic peptide with model lipid membranes. *MEMBRANES*, 10(294), 2020.

[167] M. Mikucki and Y.C. Zhou. Curvature-driven molecular flow on membrane surface. *SIAM J APPL MATH*, 77(5):1587–1605, 2017.

[168] A.R. Carotenuto, L. Lunghi, V. Piccolo, M. Babaei, K. Dayal, N. Pugno, M. Zingales, L. Deseri, and M. Fraldi. Mechanobiology predicts raft formations triggered by ligand-receptor activity across the cell membrane. *J MECH PHYS SOLIDS*, 141:103974, 2020.

[169] Mattia Serpelloni. *Response of endothelial cells to angiogenic stimuli: experiments, modeling and simulations.* PhD thesis, University of Brescia, 2020.

[170] M. Serpelloni, M. Arricca, C. Bonanno, and A. Salvadori. Modeling cells spreading, motility, and receptors dynamics: a general framework. *ACTA MECH SIN*, 37(6):1013–1030, 2021.

[171] S. Mitola, C. Ravelli, E. Moroni, V. Salvi, D. Leali, K. Ballmer-Hofer, L. Zammataro, and M. Presta. Gremlin is a novel agonist of the major

proangiogenic receptor VEGFR2. *BLOOD*, 116(18):3677–3680, November 2010.

[172] Elisabetta Grillo, Cosetta Ravelli, Michela Corsini, Kurt Ballmer-hofer, Pasqua Oreste, Giorgio Zoppetti, Chiara Tobia, Roberto Ronca, Marco Presta, and Stefania Mitola. Monomeric gremlin is a novel vascular endothelial growth factor receptor-2 antagonist. *ONCOTARGET*, 7(23):35353 – 35368, 2016.

[173] C. Ravelli, E. Grillo, M. Corsini, D. Coltrini, M. Presta, and S. Mitola. $\beta_3$ Integrin Promotes Long-Lasting Activation and Polarization of Vascular Endothelial Growth Factor Receptor 2 by Immobilized Ligand. *ARTERIOSCL THROM VAS*, 35(10):2161–2171, 2015.

[174] A. Salvadori, D. Grazioli, M.G.D. Geers, D. Danilov, and P.H.L Notten. A multiscale-compatible approach in modeling ionic transport in the electrolyte of (lithium ion) batteries. *J POWER SOURCES*, 293:892–911, 2015.

[175] A. Salvadori, D. Grazioli, M. Magri, M.G.D. Geers, D. Danilov, and P.H.L. Notten. On the role of saturation in modeling ionic transport in the electrolyte of (Li-ion) batteries. *J POWER SOURCES*, 294:696–710, 2015.

[176] L. Cabras, D. Danilov, W. Subber, V. Oancea, and A. Salvadori. A two-mechanism and multiscale compatible approach for solid state electrolytes of (li-ion) batteries. *Journal of Energy Storage*, 48:103842, 2022.

[177] C. Ravelli, E. Grillo, M. Corsini, D. Coltrini, M. Presta, and S. Mitola. $\beta_3$ integrin promotes long-lasting activation and polarization of vascular endothelial growth factor receptor 2 by immobilized ligand. *ARTERIOSCL THROM VAS*, 35(10):2161–2171, 2015.

[178] L.B. Freund and Y. Lin. The role of binder mobility in spontaneous adhesive contact and implication for cell adhesion. *J MECH PHYS SOLIDS*, 52:2455–2472, 2004.

[179] V. Shenoy and L. Freund. Growth and shape stability of a biological membrane adhesion complex in the diffusion-mediated regime. *PNAS*, 102(9):3213–3218, 2005.

[180] T. Wiegold, S. Klinge, R. P. Gilbert, and G. A. Holzapfel. Numerical simulation of the viral entry into a cell driven by the receptor diffusion. *bioRxiv*, 2019.

[181] R.C. Lee, T.R. Gowrishankar, R.M. Basch, K.K. Patel, and D.E. Golan. Cell shape-dependent rectification of surface receptor transport in a sinusoidal electric field. *BIOPHYS J*, 64:44–57, 1993.

[182] F. Mac Gabhann and A.S. Popel. Model of competitive binding of vascular endothelial growth factor and placental growth factor to VEGF receptors on endothelial cells. *AM J PHYSIOL HEART CIRC PHYSIOL*, 286:H153–H164, 2004.

[183] R.J. Filion and A.S. Popel. A reaction-diffusion model of basic fibroblast growth factor interactions with cell surface receptors. *ANN BIOMED ENG*, 32(5):645–663, 2004.

[184] C. Rattanakul, Y. Lenbury, J. Bell, V. Chatsudthipong, W. Triampo, and P.S. Crooke. Spatial turing-type pattern formation in a model of signal transduction involving membrane-based receptors coupled by g proteins. *CANCER INFORM*, 2:329–343, 2006.

[185] B.A. Earnshaw and P.C. Bressloff. Biophysical model of ampa receptor trafficking and its regulation during long-term potentiation/long-term depression. *J NEUROSCI*, 26(47):12362–12373, 2006.

[186] B.A. Earnshaw and P.C. Bressloff. Modeling the role of lateral membrane diffusion in ampa receptor trafficking along spiny dendrite. *J COMPUT NEUROSCI*, 25:366–389, 2008.

[187] D. R. Daniels. Receptor-ligand diffusion-limited reaction rates on curved membranes. *CHEM PHYS LETT*, 795, 2022.

[188] A. Kusumi, Y. Sako, and M. Yamamoto. Confined lateral diffusion of membrane receptors as studied by single particle tracking (nanovid microscopy). effects of calcium-induced differentiation in cultured epithelial cells. *BIOPHYS J*, 65:2021–2040, 1993.

[189] K. Ritchie, X-Y. Shan, J. Kondo, K. Iwasawa, T. Fujiwara, and A. Kusumi. Detection of non-brownian diffusion in the cell membrane in single molecule tracking. *BIOPHYS J*, 88:2266–2277, 2005.

[190] E. Atilgan and X. C. Sun. Shape transitions in lipid membranes and protein mediated vesicle fusion and fission. *J CHEM PHYS*, 16(095102), 2007.

[191] S.J. Briddon, J. Gandía, O.B. Amaral, S. Ferré, C. Lluís, R. Franco, S.J. Hill, and F. Ciruela. Plasma membrane diffusion of g protein-coupled receptor oligomers. *BIOCHIM BIOPHYS ACTA*, 1783:2262–2268, 2008.

[192] M.J. Paszek, D. Boettiger, V.M. Weaver, and D.A. Hammer. Integrin clustering is driven by mechanical resistance from the glycocalyx and the substrate. *PLOS COMPUT BIO*, 5(12), 2009.

[193] T. Duke and I. Graham. Equilibrium mechanisms of receptor clustering. *PROG BIOPHYS MOL BIO*, 100:18–24, 2009.

[194] Jun F. Allard, Omer Dushek, Daniel Coombs, and P.A. van der Merwe. Mechanical modulation of receptor-ligand interactions at cell-cell interfaces. *BIOPHYS J*, 102(6):1265–1273, 2012.

[195] D. Iron and J. Rumsey. A model of surface receptor aggregation. *J MATH BIOL*, 75:705–731, 2017.

[196] L. Martini, S. Brameyer, E. Hoyer, K. Jung, and U. Gerland. Dynamics of chromosomal target search by a membrane-integrated one-component receptor. *PLOS COMPUT BIO*, 17(2), 2021.

[197] G.I. Bell. Models for the specific adhesion of cells to cells. *SCIENCE*, 200(4342):618–627, 1978.

[198] E. Evans. New membrane concept applied to the analysis of fluid shear and micro-pipette deformed red blood cells. *BIOPHYS J*, 13(9):941–954, 1973.

[199] S.J. Singer and G.L. Nicolson. The fluid mosaic model of the structure of cell membranes. *SCIENCE*, 175(4023):720–731, 1972.

[200] P Sens and MS Turner. Budded membrane microdomains as tension regulators. *PHYS REV E*, 73:031918, Mar 2006.

[201] P. Liu, Y. Zhang, Q. Cheng, and C. Lu. Simulation of the spreading of a vesicle on a substrate surface mediated by receptor-ligand binding. *J MECH PHYS SOLIDS*, 55(6):1166–1181, 2007.

[202] M. Ubbink. The courtship of proteins: Understanding the encounter complex. *FEBS Letters*, 583:1060–1066, 2009.

[203] T. Selzer and G. Schreiber. New insights into the mechanism of protein-protein association. *PROTEINS*, 45:190–198, 2001.

[204] P. Bongrand. Ligand-receptor interactions. *REP PROG PHYS*, 62:921–968, 1999.

[205] Bruce Alberts. *Molecular biology of the cell.* New York : Garland Science, 4th ed. edition, 2002.

[206] A Salvadori, M Serpelloni, M Arricca, C Ravelli, E Grillo, and S Mitola. Relocation of proteins on advecting endothelial cells membranes: modeling, experiments, and simulations. submitted to J R SOC INTERFACE, 2022.

[207] G.I. Bell, M Dembo, and P. Bongrand. Cell adhesion. competition between nonspecific repulsion and specific bonding. *BIOPHYS J*, 45(6):1051–1064, 1984.

[208] B. Goldstein, C. Wofsy, and G. Bell. Interactions of low density lipoprotein receptors with coated pits on human fibroblasts: Estimate of the forward rate constant and comparison with the diffusion limit. *PNAS*, 78(9):5695–5698, 1981.

[209] B. Goldstein, R. Griego, and C. Wofsy. Diffusion-limited forward rate constants in two dimensions. application to the trapping of cell surface receptors by coated pits. *BIOPHYS J*, 46(5):573–586, 1984.

[210] A. Boulbitch, Z. Guttenberg, and E. Sackmann. Kinetics of membrane adhesion mediated by ligand-receptor interaction studied with a biomimetic system. *BIOPHYS J*, 81(5):2743–2751, 2001.

[211] Q. Cheng, P. Liu, H. Gao, and Y. Zhang. A computational modeling for micropipette-manipulated cell detachment from a substrate mediated by receptor-ligand binding. *J MECH PHYS SOLIDS*, 57:205–220, 2009.

[212] T. Sohail, T. Tang, and B. Nadler. Adhesive contact of a fluid-filled membrane driven by electrostatic forces. *INT J SOLIDS STRUCT*, 50:2678–2690, 2013.

[213] Clarence E Chan and David J Odde. Traction dynamics of filopodia on compliant substrates. *SCIENCE*, 322(5908):1687–1691, Dec 2008.